UNIVERSITY OF SOUTHAMPTON

MONTE CARLO SIMULATIONS OF DIATOMICS, POLYMERS AND ALKANES

GIULIO ROBERTO GALASSI

A dissertation submitted in partial fulfilment of the requirements for the degree of Doctor of Philosophy at the University of Southampton.

Department of Chemistry. September 1993.

CONTENTS

UNIVERSITY OF SOUTHAMPTON

ABSTRACT

FACULTY OF SCIENCE

CHEMISTRY

Doctor of Philosophy

MONTE CARLO SIMULATIONS OF DIATOMICS, POLYMERS AND ALKANES

by Giulio Roberto Galassi

The Gibbs Monte Carlo simulation method has been used to determine the liquid-vapour coexistence envelope for a range of diatomic molecules. In particular the phase diagram of chlorine has been investigated with two different potential representations of the molecule. The coexistence envelopes determined with the two potential representations of chlorine were in close agreement with one another and with the experimentally determined coexistence envelope. These simulations reveal that the phase envelope for chlorine is not sensitive to the details of the potential model used. In addition, various critical properties of the diatomic molecules were examined as a function of the molecular anisotropy and the accuracy of the RISM theory was investigated for a number of these diatomic molecules.

Monte Carlo simulations were performed of polymer chains in solution. Competitive adsorption effects between the solvent particles and the polymer chains at hard and attractive walls were investigated. The adsorption or depletion of the polymer chain at a wall was found to be sensitive not only to the details of the polymer-wall interactions, but also to the solvent-wall interactions. The scaling properties of polymer chains between walls were examined and again found to be sensitive to the details of both the polymer-wall interactions and solvent-wall interactions.

Equations of state were calculated for athermal butane, heptane and decane by performing Monte Carlo simulations between hard walls. The simulation equations of state were compared to the equations of state obtained with the wall-PRISM equation. The wall-PRISM equation was found to overestimate the pressure for the above molecules at low densities and underestimate the pressure at high densities. Simulation density profiles between the walls were compared to the density profiles of the wall-PRISM theory. The agreement between the profiles was qualitative only. Finally Monte Carlo simulations were performed in the bulk with the athermal alkanes and the radial distribution functions obtained compared to the results of PRISM theory.

ACKNOWLEDGEMENTS

I would like to thank my PhD supervisor Professor D.J. Tildesley for his friendship and guidance over the last three years. It has been a pleasure to work for one of the leaders in the field of computer simulations.

I would like to thank the following members of the chemical physics group: Dr. Andrew Emerson for his help in the first year of my PhD with computer programming and in the third year of my PhD for many interesting discussions on the Monte Carlo simulation technique; Dr. David Adolf for many invaluable discussions on Polymer Physics; Ken, Steve, Kwang Soo Kim, Martin, Doug and the other members of the chemical physics group who have helped to make the group a pleasurable one to work in.

A big thankyou is due to my parents for their help and support during the six years that I have spent in higher education.

Finally, I would like to dedicate this thesis to Collette, whose love and understanding over the last three years have kept me (somewhat) sane.

1. Phase Coexistence and The Gibbs Ensemble Method

1.1 Introduction

The ability to determine the phase coexistence properties of a given system is of importance for industrial applications. The design of industrial distillation units requires information on the vapour and liquid equilibrium compositions for the systems to be used in conjunction with the unit. Binary vapour-liquid equilibrium information is also of importance in predicting the distributions of the various components in liquid-liquid extraction [1]. Liquid-liquid extraction is a widely used method of separation both in the laboratory and on a plant scale. The basic principle of liquid extraction is that of differential solubility, where the components of a mixture can be separated by differential distribution between the two separate liquid phases created by the addition of a suitable solvent or solvent mixture. The process was first used on a large scale in the removal of aromatic hydrocarbons from kerosine [1]. It is therefore important to have available phase equilibria data for systems in which we wish to perform liquid-liquid extraction. For many binary systems the liquid-vapour equilibrium data can be obtained experimentally using the continuous distillation or recirculation still. This type of still is shown schematically in Figure 1.1 and comprises of a boiling flask, condenser and condensate receiver. Boiling occurs in the flask A, which is heated by an electric heater, gas flame or other means. Vapour rises to the offtake, B, and into the condenser G, where it falls into L, the condensate receiver. When the receiver is full, the condensate overflows and returns through N to the boiling flask. Samples of the two phases are taken at F and K. In this way the compositions of the vapour and liquid phases can be determined as a function of the temperature set by the boiling flask heater. It is more difficult to obtain phase equilibrium data and equilibrium compositions for multicomponent fluids due to the increased complexity in their compositions. In addition, although distillation stills of one form or another are widely used, specific systems and operating conditions require the use of special still designs. For instance high pressure equilibrium measurements require the construction of stills made of metal. The difficulty in obtaining phase equilibria data for multi-component systems and the need to construct specialised stills for measurements on binary systems at high pressures makes it desirable to be able to obtain this information by theoretical means or by

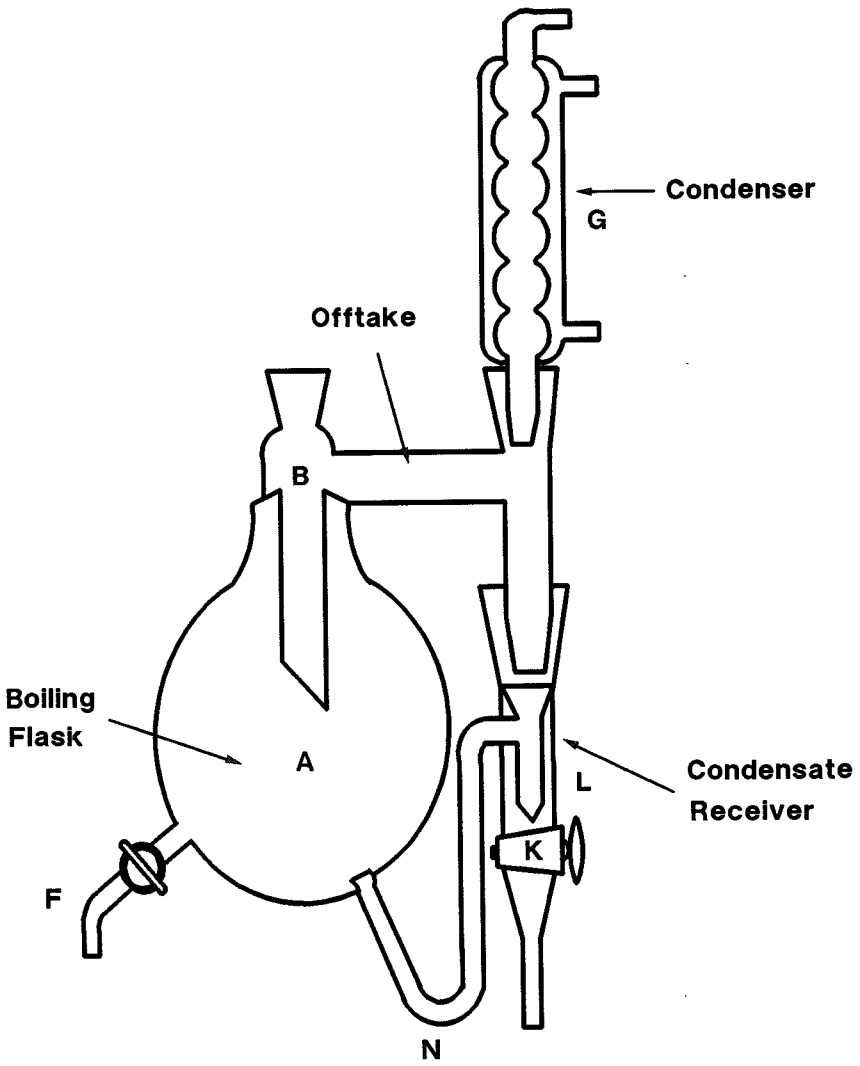

Figure 1.1. A schematic diagram of a distillation still used in the determination of equilibrium compositions of fluids in phase equilibrium.

simulation techniques. It is also of interest to be able to calculate phase equilibrium data by simulation for a given atomic or molecular system, to provide essentially exact information against which to test theories of phase equilibria. By comparing theoretical predictions with experimental results for vapour-liquid equilibrium, uncertainties are introduced about how closely a particular model mimics a real liquid or liquid-vapour system. The uncertainties about the potential model used can be removed by comparing the predictions of the theory with computer simulation results.

The determination of the coexistence properties of liquids, solids and gases has been the subject of investigation by computer simulation for the last 30 years. Over this period of time a number of simulation techniques have been developed for locating the phase envelope of a given atomic or molecular system and calculating the thermodynamic properties of the coexisting phases. A number of these methods will be discussed in this and the following chapter, including the Gibbs ensemble method, a recent simulation method for the direct determination of the coexistence properties of a given model.

1.2 Statistical Mechanics and Phase Equilibria

If we wish to determine the thermodynamic conditions under which a given model fluid exhibits phase coexistence, we have to ensure that the coexisting phases satisfy a number of well known equalities [2]. For two phases of a given single species fluid these equalities are,

$$\mu_1 = \mu_2 \ , \tag{1.1}$$

$$p_1 = p_2 \ , \tag{1.2}$$

$$T_1 = T_2 \ , \tag{1.3}$$

where μ is the chemical potential, p the pressure, T the temperature and the subscripts 1 and 2 refer to the two coexisting phases respectively.

A knowledge of the equation of state for a particular system would enable us to determine the state points that satisfy the equalities of eqns (1.1), (1.2) and (1.3). Alternatively if the free energy of the system was known as a function of volume and

temperature then it would in principle be possible to calculate the boundary lines separating the phases that the system may exhibit.

In the canonical ensemble (an ensemble at constant-NVT), the appropriate free energy that we would have to calculate is the Helmholtz free energy, A. The Helmholtz free energy is,

$$A = -k_B T \ln Q_{NVT} , \tag{1.4}$$

where Q_{NVT} is the partition function for the canonical ensemble and is defined as,

$$Q_{NVT} = \frac{h^{-3N}}{N!} \int\int \exp[-\beta H(\mathbf{r}^N, \mathbf{p}^N)] \, d\mathbf{r}^N \, d\mathbf{p}^N , \tag{1.5}$$

where the notation $\mathbf{r}^N$ is used to denote the 3N coordinates of the particles in the system. In eqn (1.5) H is the hamiltonian of the system of interest and $\beta=1/k_BT$. The hamiltonian is a function of the positions and momenta of the N particles in the system and can be written as,

$$H(\mathbf{r}^N, \mathbf{p}^N) = \frac{1}{2m} \sum_{i=1}^{N} |\mathbf{p}_i|^2 + U(\mathbf{r}^N) , \tag{1.6}$$

where m is the particle mass and $U(\mathbf{r}^N)$ is the total potential energy for the N particles. The 3N coordinates and 3N momenta that determine the value of the hamiltonian in eqn (1.6) define a phase point in a 6N-dimensional phase space. The factor h^{-3N} in eqn (1.5) ensures that the partition function is dimensionless and the factor of 1/N! takes into account the indistinguishability of the particles. Making use of the hamiltonian of eqn (1.6) in the partition function, the integration over the momenta can be carried out explicitly, yielding a factor of $(2\pi m k_B T)^{1/2}$ for each of the degrees of freedom. The partition function may be written as a product of the kinetic (ideal gas) and potential (excess) parts,

$$Q_{NVT} = Q_{id} \, Q_{ex} , \tag{1.7}$$

where Q_{id} is the partition function for the ideal gas and Q_{ex} contains the excess part.

The term Q_{id} is given by,

$$Q_{id} = \frac{V^N}{N!\,\Lambda^{3N}} , \tag{1.8}$$

where Λ is the de Broglie thermal wavelength defined by,

$$\Lambda = \left(\frac{\beta h^2}{2\pi m}\right)^{\frac{1}{2}} , \tag{1.9}$$

and the term Q_{ex} is given by,

$$Q_{ex} = \frac{1}{V^N} Z_{NVT} . \tag{1.10}$$

In eqn (1.10), Z_{NVT} is known as the configurational integral and is defined as,

$$Z_{NVT} = \int \exp\left[-\beta U(\mathbf{r}^N)\right] d\mathbf{r}^N . \tag{1.11}$$

If the free energy can be calculated then the pressure and chemical potential of the system can be obtained from the relations,

$$P = k_B T \left(\frac{\partial A}{\partial V}\right)_T , \tag{1.12}$$

$$\mu = \left(\frac{\partial A}{\partial N}\right)_{V,T} . \tag{1.13}$$

It is therefore evident that if we wish to calculate the free energy during the course of a computer simulation, it is necessary to evaluate the partition function of eqn (1.5), which in turn requires the evaluation of the configurational integral of eqn (1.11). The configurational integral depends on the total volume of phase space accessible to the system of interest. At typical liquid densities, the majority of points in the 6N-dimensional phase space include overlapped particles. Such configurations result in a zero contribution to the configurational integral. An accurate evaluation of the configurational integral therefore requires the identification and evaluation of the small number of points in phase space which make significant contributions to the integral.

In general it is difficult to do this accurately.

Although we are not able to directly calculate the free energy during a simulation, we can in fact still calculate the pressure of the system. This is because the pressure of the fluid within a simulation is a 'mechanical' property of the system. The term 'mechanical' refers to quantities that can be expressed as functions of the coordinates and momenta of the particles in the system. It is therefore possible to express mechanical properties of a system in terms of ensemble averages of the microscopic variables of the system. The pressure of a simulation can be calculated using the virial theorem,

$$PV = Nk_BT + \langle W \rangle , \tag{1.14}$$

where <W> denotes the ensemble average of the virial. For a system composed of N particles the virial is defined as,

$$W = \frac{1}{3}\sum_{i=1}^{N} \mathbf{r}_i \cdot \mathbf{f}_i , \tag{1.15}$$

$$= \frac{1}{3}\sum_{i=1}^{N}\sum_{j>i} \mathbf{r}_{ij} \cdot \mathbf{f}_{ij} , \tag{1.16}$$

where $\mathbf{r}_i$ defines the coordinates of the i^{th} particle and $\mathbf{f}_i$ denotes the force acting on particle i due to the remaining (N-1) particles in the system. Other examples of 'mechanical' properties of a system are the potential and kinetic energies of the system.

In contrast to the pressure, the chemical potential can be expressed only in terms of the partition function and cannot be expressed as an ensemble average of any function of the microscopic variables of the system. The chemical potential of a simulation is a 'thermal' property of the simulation where the term 'thermal' refers to quantities which depend on the total volume of phase space accessible to a given system. Other examples of the thermal properties of a system are the entropy and free energy. Therefore as we cannot directly calculate the free energy of a system and we require this quantity in the calculation of the chemical potential, we either need an alternative route to the free energy or another method of calculating the chemical potential.

A technique for directly calculating the chemical potential of a system is the Widom particle insertion technique [3]. This technique is based on the calculation of the ratio of the configurational integrals of two systems. Introducing eqn (1.4) into the definition of the chemical potential of eqn (1.13) yields the expression,

$$\mu = -k_B T \left(\frac{\partial \ln Q_{NVT}}{\partial N} \right)_{VT} . \tag{1.17}$$

Factoring out the configurational integral Z_{NVT}, from the partition function leads to,

$$\frac{\mu - \mu_{id}}{k_B T} = \ln V - \frac{\partial \ln Z_{NVT}}{\partial N} , \tag{1.18}$$

where μ_{id} is the value of μ for a fluid at the same temperature and density, but for which the intermolecular interaction $U(\mathbf{r}^N)$ is zero. μ_{id} is,

$$\frac{\mu_{id}}{k_B T} = \ln A^3 + \ln \rho , \tag{1.19}$$

where ρ is the density. The number derivative of eqn (1.18) for large N becomes,

$$\frac{\partial \ln Z_{NVT}}{\partial N} = \frac{\ln Z_{NVT} - \ln Z_{(N-1)VT}}{N-(N-1)} = \ln \left(\frac{Z_{NVT}}{Z_{(N-1)VT}} \right) . \tag{1.20}$$

The ratio of the configurational integrals in eqn (1.20) can be written as,

$$\frac{Z_{NVT}}{Z_{(N-1)VT}} = \frac{\int d\mathbf{r}^N \exp(-\beta U(\mathbf{r}^N))}{\int d\mathbf{r}^{N-1} \exp(-\beta U(\mathbf{r}^{N-1}))} , \tag{1.21}$$

$$= \frac{\int d\mathbf{r}_1 \int d\mathbf{r}^{N-1} \exp(-\beta \psi) \exp(-\beta U(\mathbf{r}^{N-1}))}{\int d\mathbf{r}^{N-1} \exp(-\beta U(\mathbf{r}^{N-1}))} , \tag{1.22}$$

$$= V \langle \exp[-\beta \psi] \rangle , \tag{1.23}$$

where V is the volume of the system under investigation. In eqns (1.20) and (1.21), Z_{NVT} and $Z_{(N-1)VT}$ represent the configurational integrals of systems with N and (N-1) particles respectively. In eqns (1.22) and (1.23) ψ is the potential energy of a particle

interacting with the remaining (N-1) particles in the system. We can now use eqns (1.20) and (1.23) in (1.18) to give,

$$\frac{\mu - \mu_{id}}{k_B T} = -\ln \langle \exp[-\beta\psi] \rangle , \qquad (1.24)$$

and hence eqn (1.24) gives us a route to the calculation of the chemical potential of a system. The chemical potential of a system can be calculated via eqn (1.24) without having to directly evaluate the partition function.

The Widom particle insertion technique is implemented in a simulation as follows. Fictitious particles are inserted into a system in random positions. These particle insertions are carried out at specified intervals during the course of a simulation. When the particle has been inserted, the energy of interaction, ψ, of this particle with the (N-1) particles in the system is calculated. The value of $\exp[-\beta\psi]$ is then calculated and averaged over the course of the simulation and the chemical potential of the system obtained from eqn (1.24). The particle inserted into the system does not interfere with the other particles in the system, it merely samples the potential energy of the other particles in the system.

In principle the Widom particle insertion technique is valid for simulations in both high and low density regimes. In practice however, at high densities the random insertion of a test particle into the system will result in an overlapped configuration. Consequently the value of $\exp[-\beta\psi]$ will be zero for most of the attempted insertions and so will not contribute to the average. However, the value of $\ln\langle\exp[-\beta\psi]\rangle$ is known to be large and positive at high liquid densities [4]. Therefore at high liquid densities it is likely that the calculated value for the chemical potential will not be as accurate as the chemical potentials calculated for low density systems.

Hence in computer simulations we require an alternative method to obtain the free energy of a system. In experimental situations, the free energy of a system is not directly measurable. To determine the free energy of a system at a particular state point, a reversible path is constructed which links the state point of interest to a state of known free energy, such as an ideal gas or a low-temperature harmonic crystal.

The change in free energy along the reversible path is then calculated by thermodynamic integration of the relations,

$$\left(\frac{\partial A}{\partial V}\right)_{N,T} = -P \,, \tag{1.25}$$

$$\left(\frac{\partial (A/T)}{\partial (1/T)}\right)_{N,V} = E \,, \tag{1.26}$$

where E is the internal energy of the system.

It is sometimes possible to use the above procedure in computer simulations. The method often fails however, when the path of the thermodynamic integration crosses a first order phase transition. This failure in the method is because computer simulations study small periodic systems. In such systems it is difficult to obtain two-phase coexistence, as the free energy penalty for forming an interface prevents two-phase coexistence. Instead in practice one of the phases usually becomes superheated or supercooled to a point at which it becomes mechanically unstable and transforms irreversibly into the other phase. Thus the path being followed along the thermodynamic integration is no longer reversible and the method fails. The early attempts to study first-order phase transitions by simulation [5,6,7] failed for this reason as the systems studied by these simulations typically contained between 32 and 108 particles. Using larger systems in 2 dimensions ensures that the relative contribution of the interface to the free energy diminishes, allowing two-phase coexistence to occur. The first simulation that was successful in locating the coexistence point of a first-order phase transition was described in [8]. In this work the melting transition of a two-dimensional hard disk system was investigated by thermodynamic integration through the two-phase region. In the two-phase region, the system size used in the simulations was sufficiently large (870 hard disks) to allow the two phases to coexist. Large pressure fluctuations occurred in the two phase region, necessitating long simulation runs to obtain accurate values for the pressure. In the two-phase region the pressure exhibited a small system, or, van der Waals-like loop and the densities of the coexisting phases were computed via a Maxwell equal area construction.

In three dimensional systems, the hysteresis effects associated with the solid-fluid transition are so severe that other methods are required to calculate the melting point.

The first technique designed to take care of this problem was that of Hoover and Ree [9]. Their method is as follows. Thermodynamic integration from a dilute gas to a solid is difficult because of the requirement that the path is reversible. The requirement of reversibility can be achieved by carrying out an integration along an artificial path from a reference state of known free energy to the solid under consideration. A reversible path is constructed taking as a reference system a dilute single-occupancy lattice gas that can be compressed reversibly to give the solid phase.

The method of Hoover and Ree was subsequently applied by Hansen and Verlet to the study of liquid-vapour coexistence in the 3 dimensional Lennard-Jones fluid [10]. In this work a reversible isothermal path was constructed joining continuously the two single-phase states. This was achieved by constraining the system to remain homogeneous in the transition region. Practically the homogeneity condition was attained by subdividing the system into a number of cells and setting upper and lower bounds on the number of atoms allowable in each of the cells. Large density fluctuations which lead to phase separations are thus avoided and a reversible path connecting the gaseous and liquid phases can be constructed. The numbers of particles allowable in each of the cells was chosen so that the thermodynamic properties of the two phases were not disturbed. Integration of the pressure versus volume curve along the isotherm connecting the gaseous and liquid phases yields the liquid-phase free energy and thus the transition data was determined.

Another possible route to the calculation of the free energy of a system is to simulate in the grand canonical ensemble [11]. This is a constant-μVT ensemble in which the difficulty of determining the chemical potential is avoided by specifying it as an input to the simulation. The problem now becomes one of determining the density as a function of the chemical potential. An integral part of the Grand canonical ensemble is the insertion and removal of particles from the system of interest. However, as with the Widom particle insertion technique, at high liquid densities problems are encountered when trying to insert particles into the system. In addition it is necessary to perform several simulations to obtain an accurate determination of a single phase coexistence point. As the number of components in the system increases, it is necessary to perform an ever larger number of simulations.

Powles [4] introduced a method for the calculation of phase equilibria based on the

Widom particle insertion technique. This method will be discussed in some detail in Chapter 2.

The Gibbs simulation method [12,13] is a significant improvement over these methods. The technique allows for the direct determination of phase coexistence points without recourse to the calculation of free energies or chemical potentials. The method is readily generaliseable to mixtures and yields a coexistence point from a single simulation. A description of the Gibbs ensemble method will now be given.

1.3 The Gibbs Ensemble

Consider a system at constant temperature T, volume V, and containing a number of particles N. The system is now divided into two non-interacting subsystems, 1 and 2. The particles are distributed between the two subsystems subject to the constraint of fixed total number of particles. The volumes of the two subsystems are allowed to vary such that the total volume remains constant. We can now write down a partition function appropriate for this ensemble, that takes into account the number of possible distributions of the N particles between the two subsystems, that allows for a subsystem's volume to vary between 0 and V and that considers all possible configurations of each subsystem. This partition function is [14],

$$\bar{Q}_{NVT} = \frac{1}{V\Lambda^{3N}N!}\sum_{n_1=0}^{N}\binom{N}{n_1}\int_0^V dV_1 \int_{V_1} d\mathbf{r}_1^{n_1}\exp[-\beta U_1(\mathbf{r}_1^{n_1})]$$

$$\times \int_{V-V_1} d\mathbf{r}_2^{N-n_1}\exp[-\beta U_2(\mathbf{r}_2^{N-n_1})] \qquad (1.27)$$

where n_1 denotes the number of particles in subsystem 1, V_1 denotes the volume of subsystem 1, $\mathbf{r}_1^{n_1}=\mathbf{r}_1,\ldots,\mathbf{r}_{n_1}$ and $\mathbf{r}_2^{N-n_1}=\mathbf{r}_{n_1+1},\ldots,\mathbf{r}_N$ are the positions of the particles in subsystems 1 and 2 respectively, Λ is the thermal de Broglie wavelength and $U(\mathbf{r}^{n_i})$ is the intermolecular potential for the n_i particles in the given subsystem. The bar over the Q_{NVT} is used to distinguish the partition function of the Gibbs ensemble from the partition function of the canonical ensemble (eqn (1.5)).

It is possible to make use of this definition of the partition function to define the free energy density of the Gibbs ensemble. In the thermodynamic limit this free energy

density is defined as [15],

$$f(\rho) \equiv \lim_{V\to\infty} f_V(\rho) \equiv \lim_{\substack{V\to\infty \\ N/V=\rho}} \frac{-1}{\beta V} \ln \bar{Q}_{NVT} , \qquad (1.28)$$

where $\rho=N/V$ is the density of the system.

This definition of the free energy density for the Gibbs ensemble can be used in conjunction with the saddle point theorem [16] to derive some of the properties of the ensemble. The saddle point theorem states that for a macroscopic system in equilibrium, the probability that the free energy deviates from its minimum value is small. Therefore when calculating ensemble averages in an ensemble such as the Gibbs ensemble, it is only necessary to take into account those configurations which occur when the free energy has its minimum.

The free energy density of eqn (1.28) has been shown to be identical to the free energy density of the canonical ensemble [17] in the thermodynamic limit. In the absence of any phase transitions it is possible to show that the minimum in the free energy density of eqn (1.28) occurs when both subsystems have the same density ρ, and this density is equal to the equilibrium density of the canonical ensemble at the same state point. In the presence of a first order phase transition, the minimum in the above free energy density occurs when the densities of the subsystems are not equivalent. In this situation, the subsystems attain densities ρ_l and ρ_g, the densities corresponding to the liquid and gaseous phases respectively, in the canonical ensemble at the same state point.

1.4 Computational Implementation of The Gibbs Ensemble.

Having defined the partition function of the Gibbs ensemble we now need to construct a Monte Carlo procedure which samples from the Gibbs ensemble.

1.4.1 Monte Carlo Methods

During the course of a computer simulation, we are usually interested in calculating ensemble averages of the 'mechanical' properties of the system. For instance we may be interested in calculating <U>, the ensemble average of the configurational energy.

If we are working in the canonical ensemble, this quantity is defined as,

$$<U>_{NVT} = \frac{\int d\mathbf{r}^N \, U(\mathbf{r}^N) \exp(-\beta U(\mathbf{r}^N))}{Z_{NVT}} , \qquad (1.29)$$

where $U(\mathbf{r}^N)$ is the total potential energy for a system of N particles with coordinates $\mathbf{r}^N$ and Z_{NVT} is the configurational integral for the system defined by eqn (1.11).

Many dimensional integrals such as the configurational integral are most efficiently evaluated using Monte Carlo integration techniques [18]. Such an integration scheme would involve generating a large number of random positions, N_{conf}, for the N particles in the system and the ensemble average approximated by,

$$<U>_{NVT} \approx \frac{\sum_{i=1}^{N_{conf}} U(\Gamma_i) \exp[-\beta U(\Gamma_i)]}{\sum_{i=1}^{N_{conf}} \exp[-\beta U(\Gamma_i)]} , \qquad (1.30)$$

where Γ_i represents the point in phase space corresponding to the i^{th} generated configuration. In this integration scheme, successive configurations of the particles in the system are chosen with equal probability and weighted with the exponential factor. At typical liquid densities however, a large number of the configurations have an exponential factor of zero due to overlaps with other particles in the system. Hence only a small proportion of the generated configurations will contribute to the ensemble average. Thus a large number of configurations must be generated to yield an accurate estimate of the ensemble average. It is therefore desirable to attempt to preferentially sample those regions of phase space which make important contributions to the integrals. This can be achieved by using the importance sampling technique.

In this technique, configurations are generated according to a probability distribution $\rho(\Gamma)$ and eqn (1.30) replaced by,

$$\langle U \rangle_{NVT} \approx \frac{\sum_{i=1}^{N_{conf}} U(\Gamma_i) \exp[-\beta U(\Gamma_i)] / \rho(\Gamma_i)}{\sum_{i=1}^{N_{conf}} \exp[-\beta U(\Gamma_i)] / \rho(\Gamma_i)} \quad . \tag{1.31}$$

In the canonical ensemble, the natural choice for $\rho(\Gamma)$ is the Boltzmann distribution, namely,

$$\rho_{NVT}(\Gamma) = \frac{\exp[-\beta U(\Gamma)]}{Z_{NVT}} \quad . \tag{1.32}$$

This choice of the probability distribution $\rho(\Gamma)$ is the Metropolis form of the Monte Carlo method [19]. The ensemble average $\langle U \rangle_{NVT}$ is now given by the average over the N_{conf} configurations,

$$\langle U \rangle_{NVT} = \frac{1}{N_{conf}} \sum_{i=1}^{N_{conf}} U(\Gamma_i) \; . \tag{1.33}$$

To generate a sequence of states with a probability given by $\rho(\Gamma)$ we set up a Markov chain of states in such a way that it has a limiting distribution of $\rho(\Gamma)$. A Markov chain is a sequence of trial configurations which satisfy two conditions. The first condition is that the outcome of each trial configuration depends only on the outcome of the trial configuration that immediately precedes it. The second of these conditions is that the outcome of each trial configuration must belong to a finite set of outcomes $(\Gamma_1, \Gamma_2, ..., \Gamma_m)$ called the state space. In a computer simulation this second condition is satisfied due to the fact that continuous variables such as a particles position **r** are held in a discrete form in the computer's memory. Thus the number of possible configurations attainable in a computer simulation is finite and limited by the number of significant figures available to the computer running the simulation.

To satisfy the first of the above conditions we consider two adjacent configurations Γ_m and Γ_n, linked by a transition probability π_{mn}, which is the probability of reaching the state n from state m. We denote the probabilities of the configurations m and n

occurring by ρ_m and ρ_n respectively. For very long Markov chains the probability of a given configuration occurring approaches a unique limit such that the components of the distribution satisfy,

$$\sum_m \rho_m \pi_{mn} = \rho_n \ , \tag{1.34}$$

$$\boldsymbol{\rho\pi} = \boldsymbol{\rho} \ . \tag{1.35}$$

In addition the transition probabilities π_{mn} must also satisfy the normalisation condition,

$$\sum_n \pi_{mn} = 1 \ , \tag{1.36}$$

for any given configuration m. We now wish to solve eqns (1.34) and (1.35) for the π_{mn} in such a way as to give rise to a Markov chain which in the canonical ensemble has the elements $\rho_m = \rho_{NVT}(\Gamma_m)$ for each point Γ_m in phase space as its limiting distribution. A useful trick in searching for a solution to eqns (1.34) and (1.35) is to make use of the stronger condition of microscopic reversibility,

$$\rho_m \pi_{mn} = \rho_n \pi_{nm} \ . \tag{1.37}$$

Summing over all the states m and making use of eqn (1.36) we regain equation (1.34),

$$\sum_m \rho_m \pi_{mn} = \sum_m \rho_n \pi_{nm} = \rho_n \sum_m \pi_{nm} = \rho_n \ . \tag{1.38}$$

A suitable scheme for generating a trajectory in the phase space of the canonical ensemble involves choosing a transition matrix which satisfies eqns (1.36) and (1.37). A suitable transition matrix to use is that of Metropolis et al. This is,

$$\pi_{mn} = \alpha_{mn} \qquad \rho_n \geq \rho_m \qquad m \neq n, \tag{1.39}$$

$$\pi_{mn} = \alpha_{mn} \left(\frac{\rho_n}{\rho_m} \right) \qquad \rho_n < \rho_m \qquad m \neq n, \tag{1.40}$$

$$\pi_{mm} = 1 - \sum_{n \neq m} \pi_{mn} \ , \tag{1.41}$$

where α is the underlying stochastic matrix of the Markov chain and has the property $\alpha_{mn}=\alpha_{nm}$ (ie. the matrix is symmetrical). This solution to the transition matrix is not unique and indeed, other solutions have been proposed for the problem eg. [20]. It should be noted that the solution to the problem involves the ratio ρ_n/ρ_m and is therefore independent of the configurational integral.

To implement the Metropolis solution to the transition matrix in a computer simulation, it is necessary to specify the matrix α. In this implementation of the Monte Carlo method the matrix α is designed to take the system from a state m into a neighbouring state n with equal probability. Thus in a computer simulation we can implement this requirement by choosing a particle, displacing it from its current position $\mathbf{r}_m$ with equal probability to any point $\mathbf{r}_n$ within a cube R. The cube is centred on $\mathbf{r}_m$ and is of side $2\delta r_{max}$ where δr_{max} is the maximum allowed displacement of the particle in any direction. In a computer simulation there are a finite number of trial positions within the cube, N_R, and α is simply,

$$\alpha_{mn} = \frac{1}{N_R} \qquad \mathbf{r}_n \in \mathbf{R} \ , \tag{1.42}$$

$$\alpha_{mn} = 0 \qquad \mathbf{r}_n \notin \mathbf{R} \ . \tag{1.43}$$

In deciding whether to accept this trial move we need to calculate the ratio ρ_n/ρ_m, the relative probabilities of configurations m and n occurring. To achieve this we calculate the change in potential energy for a particle moving from state m to state n. Denoting this particle as the i^{th} particle, the potential energy change is,

$$\delta U_{nm} = \sum_{j=1\neq i}^{j=N} U(r_{ij}^{n}) - \sum_{j=1\neq i}^{j=N} U(r_{ij}^{m}) \ . \tag{1.44}$$

There are two possible situations to consider. If $\delta U_{nm}\leq 0$ then $\rho_n \geq \rho_m$ and eqn (1.39) applies. Since the move was made according to the underlying stochastic matrix α_{mn}, the move is immediately accepted as a new configuration for the liquid. If $\delta U_{nm}>0$ then $\rho_n<\rho_m$ and eqn (1.40) applies. The trial configuration must be accepted with a probability given by ρ_n/ρ_m. Again the factor α_{mn} is automatically taken into account in making the move itself.

The ratio of probabilities can be expressed as the Boltzmann factor of the energy difference,

$$\frac{\rho_n}{\rho_m} = \frac{Z_{NVT}^{-1} \exp[-\beta U_n]}{Z_{NVT}^{-1} \exp[-\beta U_m]} = \exp[-\beta\, \delta U_{nm}] \ . \qquad (1.45)$$

To accept a trial move with a probability $\exp[-\beta\delta U_{nm}]$ a random number, χ, is generated in the range [0,1]. If $\exp[-\beta\delta U_{nm}]$ is greater than χ then the move is accepted. If the move is rejected then the configuration m is counted as the new configuration n of the Markov chain, in accord with the probability π_{mm} of eqn (1.41). In this procedure therefore, moves with energy changes δU_{nm} are accepted with a probability of $\exp[-\beta\delta U_{nm}]$. The entire procedure can be summarized by accepting moves whether uphill or downhill in energy with a probability $\min(1,\exp[-\beta\delta U_{nm}])$ where min has the same meaning as the FORTRAN MIN function.

1.4.2 The Gibbs ensemble Monte Carlo method

Having discussed the Metropolis Monte Carlo technique, we are now interested in applying this technique to the Gibbs ensemble. Consider now the partition function of the Gibbs ensemble eqn (1.27). If we rescale the coordinates of the particles in the boxes, the partition function for the Gibbs ensemble becomes,

$$\bar{Q}_{NVT} = \frac{1}{V\Lambda^{3N} N!} \sum_{n_1=0}^{N} \binom{N}{n_1} \int_0^V dV_1 \, V_1^{n_1} (V-V_1)^{N-n_1} \int d\xi_1^{n_1} \exp[-\beta U_1(n_1)]$$

$$\times \int d\xi_2^{N-n_1} \exp[-\beta U_2(N-n_1)] \ , \qquad (1.46)$$

where $\xi=\mathbf{r}/L$ is the scaled coordinate of a particle and L is the box length of the subsystem in which the particle is located. The notation $U_1(n_1)$ now denotes the positions of the n_1 particles within a box of unit side. We can now use this version of

the partition function to define the ensemble average of a quantity, f, in the Gibbs ensemble,

$$\langle f(\xi^N)\rangle = \frac{1}{\bar{Q}_{NVT}} \frac{1}{V\Lambda^{3N}N!} \sum_{n_1=0}^{N} \binom{N}{n_1} \int_0^V dV_1\, V_1^{n_1} (V-V_1)^{N-n_1}$$

$$\times \int d\xi_1^{n_1} \exp[-\beta U_1(n_1)] \int d\xi_2^{N-n_1} \exp[-\beta U_2(N-n_1)]\, f(\xi^N) \; . \qquad (1.47)$$

As with the case of the canonical ensemble introduced earlier, we now wish to preferentially sample those regions of phase space which make the most important contributions to the integrals of eqn (1.46). Inspection of eqn (1.46) reveals that this can be achieved by generating a Markov chain of states which has a limiting distribution proportional to,

$$\exp\left[\ln\binom{N}{n_1} + n_1 \ln V_1 + (N-n_1)\ln(V-V_1) - \beta U_1(n_1) - \beta U_2(N-n_1)\right] . \qquad (1.48)$$

If we now generate a large number of configurations with a probability proportional to eqn(1.48), the ensemble average $\langle f(\xi^N)\rangle$ is given by,

$$\langle f(\xi^N)\rangle \approx \frac{1}{N_{conf}} \sum_{i=1}^{Nconf} f(\xi^N) \; . \qquad (1.49)$$

As with the Metropolis Monte Carlo method, we are now faced with the problem of generating configurations chosen from the probability distribution given by eqn (1.48). This sampling from the distribution of eqn (1.48) can be achieved as follows.

In the definition of the Gibbs ensemble, we stated that it was a constant-NVT ensemble in which the total system is split into two subsystems. Three separate types of move are allowed to occur within the ensemble. The first of these moves allows the particles in the two subsystems to rearrange their configurations. In this move the two subsystems are independent of one another. In the second of these moves, the volumes of the subsystems are altered subject to the constraint of fixed total volume. During this move, the systems are correlated in such a way that a volume change of ΔV in subsystem 1 results in a volume change of $-\Delta V$ in subsystem 2, thus ensuring that the

requirement of fixed total volume is fulfilled. Finally, particles are allowed to interchange between the two subsystems subject to the constraint of fixed total number of particles.

In a Gibbs ensemble simulation we represent the two subsystems by separate simulation boxes which we will refer to as boxes 1 and 2 respectively. Periodic boundary conditions are applied to each of the simulation boxes. At the beginning of the simulation the total number of particles, N, are distributed between the two boxes such that n_1 particles are placed in simulation box 1 and $N-n_1$ particles are placed in box 2. The simulation proceeds by rearranging all of the particles within the two simulation boxes. At this stage of the simulation, each of the boxes is independent of the other. Box 1 now represents a simulation in the constant-$n_1 V_1 T$ ensemble and box 2 represents a constant-$(N-n_1,V-V_1,T)$ ensemble. Inspection of eqn (1.48) shows that each attempted particle rearrangement in each of the subsystems should be accepted with a probability proportional to $\exp[-\beta\delta W]$ where,

$$\delta W = \delta U^i \,. \tag{1.50}$$

In eqn (1.50), δU^i represents the change in energy for molecule i, within a given box, during an attempted displacement.

The next stage of the simulation involves making a volume change ΔV to one of the boxes and $-\Delta V$ to the other. If an attempt is made to change the volume of simulation box 1, V_1, by ΔV, then the move should be accepted with a probability proportional to $\exp[-\beta\delta W]$ where,

$$\delta W = \delta U_1 + \delta U_2 - \frac{n_1}{\beta}\ln\left(\frac{V_1+\Delta V}{V_1}\right) - \frac{N-n_1}{\beta}\ln\left(\frac{V-(V_1+\Delta V)}{V-V_1}\right). \tag{1.51}$$

In eqn (1.51) δU_1 represents the change in energy of box 1 during the attempted volume change and similarly, δU_2 represents the change in energy of box 2. During the attempted volume change stage of the simulation, box 1 represents an ensemble at constant-$n_1 P_1 T$ and similarly box 2 represents an ensemble at constant-$(N-n_1,P_2,T)$.

Finally, particle interchanges are attempted between the 2 simulation boxes. If a particle is removed from box 2 and inserted into box 1,then the move should be

accepted with a probability proportional to exp[-βδW] where,

$$\delta W = \delta U_1 + \delta U_2 + \frac{1}{\beta}\ln\left(\frac{(V-V_1)(n_1+1)}{V_1(N-n_1)}\right). \qquad (1.52)$$

During this stage of the simulation, the two boxes represent ensembles at constant-$\mu V_1 T$ and constant-$(\mu, V-V_1, T)$.

To summarise, each of the attempted moves within the simulation is accepted with a probability given by min(1,exp[-βδW]) where δW is given by eqns (1.50), (1.51) and (1.52), depending on the type of attempted move.

1.5. Computational Details

A convenient method of generating trial configurations in the Gibbs ensemble is to perform a simulation in cycles. Each cycle consists of an attempt to displace all the particles in both of the simulation boxes, a number of attempted volume changes, N_{vol}, and a number of attempted particle interchanges between the two boxes, N_{int}. The simulations were carried out in this work with homonuclear diatomic molecules and were started from either an α-fcc lattice or a previously equilibrated configuration. The choice of initial densities and number of particles in both simulation boxes is important in the Gibbs simulation methodology. If the simulations are started outside the two phase region then it is unlikely that the random fluctuations within the simulation will bring the system within the two phase region. The initial number of particles in the two boxes is also important as this determines the average number of particles that will exist in the equilibrated coexisting phases. A poor choice of initial number of particles within the boxes or the initial densities will result in a region containing very few particles on average in one of the phases producing poor statistics for the phase. Fortuitously the experimental phase diagram for chlorine was available to guide our choice of initial densities and numbers of particles in the two phases. A single Gibbs cycle is shown schematically in Figure 1.2.

A short overview of the simulations that have been performed with the Gibbs ensemble simulation technique will now be given.

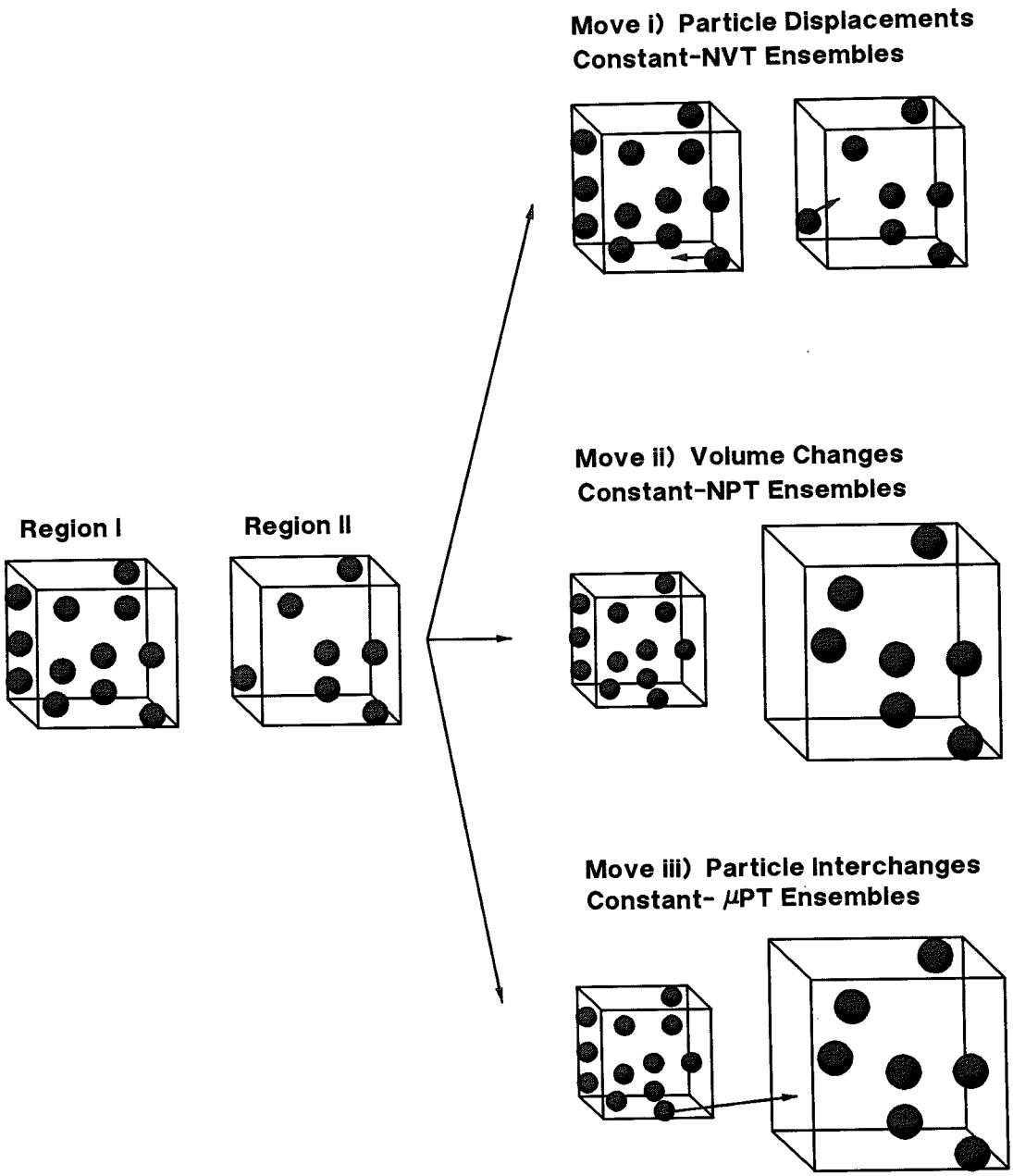

Figure 1.2. A schematic diagram of the moves applied to the 2 simulation boxes during a single Gibbs cycle.

1.6 Review of Gibbs Simulations

The Gibbs ensemble technique has been used to calculate the phase diagrams for a range of single component atomic fluids. Atomic systems studied include fluids with simple potential interactions including the Lennard-Jones fluid in two [21] and three dimensions [12,13,17] and square well fluids [22]. The calculated phase equilibrium data for the three dimensional Lennard-Jones fluid was found to be in good agreement with previous calculations obtained using indirect calculation methods [23,24,10]. In addition, Lennard-Jones systems with added quadrupole-quadrupole interactions [25] have been studied. Atomic systems with anisotropic interactions such as the Gay-Berne fluid used to model liquid crystals have also been studied [26].

The Gibbs ensemble technique has been applied to the calculation of phase equilibrium data in mixtures. Systems studied include an Ar/Kr mixture [13] and a He/N_2 system at high pressure [27]. Good agreement was found between the Gibbs simulation results and experimental results for both of the above systems.

The Gibbs ensemble technique has been used in the calculation of phase equilibria for chain fluids. Phase diagrams have been reported for pure polymer systems modelled by flexible chains of Lennard-Jones atoms [28] and pure hydrocarbon systems ranging from pentane to pentadecane [29]. Due to the idealised nature of the polymer system studied, a comparison with experimental results was not possible. The simulations with the pure alkane systems yielded vapour pressures and liquid and vapour densities lower than the experimentally measured results. Hydrocarbon fluid mixtures such as methane-n-pentane mixtures [30] have also been studied and good agreement obtained between the simulation results and the experimental data.

More extensive reviews of the Gibbs simulations performed can be found in the reviews of Panagiotopoulos [31] and Smit [32].

1.7 Outline of Chapter 2

In the following chapter an account is given of our investigations into the phase diagrams of a range of diatomic molecules. The Gibbs simulation methodology is used to obtain the phase diagrams of a number of diatomic molecules and the results of the simulations compared to the results of an integral equation theory of molecular fluid structure, the RISM equation.

1.8 References

[1] H.W. Cremer and T. Davies (Eds), "Chemical engineering practice", Vol. 5, Butterworth scientific publications, London, (1958).

[2] L.D. Landau and E.M. Lifshitz, "Statistical Physics", 3rd edn, Pergamon press, (1980).

[3] B. Widom, "Some topics in the theory of fluids", J. Chem. Phys., **39**, 2808-2812, (1963).

[4] J.G. Powles, "The liquid-vapour coexistence line by computer simulation à la Widom", Mol. Phys., **41**, 717-727, (1980).

[5] W.W. Wood and J.D. Jacobson, "Monte Carlo equation of state of molecules interacting with the Lennard-Jones potential. I. A supercritical isotherm at about twice the critical temperature", J. Chem. Phys., **27**, 720-733, (1957).

[6] W.W. Wood and J.D. Jacobson, "Preliminary results from a recalculation of the Monte Carlo equation of state of hard spheres", J. Chem. Phys., **27**, 1207, (1957).

[7] B.J. Alder and T.E. Wainwright, "Phase transitions for a hard sphere system", J. Chem. Phys., **27**, 1208, (1957).

[8] B.J. Alder and T.E. Wainwright, "Phase transitions in elastic disks", Phys. Rev., **127**, 359-361, (1962).

[9] W.G. Hoover and F.H. Ree, "Use of computer experiments to locate the melting transition and calculate the entropy in the solid phase", J. Chem. Phys., **47**, 4873-4878, (1967).

[10] J.P. Hansen and L. Verlet, "Phase transitions of the Lennard-Jones system", Phys. Rev., **184**, 151-161, (1969).

[11] D.J. Adams, "Grand canonical ensemble Monte Carlo for a Lennard-Jones fluid", Mol. Phys., **29**, 307-311, (1975).

[12] A.Z. Panagiotopoulos, "Direct determination of phase coexistence properties of fluids by Monte Carlo simulation in a new ensemble", Mol. Phys., **61**, 813-826, (1987).

[13] A.Z. Panagiotopoulos, N. Quirke, M. Stapleton and D.J. Tildesley, "Phase equilibria by simulation in the Gibbs ensemble: alternative derivation, generalization and application to mixture and membrane equilibria", Mol. Phys., **63**, 527-545, (1988).

[14] B. Smit and D. Frenkel, "Calculation of the chemical potential in the Gibbs ensemble", Mol. Phys., **68**, 951-958, (1989).

[15] D. Ruelle, "Statistical Mechanics : Rigorous results", W.A. Benjamin Inc., New York, (1969).

[16] T.L. Hill, "Statistical Mechanics : Principles and selected applications", McGraw-Hill Book Company Inc., (1956).

[17] B. Smit, "Computer simulations of phase coexistence: from atoms to surfactants", PhD thesis, Rijksuniversiteit Utrecht, The Netherlands, (1990).

[18] M.P. Allen and D.J. Tildesley, "Computer simulation of liquids", Oxford Science Publications, (1991).

[19] N. Metropolis, A.W. Rosenbluth, M.N. Rosenbluth, A.H. Teller and E. Teller, "Equation of state calculations by fast computing machines", J. Chem. Phys., **21**, 1087-1092, (1953).

[20] W.W. Wood and J.D. Jacobson, "Monte Carlo calculations in statistical mechanics", Proceedings of the Western joint computer conference, (San Francisco), 261-269, (1959).

[21] B. Smit and D. Frenkel, "Vapour-liquid equilibria of the two-dimensional Lennard-Jones fluid(s)", J. Chem. Phys., **94**, 5663-5668, (1991).

[22] L. Vega, E. de Miguel and L.F. Rull, "Phase equilibria and critical behaviour of square-well fluids of variable width by Gibbs ensemble Monte Carlo simulation", J. Chem. Phys., **96**, 2296-2305, (1992).

[23] D.J. Adams, "Calculating the low temperature vapour line by Monte Carlo", Mol. Phys., **32**, 647-657, (1976).

[24] D.J. Adams, "Calculating the high-temperature vapour line by Monte Carlo", Mol. Phys., **37**, 211-221, (1979).

[25] M.R. Stapleton, D.J. Tildesley, N. Quirke and A.Z. Panagiotopoulos, "Phase equilibrium of quadrupolar fluids by simulation in the Gibbs ensemble", Mol. Sim., **2**, 147-162, (1989).

[26] E. de Miguel, L.F. Rull, M.K. Chalam and K.E. Gubbins, "Liquid-vapour coexistence of the Gay-Berne fluid by Gibbs-ensemble simulation", Mol. Phys., **71**, 1223-1231, (1990).

[27] M.R. Stapleton and A.Z. Panagiotopoulos, "Application of excluded volume map sampling to phase equilibrium calculations in the Gibbs ensemble", J. Chem. Phys., **92**, 1285-1293, (1990).

[28] G.C.A.M. Mooij, D. Frenkel and B. Smit, "Direct simulation of phase equilibria of chain molecules", J. Phys. Condens. Matter, **4**, L255-L259, (1992).

[29] M. Laso, J.J. de Pablo and U.W. Suter, "Simulation of phase equilibria for chain molecules", J. Chem. Phys., **97**, 2817-2819, (1992).

[30] J.J. de Pablo and J.M. Prausnitz, "Phase equilibria for fluid mixtures from Monte Carlo simulation", Fluid Phase Equil., **53**, 177-189, (1989).

[31] A.Z. Panagiotopoulos, "Direct determination of fluid phase equilibria by simulation in the Gibbs ensemble: A review", Mol. Sim., **9**, 1-23, (1992).

[32] B. Smit in "Computer simulation in chemical physics", Eds. M.P. Allen and D.J. Tildesley, Kluwer Academic Publishers, (1993).

2. Phase Diagrams of Diatomic Molecules

2.1 Introduction

As described in Chapter 1, the location of the phase coexistence envelope for a given atomic or molecular species has been the subject of computational study over the last three decades. With the advent of fast desktop workstations and the Gibbs ensemble Monte Carlo simulation technique, the phase diagram of a given species or mixture can now be obtained with relative ease. Hence we are in a position to tackle problems regarding the location of the phase envelope for a given molecular system. In this work we were interested in determining the location of the phase envelope of diatomic molecules as a function of the molecular anisotropy ie. as a function of the bondlength of the molecule. The Law of Corresponding States [1] tells us that for atomic species modelled by the Lennard-Jones potential, all the phase diagrams possible with the various values of the Lennard-Jones parameters ε and σ, must in fact be conformal. But for a molecular species such as a diatomic molecule, to what extent does the molecular anisotropy force the phase diagram of the species to depart from the Law of Corresponding States? To address this question we determined the phase diagrams of a range of diatomic molecules. These molecules were modelled by placing Lennard-Jones potentials at the centres of the atoms within the molecules. These models are commonly known as diatomic Lennard-Jones molecules (DLJ molecules) and will be referred to as such in our work. Phase diagrams for DLJ molecules were obtained with reduced bondlengths varying between 0.15 and 1.00. By examining these phase diagrams and the critical properties obtained for the various diatomic molecules, we attempted to address this particular question.

Another question which we were interested in addressing was that of how sensitive the phase diagram of a given molecule is to the details of the potential used to model that molecule. To answer this question, we calculated the phase diagram of Cl_2, a molecule which has been the subject of numerous investigations by simulation [2,3]. Recent work on Cl_2 [4] has demonstrated that the structural properties of the liquid phase are indeed sensitive to the details of the potential model used and that by using an anisotropic site-site potential, thermodynamic properties of the crystal, liquid and gaseous phases can be accurately reproduced by a single potential function. However,

neither the DLJ model or this model with additional partial charges to represent the molecular quadrupole, accurately reproduce the liquid structure, although they give a reasonable account of the thermodynamic properties. We might therefore expect that as the liquid phase is sensitive to the details of the potential model used, then so might be the phase envelope. If the phase diagram of a given molecule were indeed sensitive to the details of the potential model used, then it might be possible to fit accurate potential models to the phase diagram. To investigate the dependence of the phase diagram on the potential model used, the phase diagram of Cl_2 was calculated with two different potential functions. The first of these is a DLJ representation of the molecule. As we have already mentioned, this potential function gives a fair representation of the thermodynamic properties of liquid Cl_2 but poorly reproduces structural properties such as the liquid structure factor. In focusing on the phase diagram of chlorine we compare our results to those of Powles [5], who had previously obtained the phase diagram for chlorine using an identical DLJ potential model. A description of the method used by Powles to calculate the phase diagram of Cl_2 is given in a later section. The second of the potential models used to obtain the phase diagram of Cl_2 is that of Rodger, Stone and Tildesley [4], which we will refer to as the RST potential.

Finally we were interested in investigating the accuracy of the RISM equation, an integral equation describing liquid structure. The RISM equation is solved for a number of the DLJ molecules at various points along their respective orthobaric curves. The results from the RISM equation are then compared to the results from the Gibbs simulations.

In this chapter we will first concentrate on the phase diagram of chlorine. The potential models used in the Gibbs simulation method are introduced. An account is given of the method used by Powles in the calculation of the phase diagram of chlorine. Various results are presented for chlorine and a comparison made between the various models, the results of Powles and experimental results for the phase diagram. The phase diagrams for the other diatomic molecules investigated are presented and the dependence of various critical properties of these molecules investigated as a function of the molecular anisotropy. Finally the RISM equation is introduced and the results of the equation compared to the Gibbs simulation results.

2.2 The Phase Diagram of Chlorine

2.2.1 Potentials

The interaction between two diatomic molecules depends on the separations of the centres of mass of the two molecules, $\mathbf{R}_{12}$ and the three Euler angles θ_1, θ_2 and φ_{12}. The interaction between two molecules can be represented as the sum of four site-site potentials,

$$U(R_{12},\theta_1,\theta_2,\varphi_{12}) = \sum_{\alpha=1}^{2}\sum_{\gamma=1}^{2} u_{\alpha\gamma}(r_{\alpha\gamma}) \ , \tag{2.1}$$

where α labels the sites on molecule 1, γ labels the sites on molecule 2 and $r_{\alpha\gamma}$ is the intersite separation.

In the DLJ potential the site-site potentials are represented by the Lennard-Jones potential,

$$u_{\alpha\gamma}(r_{\alpha\gamma}) = 4\epsilon_{\alpha\gamma}\left[\left(\frac{\sigma_{\alpha\gamma}}{r_{\alpha\gamma}}\right)^{12} - \left(\frac{\sigma_{\alpha\gamma}}{r_{\alpha\gamma}}\right)^{6}\right] \ . \tag{2.2}$$

The site potential of eqn (2.2) is isotropic ie. it depends only on the separation of the sites and not on the orientation of the site-site vector with respect to the bond vectors of the molecules. To calculate the phase diagram for chlorine using the DLJ potential, it is necessary to know the appropriate values of the parameters $\sigma_{\alpha\gamma}$ and $\varepsilon_{\alpha\gamma}$ for the sites and the reduced bondlength for the molecule. In this work, we have used the values of Singer *et al.* [6]. These parameters are,

$$\sigma_{\alpha\gamma} = 3.332\text{Å} \ , \tag{2.3}$$

$$\frac{\epsilon_{\alpha\gamma}}{k_B} = 178.3\text{K} \ , \tag{2.4}$$

$$L^* = \frac{L}{\sigma_{\alpha\gamma}} = 0.630 \ . \tag{2.5}$$

In eqn (2.5) L^* is the reduced bondlength for the molecule. These parameters were obtained by Singer *et al.* as follows. Molecular dynamics simulations were performed for the diatomic molecule of interest, in this case chlorine. Thermodynamically

consistent equations of state were fitted to the simulation data. These equations of state were compared to experimental data along the liquid-vapour coexistence line and the parameters $\sigma_{\alpha\gamma}$ and $\varepsilon_{\alpha\gamma}$ adjusted to give the best agreement with the experimental data.

The RST potential by contrast, accurately describes the anisotropies in the various site-site interactions. The anisotropies in the various interactions, in particular in the core repulsion, were shown by Rodger *et. al.* to be important in obtaining a good correspondence between the simulation and experimental structure factor. As such, the potential should give a much more complete description of the interactions between the atoms in chlorine molecules than the Lennard-Jones potential. The RST potential has the form,

$$u_{\alpha\gamma}(r_{\alpha\gamma}) = K\exp\left[-\alpha(r_{\alpha\gamma} - \sigma_0 - \sigma(\Omega))\right] - C\,(r_{\alpha\gamma} + \xi_0 - \sigma(\Omega))^{-6} + E_{es}\ ,$$

where,

$$\sigma(\Omega) = \sigma_{110} + \sigma_2(S_{202}+S_{022}) + \sigma_3(S_{303} + S_{033})\ ,$$

and,

$$E_{es} = \frac{1}{4\pi\varepsilon_0}\left[2Q_1^2\, S_{112}\, r_{\alpha\gamma}^{-3} + 3Q_1Q_2(S_{123} + S_{213})\, r_{\alpha\gamma}^{-4} + 6Q_2^2\, S_{224}\, r_{\alpha\gamma}^{-5}\right].$$

(2.6)

In eqn (2.6) K, α, σ_0, C, ξ_0, σ_{110}, σ_2, σ_3, Q_1 and Q_2 are constants whose values are given in Table 2.1. In eqn (2.6), the term E_{es} represents the electrostatic interaction between the two sites and contains dipole-dipole, dipole-quadrupole and quadrupole-quadrupole interactions. The orientation dependence in the potential comes from the term $\sigma(\Omega)$, which depends on the S functions. The S functions are related to spherical harmonic functions, and are functions of the intersite vector and the vectors pointing along the bonds of the molecules to the interacting sites. The S functions are given in Table 2.2.

The details of the RST potential were obtained by performing an empirical fit of the functional form of the potential to the experimental static crystal structure and lattice energies. This potential function has been shown to accurately reproduce the lattice

$\sigma_0 = 3.8630$ Å	$\sigma_{110} = 0.0221$ Å	$\sigma_2 = -0.0619$ Å	$\sigma_3 = 0.3500$ Å
$\alpha = 3.5100$ Å^{-1}	K = 1 kJ mol^{-1}	C = 10166.7 kJ Å^6 mol^{-1}	
$\xi_0 = 0.1629$ Å	$Q_1 = -0.1449$ ea$_0$	$Q_2 = 1.8901$ ea$_0^2$	1 = 1.994 Å

Table 2.1 The RST parameters as used in eqn (2.6).

$$S_{110} = \mathbf{e}_\alpha . \mathbf{e}_\beta$$

$$S_{202} = \frac{1}{2}\left[3(\mathbf{e}_\alpha . \hat{\mathbf{r}})^2 - 1\right]$$

$$S_{022} = \frac{1}{2}\left[3(\mathbf{e}_\beta . \hat{\mathbf{r}})^2 - 1\right]$$

$$S_{303} = \frac{1}{2}\left[5(\mathbf{e}_\alpha . \hat{\mathbf{r}})^3 - 3(\mathbf{e}_\alpha . \hat{\mathbf{r}})\right]$$

$$S_{033} = \frac{1}{2}\left[-5(\mathbf{e}_\beta . \hat{\mathbf{r}})^3 + 3(\mathbf{e}_\beta . \hat{\mathbf{r}})\right]$$

$$S_{112} = \frac{1}{2}\left[(\mathbf{e}_\alpha . \mathbf{e}_\beta) - 3(\mathbf{e}_\alpha . \hat{\mathbf{r}})(\mathbf{e}_\beta . \hat{\mathbf{r}})\right]$$

$$S_{213} = \frac{1}{2}(\mathbf{e}_\alpha . \hat{\mathbf{r}})\left[5(\mathbf{e}_\alpha . \hat{\mathbf{r}})(\mathbf{e}_\beta . \hat{\mathbf{r}}) - 2(\mathbf{e}_\alpha . \mathbf{e}_\beta) + 1\right]$$

$$S_{123} = -\frac{1}{2}(\mathbf{e}_\beta . \hat{\mathbf{r}})\left[5(\mathbf{e}_\beta . \hat{\mathbf{r}})(\mathbf{e}_\alpha . \hat{\mathbf{r}}) - 2(\mathbf{e}_\beta . \mathbf{e}_\alpha) + 1\right]$$

Table 2.2 The S-functions as used in eqn (2.6). $\mathbf{e}_\alpha$ and $\mathbf{e}_\beta$ are the unit vectors pointing along the bonds of the two molecules i and j, towards the sites on the respective molecules, α and β. $\hat{\mathbf{r}}$ is the unit vector pointing from site β on molecule j to site α on molecule i. The S-functions are sums of spherical harmonic functions and are defined in [4].

frequencies of the crystalline phase. The RST potential accurately reproduces the thermodynamics of the liquid phase and its structure factor S(k). In the gaseous phase the potential gives a good account of the gaseous structure and second virial coefficient.

The DLJ and RST potentials are shown in Figures 2.1 and 2.2 respectively, as a function of molecular separation, in a number of relative molecular orientations. The figures illustrate that the DLJ and RST potential functions give very different representations of the Cl_2 molecule.

The DLJ representation of Cl_2 (eqns (2.2), (2.3), (2.4) and (2.5)) has also been used by Powles to calculate the phase diagram of Cl_2. Before presenting our Gibbs simulation results for this and the RST model of Cl_2, we will first give a brief description of the Powles' method of calculation of the phase diagram.

2.2.2 Powles' Method

We have outlined in Chapter 1 some of the methods used to calculate phase coexistence. All of the methods (with the exception of the Gibbs ensemble method) are time consuming, slow or difficult to implement. Powles' method by contrast is relatively simple to implement and undemanding of computer resources.

The method of Powles' is based on the Widom particle insertion technique. As introduced in Chapter 1, the chemical potential of a system can be expressed in terms of an ensemble average over particle insertions into the system, ie.,

$$\frac{(\mu - \mu_{id})}{k_B T} = -\ln \langle \exp(-\beta \psi) \rangle \ . \qquad (2.7)$$

As explained in Chapter 1, μ_{id} is the chemical potential for a fluid at the same density and temperature as the chemical potential μ, but with the intermolecular interaction reduced to zero. We will henceforth refer to the term $\langle \exp(-\beta\psi) \rangle$ as $\langle BFT \rangle$, meaning the Boltzmann factor.

In principle then, we could evaluate $\langle BFT \rangle_l$ and $\langle BFT \rangle_g$ (where the subscripts refer to the liquid and gaseous states respectively) over a wide range of densities and/or temperatures and search for a range of states which satisfy the equalities of eqns (1.1), (1.2) and (1.3). However as we are usually interested in the properties of the liquid rather than the gas, this would entail calculating $\langle BFT \rangle_g$ for a range of states in which

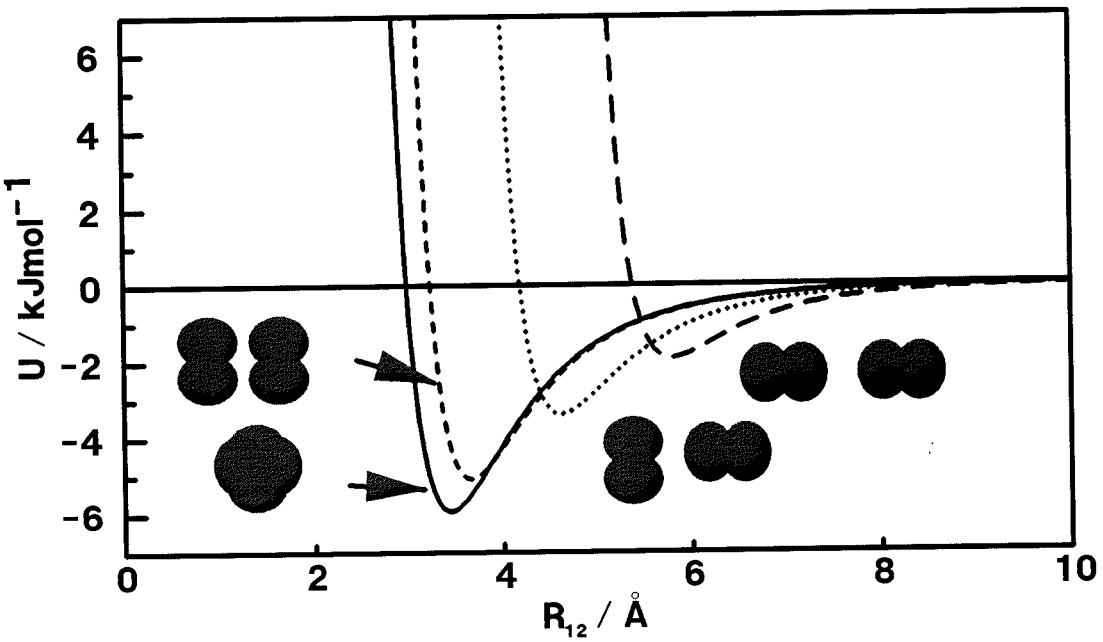

Figure 2.1 The DLJ potential representation of Cl_2, as a function of the intermolecular separation, R_{12}, in various relative molecular orientations.

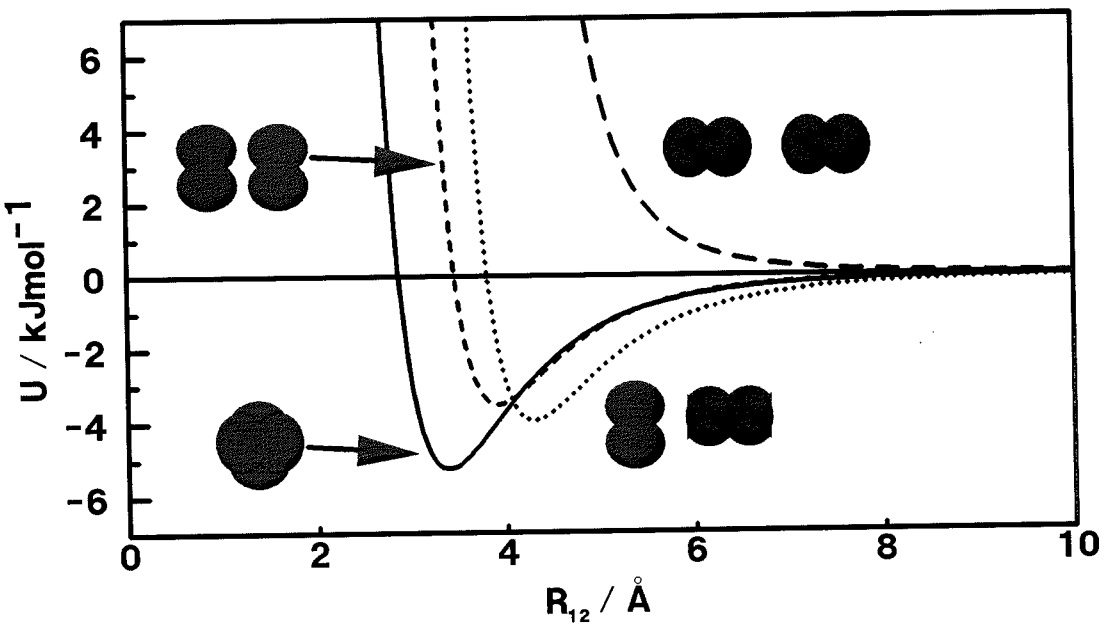

Figure 2.2 The RST potential representation of Cl_2, as a function of the intermolecular separation, R_{12}, in various relative molecular orientations.

we would not otherwise be interested. This would also result in an increased amount of computational effort in the calculation of the coexistence line. It is however possible to calculate $\langle BFT \rangle_g$ without recourse to performing simulations of the gaseous state. $\langle BFT \rangle_g$ can be calculated by expressing the term in a virial expansion.

To achieve this, use is made of the following definition of the chemical potential for the gaseous state [7],

$$\mu - \mu_{id}^{g} = \frac{\partial}{\partial N}\left[\int_{\infty}^{V}(\rho' k_B T - P')\,dV'\right]_{V,T}, \tag{2.8}$$

where μ_{id}^{g} is the chemical potential defined by eqn (1.19) for a gas of non-interacting particles at the same density as the gaseous phase. The pressure term in eqn (2.8) can be replaced by the virial expansion of the pressure defined by [8],

$$\frac{PV}{Nk_BT} = 1 + \frac{N}{N_A V}B_2(T) + \left(\frac{N}{N_A V}\right)^2 B_3(T) + \ldots, \tag{2.9}$$

$$= 1 + B_2(T)\left(\frac{P}{RT}\right) + (-B_2^2(T) + B_3(T))\left(\frac{P}{RT}\right)^2 + \ldots, \tag{2.10}$$

where $B_n(T)$ is the n^{th} virial coefficient per mole, N_A is Avogadro's number and $R=N_Ak_B$. For convenience we will now represent the virial coefficients simply by B_2, B_3 etc. Substituting the virial expansion of eqn (2.9) into the definition of the chemical potential, eqn (2.8), yields,

$$\frac{\mu - \mu_{id}^{g}}{k_BT} = 2B_2\left(\frac{P}{RT}\right) + \left(\frac{3}{2}B_3 - 2B_2^2\right)\left(\frac{P}{RT}\right)^2 + \ldots \tag{2.11}$$

Using eqn (2.11) for μ_g and eqn (2.7) for μ_l and in view of the equalities (1.1) and (1.2) we find on the coexistence line,

$$\ln\langle BFT\rangle_l = \frac{\mu_{id}^{l} - \mu_{id}^{g}}{k_BT} - 2B_2\left(\frac{P}{RT}\right) - \left(\frac{3}{2}B_3 - 2B_2^2\right)\left(\frac{P}{RT}\right)^2 + \ldots \tag{2.12}$$

where μ_{id}^{l} is the chemical potential for a fluid of non-interacting particles at the same

density as the liquid phase. But, upon using eqn (2.10),

$$\frac{\mu_{id}^{l} - \mu_{id}^{g}}{k_B T} = \ln\left(\frac{\rho_l}{\rho_g}\right) = \ln\frac{\rho_l k_B T}{P} + B_2\left(\frac{P}{RT}\right) + \left(B_3 - \frac{3}{2}B_2^2\right)\left(\frac{P}{RT}\right)^2 = \ldots . \tag{2.13}$$

Substituting eqn (2.13) into eqn (2.12) results in the following expression on the coexistence line,

$$\ln\langle BFT\rangle_l = \ln\left(\frac{\rho_l k_B T}{P}\right) - B_2\left(\frac{P}{RT}\right) + \frac{1}{2}\left(B_2^2 - B_3\right)\left(\frac{P}{RT}\right)^2 + \left(-\frac{2}{3}B_2^3 + B_2 B_3 - \frac{1}{3}B_4\right)\left(\frac{P}{RT}\right)^3 + \ldots . \tag{2.14}$$

Eqn (2.14) is more conveniently expressed in reduced units,

$$\ln\langle BFT\rangle_l = \ln\left(\frac{\rho_l^* T^*}{P^*}\right) - B_2^*\left(\frac{P^*}{T^*}\right) + \ldots , \tag{2.15}$$

where the reduced parameters take their usual definitions [9],

$$\rho_l^* = \rho_l \sigma^3 , \tag{2.16}$$

$$T^* = \frac{k_B T}{\epsilon} , \tag{2.17}$$

$$P^* = \frac{P\sigma^3}{\epsilon} , \tag{2.18}$$

$$B_2^* = \frac{B_2}{\sigma^3} . \tag{2.19}$$

In eqns (2.16)-(2.19) ε and σ are the Lennard-Jones energy and length parameters respectively.

Taking note of the fact that $B_3 \ll B_2^3$, $B_4 \ll B_2^2$ [5] etc, eqn (2.15) can be written as,

$$\ln \langle BFT \rangle_l \simeq \ln\left(\frac{\rho_l^* T^*}{P^*}\right) - B_2^*\left(\frac{P^*}{T^*}\right) + \frac{1}{2}B_2^{*2}\left(\frac{P^*}{T^*}\right)^2 - \frac{2}{3}B_2^{*3}\left(\frac{P^*}{T^*}\right)^3 + .. ,$$

(2.20)

Finally we need to obtain B_2^* which can be calculated from,

$$B_2^* = -\frac{1}{4}\int_0^{\infty}\int_0^{2\pi}\int_{-1}^{+1}\int_{-1}^{+1}\left(\exp[-\beta U(r^*, \theta_1, \theta_2 \varphi_{12})] - 1\right) r^{*2}\, d\cos\theta_1\, d\cos\theta_2\, d\cos\phi_{12}\, dr^* ,$$

(2.21)

where r^* is the reduced distance defined as,

$$r^* = \frac{r}{\sigma} . \qquad (2.22)$$

The coexistence line can now be predicted using eqn (2.20) as follows. Simulations are performed on the model fluid of interest. The simulations performed need not lie on the coexistence line and hence a prior knowledge of the phase diagram is not necessary in this technique. At each state point we specify T and ρ_l and calculate $\ln\langle BFT\rangle_l$ and P during the course of the simulation. The values of ρ_l, P and T can be used to calculate the right hand side of eqn (2.20) and the simulation directly yields the left hand side of eqn (2.20). $\ln\langle BFT\rangle_l$ and the right hand side of eqn (2.20) can now be plotted as a function of T^* at a fixed V^*. The point at which the two lines cross yields the coexistence value of T^*. By subsequently plotting T^* as a function of V^* the coexisting liquid density is obtained.

This procedure was used by Powles to calculate the phase diagram of the DLJ model of Cl_2. These results will be compared to those of our Gibbs simulations, details of which will now be given.

2.2.3. Simulation Details

The phase diagram for chlorine has been calculated using the Gibbs ensemble method for both the DLJ and RST representations of the molecule. The simulations with the DLJ potential were started from either an α-fcc lattice, or a previously equilibrated configuration. A total of 512 molecules were distributed between the two boxes. Periodic boundary conditions and minimum imaging were applied to the molecular centres, and long range corrections to the pressure and energy calculated for the cutoffs based on centre of mass separations rather than the separation of the sites. The parameters controlling the maximum allowed volume change of the boxes and the maximum allowed translation and rotation of the molecules were not adjusted during the production phase of the simulations. The number of attempted particle interchanges, was chosen so that a minimum of 2000 successful interchanges occurred during the course of a simulation. In extending the simulation phase diagram for chlorine (L^*=0.630) towards the triple point, it became necessary to implement grid maps [10] to offset the computational cost of the rapid increase in the number of attempted interchanges. Grid maps are an efficient method of detecting attempted particle insertions which create a significant overlap with other particles, without recourse to a complete calculation of the trial insertion potential. All the simulations for chlorine below 300K, used grid maps. Typically, close to the critical point, 300 attempted interchanges per cycle were sufficient to equate the chemical potentials in the two regions. However at temperatures closer to the triple point, 15×10^3 attempted interchanges per cycle were required to achieve equilibrium.

A typical simulation required at least 1000 equilibration cycles followed by 3000 production cycles. A cycle consists of an attempt to alter the positions and orientations of all the molecules in the boxes, one attempted volume change and a number of attempted particle interchanges.

We have also calculated the phase diagram for chlorine using the RST potential of eqn (2.6). To calculate the pressure from the RST potential, it is necessary to obtain the analytical derivative of the potential and a method outlined in [11] was used to do so. The angular average of the intermolecular potential [12] and virial were calculated by direct integration over an n-cube (NAG routine D01FCF). The long range corrections were calculated for a range of cutoff distances ranging from 3Å to 50Å, in

steps of 0.05Å. The cutoff required for a particular attempted move was obtained from the look-up table by linear interpolation. The calculation of the long range corrections to the energy and pressure were relatively expensive, requiring approximately 2 hours of CPU time on an IBM 3090 mainframe. However it was necessary to obtain accurate estimates of the long range corrections because of their magnitude. For instance in an NVT simulation at 400K and a density of approximately 0.0137 mol cm^{-3} (corresponding to the coexisting liquid density at that temperature) a cutoff distance of approximately 10 Å is used. Under these conditions, the overall pressure of the simulation is 5.0±6.4 MPa where the long range correction has contributed -10.7 MPa to the pressure.

The RST potential contains an exponential repulsive term. At small intersite separations the potential becomes attractive. The actual intersite separation at which this occurs is dependent on the relative orientations of the two molecules. To ensure that this feature of the potential did not cause any difficulties in our simulations, a minimum intersite separation was used, set to 1Å. All site-site interactions at this separation are repulsive, regardless of the orientations of the two molecules. This minimum intersite cutoff was employed in all of the Gibbs simulation moves.

Monte Carlo simulations using the RST potential can become locked in regions of phase space, leading to non-ergodic simulations. Initial Monte Carlo simulations carried out using the RST potential in the constant-NVT ensemble, did not agree with the previous molecular dynamics results [4]. For example, the Monte Carlo simulation at T=175K, ρ=0.024459 mol cm^{-3} was started from an α-fcc lattice with 108 molecules, equilibrated for 6000 cycles and 14000 production cycles performed. A cycle refers to an attempted translation and rotation of all the molecules. The simulation gave a total energy of -20.34±0.11 $kJmol^{-1}$, the quoted error being calculated by splitting the simulation up into 14 sub-averages and calculating 1 standard deviation in the mean. There was no significant drift in the energy over the final 5000 cycles of the production period. In contrast, at the same state point, the molecular dynamics results gave an energy of -18.55±0.03 $kJmol^{-1}$. By running our simulations from equilibrated Molecular dynamics configurations, or by heating the systems up to high reduced temperatures during the equilibration phase of the simulation, agreement was obtained between the two sets of results. For example, a Monte Carlo constant-NVT simulation was carried

out at T=175K, ρ=0.024459 mol cm^{-3} with 108 molecules. The simulation was started from an α-fcc lattice and equilibrated at T=601K for 2000 cycles. The temperature of the system was gradually annealed down to T=175K over the following 4000 cycles and finally 6000 production cycles were carried out. The simulation gave a total energy of -18.56±0.11 $kJmol^{-1}$, in agreement with the molecular dynamics results.

To avoid this problem in our Gibbs simulations with the RST potential, all the simulations were started from a configuration that had been equilibrated by the annealing constant-NVT method described above. As a check on the accuracy of our results an annealing constant-NVT simulation was carried out for the state on the orthobaric curve at T=325K and ρ_{liq}=0.0182 mol cm^{-3}. The configurational energy of the liquid phase at this state point in the Gibbs simulation is -15.11±0.29 $kJmol^{-1}$ and the resulting energy from the annealed simulation is -15.06±0.08 $kJmol^{-1}$. The agreement between the two simulations confirms that the Gibbs simulation had not become trapped in a metastable region. All the simulations with the RST potential were carried out with 216 molecules distributed between the two boxes and details of the Gibbs simulations performed are similar to those described for the DLJ potential.

2.2.4 Results for Chlorine

Table 2.3 contains the results of our simulations of chlorine at ten different coexistence points. The table compares the experimental coexisting pressures and densities of the two phases [13], with those values calculated using the DLJ potential. The estimated errors in the table were calculated by dividing the production period of each simulation into 10 batches. The errors quoted in the table represent 1 standard deviation of the mean of the batch averages.

It is clear from Table 2.3 that the DLJ potential gives coexisting pressures and densities that are in reasonable agreement with the experimental data. Most of the calculated pressures and densities agree with the experimental data to within the error of our data. At temperatures below 240.7K it became difficult to obtain sufficient interchanges between the boxes to ensure that the chemical potentials of the two phases are the same and so no results are reported for this region of the coexistence envelope for the DLJ potential.

T / K	ρ_{liq} / mol cm^{-3}		ρ_{vap} / mol cm^{-3}		P_{liq} / MPa	P_{vap} / MPa	
	DLJ	Exp.	DLJ	Exp.	DLJ	DLJ	Exp.
410	0.0129±0.0011	0.0118	0.00383±0.00028	0.00477	7.74±1.66	7.13±0.25	7.18
400	0.0132±0.0006	0.0133	0.00289±0.00026	0.00351	5.26±0.99	5.75±0.39	6.15
375	0.0161±0.0003	0.0155	0.00203±0.00012	0.00197	4.23±1.95	4.31±0.11	4.07
350	0.0173±0.0002	0.0171	0.00122±0.00015	0.00116	2.81±1.21	2.74±0.32	2.57
325	0.0184±0.0002	0.0184	0.00060±0.00009	0.00067	0.94±2.68	1.31±0.22	1.51
300	0.0197±0.0001	0.0195	0.00034±0.00002	0.00036	0.27±1.95	0.79±0.05	0.81
285.2	0.0203±0.00007	0.0202	0.00025±0.00004	0.00024	0.87±1.12	0.54±0.07	0.53
267.4	0.0211±0.00005	0.0209	0.00015±0.00001	0.00014	0.57±1.44	0.32±0.03	0.30
258.5	0.0213±0.00009	0.0212	0.00010±0.00001	0.00010	0.03±1.92	0.22±0.01	0.22
240.7	0.0221±0.0001	0.0219	0.00006±0.00001	0.00005	1.51±1.83	0.119±0.006	0.10

Table 2.3 Experimental phase coexistence data and the corresponding DLJ simulation results. The chemical potentials in both phases are equal to within the estimated error.

The critical temperature and density have been calculated for the DLJ potential by fitting the data to the law of rectilinear diameters,

$$\left(\frac{\rho_l + \rho_g}{2}\right) = A(T - T_c) + \rho_c \ , \tag{2.23}$$

and the appropriate scaling law for the density [14],

$$\rho_l - \rho_g = A|T - T_c|^{\beta}. \tag{2.24}$$

The law of rectilinear diameters is an empirical law based on the observation that if diameters are drawn across the graph of the orthobaric densities as functions of the temperature, then the midpoints of these diameters lie on a straight line which passes through the critical density [14].

The scaling law for the density of eqn (2.24) is used to describe the asymptotic behaviour of the deviation of ρ from ρ_c, the critical density, as a function of the deviation of T from T_c, the critical temperature. Experimentally it has been known for many decades that a large number of thermodynamic properties show anomalous behaviour in the region of the critical point. These anomalies are the consequence of large density fluctuations characteristic of the critical region, which give rise to singularities in many observable quantities. For instance, the compressibility χ_T, defined by,

$$\rho k_B T \chi_T = \frac{\langle N^2 \rangle - \langle N \rangle^2}{\langle N \rangle} \ , \tag{2.25}$$

becomes infinite at the critical point. The singular behaviour of χ_T in the region of the critical point can be described by a scaling law similar to that of eqn (2.24),

$$\chi_T = C(T - T_c)^{-\gamma} \ , \quad T > T_c \ , \tag{2.26}$$

where γ is a critical exponent that can be determined experimentally from the slope of a log-log plot of χ_T versus $(T-T_c)$ which is a straight line if T is not too far from T_c, ie.,

$$\gamma = -\lim_{T \to T_c^+} \frac{\log \chi_T}{\log(T - T_c)} \ . \tag{2.27}$$

The numerical values of the critical exponents β and γ appear to be identical, within experimental uncertainties, for all substances on which measurements have been made. The fact that the critical exponents are independent of the precise nature of the substance under investigation is a reflection of the universality of critical point behaviour.

The experimentally observed scaling exponent, β=0.32, has been used in the fitting of the data to the scaling law for the density. In order to obtain an idea of the influence of the scaling exponent on the calculated critical point, a range of other β values have been used in the fitting procedure. Two of the values used for the exponent are β=0.5 and 0.33, the exponents corresponding to the mean field exponent and the 3D Ising exponent respectively. The critical densities and temperatures calculated using the various values of β are presented in Table 2.4 where they are compared to the experimental values. The value F_n in Table 2.4 is a measure of the mean-squared deviation of the fit and is defined by,

$$F_n = \frac{1}{N}\sum_N (\rho_l - \rho_g - A|T-T_c|^\beta)^2 , \qquad (2.28)$$

where N is the number of points along the coexistence line. This fit has to be conducted with considerable care as the final value of F_n is quite sensitive to the initial guess. The critical temperature and density calculated from the Gibbs simulation using β=0.32 agree with experiment to within 1%. This is a remarkable result for such a simple potential model. The Table demonstrates that the critical exponent used can alter the calculated critical temperature by approximately 21K (5%) and the critical density by approximately 0.00033 mol cm^{-3} (4%). In view of the known defects in the potential model the agreement with experiment must be somewhat fortuitous.

In Figure 2.3 the coexisting densities produced by the DLJ simulations are compared with the experimental results. Included in the figure are the simulation results of Powles [5]. Powles' results were obtained using the method described in section 2.2.2. We again stress that the DLJ model for chlorine used by Powles is identical to the DLJ model used in this work. Figure 2.3 spans the entire liquid-vapour coexistence region from the triple point at T=172.17K to the critical point at T=416.96K. The experimental curve shown in Figure 2.3 was calculated by an equation of state obtained by fitting

β	T_c / K	ρ_c / mol cm^{-3}	F_n / 10^{-7}
0.31	419.5	0.00812	0.5625
0.32	420.3	0.00810	0.7758
0.33	422.1	0.00808	6.677
0.34	422.7	0.00807	9.085
0.35	440.9	0.00779	1.069
Expt.	416.95	0.008134	

Table 2.4 The predicted critical temperatures and densities for the DLJ model of chlorine compared with the experimental values.

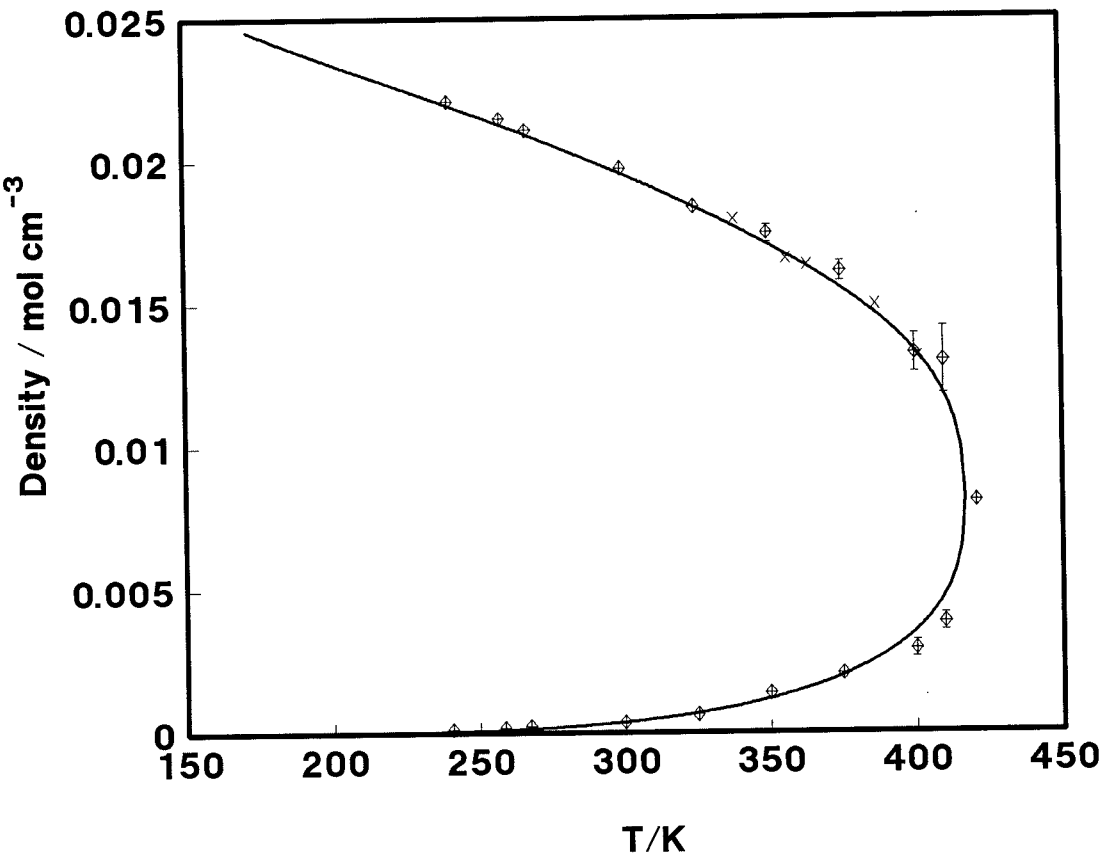

Figure 2.3 The coexistence curve determined from the Gibbs simulations with the DLJ potential. The symbols are the Gibbs simulation results, crosses are the results of Powles and the line represents the experimental data.

experimental data [13]. The coexistence densities calculated from the equation of state differ from most of the experimental data by less than 1%.

Figure 2.3 illustrates that the DLJ potential gives a good description of the coexistence densities over almost the entire coexistence region. We are able to use the Gibbs method to investigate temperatures to within 68K of the triple point where the range of the orthobaric curve is 244K. The results of Powles are in good agreement.

In Figure 2.4 the coexisting vapour pressures produced by the DLJ simulations are compared with the experimental results and the simulation results of Powles. Once again the experimental data is calculated from an experimental equation of state [13]. In this case, the pressures calculated from the equation of state deviate from the experimental data by less than 4%. The DLJ potential gives a good description of the vapour coexistence pressures in the Gibbs simulation method, but a rather poorer description of the pressures when used in the Powles method. It should be pointed out however that Powles obtained a significantly better fit to the vapour pressures by altering the values of ε and σ used in the DLJ potential to,

$$\sigma_{\alpha\gamma} = 3.415\text{Å} \ , \tag{2.29}$$

$$\frac{\epsilon_{\alpha\gamma}}{k_B} = 185.0\,\text{K} \ . \tag{2.30}$$

We did not find that such a scaling of the parameters was necessary.

Simulations of chlorine were also carried out using the RST potential. Table 2.5 contains the results of our simulations of chlorine at 5 different coexistence points. A comparison of the times required to complete the DLJ and RST simulations was made at T=350K. Both simulations employed 216 molecules and a cycle consisted of an attempted move for every molecule, 1 attempted volume change and 500 attempted particle exchanges.

The simulations were performed on one processor of an Alliant FX80. Each cycle required 6s of CPU time for the DLJ potential and each cycle with the RST potential required 42.3s. The increase in the required CPU time for the RST potential when compared to the DLJ potential is due to the complicated form of the potential and the extra computation involved in calculating the pressure. The increase in the complexity

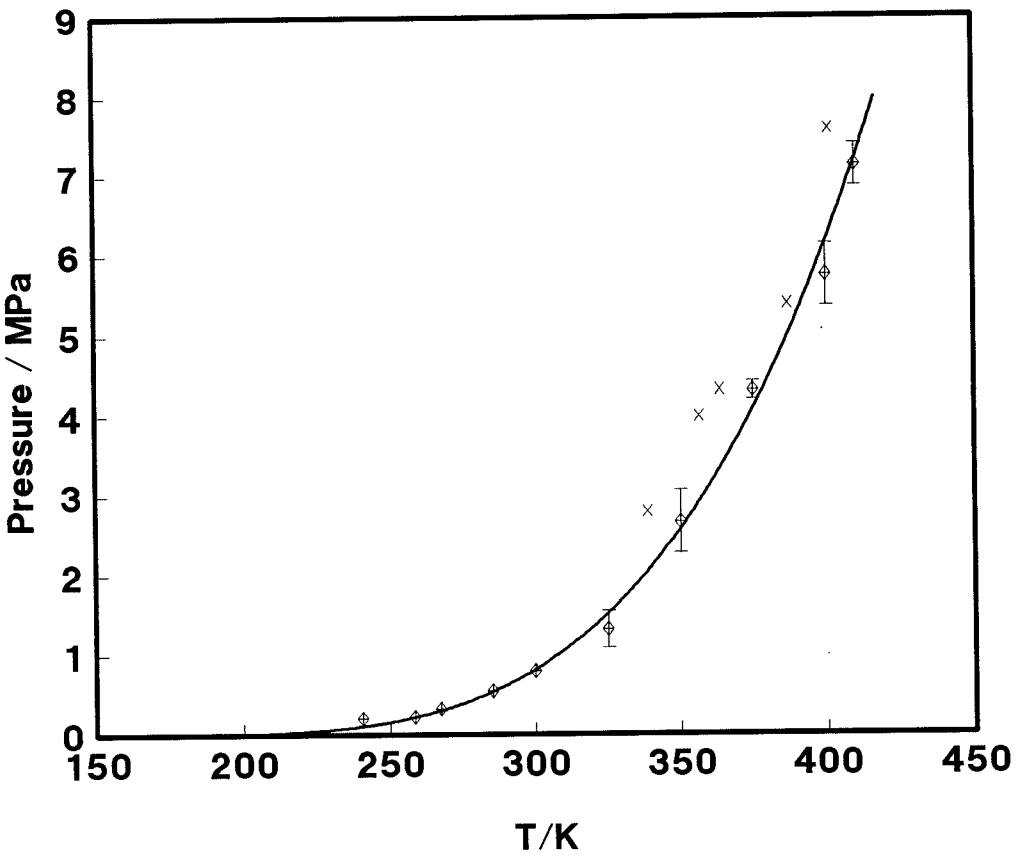

Figure 2.4 The coexistence vapour pressures determined from the Gibbs simulations with the DLJ potential. The symbols are the Gibbs simulation results, crosses are the results of Powles and the line represents the experimental data.

T / K	ρ_{liq} / mol cm^{-3}		ρ_{vap} / mol cm^{-3}		P_{liq} / MPa	P_{vap} / MPa	
	RST	Exp.	RST	Exp.	RST	RST	Exp.
400	0.0137±0.0004	0.0133	0.00394±0.00028	0.00351	7.72±3.73	6.50±0.56	6.15
375	0.0150±0.0007	0.0155	0.00188±0.00031	0.00197	6.55±6.88	4.10±0.45	4.07
350	0.0173±0.0003	0.0171	0.00127±0.00009	0.00116	4.33±3.80	2.89±0.24	2.57
325	0.0182±0.0003	0.0184	0.00060±0.00004	0.00067	-1.06±6.17	1.40±0.11	1.51
300	0.0197±0.0002	0.0195	0.00040±0.00004	0.00036	5.80±6.49	0.90±0.06	0.81

Table 2.5 The experimental phase coexistence data and the corresponding RST results. The chemical potentials in the two phases are equal to within the estimated error.

of the potential is especially costly during the volume fluctuation move of the Gibbs simulation method, as the configurational energy for the particles has to be calculated before and after the volume change and is an $o(N^2)$ operation. The lowest temperature simulation carried out with the RST potential was at a temperature of 300K. Grid maps were not implemented for this complicated potential as the excluded volume of an atom is now a complicated function of the intermolecular orientations and it is unlikely that grid maps would offer a significant time saving in this situation. The errors quoted in the Table were obtained by the same method as for the DLJ results. Table 2.5 clearly illustrates that the RST potential gives coexisting pressures and densities that are in reasonable agreement with the experimental data. Critical temperatures and densities have been calculated for the RST potential by the same method as described for the DLJ potential. The critical temperatures and densities calculated using the various values of β are presented in Table 2.6. The critical temperature calculated using the value β=0.32 agrees with experiment to within 1% and the density to within 3%. The table demonstrates that the critical exponent used can alter the critical temperature by approximately 24K (6%) and the critical density by 0.00031 mol cm^{-3} (4%).

Having presented our results for the DLJ potential, we now present the results of our simulations with the RST potential. In Figure 2.5 the coexisting densities produced by the RST simulations is compared with the experimental results. The RST potential provides a good description of the coexistence densities with most of the densities falling within one error bar of the experimental values.

In Figure 2.6 the coexisting vapour pressures are presented. Once again most of the simulation results fall within one error bar of the experimental results.

Comparison of the results for the DLJ and RST models of chlorine shows neither model to be qualitatively superior to the other. Both potential models produce densities and pressures that are in good agreement with the experimental results. The RST potential gives a critical temperature that is below that of the experimental and a critical density that is above the experimentally measured value. The DLJ potential by contrast yields a critical temperature above the experimental value and a critical density below the experimental value.

Despite the agreement between the two potential models in determining the coexisting pressures and densities, they both provide very different descriptions of the

β	T_c / K	ρ_c / mol cm^{-3}	F_n / 10^{-7}
0.31	412.4	0.00841	0.5263
0.32	413.8	0.00839	0.4997
0.33	414.6	0.00838	0.4246
0.34	414.7	0.00837	0.3658
0.50	390.2	0.00868	68.24
Expt.	416.95	0.008134	

Table 2.6 The predicted critical temperatures and densities for the RST model of chlorine compared with the experimental values.

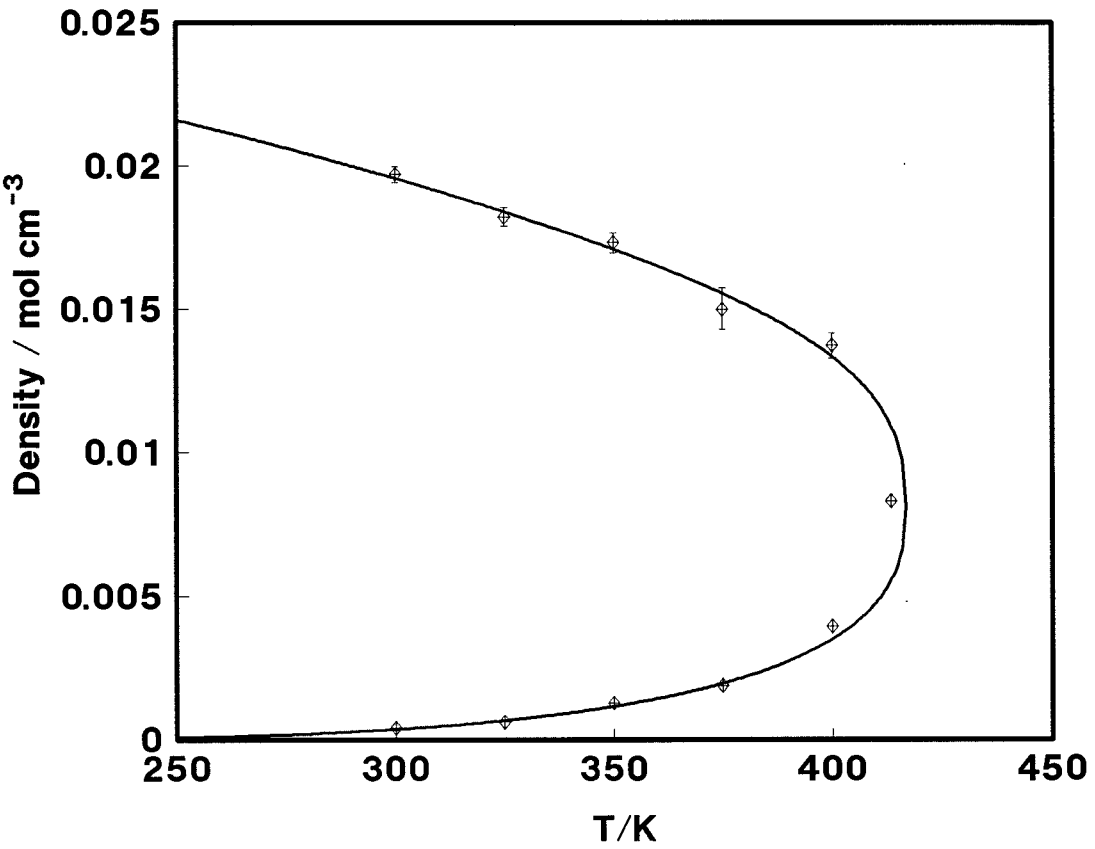

Figure 2.5 The coexistence curve determined from the Gibbs simulations with the RST potential. The symbols are the Gibbs simulation results and the line represents the experimental data.

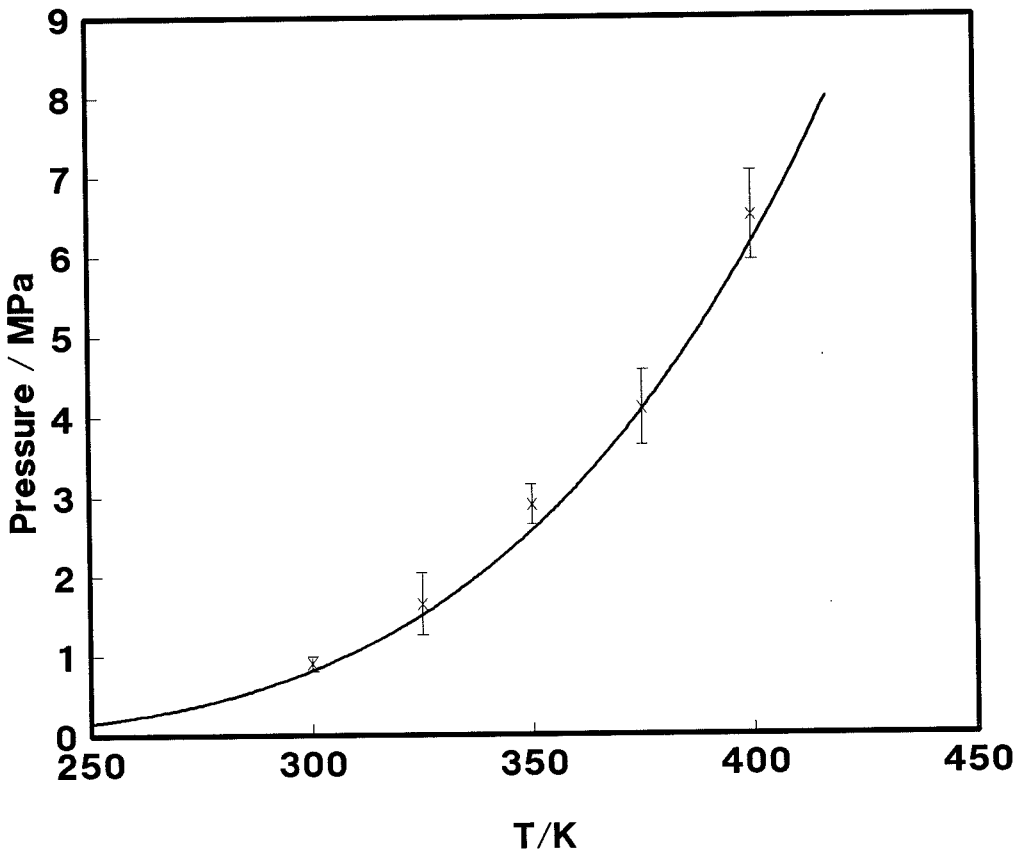

Figure 2.6 The coexistence vapour pressures determined from the Gibbs simulations with the RST potential. The crosses are the Gibbs simulation results and the line represents the experimental data.

structure of the liquid phase. To illustrate this, Figure 2.7 presents site-site radial distribution functions produced by the two potential models. The site-site radial distribution function $g_{\alpha\delta}$ is defined by [8],

$$\rho^2 g_{\alpha\delta}(\mathbf{r}) = \left\langle \sum_{i=1}^{N} \sum_{j \neq i}^{N} \delta(\mathbf{r}_{i\alpha}) \, \delta(\mathbf{r}_{j\delta} - \mathbf{r}) \right\rangle , \qquad (2.31)$$

where $\mathbf{r}_{i\alpha}$ represents the coordinates of site α on molecule i and $\mathbf{r}_{j\delta}$ the coordinates of site δ on molecule j and the angular brackets denote an ensemble average. The distribution functions presented in Figure 2.7 were taken from the resulting liquid phases of Gibbs simulations performed with the two potential models at 300K. At this temperature both models predict densities for the liquid phase of 0.0197 mol cm^{-3} as opposed to the experimentally measured density of 0.0195 mol cm^{-3}. Clearly however the models give very different liquid structures. The RST potential produces a second peak in the function $g_{\alpha\delta}$ which is much more pronounced than the corresponding peak for the DLJ model. This is due to the fact that the RST potential favours T-orientations of Cl_2 molecules more strongly than the DLJ potential.

The agreement between these two different models of chlorine illustrate the fact that the precise form of the dispersion term in the site-site potential and the representation of the electrostatic interactions is relatively unimportant in determining the locus of the phase coexistence envelope. Fitting potentials to the coexistence envelope is therefore unlikely to yield better parameters for complicated potential functions and, furthermore, simple potentials which are known to fail in reproducing the liquid structure may be adequate to describe the phase envelope.

2.3 Phase Diagrams For Other Diatomics

We now proceed to investigate the phase diagrams for a range of DLJ molecules using the Gibbs simulation technique. The phase diagrams for DLJ molecules with L^*=0.15, 0.30, 0.50, 0.63, 0.75, and 1.00 have been calculated. The details of the simulations performed with these diatomics are similar to those described in section 2.2.3. The phase diagrams obtained for all the diatomics investigated are presented in the ρ-T plane in Figure 2.8.

Upon obtaining the phase diagrams of the various DLJ molecules we investigated

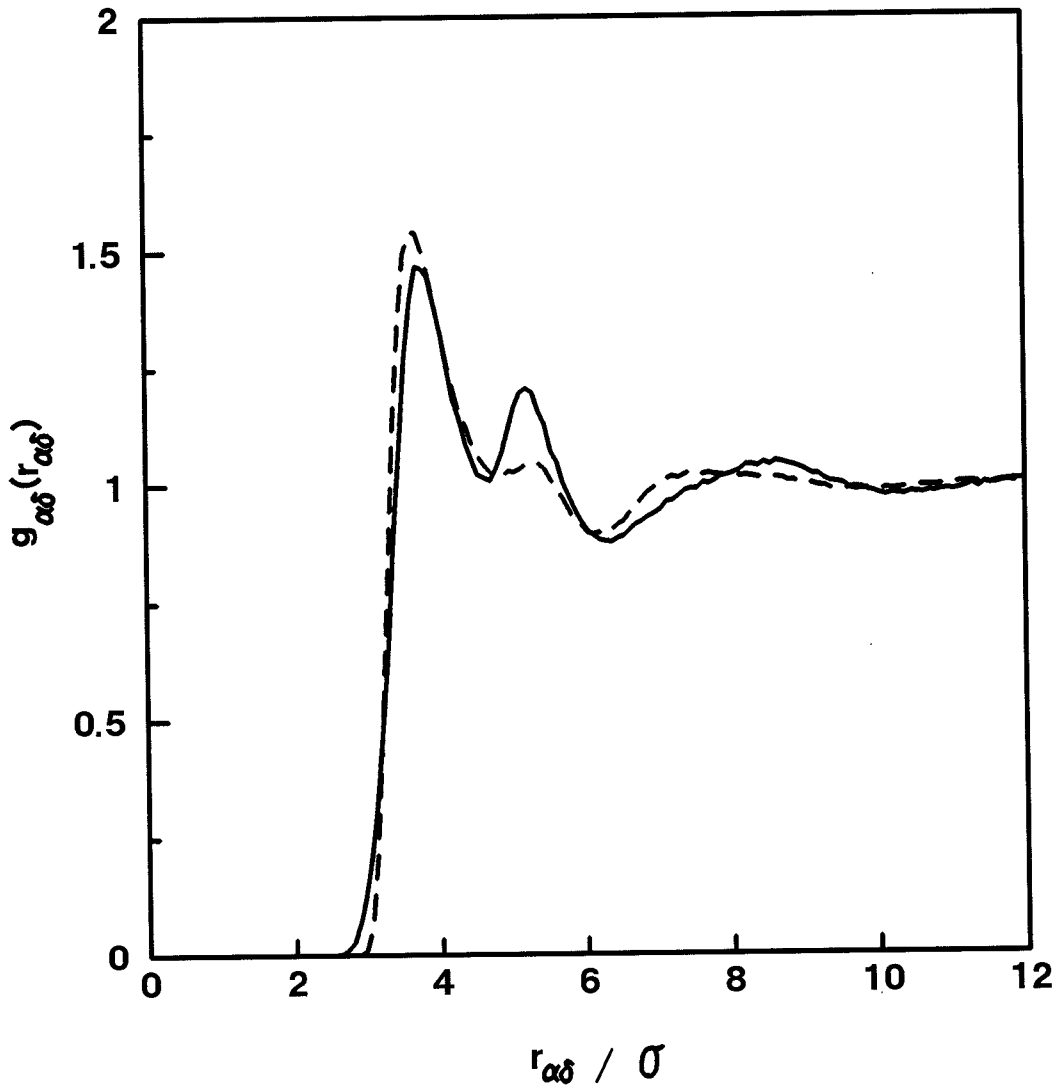

Figure 2.7 Comparison of the site-site radial distribution functions for the RST potential (solid line) and the DLJ potential (dotted line).

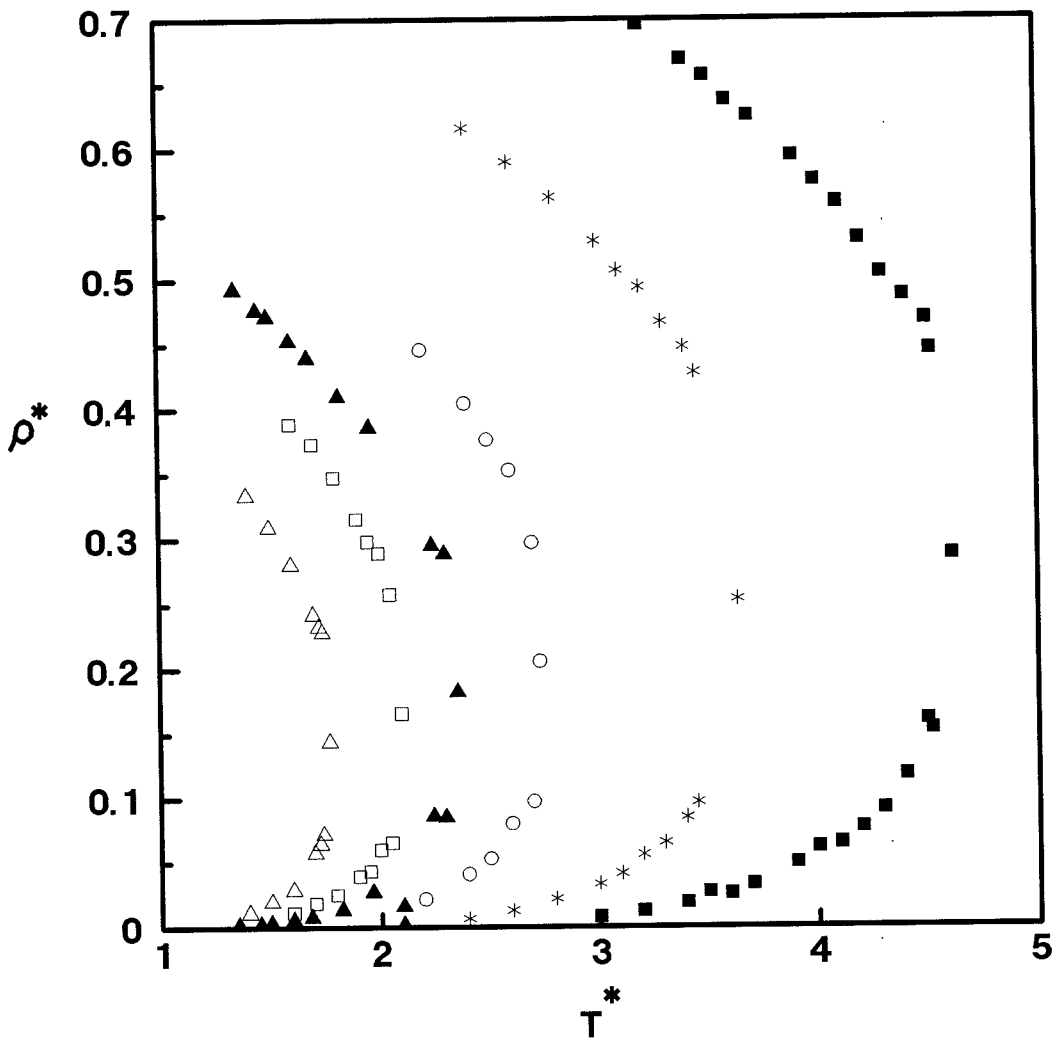

Figure 2.8 The phase diagrams for the DLJ diatomics with bondlengths ranging from 0.15 to 1.00, as calculated by the Gibbs simulation method. The bondlengths represented are; L^*=0.15 (■), L^*=0.30 (*), L^*=0.50 (○), L^*=0.63 (▲), L^*=0.75 (□) and L^*=1.00 (△).

several of the critical properties of the molecules. The critical densities and temperatures were calculated for these molecules using the same method as described in section 2.2.4, and are reported in Table 2.7. Using this information we have calculated the critical packing fractions as a function of bondlength. The reduced critical packing fraction can be calculated from,

$$\eta_c^* = \rho_c^* V^* , \tag{2.32}$$

where V^* is the reduced molecular volume defined as,

$$V^* = \frac{V}{\sigma^3} . \tag{2.33}$$

The reduced molecular volume for a diatomic molecule can be calculated from the expression [15],

$$V^* = \frac{\pi}{\sigma^3}\left(1 + \frac{3}{2}L^* - \frac{1}{2}L^{*3}\right). \tag{2.34}$$

In Figure 2.9 we present our results for the critical packing fractions as a function of bondlength. The simulation point at the reduced bondlength of 0.0 is taken from Panagiotopoulos [16] and represents the critical point for Lennard-Jones atoms. This critical point was obtained from Gibbs simulations. Also presented in Figure 2.9 are a number of experimentally measured critical packing fractions. The experimentally measured critical temperatures and densities [13,17] and the Lennard-Jones parameters [6,18,19] required to put the experimental data into reduced units are presented in Table 2.8. As can be seen from the figure, the simulation results are in good agreement with the experimental results. The critical density from the Gibbs simulation of chlorine using the DLJ potential is within about 0.5% of the experimental results for chlorine and the critical density for the simulation of a DLJ molecule with L^*=0.500 is also within 0.5% of the experimentally measured value for fluorine (Tables 2.7 and 2.8).

In Figure 2.10 we present our results for the critical temperatures as a function of bondlength. Once again, included in the figure are the experimentally measured critical points for a number of diatomic molecules as presented in Table 2.8. Again, we find that the correspondence between the simulation and experimental results is good, with

l^*	T_c^*	ρ_c^*
0.15	4.612	0.2875
0.30	3.640	0.2537
0.50	2.734	0.2061
0.63	2.357	0.1822
0.75	2.099	0.1660
1.00	1.771	0.1441

Table 2.7 Critical points for the Lennard-Jones diatomics

	L^*	(ε/k_B) / K	σ / Å	T_c^*	ρ_c^*
Ar	0.0	119.8	3.405	1.25	0.318
N_2	0.329	37.30	3.310	3.38	0.245
F_2	0.505	52.8	2.825	2.73	0.205
Cl_2	0.630	178.3	3.332	2.33	0.181

Table 2.8 Critical properties and the appropriate Lennard-Jones parameters for a range of molecules from experiment.

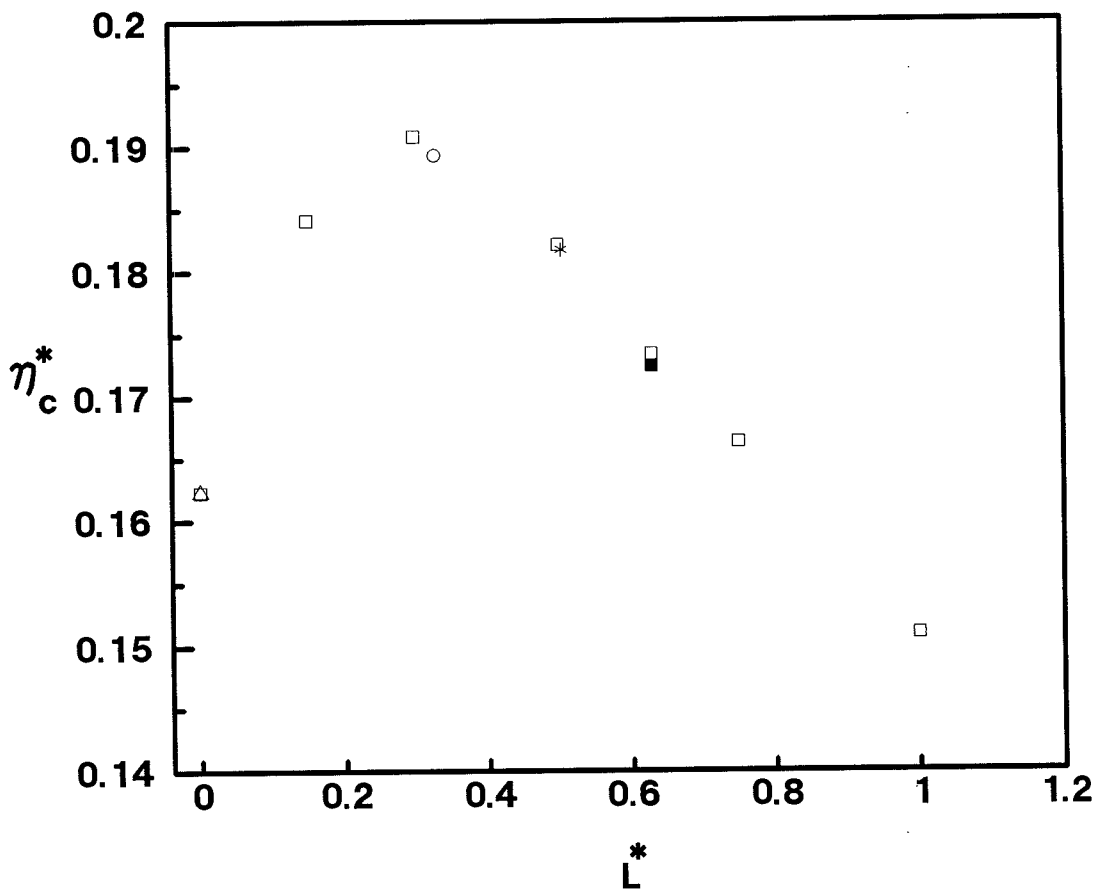

Figure 2.9 The critical packing fractions as a function of bondlength for the DLJ molecules. The experimental results are shown for Ar (△), N_2 (○), F_2 (*), and Cl_2 (■) and are compared with the Gibbs simulation results (□).

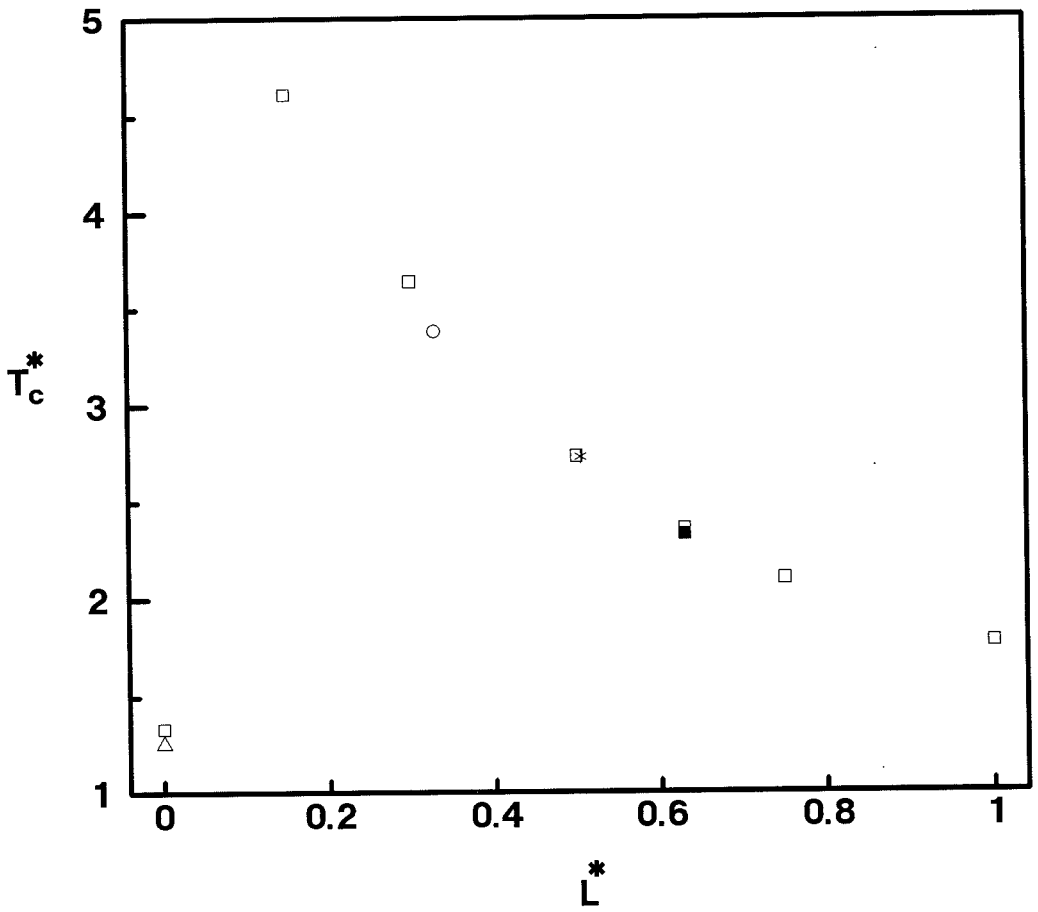

Figure 2.10 The critical temperatures as a function of bondlength for the DLJ molecules. The experimental results are shown for Ar (△), N_2 (○), F_2 (*), and Cl_2 (■) and are compared with the Gibbs simulation results (□).

the critical temperature rising with a decrease in the bondlength.

The final property of the phase diagrams that we were interested in investigating was whether the phase diagrams are conformal and hence obey the law of corresponding states. To answer this question we have plotted the coexistence curves for DLJ molecules with L^*=0.15, 0.50 and 0.75 in Figure 2.11. The curves are plotted in units that are reduced by the critical temperatures and critical packing fractions. The figure illustrates the departure of the molecules from the principle of corresponding states, but only in the liquid phase. The increase in molecular anisotropy with increasing bondlength causes a broadening of the coexistence region. The gaseous phases however do obey the principle of corresponding states.

Having presented the critical properties of the DLJ molecules, we now wish to compare the results of our simulations with those of the RISM equation. Before introducing the RISM equation, we will first give a brief description of the Ornstein-Zernike equation, an equation closely related to the RISM equation.

2.4 The RISM Equation

2.4.1 The Ornstein-Zernike Equation

The central problem in classical equilibrium statistical mechanics, is in the evaluation of the partition function. Once this has been achieved, then it can be used to calculate any required thermodynamic quantities. However, the partition function can only be evaluated analytically for a very few simple cases [20]. For instance, the partition function can be evaluated for a system in one dimension, involving interactions between hard cores on a line.

Thus for a simple liquid, a different route to the thermodynamic variables is required. This is achieved by replacing the problem of the evaluation of the partition function, with the equivalent problem of the evaluation of the grand canonical correlation function [15]. This approach leads to the evaluation of the two particle correlation function g(1,2), which is equivalent to the evaluation of the partition function for pair-additive potentials. The notation (1,2) denotes that g is a function of the positions and orientations of the particles 1 and 2 ie., $1\equiv\mathbf{r}_1\omega_1$ and $2\equiv\mathbf{r}_2\omega_2$ where $\omega_1=(d\cos\theta_1\ d\phi_1)/4\pi$ for a linear molecule and similarly for particle 2.

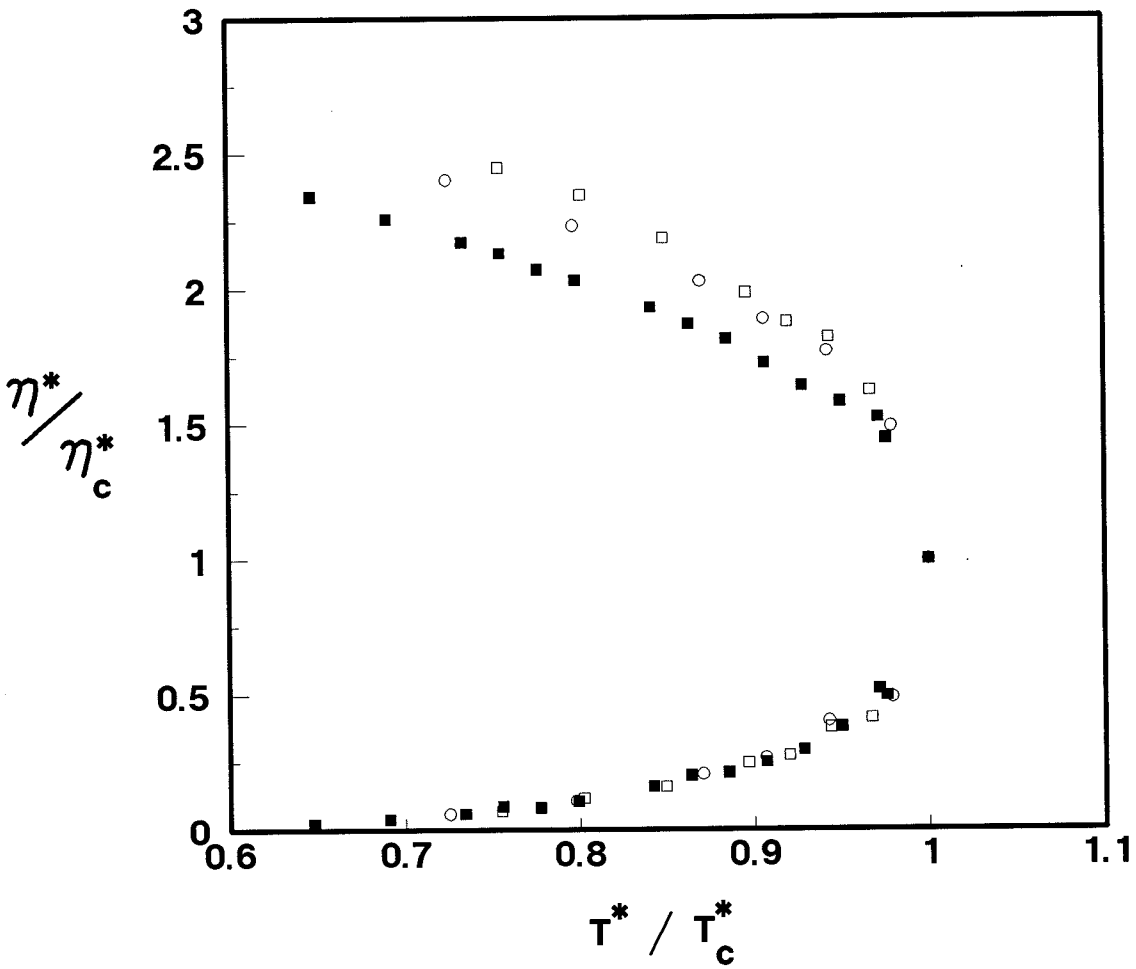

Figure 2.11 The packing fractions for DLJ molecules with L^*=0.15 (■), 0.50 (○) and 0.75 (□) as a function of reduced temperature. The packing fractions and temperatures are reduced by their critical values.

Most of the thermodynamic properties of the liquid can be obtained from integrals involving the two particle correlation function, ie.,

$$\rho^2 g(1,2) = \frac{N(N-1)}{Z_{NVT}} \int d3\ d4\ \ldots\ dN\ \exp(-\beta U(1,2,\ldots N)) \qquad (2.35)$$

In eqn (2.35) Z_{NVT} is the configurational integral defined by eqn (1.11) and the notation U(1,2,..N) is used to denote the total potential energy of the N particles. For an isotropic system, containing spherically symmetric atoms, the two particle distribution function reduces to the usual radial distribution function, g(r). The correlation function g(1,2) can be shown [21] to be the solution of two coupled equations, the first is exact and the other approximate. The exact equation is known as the Ornstein-Zernike equation (OZ equation),

$$h(1,2) = c(1,2) + \rho \int d3\ c(1,3)\, h(3,2)\ . \qquad (2.36)$$

In eqn (2.36), the notation d3 denotes the position and orientation of particle 3, c(1,2) is the direct correlation function between particles 1 and 2, and h(1,2) is the total correlation function between particles 1 and 2. c(1,2) is termed the direct correlation function because it describes correlations directly between the two specified particles. h(1,2) is termed the total correlation function because it describes the total interaction between the given particles ie. interacting directly and interacting through a third particle, interacting through a fourth particle etc.

The OZ equation cannot be solved directly as it is an equation in two unknowns, the total and direct correlation functions. Therefore to solve the OZ equation another relationship is needed between the two correlation functions. This second equation is known as a closure relation. There are two main closure relations used with the OZ equation, both of which are approximate. These closure relations are the Percus-Yevick (PY) closure,

$$c(1,2) = \{1-\exp[\beta U(1,2)]\}\ \{1+h(1,2)\}\ , \qquad (2.37)$$

and the hyper-netted chain (HNC) approximation,

$$c(1,2) = -\beta U(1,2) + h(1,2) - \log[1+h(1,2)]\ . \qquad (2.38)$$

Either eqn (2.37) or (2.38) can be used together with the OZ equation to obtain h(1,2) and c(1,2). Once the total correlation function has been obtained, the pair correlation function g(1,2) can easily be obtained since,

$$g(1,2) = 1 + h(1,2) \ . \tag{2.39}$$

Once the pair correlation function has been obtained from eqn (2.39), the thermodynamic variables of the system can be evaluated in the standard way, eg.,

$$U = \frac{1}{2} N\rho \int d1 \int d2 \ u(1,2)\, g(1,2) \ . \tag{2.40}$$

The OZ equation is applicable to both atomic and molecular fluids. When dealing with atomic fluids the notation (1,2) simply denotes the positions of atoms 1 and 2. In this case it is possible to solve the OZ equation to obtain the atomic correlation functions. However, when applying the OZ equation to molecular fluids the solution of the equation becomes significantly more difficult. This is because the correlation functions for even the simplest case of linear diatomic molecules now depend on the separations of the centres of mass of the molecules, and on the three angles required to specify their relative orientations (cf. eqn (2.1)). The tabulation of the correlation functions now becomes a daunting task as the orientational and translational coordinates of even a linear diatomic molecule are coupled in a non-trivial way.

To simplify this problem of the complexity in the correlation functions, it is fruitful to rewrite the OZ equation in a form suitable to describe site-site correlation functions [15]. This new equation is known as the Site-Site Ornstein-Zernike equation (SSOZ), or the Reduced Interaction Site Model (RISM) [22] and it is an approximate equation for a molecular fluid.

2.4.2 The RISM Equation

The key ingredient in the RISM equation is an Ornstein-Zernike-like relation between the site-site total correlation function $h_{\alpha\beta}(r_{\alpha\beta})$ and the site-site direct correlation function $c_{\alpha\beta}(r_{\alpha\beta})$. In the Ornstein-Zernike equation the total correlation between particles 1 and 2 is the sum of all possible paths of direct correlations that propagate via intermediate particles 3, 4 etc. The same idea is used in the RISM equation for site-site

correlations with the exception that the RISM equation also includes correlations that propagate via the intramolecular bonds. The RISM equation can be written as,

$$H = WCW + \rho WCWCW + \rho^2 WCWCWCW + \ldots , \tag{2.41}$$

or in a more compact form,

$$H = WCW + \rho WCH , \tag{2.42}$$

where H and C are matrices whose elements are given by,

$$h_{\alpha\beta}(r_{\alpha\beta}) , \tag{2.43}$$

$$c_{\alpha\beta}(r_{\alpha\beta}) . \tag{2.44}$$

The correlation functions $c_{\alpha\beta}$ and $h_{\alpha\beta}$ are directly analogous to their counterparts for the atomic liquids case. The elements of the matrix W are given by,

$$w_{\alpha\beta} = \delta_{\alpha\beta}\,\delta(r_{\alpha\beta}) + s_{\alpha\beta}(r_{\alpha\beta}) , \tag{2.45}$$

where $s_{\alpha\beta}(r_{\alpha\beta})$ is the intramolecular correlation function, which describes the distribution of sites within a single molecule and for a linear diatomic molecule is given by,

$$s_{\alpha\beta}(r_{\alpha\beta}) = \frac{(1-\delta_{\alpha\beta})\;\delta(r_{\alpha\beta}-\ell_{\alpha\beta})}{4\pi\ell_{\alpha\beta}^2} . \tag{2.46}$$

In eqn (2.46) $\ell_{\alpha\beta}$ is the distance between sites within a single molecule. The functions $\delta_{\alpha\beta}$ and $\delta(r_{\alpha\beta})$ are the Kronecker-delta and Dirac-delta functions respectively. The matrix products in eqn (2.42) denote the operations of a matrix multiplication together with a convolution ie,

$$(CH)_{\alpha\gamma} = \sum_{\beta} \int d\mathbf{r}'\; c_{\alpha\beta}(|\mathbf{r}-\mathbf{r}'|)\; h_{\beta\gamma}(\mathbf{r}') . \tag{2.47}$$

As in the OZ equation, a closure relation is required to solve the RISM equation and one such closure is the Percus-Yevick-like closure,

$$c_{\alpha\beta}(r_{\alpha\beta}) = y_{\alpha\beta}(r_{\alpha\beta})\, f_{\alpha\beta}(r_{\alpha\beta}) , \tag{2.48}$$

where,

$$y_{\alpha\beta}(r_{\alpha\beta}) = g_{\alpha\beta}(r_{\alpha\beta})\, \exp[\beta u_{\alpha\beta}(r_{\alpha\beta})] , \tag{2.49}$$

and $g_{\alpha\beta}(r_{\alpha\beta})$ is the site-site radial distribution function. The term $f_{\alpha\beta}(r_{\alpha\beta})$ is the site-site Mayer f-function defined as,

$$f_{\alpha\beta}(r_{\alpha\beta}) = -1 + \exp[-\beta u_{\alpha\beta}(r_{\alpha\beta})] . \tag{2.50}$$

For the homonuclear diatomic molecules considered in this study (the DLJ molecules), the RISM equation reduces to a scalar equation in k-space, ie.,

$$\begin{pmatrix} \hat{h} & \hat{h} \\ \hat{h} & \hat{h} \end{pmatrix} = \begin{pmatrix} 1 & \hat{s} \\ \hat{s} & 1 \end{pmatrix} \begin{pmatrix} \hat{c} & \hat{c} \\ \hat{c} & \hat{c} \end{pmatrix} \begin{pmatrix} 1 & \hat{s} \\ \hat{s} & 1 \end{pmatrix} + \rho \begin{pmatrix} 1 & \hat{s} \\ \hat{s} & 1 \end{pmatrix} \begin{pmatrix} \hat{c} & \hat{c} \\ \hat{c} & \hat{c} \end{pmatrix} \begin{pmatrix} \hat{h} & \hat{h} \\ \hat{h} & \hat{h} \end{pmatrix} , \tag{2.51}$$

where the carets denote Fourier transforms defined by,

$$\hat{h}(k) = \int h_{\alpha\beta}(r_{\alpha\beta})\, e^{ik.r_{\alpha\beta}}\, dr_{\alpha\beta} . \tag{2.52}$$

The RISM equation presented above, has been numerically solved in this work using the Gillan method [23], as modified by Monson [24]. The Gillan method was used to solve the Ornstein-Zernike equation for atomic fluids and Monson extended the method for use in solving the RISM equation for molecular fluids. Gillan's method uses a powerful multidimensional, non-linear Newton-Raphson technique to search for solutions to the RISM equation.

To investigate the accuracy of the RISM equation, three diatomic molecules were investigated. The bondlengths of these molecules were chosen so that they investigated the RISM equation for bondlengths ranging from the very small to the very large. The three DLJ molecules investigated were those with reduced bondlengths of 0.63 (chlorine), 0.30 and 1.00. The RISM equation was solved numerically by the method of Gillan to obtain the site-site distribution function $g_{\alpha\beta}(r_{\alpha\beta})$. The results obtained from the RISM equation are compared to those of our Gibbs simulations in Figures 2.12, 2.13

and 2.14. The Gibbs simulation data represents the site-site distribution function from the liquid phases only. The gaseous phase results are presented separately. Three distribution functions are presented for each of the bondlengths and represent temperatures close to the triple point, close to the critical point and intermediate between the two temperatures for each of the diatomics. As can be seen from the figures the agreement between the simulation and RISM results is good in these high density regimes.

The gaseous phase results from the Gibbs simulations are noisy. The reason for this is that in all the simulations carried out the number of molecules in equilibrium in the gaseous phases were insufficient to obtain smooth distribution functions. Three of these distribution functions are shown in Figure 2.15. Obviously it would be difficult to compare these distribution functions with those obtained from the numerical solution of the RISM equation. In order that we could obtain a comparison between the simulations and RISM in the low density limit, we carried out a separate NVT simulation. In this simulation, the density and temperature were set equal to those of the gaseous phase from a Gibbs simulation. The simulation was carried out for chlorine's gaseous phase at $T^*=1.90$, a point somewhat removed from the critical point. The resulting $g_{\alpha\beta}(r)$ was in very close agreement with the Gibbs result, but a lot smoother. The results of this simulation are compared with those of the RISM equation in Figure 2.16. The RISM equation is in good agreement with the simulation results in the higher density regimes of the coexisting liquid phases, but in significantly poorer agreement in the low density gaseous regime.

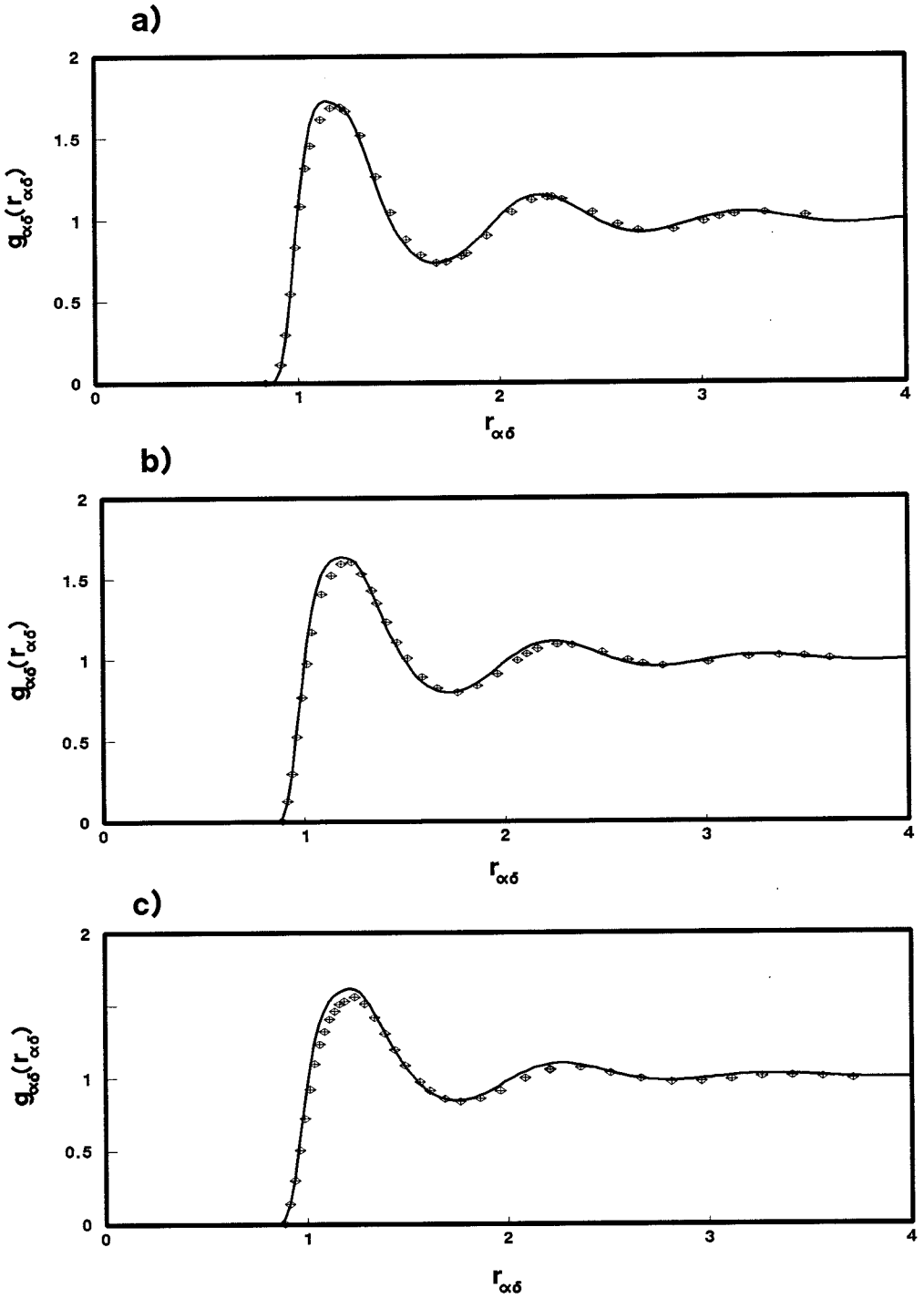

Figure 2.12 The site-site radial distribution function $g_{\alpha\delta}(r_{\alpha\delta})$ as a function of the reduced distance $r_{\alpha\delta}$, for the DLJ molecule with $L^*=0.30$. The symbols are from the Gibbs simulations and the solid line represents the RISM result. The state points investigated are: a) $T^*=2.50$, $\rho^*=0.606$, b) $T^*=3.00$, $\rho^*=0.528$ and c) $T^*=3.30$ $\rho^*=0.465$.

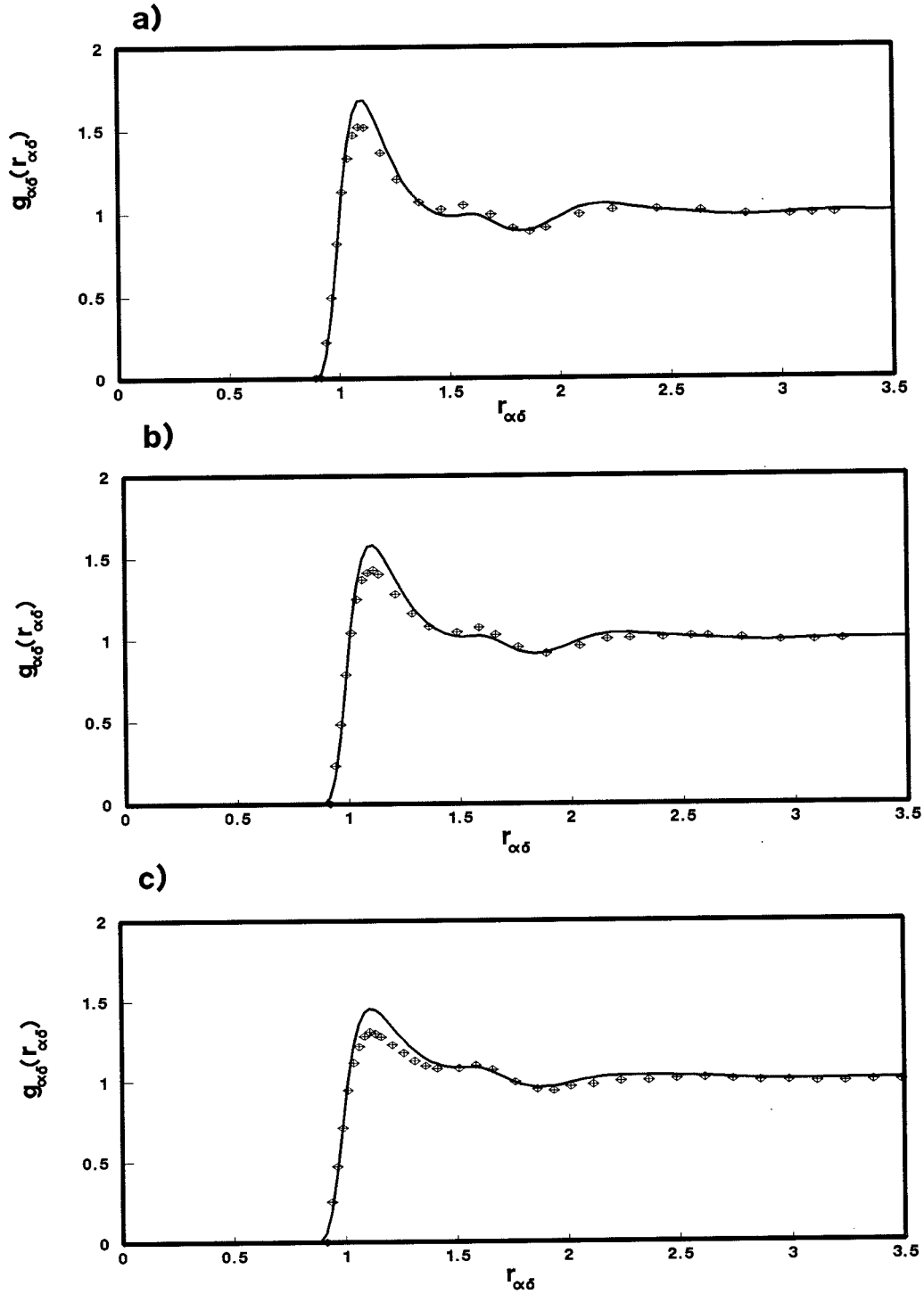

Figure 2.13 The site-site radial distribution function $g_{\alpha\delta}(r_{\alpha\delta})$ as a function of the reduced distance $r_{\alpha\delta}$, for the DLJ molecule with $L^*=0.630$ (chlorine). The symbols are from the Gibbs simulations and the solid line represents the RISM result. The state points investigated are: a) $T^*=1.70$, $\rho^*=0.427$, b) $T^*=1.90$, $\rho^*=0.402$ and c) $T^*=2.20$ $\rho^*=0.325$.

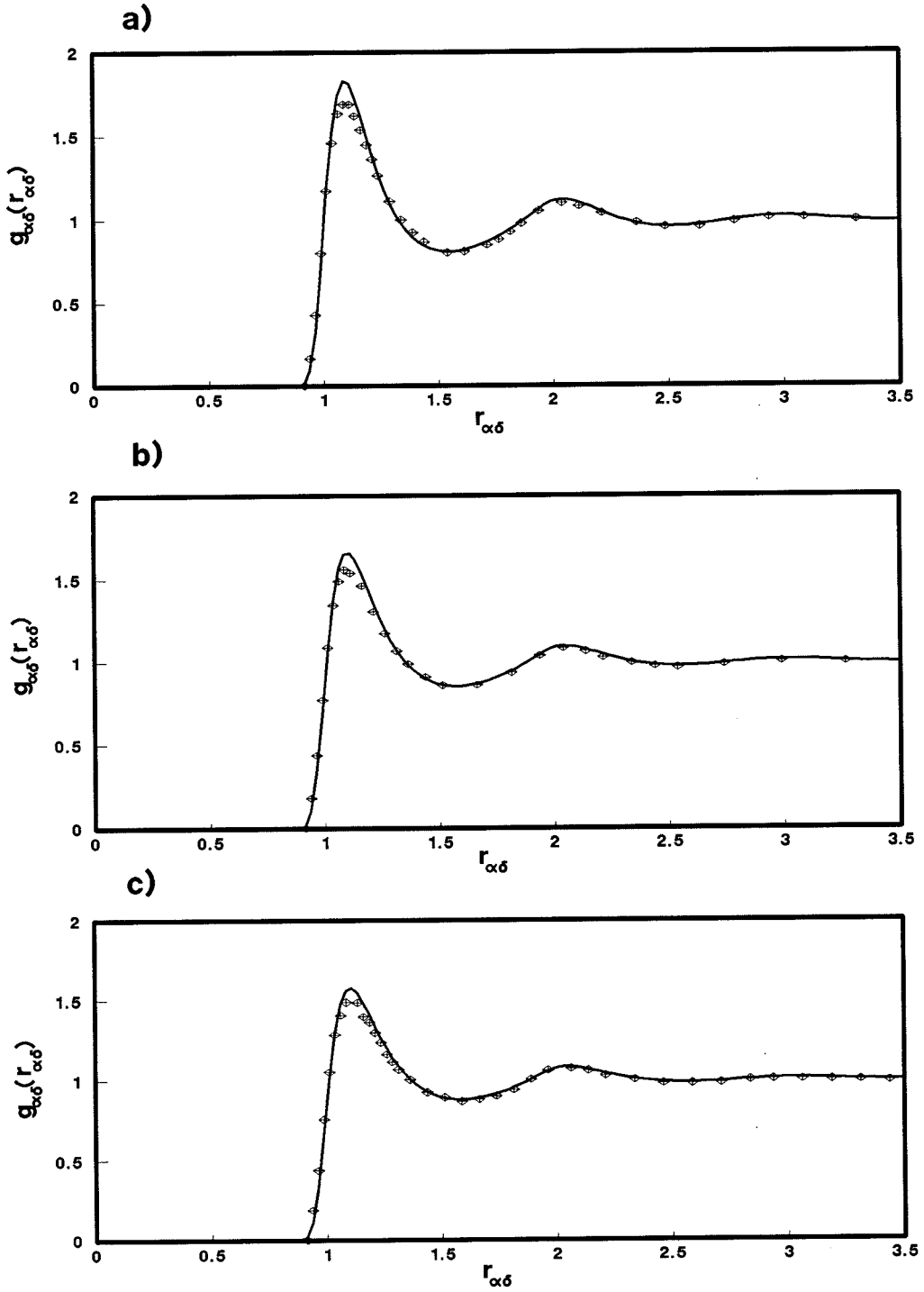

Figure 2.14 The site-site radial distribution function $g_{\alpha\delta}(r_{\alpha\delta})$ as a function of the reduced distance $r_{\alpha\delta}$, for the DLJ molecule with $L^*=1.00$. The symbols are from the Gibbs simulations and the solid line represents the RISM result. The state points investigated are: a) $T^*=1.40$, $\rho^*=0.334$, b) $T^*=1.55$, $\rho^*=0.292$ and c) $T^*=1.65$ $\rho^*=0.264$.

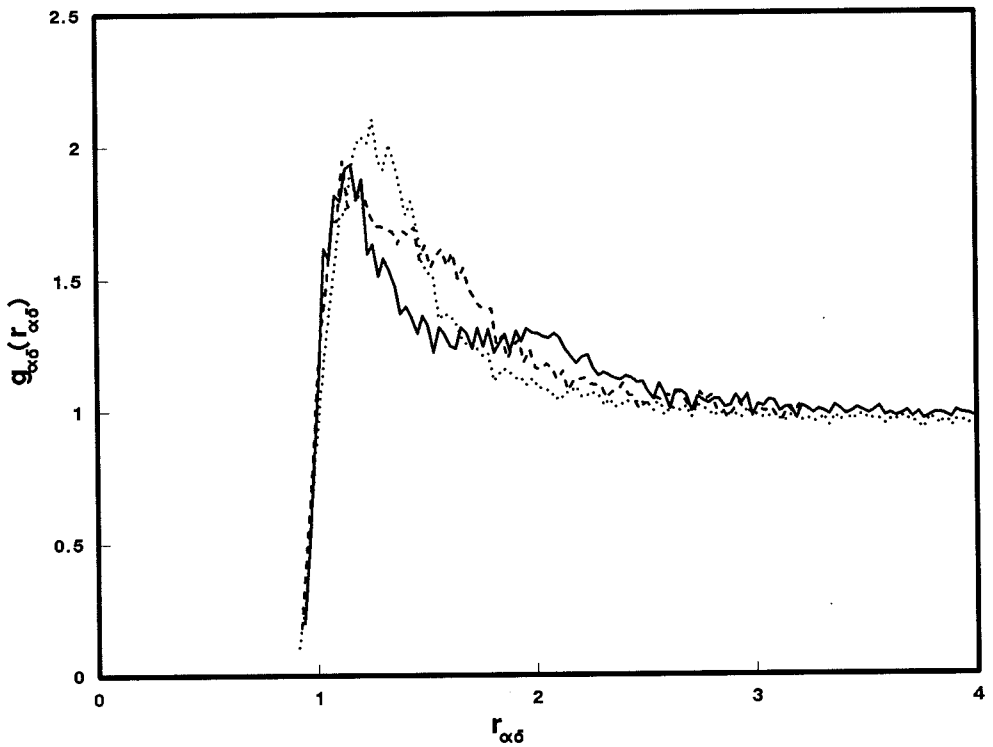

Figure 2.15 The site-site radial distribution function $g_{\alpha\delta}(r_{\alpha\delta})$ as a function of the reduced distance $r_{\alpha\delta}$, obtained from Gibbs simulations of the gaseous phases of the DLJ molecules. The state points investigated are a) $L^*=0.63$ $T^*=1.90$ $\rho^*=0.018$ (dashed line), b) $L^*=1.00$ $T^*=1.55$ $\rho^*=0.023$ (full line) and c) $L^*=0.30$ $T^*=3.00$ $\rho^*=0.036$ (dotted line).

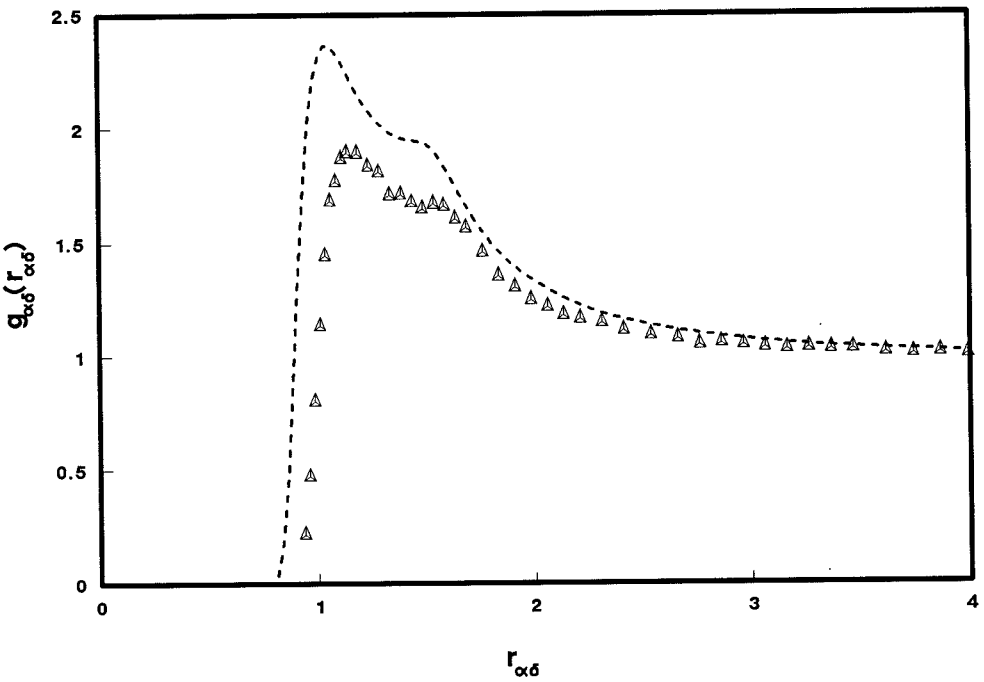

Figure 2.16 The site-site radial distribution function $g_{\alpha\delta}(r_{\alpha\delta})$ as a function of the reduced distance $r_{\alpha\delta}$, for the DLJ molecule with $L^*=0.63$ (chlorine). The line represents the RISM result and the symbols the NVT simulation. The simulation was performed at the state point $T^*=1.90$ $\rho^*=0.018$.

2.5 References

[1] L.D. Landau and E.M. Lifshitz, "Statistical physics", 3rd edn, Pergamon press, (1980).

[2] S. Romano and K. Singer, "Calculation of the entropy of liquid chlorine and bromine by computer simulation", Mol. Phys., **37**, 1765-1772, (1979).

[3] M.C. Wojcik, K.E. Gubbins and J.G. Powles, "The thermodynamics of symmetric two centre Lennard-Jones liquids", Mol. Phys., **45**, 1209-1225, (1982).

[4] P.M. Rodger, A.J. Stone and D.J. Tildesley, "The intermolecular potential of chlorine. A three phase study", Mol. Phys., **63**, 173-188, (1988).

[5] J.G. Powles, "The liquid-vapour coexistence line by computer simulation à la Widom", Mol. Phys., **41**, 715-727, (1980).

[6] K. Singer, A. Taylor and J.V.L. Singer, "Thermodynamic and structural properties of liquids modelled by '2-Lennard-Jones centres' pair potentials", Mol. Phys., **33**, 1757-1795, (1977).

[7] T.M. Reed and R.E. Gubbins, "Applied statistical mechanics", Mcgraw-Hill, (1973).

[8] J.P. Hansen and I.R. McDonald, "Theory of simple liquids", Academic press, (1986).

[9] M.P. Allen and D.J. Tildesley, "Computer simulation of liquids", Oxford science publications, (1991).

[10] M.R. Stapleton and A.Z. Panagiotopoulos, "Application of excluded volume map sampling to phase equilibrium calculations in the Gibbs ensemble", J. Chem. Phys., **92**, 1285-1293, (1990).

[11] P.M. Rodger, A.J. Stone and D.J. Tildesley, "Anisotropic site-site potentials in Molecular Dynamics", Molec. Simulation, **8**, 145-164, (1992).

[12] J.R. Sweet and W.A. Steele, "Statistical mechanics of linear molecules. I. Potential energy functions", J. Chem. Phys., **47**, 3022-3028, (1969).

[13] S. Angus, B. Armstrong and K.M. De Reuck, (editors), "Chlorine, international thermodynamic tables of the fluid state", Vol. 8 (Chemical data series, No. 31) (Pergamon press), (1984).

[14] J.S. Rowlinson and F.L. Swinton, "Liquids and liquid mixtures", Butterworth scientific, (1982).

[15] P.A. Monson and G.P. Morriss, "Recent progress in the statistical mechanics of interaction site fluids", Adv. Chem. Phys., **77**, 451-550, (1990).

[16] A.Z. Panagiotopoulos, "Direct determination of phase coexistence properties of fluids by Monte Carlo simulation in a new ensemble", Mol. Phys., **61,** 813-826, (1987).

[17] G.W.C. Kaye and T.H. Laby, "Tables of physical and chemical constants and some mathematical functions", (London), (1986).

[18] P.S.Y. Cheung and J.G. Powles, "The properties of liquid nitrogen. IV. A computer simulation", Mol. Phys., **30**, 921-949, (1975).

[19] G.C. Maitland, M. Rigby, E.B. Smith and W.A. Wakeham, "Intermolecular forces: Their origin and determination", Clarendon press, Oxford, (1981).

[20] S. Ma, "Statistical mechanics", World scientific, (1985).

[21] H.C. Andersen, "Modern theoretical chemistry, Vol. 5: Statistical mechanics", B.J. Berne, Ed., Plenum, New York, (1977).

[22] B.M. Ladanyi and D. Chandler, "New type of cluster theory for molecular fluids: Interaction site cluster expansion", J. Chem. Phys., **62**, 4308-4324, (1975).

[23] M.J. Gillan, "A new method of solving the liquid-structure integral equations", Mol. Phys., **38**, 1781-1794, (1979).

[24] P.A. Monson, "Numerical solution of the RISM equation for the site-site 12-6 potential", Mol. Phys., **47**, 435-442, (1982).

3. The Computer Simulation of Polymers

3.1 Introduction

Polymers are chain molecules that are built up of repeating units, or monomers. Some typical polymers and their respective monomers are,

Polyethylene $[CH_2]_N$,

Polydimethylsiloxane $[Si(CH_3)_2O]_N$,

Polystyrene $[CH_2(CH(C_6H_5))]_N$.

To perform atomistic simulations of polymers, whether by the Monte Carlo or molecular dynamics methods [1], would be difficult because of the large range of time and length scales spanned by the motions of a polymer chain. Local oscillations within a polymer chain, such as bond angle oscillations, occur on a timescale of approximately 10^{-13}s, necessitating MD timesteps of 10^{-14} seconds. However, diffusion processes for polymer chains in melts typically occur on the timescale of 10^{-4} to 10^{1} seconds. It is not possible to cover this range of timescales with the fastest computers currently available. Polymer chains also exhibit structure on a range of length scales from a single chemical bond (≈1Å), to the persistence length (≈10Å), to the coil radius (≈100Å).

Despite these apparent difficulties, simulations of polymer models are still possible. In many cases the inclusion of full atomistic detail in the simulation of a polymer is not in fact necessary. This is because polymers exhibit universal behaviour which is independent of the local chemical structure of a polymer chain. For instance a single chain in a solvent has a square end-to-end distance, R^2, given by [2],

$$\langle R^2(N) \rangle \cong A N^{2\nu} . \qquad (3.1)$$

In eqn (3.1), the symbol ≅ is used to denote that only the scaling law is stated and all numerical factors are ignored. In eqn (3.1) A is a constant that depends on the detailed atomistic structure of the polymer chain, N is the number of repeat units in the chain (the degree of polymerization) and ν is a universal scaling exponent whose value is determined by the quality of the solvent that the polymer chain is immersed in. For a three dimensional linear polymer chain in a good solvent, ν has a value of 0.59. The

method used to obtain the value of the exponent ν is outlined in section 4.5. Therefore if the length of a given chain in a good solvent is doubled, we see from eqn (3.1) that its square end-to-end distance is increased by a factor of 2^{ν}. Such a scaling law only holds for flexible chains with large N.

Insight into this scaling behaviour can be gained if we think about the detailed structure of a given polymer, polyethylene for instance. The repeat unit, or monomer, of polyethylene is the CH_2 group. The angle θ between successive C-C bonds is essentially fixed, but as successive CH_2 units are added to the chain, an extra angle ϕ is needed to define the conformation of groups of four carbon atoms. The angle ϕ defines the torsional angle between four successive carbon atoms and has associated with it a potential known as a torsional potential. The torsional angle ϕ between four carbon atoms is illustrated in Figure 3.1. The torsional potential associated with this angle is also shown in the figure. The torsional potential displayed in the figure is that of Ryckaert and Bellemans [3], a potential widely used in the simulation of alkane systems. The torsional potential has three minima, corresponding to the three principal conformations, the gauche$^+$, gauche$^-$ and trans conformations. There is an energy difference of $\Delta\varepsilon$ between the minima. If $\Delta\varepsilon$ is of the order of the thermal energy, k_BT, then the chain is said to be statically flexible. In this situation, there are significant torsional populations in the gauche state as well as the trans state. On the scale of the whole chain (hundreds of angstroms), the ability of successive carbon atoms to adopt different conformations causes the chain to become a random coil. If the temperature is lowered, the preference for the trans state will increase and the numbers of torsional angles in the gauche states will decrease. On the scale of a few bond lengths the chain will appear to be rigid due to the marked preference for the trans conformation. However, on a large enough scale, the chain will still appear to be a random coil. If the temperature is lowered far enough, the trans state will be the only state occupied and the chain will become a rigid rod.

More generally, when the details of a given chain smaller than a given characteristic length, l_p, are ignored, the chain is seen as a continuous flexible coil. The parameter l_p is called the persistence length [4] of the chain and is defined as the average sum of the projections of all bonds in the chain onto the first bond on the chain, in an indefinitely long chain [53].

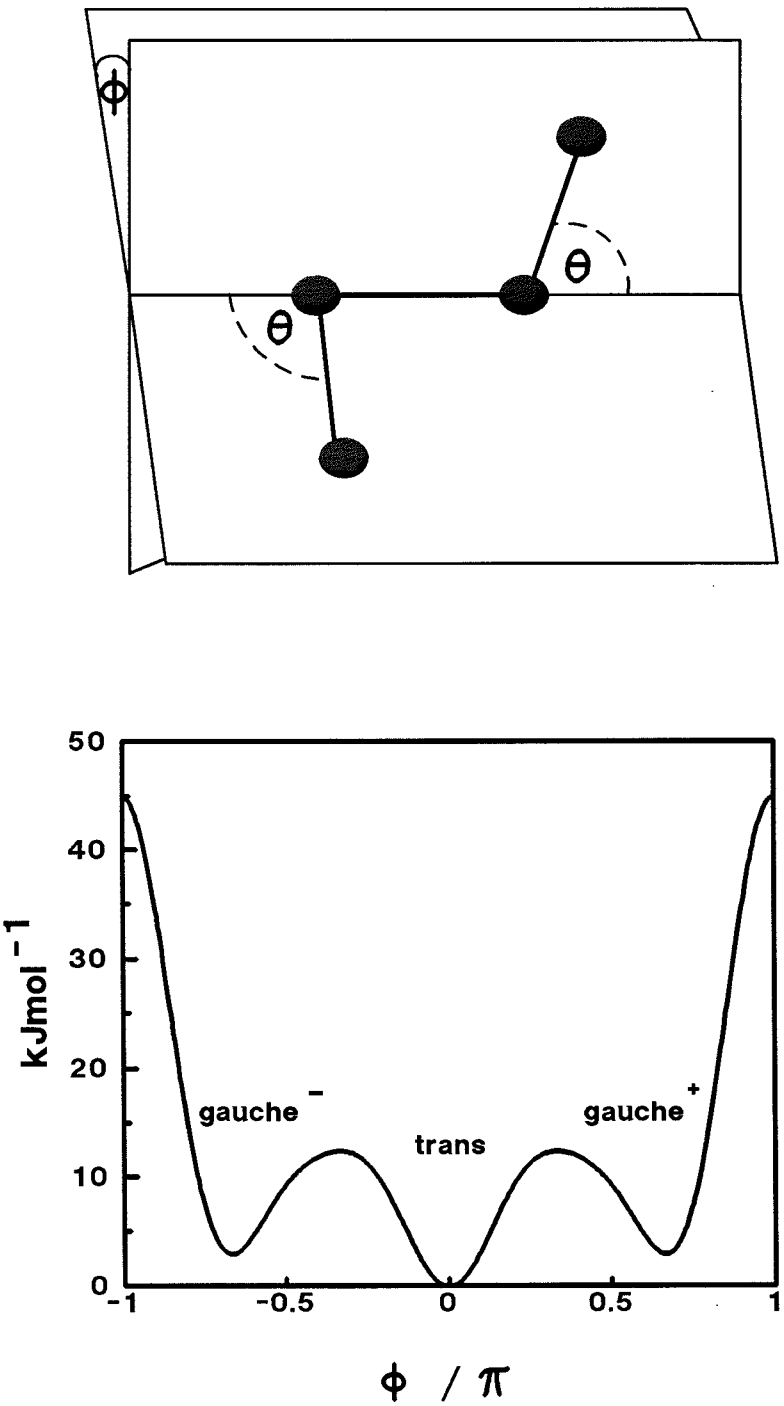

Figure 3.1 The torsional angle between four carbon atoms and the corresponding torsional potential of Ryckaert and Bellemans [3].

If we denote the unit vector defining the direction of the first bond in the chain by $\mathbf{e}_1$ and the i^{th} unit vector in the chain as $\mathbf{e}_i$, then the persistence length is given by,

$$l_p = l\sum_{i=1}^{\infty} \mathbf{e}_i.\mathbf{e}_1 \ , \tag{3.2}$$

where l is the bond length of the monomers within the polymer chain. If l_p is much smaller than L, the total length of the chain, then we can choose to look at the polymer chain on a length scale in which the rigid portions of the molecule (of size $\sim l_p$) are too small to be seen. The polymer chain will now appear to be a flexible coil. If however l_p is of the order of L, then the chain is a rigid rod on all length scales. The idea of chain rigidity on small length scales and chain flexibility on large length scales is illustrated in Figure 3.2. Therefore we can see that on length scales above the persistence length, all linear polymer chains share similar properties, regardless of their detailed chemical structure.

In computer simulations of polymers we can make use of the fact that the detailed chemical structure of a given polymer is only important on length scales smaller than the persistence length of the polymer, to construct 'coarse-grained' models of polymers. In these models we make no attempt to include the full atomistic details of any given polymer but instead focus our attention on details of polymers on length scales larger than the persistence length. Hence in our simulations we try to obtain information about the universal features of polymers which remain true for a large class of macromolecules ie. the square end-to-end distance of eqn (3.1). This is achieved by constructing models of polymer chains consisting of beads bonded together. Each of the beads in the model corresponds to several chemical monomers in a real polymer chain and each bond between the beads is of length of the order of the persistence length. A disadvantage to this approach to the modelling of polymers is that all chemical details of the polymer are lost and it is not clear how to map the properties of these coarse grained model polymers onto the properties of a particular real polymer [5]. However this approach to the modelling of polymers will allow us to investigate universal properties of polymer chains such as the scaling of the square end-to-end distance of a polymer chain in a solvent (eqn (3.1)).

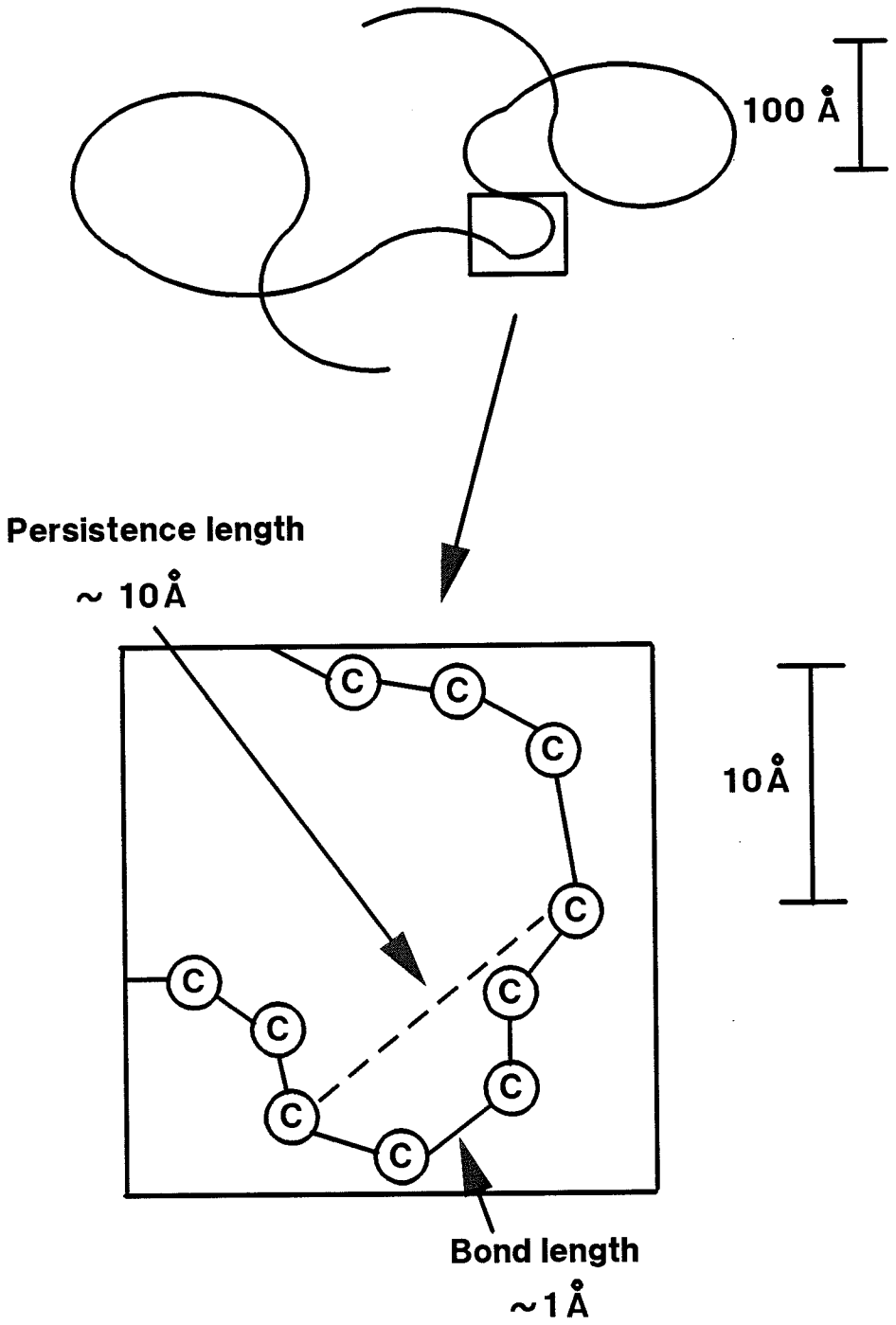

Figure 3.2 The different length scales relevant in polymer problems for the simple example of polyethylene.

There are in general three classes of models used in the computer simulation of polymers. These are lattice models, bead-rod models (hard beads separated by bonds of fixed length) and bead-spring models (hard beads separated by bonds of variable length). The first of these models is used exclusively in conjunction with the Monte Carlo method. The other two models are continuum models, the first of which is usually used in Monte Carlo simulations and the second is usually used in molecular dynamics simulations of polymer chains.

A short description of the three models will now be given and this will be followed by a brief review of some of the recent polymer simulations that have been performed.

3.2 Polymer models

3.2.1 Lattice Models

Lattice models of polymers are the simplest to implement both conceptually and computationally. In these models, a flexible polymer chain is replaced by a random walk on a periodic lattice. The most widely studied of the lattice models is the self-avoiding walk (SAW). In this model each of the lattice points can only be occupied once (an excluded volume condition). Occupied lattice points represent the beads in the polymer and these are bonded together along the lines connecting the lattice points. Although it is a formidable problem to calculate the properties of self-avoiding walks mathematically, the model is well suited to investigation by Monte Carlo methods. Lattice simulations can be used to investigate isolated polymer chains, polymer melts and polymer-solvent systems and these models can be generalized to include attractive interactions between the various beads. An illustration of a SAW on a two dimensional square lattice is shown in Figure 3.3. Although a two dimensional square lattice is shown in Figure 3.3, lattices with other connectivities are also commonly used, such as the tetrahedral lattice.

Early simulations of polymers concentrated on calculating the properties of SAWs confined to two and three dimensional lattices [6,7]. Typically these simulations investigated static properties of the SAWs such as the square end-to-end distance as a function of the number of beads in the chain. One of the findings of these simulations was that the square end-to-end distance of the chains obeyed a scaling law of the form of eqn (3.1) and that the scaling exponent ν was independent of the symmetry of the

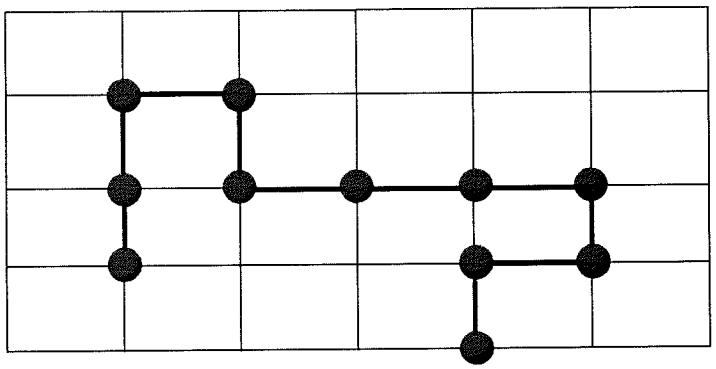

Figure 3.3 A self-avoiding walk on a two dimensional square lattice.

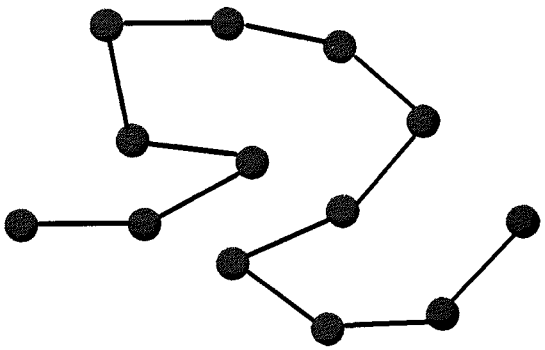

Figure 3.4 A bead-rod model of a polymer as used in Monte Carlo simulations of polymers.

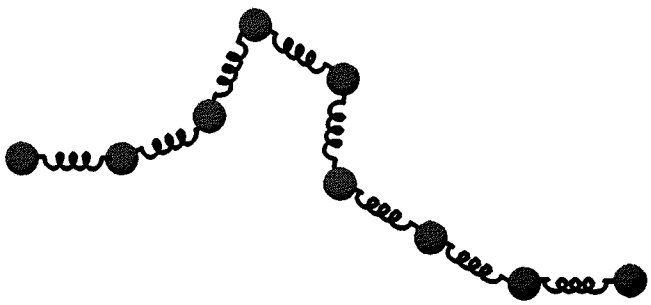

Figure 3.5 A bead-spring model of a polymer as used in the molecular dynamics method.

lattice used to produce the SAW. More recently the scaling exponent ν has been determined to a higher degree of accuracy in two and three dimensions using algorithms that allow the efficient simulation of chains of long length [46]. Various properties of polymer chains confined to lattices are still of interest, such as the square end-to-end distance of the chain as a function of the quality of the solvent and the structure function of ideal and excluded volume linear polymer chains [8,9].

Lattice simulations have been useful in the investigation of the scaling behaviour of polymer chains in various situations. For instance, lattice simulations of polymer chains verified the scaling behaviour predicted by Daoud and de Gennes [10] for polymer chains confined between two and three dimensional surfaces [11]. Other lattice simulations have investigated the dynamics of polymer chains confined in tubes [12], the adsorption behaviour of chains near surfaces [13] and various properties of polymer chains in solution [14,15].

More recently, lattice simulations have been used to examine the structure of polymer melts confined between walls and the forces exerted between the walls as a function of the wall separation [41,42]. Polymers grafted to a surface have also received recent attention, with the structure of the polymer layers examined as a function of the density of chains attached to the surface [34,35,36].

3.2.2 Bead-Rod Models

The bead-rod model is also commonly referred to as the pearl necklace model of a polymer chain. This model consists of beads connected by hard rods of a given length and negligible diameter. No bond angle restrictions are placed on the angles between neighbouring beads. The beads in the chain are commonly modelled with the hard sphere potential and the repulsive Lennard-Jones potential (the WCA potential [16]) which has the form,

$$u(r) = 4\epsilon\left[\left(\frac{\sigma}{r}\right)^{12} - \left(\frac{\sigma}{r}\right)^{6} + \frac{1}{4}\right] \qquad r \le 2^{\frac{1}{6}}\sigma\ , \tag{3.3}$$

$$u(r) = 0 \qquad r > 2^{\frac{1}{6}}\sigma\ . \tag{3.4}$$

An illustration of a bead-rod polymer chain is given in Figure 3.4. Bead-rod models

have been used to investigate similar systems to the lattice models mentioned in section 3.2.1 and have been especially useful in the study of polymeric systems in confined geometries (ie. between walls) [17,18,19].

3.2.3 Bead-Spring Models

The bead-spring model consists of beads modelled by the WCA potential, connected by springs and is used in molecular dynamics simulations of polymer chains. The springs are modelled by modified harmonic potentials of the form,

$$u(r) = k_c R_0^2 \ln\left[1-\left(\frac{r}{R_0}\right)^2\right], \tag{3.5}$$

where r is the distance between successive beads in the polymer chain, k_c is an energy parameter ($k_c<0$) and R_0 is a length parameter. This type of spring is referred to as a FENE spring [20] (finite extensibility nonelastic springs) and is very similar to harmonic potentials for $r/R_0 << 1$. Unlike harmonic potentials however, the FENE potential diverges when $r \rightarrow R_0$ and in this way the bond length is not allowed to exceed R_0. If the distance between bonded monomers is allowed to become too large then there is a possibility that part of the polymer chain will be able to cross through itself. The constants R_0 and k_c are usually assigned values that make it impossible for the polymer chain to cut through itself. An illustration of a bead-spring polymer chain is given in Figure 3.5 while Figure 3.6 shows the total potential between two bonded monomers, where the potential is comprised of the WCA potential of eqns (3.3) and (3.4) and the FENE potential of eqn (3.5). Figure 3.7 illustrates the situation of a polymer chain cutting through itself because of the distance between bonded beads becoming too large. Bead-spring models have been used to investigate polymer systems in a wide variety of situations including the dynamics of polymers in melts in the bulk [21] and confined between walls [22]. A number of simulations with this model have studied the effects of solvents on the properties of polymer chains such as the square end-to-end distance [23,24,25,26,27].

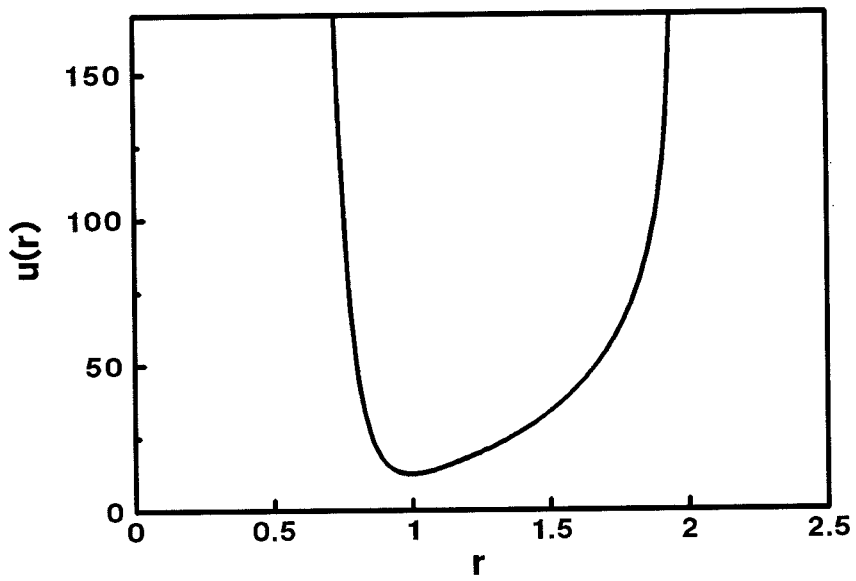

Figure 3.6. The total potential acting between two bonded monomers. The parameters $R_0=1.95\sigma$ and $k_c=-20\varepsilon/\sigma^2$ [28] are being used in the harmonic potential of eqn (3.5).

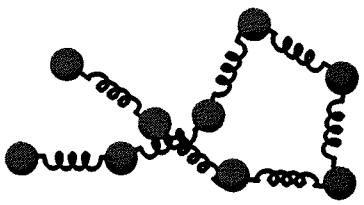

Figure 3.7. An illustration of the situation where the distance between bonded monomers has become large enough for the polymer chain to be able to cut through itself.

3.3 Recent Polymer Simulations

An area of ongoing interest lies in the properties of polymer systems in anisotropic geometries, for instance, confined between surfaces. Polymer chains between surfaces are of practical importance in a number of manufactured materials including foils, coatings and laminates. Polymer systems in confined geometries are of interest from a theoretical point of view because of the deviation of the properties of these systems from the properties of the corresponding systems in the bulk. For instance the scaling exponent of eqn (3.1) for the square end-to-end distance of a polymer in a solvent, is altered when placed between walls. This will be discussed in more detail in chapter 4. Diffusion properties of the chains are altered by the presence of walls and the density profile next to the walls is perturbed relative to the density profile of the system in the bulk.

One class of polymer systems of recent interest is that of polymers attached (grafted) by one end to a substrate. These systems are of technological importance because colloidal particles may be kept in suspension by grafting polymers onto their surfaces. Equilibrium conformations of, and forces between such polymer 'brushes' have been the subject of experimental [29,30], theoretical [31,32] and simulation studies [33,34,35,36,37].

Another class of polymer system that has been of recent interest is that of polymer melts confined between walls. Experimental studies were performed by Israelachvili *et. al.* [38] on these systems and long range repulsive forces were observed between the plates. The repulsive forces were of range approximately 6-10 S^2, where S^2 is the radius of gyration of the polymer, defined in eqn (3.7). These findings conflicted with the theoretical work of de Gennes [39] which predicted that no long range forces should exist (ie. beyond $\sim S^2$). Subsequent experimental work [40] revealed that the long range forces measured by Israelachvili [38] were viscous in nature, and resulted from the incomplete equilibration of the melt between measurements at successive wall separations. A number of simulation [41,22,42] and theoretical [43] studies have been performed on these systems in an attempt to try to understand the melt structure and properties of the polymer between the walls in greater detail.

Polymer adsorption at surfaces is of interest because of the practical applications of these processes in the stabilisation of colloids and in chromatographic applications.

Lattice simulations have been performed on polymers in good solvents between hard walls [44] to determine the shape and orientation of the polymer chain as a function of the ratio of the length of the chain to the separation between the walls. The scaling behaviour of polymer chains adsorbed at surfaces has also been the subject of study by lattice simulations [13]. Lattice simulations have the advantage that they are computationally more efficient than continuous space simulations. Our interest in this work lies in systems of polymer chains in good solvents between walls. In particular we were interested in examining the competitive adsorption effects between the solvent particles and polymer chains. As mentioned in section 3.2.1 in lattice models the beads in the polymer are modelled by occupied lattice points. In lattice simulations of polymers in solvents, the solvent particles are considered to occupy any of the lattice points not occupied by the polymer chains. It would not be possible to observe competitive adsorption effects in such systems due to the absence of the solvent particles. Lattice simulations also have the limitation that the effects of packing of molecules next to surfaces can not be observed [17,19]. To obtain the local structure of fluids next to walls therefore, one has to use continuous space models to investigate the system of interest. In this work we have performed Monte Carlo simulations of polymer chains and solvent particles between walls of varying nature. It is appropriate at this stage to introduce some of the Monte Carlo algorithms that are used in the simulations of polymers.

3.4 Monte Carlo Algorithms

In Monte Carlo methods it is necessary to design an algorithm which is not only appropriate for the study of the system of interest but that also explores the phase space of the system efficiently. The designing of efficient algorithms for the simulation of polymers is a difficult problem. In recent years a number of Monte Carlo algorithms have been introduced for the simulation of chain molecules.

The pivot algorithm of Lal [45,46] is a conceptually simple and efficient algorithm for the simulation of polymer chains. In this algorithm a point in the polymer chain is chosen randomly. Then one of the sections of the chain to the left or right of this point is rotated into a randomly chosen new position (conserving bond lengths and connectivities). The energy change in moving from the old state m to the new state n

is calculated, $\delta u_{nm} = u_n - u_m$, and the move accepted with the standard Monte Carlo criteria described in section 1.4.1, ie. accepted with a probability given by $\min(1,\exp(-\beta\delta u_{nm}))$. The algorithm is readily applicable to chains on lattices and in the continuum. In a vacuum the algorithm suffers from the problem of high rejection ratios for the attempted moves due to the chain overlapping with itself. Despite the high rejection ratios for attempted moves, the algorithm is an efficient method for generating polymer chain configurations. This is because each accepted polymer configuration is radically different from the preceding configuration. The detailed analysis of Madras and Sokal [46] revealed that for a polymer chain containing N bonds moved by the pivot algorithm, the square end-to-end distance converged an order of N times faster than for polymers moved by other algorithms such as the reptation algorithm discussed in a following section. However the problem of high rejection ratios rapidly worsens in solutions or in polymer melts, as the polymer chain can now overlap not only with itself, but also with the other particles in the system. This algorithm is therefore well suited to the simulation of isolated chains in vacuums but poorly suited to the simulation of polymer melts or polymers in solution.

A recently introduced algorithm for the simulation of polymers on square lattices is the bond fluctuation algorithm of Carmesin and Kremer [47]. In this algorithm each of the monomers in a polymer chain is represented by 2^d sites on a square lattice, where d is the dimensionality of the lattice in use. Hence on a three dimensional lattice each of the monomers within a polymer chain is represented by the occupation of the eight lattice sites surrounding the monomer. The bond fluctuation algorithm generates new polymer configurations as follows. A given monomer within the polymer chain is chosen at random. An attempt is then made to move the 2^d sites representing the chosen monomer to a new position on the lattice. For the attempted move to be accepted the 2^d sites that the monomer is moved to must be unoccupied to satisfy the excluded volume condition for the monomers within the chain. It can be seen that attempted moves do not therefore conserve bond lengths or angles. A maximum allowed displacement of the 2^d sites is chosen so that the bond length between neighbouring monomers remains within a required range. An illustration of the bond fluctuation algorithm for a linear polymer chain on a two dimensional square lattice is shown in Figure 3.8. One of the advantages of this algorithm is that it allows the simulation of

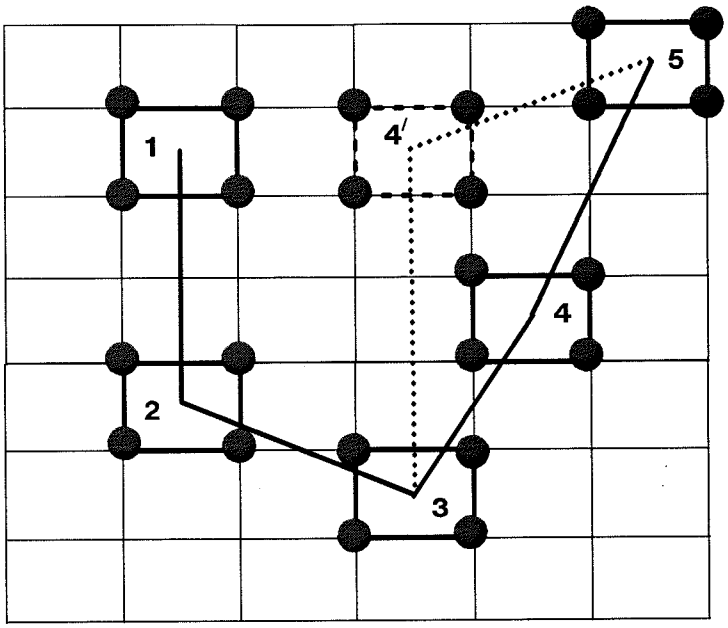

Figure 3.8. An illustration of an attempted move for a linear polymer chain on a two dimensional square lattice using the bond fluctuation algorithm. The polymer chain contains five monomers, numbered from one to five. Each of the monomers is defined by the four occupied lattice sites surrounding it and the bond fluctuation algorithm is making an attempt to move monomer 4 to a new trial position 4′.

very high density systems and is readily vectorisable to provide fast efficient codes. However the algorithm is not generalisable to chains in the continuum.

Another recently introduced algorithm is the concerted-rotation algorithm [48]. In this technique, the trial move consists of a multiple rotation about seven adjacent bonds in the polymer chain. A change in the first torsional angle ϕ_1 of the seven beads is used to drive the move. The subsequent six torsions are determined by the six constraints that ensure that the moving portions of the chain retain their connectivity with the sections of the chain that are not moved. The determination of the possible solutions to the geometric constraints is a difficult but tractable numerical problem. For some choices of ϕ_1 there will not be any physically reasonable solutions to the problem. For other choices of ϕ_1 there will be a number of possible solutions, one of which is chosen at random to be the attempted move. The method appears to be one of the more efficient methods for the simulation of polymer systems.

With the exception of the concerted rotation algorithm, the algorithms that we have presented are either only suitable for use in lattice simulations or are continuum algorithms that are not suited to the simulation of polymer chains in solution. To perform continuum simulations of polymer chains in solution we therefore need to use alternative algorithms to the ones presented above. In our work we have used the reptation and kinkjump algorithms, both of which are suitable for continuum simulations of polymer chains in solution. We will now describe the reptation and kinkjump algorithms in some detail.

3.4.1 The Reptation Algorithm

The reptation or 'slithering snake' algorithm is an efficient Monte Carlo algorithm for the simulation of polymers and was introduced by Wall and Mandel [49]. It is referred to as the reptation algorithm because the chain is made to move like a snake with two heads, along its own contour. Consider a chain of N_l bonds and N_l+1 monomers. The algorithm proceeds as follows. One end of the chain is chosen at random to be the head of the chain (ie. bead 5 in Figure 3.10). The energy of the tail bead is calculated and the bead removed from the chain. The tail bead is attached to the head of the chain in a random orientation and becomes the new head of the chain. The energy of the new head bead is calculated. The energy change in this process can be

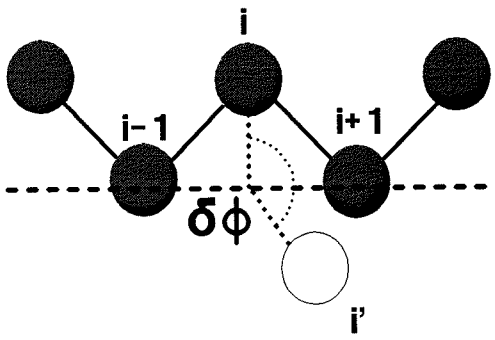

Figure 3.9 A schematic representation of the kinkjump algorithm.

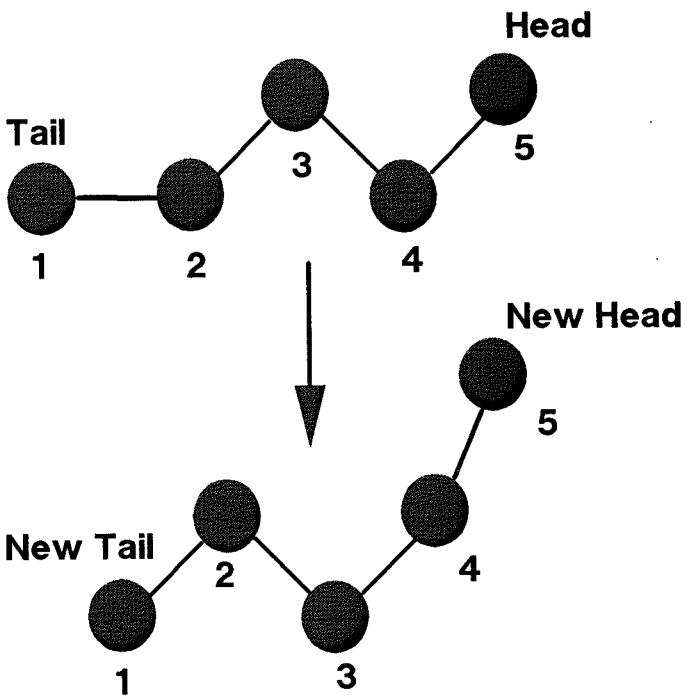

Figure 3.10 A schematic representation of the reptation algorithm.

denoted by $\delta u_{nm} = u^{new\ head} - u^{old\ tail}$. The move is accepted with a probability given by $\min(1, \exp(-\beta \delta u_{nm}))$. This algorithm is shown schematically in Figure 3.10.

The reptation algorithm suffers from the drawback of being non-ergodic ie. it is known that there are acceptable chain configurations that the algorithm cannot generate. This can be most easily demonstrated by considering the linear polymer chain on a 2 dimensional lattice shown in Figure 3.11. It is possible to see from the figure that in such a configuration it is not possible for the reptation algorithm to move the chain. No matter which end of the chain is chosen to be the head, the chain cannot move as there are no available lattice points for the head of the chain to move to. Clearly then, if a linear chain were to enter such a configuration using the reptation algorithm, it would be permanently locked into this configuration. However the chain moves like a snake following the movement of the head of the chain. Therefore it is not possible for the reptation algorithm to result in a configuration in which both the head and tail of the chain are simultaneously trapped. The configuration displayed in Figure 3.11 is a valid configuration and hence the reptation algorithm is not able to generate any configurations in which the head and tail of the chain take on configurations similar to those shown in Figure 3.11. The reptation algorithm is therefore non-ergodic. In practice however this non-sampling of regions of phase space is not expected to be a serious problem. The class of configurations in which both the head and tail of the chain are trapped into configurations similar to those shown in Figure 3.11 is expected to be small. As the chains are taken off the lattice and transferred into a 3 dimensional continuum this class of configurations is expected to become an even smaller subset of the total number of polymer configurations.

3.4.2 The Kink-Jump Algorithm

The kink-jump algorithm was first introduced to simulate polymers on a lattice by Verdier and Stockmayer [50] and was later applied to the calculation of properties of polymer chains in a continuum [51].

The algorithm proceeds as follows. Consider a chain of N_l bonds and N_l+1 monomers. A monomer, i, is chosen at random within the chain. The energy of monomer i is calculated. An attempt is made to rotate this monomer around the line joining the monomers i-1 and i+1. An angle $\delta\phi$ is chosen at random in the range $-\delta\phi_{max}$

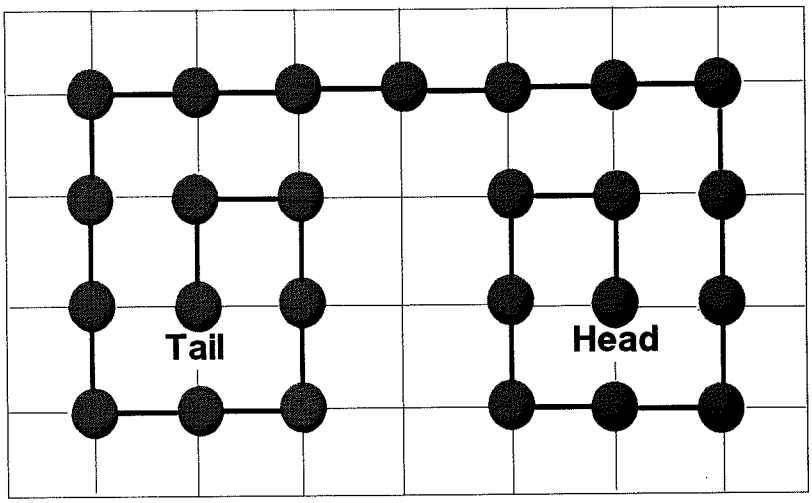

Figure 3.11 A configuration which the reptation algorithm is not able to generate. If the algorithm could generate such a configuration, then it would not be able to move the polymer chain out of this configuration.

to $\delta\phi_{max}$ and monomer i rotated in a circle through this angle. The energy of monomer i is calculated in its new position i'. The change in energy in moving from the old state m to the new state n is calculated and can be denoted by, $\delta u_{nm}=u^{i'}-u^{i}$. The move is accepted or rejected according to the standard Monte Carlo criterion ie. accepted with a probability given by $\min(1,\exp(-\beta\delta u_{nm}))$. If monomer i is the first or last monomer in the chain then the monomer is rotated to a new position subject to the constraint of the bond length. The energy change incurred during the move is calculated and the move accepted with the usual Monte Carlo acceptance criteria. The algorithm is shown schematically in Figure 3.9. Unlike the reptation algorithm, this algorithm is ergodic as it is possible to generate any acceptable polymer configuration with this algorithm.

3.4.3 Comparison of the Efficiency Of The Reptation and Kinkjump Algorithms

The efficiency of the reptation and kinkjump algorithms introduced in sections 3.4.1 and 3.4.2 can be illustrated by performing Monte Carlo simulations on the Non-Excluded Volume (NEV) or Freely Jointed Chain (FJC) model of a polymer chain. The NEV model is one in which the beads in the chain do not interact with one another and therefore it is possible for two beads to occupy the same point in space. We will focus on a 101 bead NEV chain with a unit bond length. Monte Carlo simulations were performed on this system in a vacuum, with both the reptation and kinkjump algorithms. During the simulations the square end-to-end distance was calculated. This is defined by [52],

$$\langle R^2 \rangle = \langle (\mathbf{r}_{101} - \mathbf{r}_1)^2 \rangle , \tag{3.6}$$

where $\mathbf{r}_{101}$ and $\mathbf{r}_1$ denote the coordinates of the first and last beads in the chain respectively. The mean square radius of gyration of the chain was also calculated and is defined by [52],

$$\langle S^2 \rangle = \frac{1}{N+1} \sum_{n=1}^{N+1} \langle (\mathbf{r}_n - \mathbf{r}_{cm})^2 \rangle , \tag{3.7}$$

where N is the number of bonds in the chain, N+1 the number of beads, and $\mathbf{r}_{cm}$ denotes the coordinates of the centre of mass of the chain. For an NEV model of a polymer chain it is possible to calculate the square end-to-end distance and the radius of gyration

of the chain analytically [53]. The end-to-end vector of a chain can be written as,

$$\mathbf{R} = \sum_{i=1}^{N} \mathbf{l}_i \,, \tag{3.8}$$

where the $\mathbf{l}_i$ are vectors between the beads in the chain, of length l. The square end-to-end distance is therefore given by,

$$\langle R^2 \rangle = \sum_{i=1}^{N}\sum_{j=1}^{N} \langle \mathbf{l}_i . \mathbf{l}_j \rangle = \sum_{i=1}^{N} \langle l_i^2 \rangle = Nl^2 \tag{3.9}$$

where all the cross products vanish in eqn (3.9) as all the vectors $\mathbf{l}_i$ are uncorrelated in the NEV model. The mean square radius of gyration of eqn (3.7) can be rewritten as [53],

$$\langle S^2 \rangle = \frac{1}{(N+1)^2} \sum_{i=0}^{N-1} \sum_{j=i+1}^{N} \langle R_{ij}^2 \rangle \,, \tag{3.10}$$

where R_{ij} is the distance between monomers i and j. Now, eqn (3.9) implies that

$$\langle R_{ij}^2 \rangle = (j-1)l^2 \,, \tag{3.11}$$

and substituting eqn (3.11) into eqn (3.10) we find,

$$\langle S^2 \rangle = \frac{l^2}{(N+1)^2} \sum_{i=0}^{N-1} \sum_{j=i+1}^{N} (j-i) = \frac{l^2}{(N+1)^2} \sum_{j=1}^{N} \sum_{k=1}^{j} k = \frac{l^2}{(N+1)^2} \sum_{j=1}^{N} \frac{j(j+1)}{2} \,. \tag{3.12}$$

Evaluation of the summations over j^2 and j yields the result,

$$\langle S^2 \rangle = l^2 \frac{N(N+2)}{6(N+1)} \,. \tag{3.13}$$

In Figure 3.12 we compare the results of the kinkjump and reptation algorithm with the analytic results of eqns (3.9) and (3.13). In Figure 3.12 the square end-to-end distance and radius of gyration of the chains are plotted against the number of sampled configurations. 101 polymer configurations were generated by the reptation and kinkjump algorithms between each of these sampled configurations. The figure demonstrates that both algorithms converge on the analytic results, but the reptation

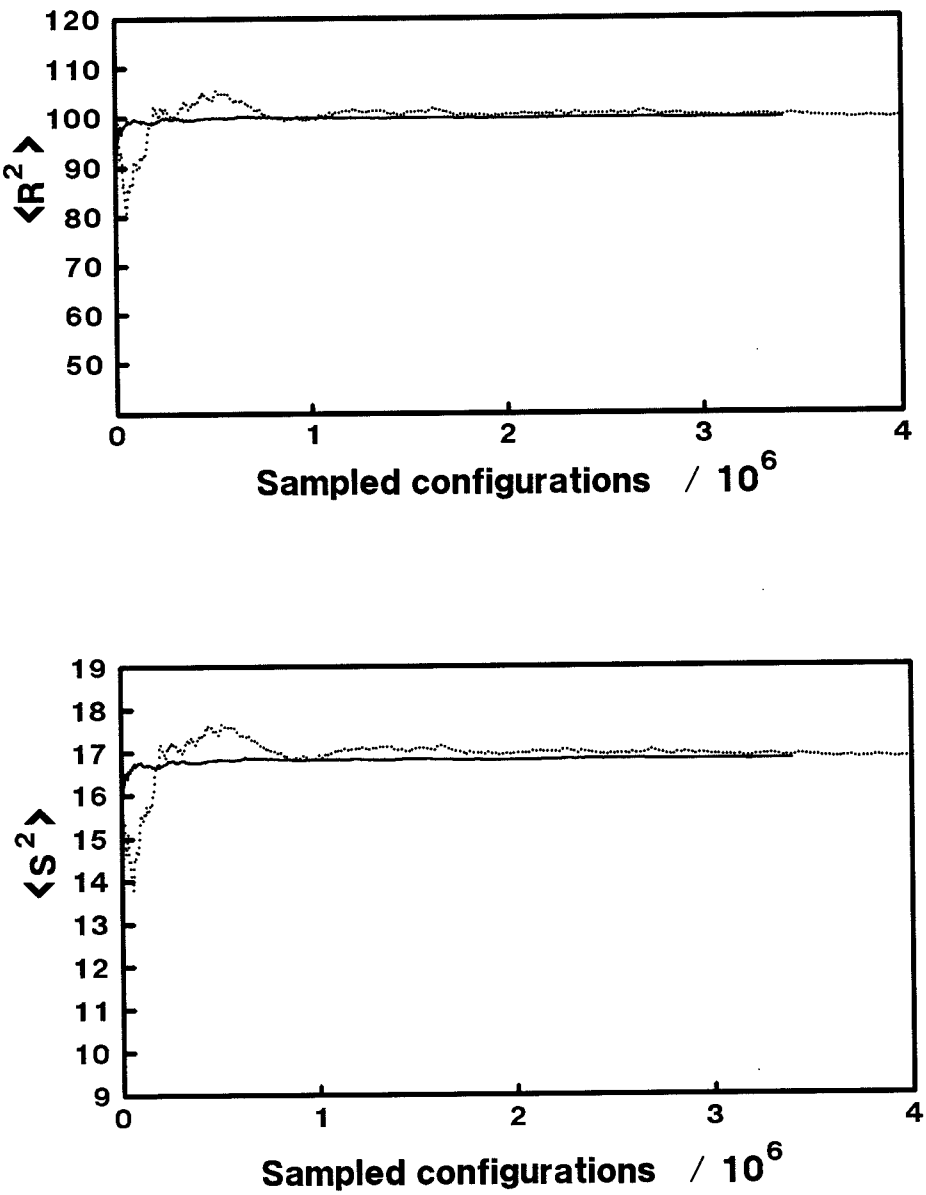

Figure 3.12 A comparison of the efficiency of the reptation and kinkjump algorithms. The broken lines are the kinkjump results and the full lines are the reptation results.

algorithm converges to the exact result in fewer cycles than the kinkjump algorithm. The relative efficiencies of the two algorithms can be analysed in terms of the time T_N, the CPU time required for a given algorithm to generate sufficient polymer configurations that the midpoint in the chain has diffused along the length of the chain. For the reptation algorithm in three dimensions, $T_N \propto N^{2.02}$, where N is the number of links or bonds in the chain, whereas the kinkjump algorithm in three dimensions yields $T_N \propto N^3$ [5]. The reptation algorithm is therefore more computationally efficient at exploring the phase space of a polymer chain than the kinkjump algorithm.

An efficient algorithm for the simulation of polymer chains (whether on lattices or in a continuum) can therefore be created by combining the reptation and kinkjump algorithms. As the kinkjump algorithm is ergodic, the combination of the two algorithms should also be ergodic. By combining the kinkjump algorithm with the reptation algorithm, it is possible to generate configurations similar to the one shown in Figure 3.11 without becoming locked into the configuration. A suitable algorithm for exploring the phase space of a polymer chain would therefore be one where reptation and kinkjump moves are performed one after the other. However as has already been detailed, the reptation algorithm achieves convergence in the calculated conformational properties of a polymer chain with fewer generated configurations than the kinkjump algorithm. It is therefore more efficient to use the reptation algorithm to make the majority of the polymer moves, thus retaining its efficient exploration of the phase space of the polymer. A typical simulation combining the two algorithms might therefore proceed by making 4 reptation moves followed by a kinkjump move.

Once the algorithm used to move the polymer has been chosen, we need a method of generating starting configurations. A number of methods used to do this will now be described.

3.5 The Starting Configurations

In simulations of simple atomic or molecular systems, it is usual to initiate a simulation from a lattice configuration [1] ie. in Chapter 2 we initiated our simulations with diatomic molecules from an α-fcc lattice. With polymeric systems, it is necessary to think more carefully about the starting conditions. At low densities it is possible to set up non-overlapping configurations with relative ease. At higher densities it is

necessary to produce starting configurations with more care.

A number of methods have been used to equilibrate a starting configuration. A recently proposed method [54] for the equilibration of polymeric and alkane systems is as follows. The alkane or polymeric system has all the intermolecular potentials stripped away and replaced by hard sphere potentials. Bond angles and bond lengths are constrained to be constant. The algorithm proceeds in four stages. In the first stage an attempt is made to place the head of each chain within the simulation box, subject to the constraint of the excluded volume. Once all the heads are placed in the box, the chains are 'grown'. Chains are selected at random. If the selected chain is less than a predetermined length (usually 3 segments), an attempt is made to grow the chain. The next stage of the algorithm is the growth and equilibration of the chains. If a chosen chain exceeds a given minimum length then a random choice is made to either further grow the chain or to equilibrate the chain by carrying out one of a number of trial moves. The trial moves possible are reptation and kinkjump moves. Finally once all the chains have been placed into the simulation box, the intra-molecular potentials are switched on and the system allowed to reach conformational equilibrium.

Another method that has been used to generate initial starting configurations proceeds by randomly inserting chains into the system [17]. After insertion of each of the chains into the system, all the chains are displaced in the system. This procedure is continued until the required number of chains has been inserted into the system.

The above methods of generating starting configurations are applicable to polymer melts where the density of chains in the system makes it difficult to generate low energy starting configurations. In the simulations that we have performed we have a single polymer chain immersed in a solvent. It is therefore convenient to generate starting configurations by first placing the polymer chain in the simulation cell in a random configuration. The solvent particles then need to be placed in the simulation cell in such a way as to provide a non-overlapped starting configuration. The generation of the starting configuration in our simulations will be discussed in more detail in chapter 4.

3.6 Periodic Boundary Conditions

Periodic boundary conditions need to be implemented in a polymer simulation with some care. If the dimensions of the simulation cell used are not sufficiently large, then it may be possible for a polymer chain to interact with itself through the periodic boundaries. This situation is illustrated in Figure 3.13 for the case of a single polymer chain in a vacuum. Should the polymer chain interact with itself through the periodic boundaries then the system that we are actually simulating is not the one we wish to simulate. Figure 3.13 illustrates that although we may think that we are simulating a single polymer chain in a vacuum, we will in fact be simulating a polymer chain in a dilute melt. Periodic boundary conditions can also cause problems because of hydrodynamic coupling. Recent simulations performed by Dünweg and Kremer [55] on linear polymer chains of 30-60 beads in 8000 solvent particles discovered that hydrodynamic coupling took place between the polymer chain and its periodic images. To try to ensure that the polymer chain cannot interfere with itself through the periodic boundaries, it is advisable to make the simulation cell much larger than the overall size of the polymer chain (as determined by the square end-to-end distance and radius of gyration of the polymer chain, both of which are defined in section 3.4.3).

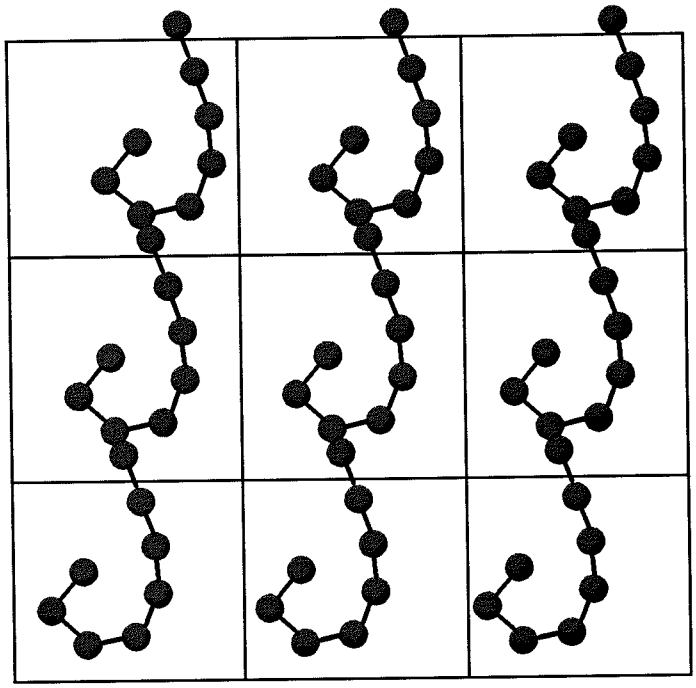

Figure 3.13 An illustration of a linear polymer chain interacting with its periodic images.

3.7 References

[1] M.P. Allen and D.J. Tildesley, "Computer simulation of liquids", Oxford science publications, (1987).

[2] P.G. de Gennes, "Scaling concepts in polymer physics", Cornell University Press, (1979).

[3] J.P. Ryckaert and A. Bellemans, "Molecular dynamics of liquid n-butane near its boiling point", Chem. Phys. Lett., **30**, 123-125, (1975).; "Molecular dynamics of liquid alkanes", Discuss. Faraday Soc., **66**, 95-106, (1978).

[4] T. Birshtein and O. Ptitsyn, "Conformations of macromolecules", John Wiley and sons, New York, (1966).

[5] K. Kremer, "Computer simulation in chemical physics", Eds. M.P. Allen and D.J. Tildesley, Kluwer academic publishers, (1993).

[6] F.T. Wall, L.A. Hiller and D.J. Wheeler, "Statistical computation of mean dimensions of macromolecules. I.", J. Chem. Phys., **22,** 1036-1041, (1954).

[7] M.N. Rosenbluth and A.W. Rosenbluth, "Monte Carlo calculation of the average extension of molecular chains", J. Chem. Phys., **23**, 356-359, (1955).

[8] F. Mandel, "Macromolecular dimensions obtained by an efficient Monte Carlo method: The mean square end-to-end separation", J. Chem. Phys., **70**, 3984-3988, (1979).

[9] M. Bishop and C.J Saltiel, "Structure function of linear polymers in the ideal and excluded volume regime", J. Chem. Phys., **94**, 6920-6923, (1991).

[10] M. Daoud and P.G. de Gennes, "Statistics of macromolecular solutions trapped in small pores", J. Phys., **38**, 85-93, (1977).

[11] F.T. Wall, W.A. Seitz, J.C. Chin and P.G. de Gennes, "Statistics of self-avoiding walks confined to strips and capillaries", Proc. Natl. Acad. Sci. USA, **75**, 2069-2070, (1978).

[12] K. Kremer and K. Binder, "Dynamics of polymer chains confined into tubes: Scaling theory and Monte Carlo simulations", J. Chem. Phys., **81**, 6381-6394, (1984).

[13] E. Eisenriegler, K. Kremer and K. Binder, "Adsorption of polymer chains at surfaces: Scaling and Monte Carlo analyses", J. Chem. Phys., **77**, 6296-6320, (1982).

[14] A.L. Rodriguez and J.J. Freire, "Monte carlo study of polymer chains in dilute and nondilute solution with varying solvent conditions", Macromolecules, **24**, 3578-3583, (1991).

[15] W. Paul, K. Binder, D.W. Heerman and K. Kremer, "Crossover scaling in semidilute polymer solutions : a Monte Carlo test", J. de Phys. II, **1**, 37-60, (1991).

[16] J.D. Weeks, D. Chandler and H.C. Andersen, "Role of repulsive forces in determining the structure of simple liquids", J. Chem. Phys., **54**, 5237-5247, (1971).

[17] A. Yethiraj and C.K. Hall, "Monte carlo simulation of hard chain-hard sphere mixtures in slitlike pores", J. Chem. Phys., **91**, 4827-4837, (1989).

[18] A. Yethiraj and C.K. Hall, "Square well chains: Bulk equation of state using perturbation theory and Monte Carlo simulations of the bulk pressure and of the density profiles near walls", J. Chem. Phys., **95**, 1999-2005, (1991).

[19] R. Dickman and C.K. Hall, "High density Monte Carlo simulations of chain molecules: Bulk equation of state and density profile near walls", J. Chem. Phys., **89**, 3168-3174, (1988).

[20] R.B. Bird, O. Hassager, R.C. Armstrong and C.F. Curtiss, "Dynamics of polymer liquids. Kinetic theory", Vol. 2, 2nd edition, Wiley, New York, (1987).

[21] K. Kremer and G.S. Grest, "Dynamics of entangled polymer melts - a molecular dynamics simulation", J. Chem. Phys., **92**, 5057-5086, (1990); K. Kremer and G.S. Grest, "Correction", J. Chem. Phys., **94**, 4103, (1991).

[22] I. Bitsanis and G. Hadziioannou, "Molecular dynamics simulations of the structure and dynamics of confined polymer melts", J. Chem. Phys. **92**, 3827-3847, (1990).

[23] Y.S. Lee and T. Ree, "Molecular dynamics study of a polymeric solution (I). Chain-length effect", Bull. Korean Chem. Soc., **3**, 44-49, (1982).

[24] I.J. Oh, Y.S. Lee and T. Ree, "Molecular dynamics study of a polymeric solution (II). Solvent effect", Bull. Korean Chem. Soc., **4**, 87-91, (1983).

[25] P.G. Khalatur, Y.G. Papulov and A.S. Pavlov, "The influence of solvent on the static properties of polymer chains in solution. A molecular dynamics study", Mol. Phys., **58**, 887-895, (1986).

[26] B. Smit, A. van der Put, C.J. Peters and J. de swaan Arons, "The influence of solvent quality on the static properties of a linear polymer : A molecular dynamics study", Chem. Phys. Lett., **144**, 555-557, (1988).

[27] B. Smit, K.R. Cox and J.P.J. Michels, "The influence of the quality of the solvent on the properties of a polymer. A thermodynamic model and molecular dynamics calculations", Mol. Phys., **66**, 97-112, (1989).

[28] M. Bishop, M.H. Kalos and H.L. Frisch, "Molecular dynamics of polymeric systems", J. Chem. Phys., **70**, 1299-1304, (1979).

[29] P. Auroy, L. Auvray and L. Leger, "Characterization of the brush regime for grafted polymer layers at the solid-liquid interface", Phys. Rev. Lett., **66**, 719-722, (1991).

[30] P. Auroy, L. Auvray and L. Leger, "Structures of end-grafted polymer layers - a small angle neutron-scattering study", Macromolecules, **24**, 2523-2528, (1991).

[31] S.T. Milner, T.A. Witten and M.E. Cates, "Theory of grafted polymer brush", Macromolecules, **21**, 2610-2619, (1988).

[32] C.M. Wijmans, J.M.H.M. Scheutjens and E.B. Zhulina, "Self-consistent field theories for polymer brushes. Lattice calculations and an asymptotic analytical description", Macromolecules, **25**, 2657-2665, (1992).

[33] M. Murat and G.S. Grest, "Interaction between grafted polymeric brushes : A molecular-dynamics study", Phys. Rev. Lett., **63**, 1074-1077, (1989).

[34] P.Y. Lai and K. Binder, "Structure and dynamics of grafted polymer layers : A Monte Carlo simulation", J. Chem. Phys., **95**, 9288-9299, (1991).

[35] R. Dickman and D.C. Hong, "New simulation method for grafted polymeric brushes", **95**, 4650-4655, (1991).

[36] E.B. Zhulina and T. Pakula, "Structure of dense polymer layers between end-grafting and end-adsorbing walls", Macromolecules, **25**, 754-758, (1992).

[37] T. Pakula and E.B. Zhulina, "Computer simulation of polymers in thin layers. II. Structure of polymer melt layers consisting of end-to-wall grafted chains", J. Chem. Phys. **95**, 4691-4697, (1991).

[38] J.N. Israelachvili and S.J. Kott, "Liquid structuring at solid interfaces as probed by direct force measurements - the transition from simple to complex liquids and polymer fluids", J. Chem. Phys., **88**, 7162-7166, (1988).

[39] P.G. de Gennes, "Interactions between plates in a polymer melt", C.R. Acad. Sci. Paris, **305**, 1181-1184, (1987).

[40] R.G. Horn, S.J. Hirz, G. Hadziioannou, C.W. Frank and J.M. Catala, "A reevaluation of forces measured across thin polymer-films - nonequilibrium and pinning effects", J. Chem. Phys., **90**, 6767-6774, (1989).

[41] T. Pakula, "Computer simulation of polymers in thin layers. 1. Polymer melt between neutral walls - static properties", J. Chem. Phys., **95**, 4685-4690, (1991).

[42] G. ten Brinke, D. Ausserre and G. Hadziioannou, "Interaction between plates in a polymer melt", J. Chem. Phys., **89**, 4374-4380, (1988).

[43] D.N. Theodorou, "Microscopic structure and thermodynamic properties of bulk-copolymers and surface-active polymers at interfaces. I. Theory", Macromolecules, **21**, 1411-1421, (1988).

[44] J.H. van Vliet and G. ten Brinke, "Orientation and shape of flexible polymers in a slit", J. Chem. Phys., **93**, 1436-1441, (1990).

[45] M. Lal, "Monte Carlo computer simulation of chain molecules. I.", Mol. Phys., **17**, 57-64, (1969).

[46] N. Madras and A.D. Sokal, "The pivot algorithm - a highly efficient Monte-Carlo method for the self-avoiding walk", J. Stat. Phys., **50**, 109-186, (1988).

[47] I. Carmesin and K. Kremer, "The bond fluctuation method : A new effective algorithm for the dynamics of polymers in all spatial dimensions", Macromolecules, **21**, 2819-2823, (1988).

[48] L.R. Dodd, T.D. Boone and D.N. Theodorou, "A concerted rotation algorithm for atomistic Monte-Carlo simulation of polymer melts and glasses", Mol. Phys., **78**, 961-996, (1993).

[49] F.T. Wall and F. Mandel, "Macromolecular dimensions obtained by an efficient Monte Carlo method without sample attrition", J. Chem. Phys., **63**, 4592-4595, (1975).

[50] P.H. Verdier and W.H. Stockmayer, "Monte Carlo calculation on the dynamics of polymers in dilute solution", J. Chem. Phys., **36**, 227-231, (1962).

[51] A. Baumgartner and K. Binder, "Monte Carlo studies on the freely jointed polymer chain with excluded volume interaction", J. Chem. Phys., **71**, 2541-2545, (1979).

[52] M.Doi and S.F. Edwards, "The theory of polymer dynamics", Oxford science publications, (1986).

[53] P.J. Flory, "Statistical mechanics of chain molecules", Interscience publishers, (1969).

[54] S. Gupta, G.B. Westermann-Clark and I. Bitsanis, "A continuous Monte Carlo method for growth and equilibration of polymer chains at high densities", J. Chem. Phys., **98**, 634-637, (1993).

[55] B. Dünweg and K. Kremer, "Microscopic verification of dynamic scaling in dilute polymer-solutions - A molecular-dynamics simulation", Phys. Rev. Lett., **66**, 2996-2999, (1991).

4. The Competitive Adsorption of Polymer Chains and Solvent Particles At Surfaces

4.1 Introduction

As described in Chapter 3, the adsorption of polymers at surfaces is of interest for both practical and theoretical reasons. The scaling properties of linear polymer chains in a good solvent between walls and adsorbed at surfaces have been the subject of theoretical and computational investigations as detailed in section 3.3. In this chapter we are interested in understanding the competitive adsorption between the polymer chains and the solvent particles in a confined geometry. Also of interest are the conformational changes of the chain on adsorption at the solid-liquid interface. The theoretical and computational studies that have been carried out on polymer chains in good solvents near surfaces [1,2,3] ignore any possible competitive adsorption effects between the solvent particles and the polymer chain. However competitive adsorption effects are known to be of importance in a number of systems, in particular in the stabilization of colloidal dispersions [4]. For instance, food colloids contain two classes of molecules which have a strong tendency to adsorb at surfaces. These molecules are proteins and small molecule surfactants (lipids). Proteins adsorbed at surfaces are capable of conferring long-term stability to an emulsion or foam. The composition of the adsorbed layer in food emulsions will depend not only on the competitive adsorption between different proteins but also on the competitive adsorption between the proteins and the surfactants. We are therefore also interested in determining the effect, if any, this competitive adsorption might have on the scaling behaviour of the chains between the walls.

To study the adsorption behaviour of linear polymer chains between walls and the effects of the competitive adsorption on the properties of the polymer chains we carried out a number of continuum Monte Carlo simulations. Extensive simulations of 8-mer chains between walls in a solvent comprised of its own monomers were performed. In this system we can consider the chain to be a crude model of an alkane and the solvent particles to be models of methane. The use of 8-mer chains in our simulations was motivated by the desire to study chains of sufficient length to exhibit polymeric behaviour. 8-mer chains have been used in several simulation studies of polymer chains

[5,6,7] and are generally considered to be of sufficient length to exhibit polymeric behaviour. Simulations were then performed with chains of longer length to examine the scaling behaviour of the polymer chains under various conditions.

In section 4.2 we outline the potentials used in the simulations. Section 4.3 describes the simulation method used in our work. Section 4.4 contains our results for the simulations with 8-mer chains and examines in detail the adsorption behaviour of the chains. Section 4.5 contains our results for chains of longer length and an analysis of the chains' scaling behaviour between the walls and section 4.6 contains our conclusions.

4.2 Potentials

In this chapter we were interested in studying polymer chains immersed in a good solvent. The quality of a solvent is usually defined in terms of the Flory χ parameter [1] given by,

$$\chi = \chi_{ms} - \frac{1}{2}(\chi_{mm} + \chi_{ss}) , \qquad (4.1)$$

where χ_{mm}, χ_{ms} and χ_{ss} are related to the monomer-monomer, monomer-solvent and solvent-solvent interactions respectively. The parameter χ is dimensionless and is dependent on the temperature and pressure. Good solvents have a low χ value whilst poor solvents have high χ values. The interaction parameters χ_{ms}, χ_{mm} and χ_{ss} are related to the van der Waals attractions between the given particles and are essentially proportional to the product of the electronic polarizabilities of the various particles. When the solvent particles are similar to the monomers within the polymer chain the parameter χ is equal to zero and hence the polymer chain is immersed in a good solvent. Therefore if we wish to perform a computational study of a polymer chain in a good solvent, we need to model the various interparticle interactions by a single potential function. If the various interparticle interactions are modelled by differing potentials then the quality of the solvent is dependent on the details of the various interparticle interactions. A number of computational studies have sought to investigate the effects of the quality of the solvent on the conformational properties of polymer chains [6,7]. Typically in computational studies of polymer chains in a good solvent,

the monomers within the polymer chain and the solvent particles are modelled by the WCA potential introduced in section 3.2.2. In this study we have also modelled the solvent particles and the monomers within the polymer chain by the WCA potential of eqns (3.3) and (3.4). This potential is a shifted Lennard-Jones potential and as such is purely repulsive. This potential models the excluded volume interactions between the various particles in the simulation. The polymer chains used in our simulations are of the bead-rod type introduced in section 3.2.2 and of unit reduced bond length. The chosen bond length is relatively unimportant as the scaling properties of the chains that we will present in section 4.5 are independent of the bond length (cf. eqn (3.1)) and a unit bond length is chosen for convenience.

Smooth structureless planar walls were used in this study. The walls were placed in the x-y plane, separated by a distance $H\sigma$ along the z axis. Two different types of wall were used in our simulations. The first of these is a hard wall, defined so that the pair potential between the wall and either a solvent particle or a site within the polymer chain is given by,

$$u_{wall}(z) = \infty \qquad z \leq 0 \text{ or } z \geq H\sigma, \tag{4.2}$$

$$u_{wall}(z) = 0 \qquad 0 < z < H\sigma \ . \tag{4.3}$$

The attractive walls are modelled using a 9-3 Lennard-Jones potential [8]. This potential is obtained by regarding the walls as consisting of a continuum of 12-6 Lennard-Jones particles at a particular density ρ and integrating over the two directions parallel to the wall and the direction perpendicular to the wall, below the surface. The 9-3 potential has the functional form,

$$u_{wall}(z) = \frac{2}{3}\pi\rho\epsilon_w\sigma_w^3\left[\frac{2}{15}\left(\frac{\sigma_w}{z}\right)^9 - \left(\frac{\sigma_w}{z}\right)^3\right]. \tag{4.4}$$

In eqn (4.4) σ_w and ε_w are the length and energy parameters of the interaction between sites above the wall and the atoms within the wall. In all the simulations carried out we have set $\sigma=\sigma_w$ ie. the particles in the wall, the solvent particles and the monomers in the polymers are all of the same size. Thus in our simulations, the polymer chain is immersed in a solvent composed of its own monomers. The parameter ρ was set to

ρ=0.114 atoms Å $^{-3}$, the value appropriate for graphite [9]. In our work we have used the parameter ε_w as a variable to control the interactions of the various particles with the wall. We have used values for ε_w ranging from 0.2 to 1.0. In this chapter we quote the ε_w values in terms of the Lennard-Jones parameter ε ie. ε_w=0.2 represents ε_w=0.2ε. It is possible to make our simulations richer by allowing the particles within the polymer and the solvent particles to interact with wall potentials characterised by different well depths ie. different values of ε_w. This can be achieved by describing the wall-monomer interaction by the parameter ε_{wp} and the wall-solvent interaction by the parameter ε_{ws}. By setting ε_{wp}=ε_{ws} the polymer and solvent particles interact with wall potentials that are identical. By setting $\varepsilon_{wp}\neq\varepsilon_{ws}$ it is possible to investigate situations in which either the polymer or solvent particles are more strongly attracted to the walls.

To facilitate the comparison of the density profiles of the systems placed between hard and attractive walls, we have defined the 9-3 walls as starting at -0.714σ. With the wall at this position the distance of closest approach a particle can make to the 9-3 walls occurs at approximately 0σ.

4.3 Simulation Method

Off-lattice constant-NVT simulations of single linear polymer chains in a solvent were performed. The systems were placed between walls lying in the x-y plane and simulations carried out with chains containing 8, 16, 24 and 32-mers. Our simulations were performed at k_BT=2.0ε and an overall density of ρ^*=0.4, conditions similar to those used in a number of previous simulation studies of linear polymer chains in a good solvent [5,7]. Periodic boundary conditions were imposed in the x and y directions.

Starting configurations were generated by placing the polymer between the walls in a random configuration and then placing the solvent particles on a regular cubic lattice between the walls. A lattice site is left unoccupied if filling it would cause an overlap with any part of the polymer chain.

The simulations can be conveniently divided up into cycles, which consist of an attempt to move the polymer chain followed by attempted displacements of all the solvent particles. The polymer chains were moved by a combination of the reptation and kinkjump algorithms introduced in sections 3.4.1 and 3.4.2 respectively. As explained in section 3.4.3 the combination of these two algorithms should ensure an efficient and

ergodic algorithm for the exploration of the phase space of the polymer chain. A typical sequence of polymer moves involved making attempted reptation moves on 4 consecutive cycles followed by an attempted kinkjump move on the 5th cycle. The parameters controlling the movement of the polymer chain were not adjusted during the course of a simulation and typically 17-30% of the attempted polymer moves were accepted. The attempted solvent particle displacements were handled using the usual Monte Carlo method. Cell-linked lists [10] were implemented in our code to speed up the calculations.

During the simulations conformational properties of the chain were calculated. In particular the mean square radius of gyration parallel to the walls,

$$S_{\parallel}^2 = \left\langle \frac{1}{N_m} \sum_{i=1}^{N_m} (x_i - x_{cm})^2 + (y_i - y_{cm})^2 \right\rangle , \tag{4.5}$$

and perpendicular to the walls,

$$S_{\perp}^2 = \left\langle \frac{1}{N_m} \sum_{i=1}^{N_m} (z_i - z_{cm})^2 \right\rangle , \tag{4.6}$$

were calculated. The components of the mean square radius of gyration are related to the mean square radius of gyration by,

$$S^2 = S_{\parallel}^2 + S_{\perp}^2 . \tag{4.7}$$

In eqns (4.5) and (4.6) x_{cm}, y_{cm} and z_{cm} are the centres of mass of the polymer and N_m is the number of monomers in the polymer chain.

The statistical inefficiency [10], s, was calculated for the polymer configurations generated by the combined kinkjump and reptation algorithms. The statistical inefficiency was calculated for the mean square radius of gyration during an 8-mer simulation confined between walls separated by 5.428σ and with a value for ε_w of 0.2. If the simulation results of τ_{run} cycles is broken up into n_b blocks of length τ_b, then the statistical inefficiency in the calculation of a property A is defined as,

$$s = \lim_{\tau_b \to \infty} \frac{\tau_b \, \sigma^2(\langle A \rangle_b)}{\sigma^2(A)} , \tag{4.8}$$

where,

$$\sigma^2(A) = \frac{1}{\tau_{run}} \sum_{\tau=1}^{\tau_{run}} (A(\tau) - \langle A \rangle_{run})^2 , \tag{4.9}$$

and,

$$\sigma^2(\langle A \rangle_b) = \frac{1}{n_b} \sum_{b=1}^{n_b} (\langle A \rangle_b - \langle A \rangle_{run})^2 . \tag{4.10}$$

In eqns (4.9) and (4.10), $\langle A \rangle_{run}$ is given by,

$$\langle A \rangle_{run} = \frac{1}{\tau_{run}} \sum_{\tau=1}^{\tau_{run}} A(\tau) . \tag{4.11}$$

The statistical inefficiency in the mean square radius of gyration was calculated to be 104. This means that only 1 in approximately every 104 generated polymer configurations contributes new information to the calculation of S^2. Because of this high degree of correlation between generated polymer configurations, the conformational properties of the polymers were sampled every 10 cycles in our simulations rather than at every cycle.

Each simulation was continued for a sufficient number of cycles to obtain good convergence in the calculated conformational properties. The errors reported in the conformational properties were calculated by dividing the simulations up into a number of sub-averages and calculating 1 standard deviation in the mean of these blocks. For the 8-mer runs sub-averages were calculated every $2x10^4$ cycles and typically $2x10^4$ equilibration and $14x10^4$ production cycles performed. This number of cycles was generally sufficient to obtain good convergence in the chain conformational properties. For the 16, 24 and 32-mer chains sub-averages were calculated every 10^5 cycles and typically 10^5 equilibration and $5x10^5$ production cycles performed. Details of each simulation performed are given in Table 4.1.

The density profiles of the solvent and polymer particles were recorded during the simulations by dividing the region between the walls into a number of equally sized bins. Typically the density profiles were calculated every 100 cycles. In analysing the resulting concentration profiles, we have made use of the symmetry of the simulation cells to combine the profiles in the left and right half of the cells in the z direction.

Site profiles for the polymer chain were recorded during the simulations. The sites within the 8-mer chain were labelled from 1 to 4 starting from the head of the polymer. The head and tail of the polymer were both labelled as the 1st site (making use of the equivalence of the head and tail within the chain). Similarly the 2nd and 7th sites were labelled as the 2nd site etc.

As a measure of the solvent adsorption at the wall, the surface excess adsorption of the solvent particles was calculated in the simulations performed. The surface excess adsorption of solvent particles [8] is given by,

$$\Gamma_s = \int_0^{z_b} \left[\rho(z) - \rho_b\right] dz \ , \tag{4.12}$$

where ρ_b is the bulk value of the density measured in the centre of the pore. The calculated surface excess adsorption for the solvent particles in the various simulations are presented in Table 4.1.

4.4 Results for the 8-mer Chain

Simulations were performed with 8-mer chains to examine the polymer adsorption behaviour under different conditions. In all the simulations reported for the 8-mer chains, the sides of the central box are 12.5σ in the x and y directions; with a cell of this size it is not possible for the chain to interact with one of its images through the periodic boundaries.

4.4.1 Effect of the Wall Potential

Simulations were performed with both hard walls and attractive 9-3 walls. For the attractive walls, values of ε_w=0.2, 0.4, 0.6, 0.8 and 1.0 were used with $\varepsilon_{ws}=\varepsilon_{wp}=\varepsilon_w$. Details of the simulations performed are given in Table 4.1.

Figure 4.1 shows the density profiles of the polymer and solvent particles between

H/σ	N_T	ε_w	ρ_b	Γ_s
4	250	-	0.3454	0.0873
8	500	-	0.3735	0.0879
5.428	250	0.2	0.3165	0.1004
5.428	250	0.4	0.2857	0.1729
5.428	250	0.6	0.2565	0.2409
5.428	250	0.8	0.2252	0.3058
5.428	250	1.0	0.1934	0.3769
9.428	500	0.2	0.3547	0.0942
9.428	500	0.4	0.3381	0.1779
9.428	500	0.6	0.3223	0.2573
9.428	500	0.8	0.3058	0.3258
9.428	500	1.0	0.2885	0.3950

Table 4.1 Parameters for the 8-mer simulations. $2x10^4$ equilibration and $14x10^4$ production cycles were performed in each of the simulations. N_T is the total number of sites used in the simulation ($N_T=N_m+N_s$ where N_m is the number of monomers in the polymer chain and N_s is the number of solvent particles.) ρ_b is the bulk density measured in the centre of the pore and Γ_s is the excess surface adsorption of the solvent, defined by eqn (4.12).

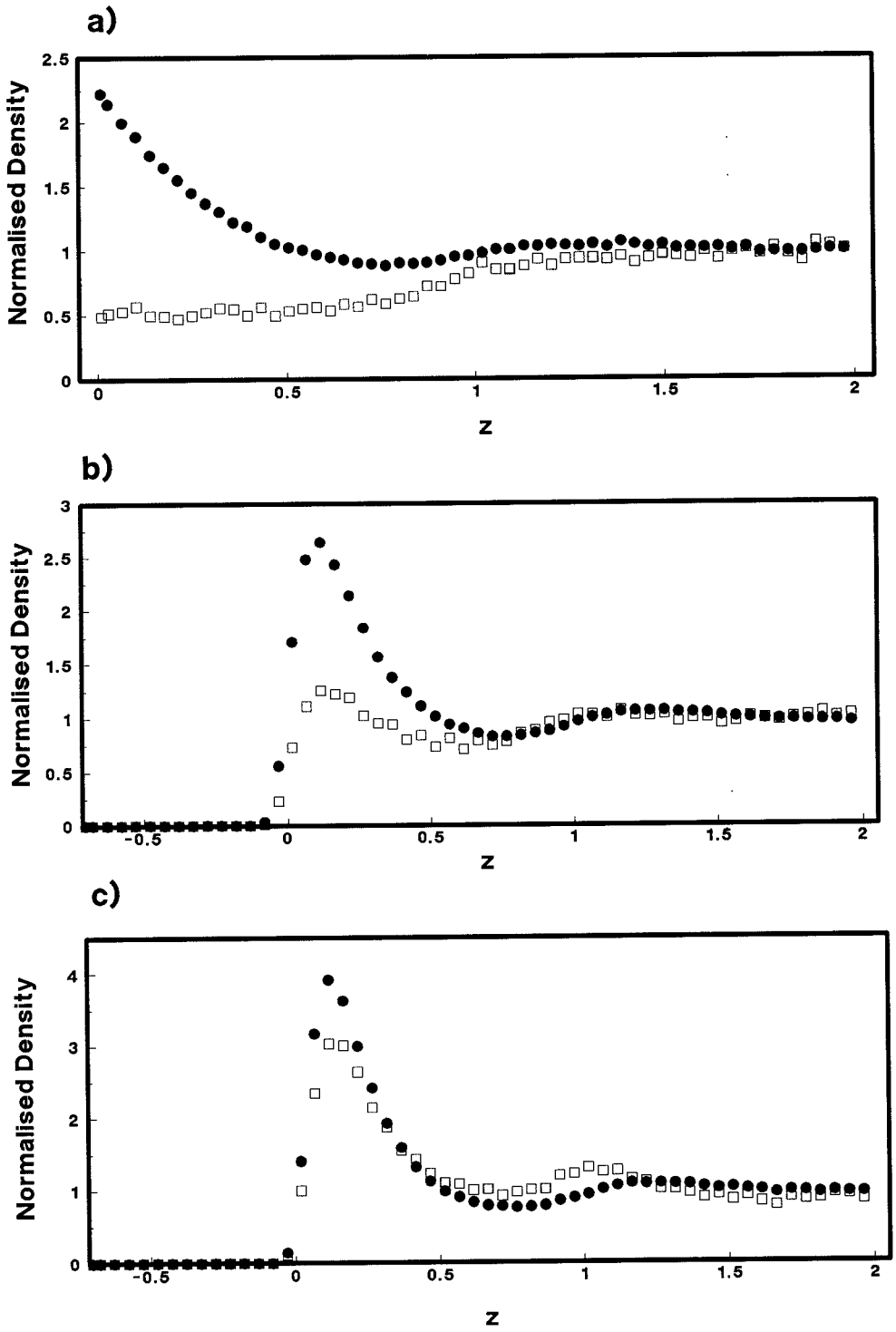

Figure 4.1 The polymer (□) and solvent (●) density profiles plotted against the reduced distance from the wall, z. The profiles were recorded for the systems placed between hard walls (a) and 9-3 walls with ε_w=0.2 (b) and ε_w=0.4 (c).

hard walls and attractive walls with ε_w=0.2 and ε_w=0.4. In Figure 4.1 the density profiles are plotted as a function of the reduced distance from the wall, z. The profiles have been normalised by their values in the centre of the pore (see Table 4.1). The solvent profiles are enhanced at the walls relative to the centre of the pore for both wall models as can be seen from the positive values of the surface excess adsorption of the solvent particles (see Table 4.1). Between the hard walls the solvent particle density is enhanced at the walls due to packing effects. Between the attractive walls, a combination of packing and energetic factors lead to a greater enhancement of the solvent profiles at the wall than with the hard walls. This behaviour can be seen clearly in the surface excess adsorption of the solvent particles which rises from a value of 0.0873 between hard walls separated by 4σ, to a value of 0.3769 between soft walls separated by 5.428σ with ε_w=1.0. Also displayed in Figure 4.1 are the polymer density profiles between the various walls. Again the profiles are normalised by their values in the middle of the pore. In contrast to the solvent particles, in the hard walls case the polymer chain is depleted at the walls relative to the middle of the pore. There is no energetic advantage for the polymer chain to be either close to the wall, or in the middle of the pore. The depletion of the polymer chain at the wall must therefore be due to the loss of configurational entropy experienced by the chain close to the wall. It is much more difficult for the polymer chain to find acceptable configurations close to the wall than in the middle of the pore leading to a depletion of the chain at the wall. This is a phenomenon which has been observed in previous simulations [11,12,13]. However, in the case of the attractive wall with ε_w=0.2, the polymer chain is no longer depleted at the wall. The gain in configurational energy on approaching the walls almost exactly balances the loss in configurational entropy in doing so. This leads to a slight enhancement of the polymer chain at the walls with the chain being weakly adsorbed. With ε_w=0.4 the polymer chain is more strongly adsorbed at the wall and the concentration profile has developed a cusp close to Z=σ. This cusp is due to the fixed bond length between neighbouring chain segments. If the chain is only partially adsorbed at the wall and has not become fully two dimensional, then some of the bonded monomers will project into the centre of the pore resulting in the cusp at σ.

Figure 4.2 presents the site density profiles for the polymer chain between hard walls and the attractive walls with ε_w=0.2 and ε_w=0.4. Once again the site profiles have been

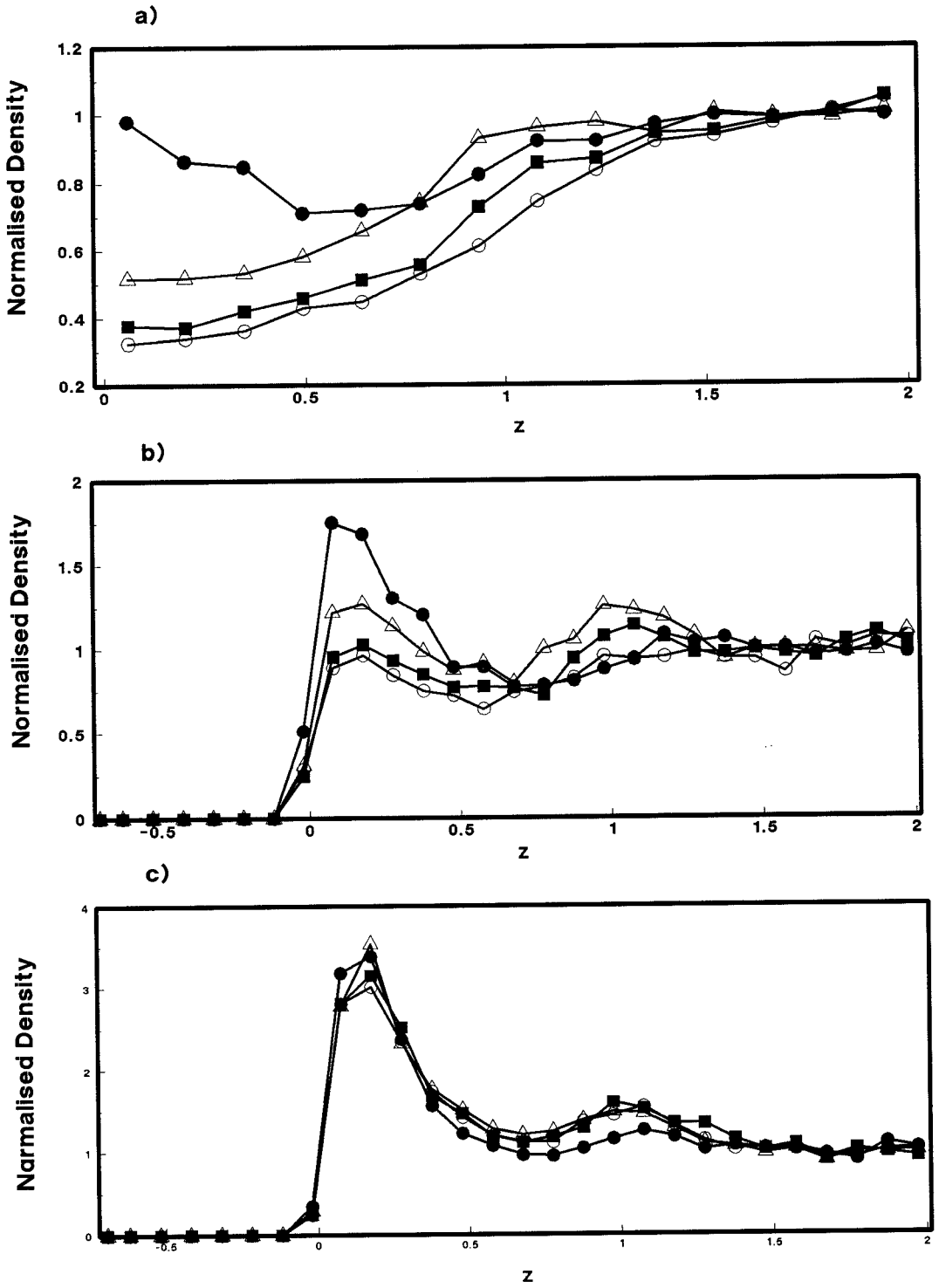

Figure 4.2 The polymer site profiles plotted against the reduced distance from the walls, z. Profiles are shown for the first (●), second (▵), third (■) and fourth sites (○) within the polymer chain. The profiles were recorded for polymer chains between hard walls (a) and 9-3 walls with ε_w=0.2 (b) and ε_w=0.4 (c).

normalised by their values in the centre of the pore. Between the hard walls site 1 at the end of the chain is slightly enhanced at the wall, while sites 2-4 within the chain are depleted at the wall. For a monomer within the centre of the polymer chain to approach the wall requires the remainder of the monomers within the polymer chain to also be within close proximity to the wall. This is less easy for the chain to achieve than to have the head of the chain close to the wall, which can occur while the remainder of the chain is projecting into the centre of the pore, well away from the wall. There is therefore less of an entropic restriction for the head of the chain to be close to the wall than for the rest of the body of the chain. This preference for the end of the chain to be close to the wall rather than the middle of the chain has been previously observed in simulation studies of polymer melts between walls and mixtures of polymer chains and solvent particles between hard walls [12,11]. With the attractive walls and ε_w=0.2, the sites are enhanced at the wall. However site 1 is still more favoured at the wall than the other sites indicating that entropic effects are still more important than the attractive energy associated with polymer adsorption. With attractive walls and ε_w=0.4 all the site profiles are enhanced at the walls and have become essentially identical. The 1st site is now only marginally more likely to be at the wall than the other sites in the chain. The profiles show a large enhancement at the wall indicative of strong adsorption taking place.

To examine the adsorption behaviour of the chains we have calculated the components of the mean square radius of gyration of the polymer chains. Table 4.2 compares the components of the mean square radius of gyration calculated parallel and perpendicular to the walls for the 6 simulations. The wall acts as an external field in the z direction and the chain is anisotropic. As the surface field becomes weak, the chain becomes isotropic and the component of the mean square radius of gyration parallel to the walls would be twice that perpendicular to the walls (eqns (4.5) and (4.6)). With the attractive wall, the component of the mean square radius of gyration parallel to the walls increases with an increase in ε_w and commensurately the component perpendicular to the walls decreases. As the value of ε_w is increased to 1.0, the component of the mean square radius of gyration perpendicular to the walls becomes extremely small indicating that the polymer chain has become essentially two dimensional.

To examine the structure of the adsorbed chain in more detail we have calculated the

Wall Type	$\langle S^2 \rangle$	$\langle S_\perp{}^2 \rangle$	$\langle S_\parallel{}^2 \rangle$
Hard	1.92±0.04	0.44±0.03	1.47±0.06
9-3 ε_w=0.2	1.95±0.04	0.46±0.03	1.49±0.05
9-3 ε_w=0.4	2.02±0.11	0.43±0.04	1.59±0.13
9-3 ε_w=0.6	2.09±0.06	0.30±0.05	1.78±0.07
9-3 ε_w=0.8	2.18±0.12	0.19±0.06	1.99±0.15
9-3 ε_w=1.0	2.26±0.14	0.11±0.04	2.14±0.16

Table 4.2 The components of the mean square radius of gyration as a function of the wall potential.

principal axes of the chains [14] and denote them as λ_1, λ_2 and λ_3. The principal axes of a polymer chain are defined as the eigenvalues of the tensor of components of the mean square radius of gyration, $\langle S^2 \rangle$. This tensor is defined as [15],

$$T_{\alpha\beta} = \frac{1}{N_m} \sum_{i=1}^{N_m} (\mathbf{R}_i - \mathbf{R}_{cm})_\alpha \, (\mathbf{R}_i - \mathbf{R}_{cm})_\beta \, , \tag{4.13}$$

where $\mathbf{R}_{cm}$ represents the coordinates of the centre of mass of the polymer chain. Diagonalisation of the tensor $T_{\alpha\beta}$ yields the three principal axes of the polymer chain, with the largest eigenvalue of the tensor representing the longest axis of the polymer chain and the smallest eigenvalue of the tensor representing the smallest axis of the polymer chain. The principal axes are related to the radius of gyration by,

$$\langle S^2 \rangle = \lambda_1 + \lambda_2 + \lambda_3 \, . \tag{4.14}$$

In three dimensional space, the square roots of the eigenvalues of the tensor $T_{\alpha\beta}$ can be pictured as half the lengths of the principal axes of an ellipsoid which characterises the shape of the polymer chain. If a polymer chain were highly symmetric (ie. spherical) then its three principal axes would be of equal magnitudes. As the polymer chain becomes more linear one of the principal axes of the chain becomes greater than the other two. We have ordered the principal axes such that,

$$\lambda_1 > \lambda_2 > \lambda_3 \, , \tag{4.15}$$

and hence λ_1 represents the longest axis of the polymer chain. We have also calculated the functions $\overline{P}_2(\cos\theta_1)$, $\overline{P}_2(\cos\theta_2)$ and $\overline{P}_2(\cos\theta_3)$ which are functions of the angles between the 3 principal axes and the z axis. θ_1, θ_2 and θ_3 are the angles between the 1st, 2nd and 3rd principal axes and the z axis respectively and lie in the range of 0° to 90°. The function $\overline{P}_2(\cos\theta)$ is defined by,

$$\overline{P}_2(\cos\theta) = \left\langle \frac{3}{2}\cos^2\theta - \frac{1}{2} \right\rangle , \tag{4.16}$$

where the function $\overline{P}_2(\cos\theta)$ takes the value 1.0 when θ is 0° and -0.5 when θ is 90°. Table 4.3 presents the results for the principal axes of the chains obtained with the various wall potentials. We see that as the polymer adsorbs at the attractive wall the 1st

Wall Type	$\langle\lambda_1\rangle$	$\langle\lambda_2\rangle$	$\langle\lambda_3\rangle$
Hard	1.520±0.050	0.312±0.004	0.091±0.003
9-3 ε_w=0.2	1.550±0.055	0.311±0.009	0.091±0.002
9-3 ε_w=0.4	1.630±0.127	0.310±0.008	0.084±0.006
9-3 ε_w=0.6	1.709±0.065	0.309±0.014	0.076±0.003
9-3 ε_w=0.8	1.819±0.142	0.306±0.031	0.061±0.003
9-3 ε_w=1.0	1.904±0.168	0.307±0.030	0.049±0.009

Table 4.3 The principal axes of the polymer chain as a function of the wall potential.

principal axis increases in magnitude by approximately 25% relative to the hard walls case. Commensurately the 3rd principal axis decreases in magnitude by approximately 50% and the second principal axes decreases marginally in magnitude. If the polymer chain is pictured as an ellipsoid whose dimensions are given by twice the square roots of the eigenvalues λ_1, λ_2 and λ_3, then as the chain adsorbs against one of the walls, the ellipsoid elongates. Table 4.4 presents the functions $\overline{P}_2(\cos\theta_1)$, $\overline{P}_2(\cos\theta_2)$ and $\overline{P}_2(\cos\theta_3)$ obtained with the various wall potentials. Between the hard walls, the polymer chain's principal axes are not isotropically distributed about the z axis as they would be if the chain were in an infinitely dilute solution. As the attractive wall potential is increased $\overline{P}_2(\cos\theta_1)$ tends to approximately -0.5 indicating that the 1st principal axis is aligned parallel to the walls. $\overline{P}_2(\cos\theta_2)$ at the same time tends to a value of 0 and $\overline{P}_2(\cos\theta_3)$ increases from 0.091 between the hard walls to 0.439 between the attractive walls with ε_w=1.0. The increase in $\overline{P}_2(\cos\theta_3)$ from 0.091 to 0.439 indicates that the 3rd principal axis becomes increasingly aligned with the z axis as the wall potential is increased.

To examine the orientation functions more closely, Figures 4.3 and 4.4 present the probability of the cosines of each of the angles θ_1, θ_2 and θ_3 occurring, n(cosθ), as recorded during simulations with 8-mer chains between hard and attractive walls. Figure 4.3 shows that the first principal axis has a broad maxima close to a value of cosθ=0 indicating that the first principal axis' preferred orientation is close to parallel to the walls. The second and third principal axes are reasonably isotropically distributed around the z axis. The similarity between the angular distributions for the second and third principal axes is reflected in the calculated functions $\overline{P}_2(\cos\theta_2)$ and $\overline{P}_2(\cos\theta_3)$ which agree with one another to within the error in our data (Table 4.4). Figure 4.3 therefore demonstrates that the effective field created by the hard walls along the z axis has the effect of weakly orientating the polymer parallel to the walls. In Figure 4.4 the corresponding plots for the 8-mer chain between attractive walls are shown. The orientations of the three principal axes can be seen to be markedly different from the corresponding orientations between hard walls. The first principal axis is strongly orientated parallel to the walls and has a low probability of deviating from this orientation. The second principal axis is also strongly orientated parallel to the walls but has an appreciable probability of sampling other orientations. Finally the third principal axis is reasonable isotropically distributed but has an appreciable preference for the

Wall Type	$\overline{P}_2(\cos\theta_1)$	$\overline{P}_2(\cos\theta_2)$	$\overline{P}_2(\cos\theta_3)$
Hard	-0.150±0.027	0.042±0.031	0.091±0.029
9-3 ε_w=0.2	-0.143±0.020	0.047±0.019	0.092±0.013
9-3 ε_w=0.4	-0.176±0.027	0.035±0.030	0.137±0.030
9-3 ε_w=0.6	-0.288±0.033	0.045±0.029	0.238±0.046
9-3 ε_w=0.8	-0.384±0.042	0.016±0.063	0.367±0.049
9-3 ε_w=1.0	-0.441±0.020	0.001±0.092	0.439±0.092

Table 4.4 The orientation functions of the principal axes as a function of the wall potential.

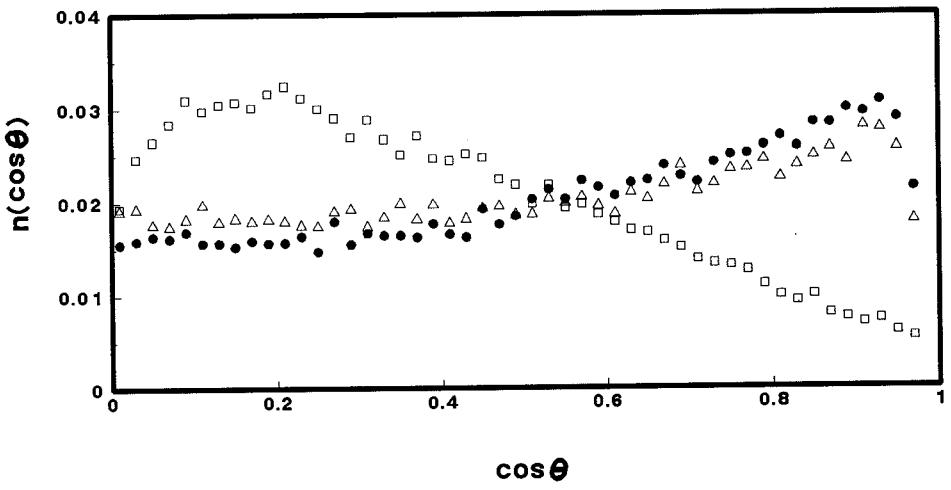

Figure 4.3 Probability plots for the cosines of the angles between the principal axes and the z axis for an 8-mer chain between hard walls. The plots shown represent the results for the first (□), second (△), and third (●) principal axes.

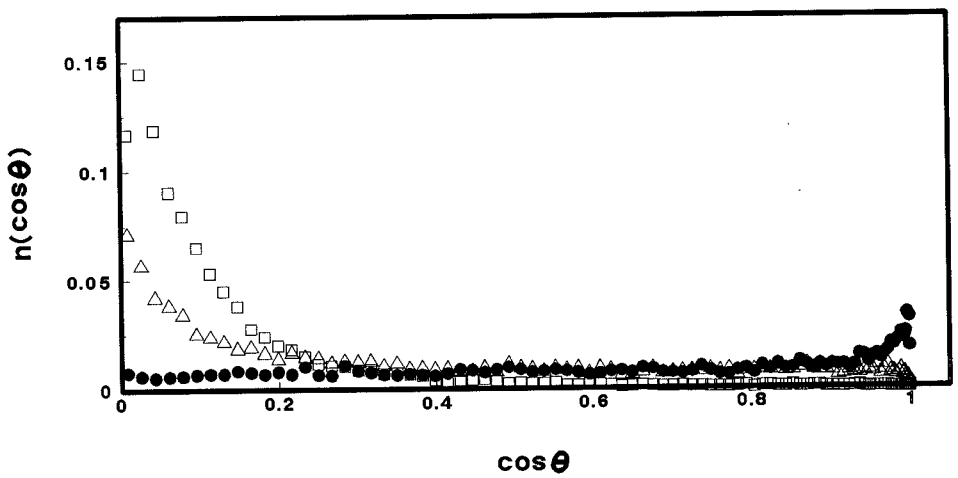

Figure 4.4 Probability plots for the cosines of the angles between the principal axes and the z axis for an 8-mer chain between attractive walls with ε_w=1.0. The plots shown represent the results for the first (□), second (△), and third (●) principal axes.

value of $\cos\theta=1.0$ indicating that its preferred orientation is perpendicular to the walls.

The walls in our simulations therefore have a number of effects on the polymer chains. Between the hard walls separated by 4σ, the chain is not isotropic in shape or orientation due to the field created by the walls along the z axis. Between attractive walls, the polymer chain adsorbs at one of the walls as evidenced by the polymer density profiles of Figures 4.1 and 4.2. As the chain adsorbs at the wall, it becomes increasingly two dimensional, lying flat against the wall. Evidence for this two dimensional behaviour is provided by the increase in the components of the mean square radius of gyration parallel to the wall (Table 4.2) and the changes in the magnitudes of the principal axes of the polymer chain (Table 4.3) along with their preferred orientations (Figures 4.3 and 4.4 and Table 4.4).

4.4.2 Effect of the Wall Separation

To examine the effects of the wall separation on the polymer shape, simulations were performed with hard walls from 4σ to 8σ and soft walls separated from 5.428σ to 9.428σ. 5 simulations were performed at the new value of $H=9.428\sigma$ for the 9-3 potential, utilising the same values of ε_w detailed in section 4.4.1. Details of the simulations performed are contained in Table 4.1. Table 4.5 presents the components of the radius of gyration calculated in the 6 simulations. With hard walls separated by 8σ the chain is larger perpendicular to the walls than it was with the walls at 4σ. At the same time the chain is less extended parallel to the walls in the 8σ case than in the 4σ case. This indicates that with the walls separated by 8σ the polymer chain is more 3 dimensional in nature than with the walls at 4σ. This can be accounted for by the fact that the walls exert less of a confining effect on the polymer with the walls at 8σ than at 4σ. With the 9-3 walls, increasing the value of ε_w increases the magnitude of the chain parallel to the walls and decreases its magnitude perpendicular to the walls. With $\varepsilon_w=1.0$ and the walls at 9.428σ we find that the chain is of almost identical extension perpendicular and parallel to the walls as the simulation performed with the walls at 5.428σ (Tables 4.2 and 4.5).

Therefore in the case of hard walls or 9-3 walls with low ε_w value, increasing the wall separation causes the polymer chain to become more 3 dimensional in nature. However with $\varepsilon_w=1.0$ the separation between the walls becomes an unimportant factor

Wall Type	$\langle S^2 \rangle$	$\langle S_\perp^2 \rangle$	$\langle S_\parallel^2 \rangle$
Hard	1.97±0.03	0.57±0.06	1.39±0.08
9-3 ε_w=0.2	1.95±0.03	0.54±0.05	1.41±0.06
9-3 ε_w=0.4	1.98±0.05	0.48±0.11	1.49±0.10
9-3 ε_w=0.6	1.97±0.06	0.37±0.08	1.60±0.13
9-3 ε_w=0.8	2.07±0.14	0.18±0.06	1.89±0.12
9-3 ε_w=1.0	2.23±0.24	0.12±0.03	2.10±0.24

Table 4.5 The components of the radius of gyration as a function of the wall potential.

in determining the chain's dimensions. This is because the chain is now strongly adsorbed at one of the surfaces.

4.4.3 Effect of Differing Polymer-Wall and Solvent-Wall Interactions

In the simulations described so far the polymer and solvent particles have interacted identically with the walls ie. $\varepsilon_{wp}=\varepsilon_{ws}$. However by altering the relative values of ε_{ws} and ε_{wp} it is possible to examine the polymer adsorption behaviour under conditions of the wall interacting more strongly with either the solvent particles or the monomers in the polymer chain. To investigate this situation 5 sets of simulations were performed. In these simulations we have set $\varepsilon_{ws}=\alpha\varepsilon_{wp}$ where α=0.75, 1.25, 1.50, 1.75 and 2.00. We have used ε_{wp}=0.2, 0.4, 0.6, 0.8 and 1.0 with each of the values of α. Each of the simulations was of an 8 monomer polymer chain in 242 solvent particles, placed between walls separated by 5.428σ. The systems were equilibrated for $2\text{x}10^4$ cycles and $14\text{x}10^4$ production cycles performed.

Figures 4.5 and 4.6 present the components of the mean square radius of gyration calculated parallel and perpendicular to the walls respectively. In the Figures the components of the mean square radius of gyration are plotted for constant values of ε_{wp} as a function of the parameter α. By holding the polymer-wall interaction constant while varying the strength of the solvent-wall interaction (through the parameter α), we are able to investigate the effects of the strength of the solvent adsorption on the adsorption of the polymer chain. The results of the simulations performed with $\varepsilon_{ws}=\varepsilon_{wp}$ are included in Figures 4.5 and 4.6 for convenience. Figure 4.5 shows that for a small value of α (1.00), increasing ε_{wp} from 0.2 to 1.0 leads to a large increase in the value of the parallel component of the mean square radius of gyration. Figure 4.6 shows that this is commensurate with a decrease in the component of the mean square radius of gyration perpendicular to the walls. Decreasing the value of α to 0.75 while keeping the value of ε_{wp} fixed, leads to a marginal increase in the elongation of the chain parallel to the walls. Increasing α from 1.00 to 1.25 however, leads to a decrease in the elongation of the chain parallel to the walls. Increasing the value of α further to 1.5 results in another decrease in the elongation of the chain parallel to the walls and a commensurate increase in the perpendicular component of the radius of gyration. Increasing the value of α from 1.5 to 2.0 results in little change in the chain's dimensions.

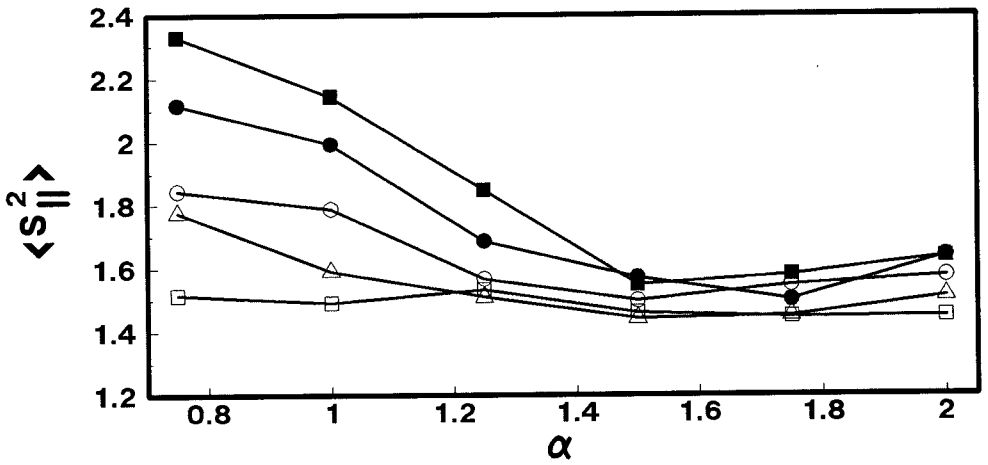

Figure 4.5 The components of the radius of gyration parallel to the walls. Results are shown for ε_{wp}=0.2 (□), ε_{wp}=0.4 (△), ε_{wp}=0.6 (○), ε_{wp}=0.8 (●), ε_{wp}=1.0 (■).

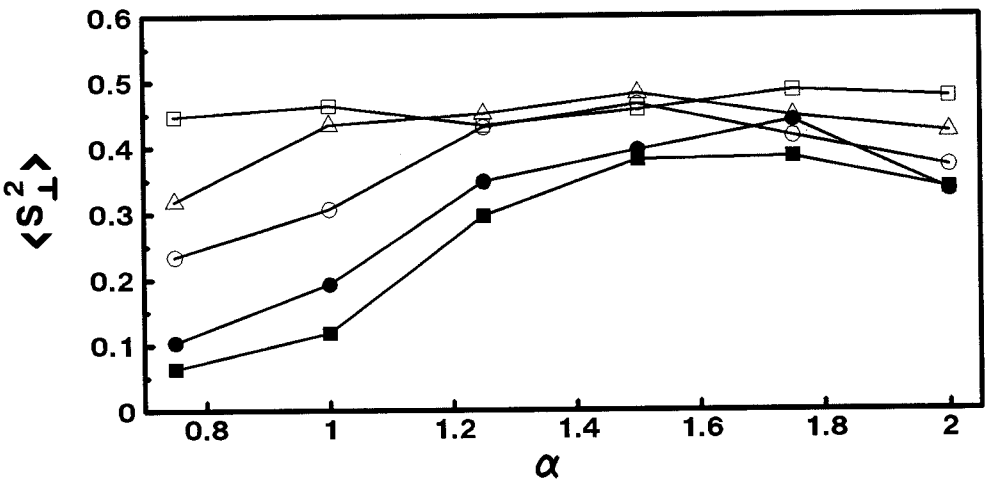

Figure 4.6 The components of the radius of gyration perpendicular to the walls. Results are shown for ε_{wp}=0.2 (□), ε_{wp}=0.4 (△), ε_{wp}=0.6 (○), ε_{wp}=0.8 (●), ε_{wp}=1.0 (■).

To better understand the behaviour of the chains between the walls Figures 4.7 and 4.8 present the density profiles for the simulations performed with ε_{wp}=0.6 and the various values used for α. Figure 4.7 shows that with $\alpha \leq 1.25$ the profiles show a strong enhancement at the wall. As the value of α is increased from 1.50 to 2.00 the chain profiles displayed in Figure 4.8 change markedly. The chains show a weak enhancement and a weak depletion at the walls with α=1.50 and α=1.75 respectively. With α=2.00 the chain is depleted at the walls and is now confined to the centre of the pore. The profile at α=2.00 does not monotonically decrease close to the walls but rather shows a minima close to z=½σ and then increases slightly on approaching the wall. Figure 4.9 shows the site density profiles for the chain with ε_{wp}=0.6 and α=2.00. The Figure clearly demonstrates that all the sites are more likely to be in the centre of the pore than close to the walls. However next to the walls it is clear that there is an increased probability of finding the end site rather than sites in the middle of the chain. The polymer density profiles presented in Figures 4.7 and 4.8 clearly demonstrate that the adsorption of the polymer chain is strongly dependent on the strength of adsorption of the solvent particles at the wall. Increasing the value of α from 1.0 to 2.0 produces a much stronger adsorption of the solvent particles at the wall and these displace the polymer chain from the wall and into the centre of the pore.

An obvious question that arises is whether this displacement of the polymer chain from the wall by the solvent particles affects the overall size and orientation of the polymer chain. As the polymer chains are confined to the centre of the pore are they still aligned parallel to the walls or do they become more isotropic in nature. To address this question we present in Table 4.6 the principal axes of the chains and their corresponding orientation functions in the simulations performed with $\varepsilon_{ws}=\alpha\varepsilon_{wp}$ where α=1.00, 1.25, 1.50, 1.75 and 2.00 and ε_{wp}=0.6. The Table illustrates that increasing α from 1.00 to 1.50 results in the 1st principal axis decreasing in size whilst the 2nd and 3rd principal axes increase marginally in size. This behaviour is consistent with the polymer chain being progressively displaced from the walls and being confined to the centre of the pore with the increase in α. Increasing α from 1.50 to 2.00 causes no appreciable difference in the magnitudes of the principal axes (to within the error in our data). The marginal increase in the polymer chain's component of the mean square radius of gyration parallel to the walls as α is increased from 1.50 to 2.00 must

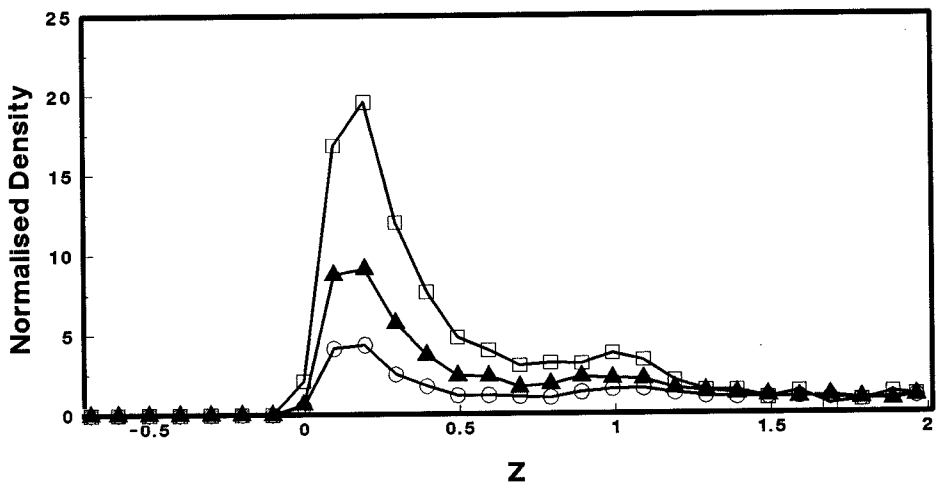

Figure 4.7 The polymer density profiles plotted against the reduced distance from the walls. z. Profiles are shown for ε_{wp}=0.6 and α=0.75 (□), α=1.00 (▲) and α=1.25 (○).

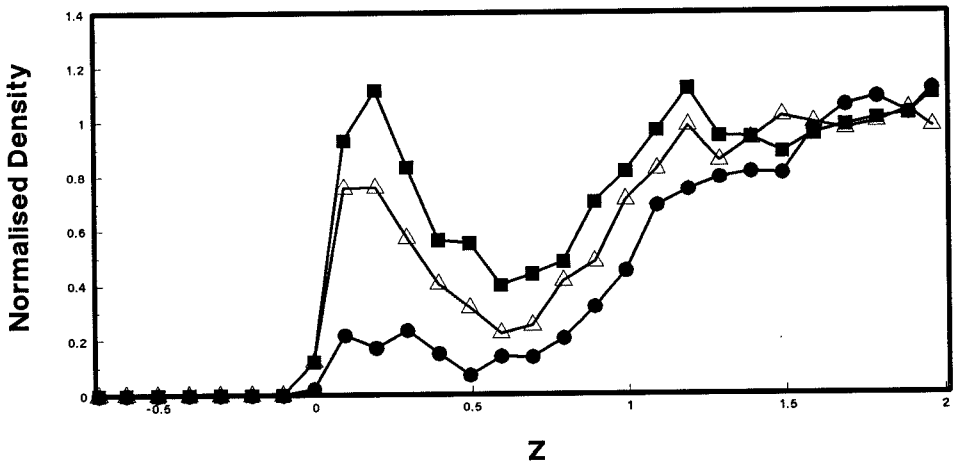

Figure 4.8 The polymer density profiles plotted against the reduced distance from the walls. z. Profiles are shown for ε_{wp}=0.6 and α=1.50 (●), α=1.75 (■) and α=2.00 (▵).

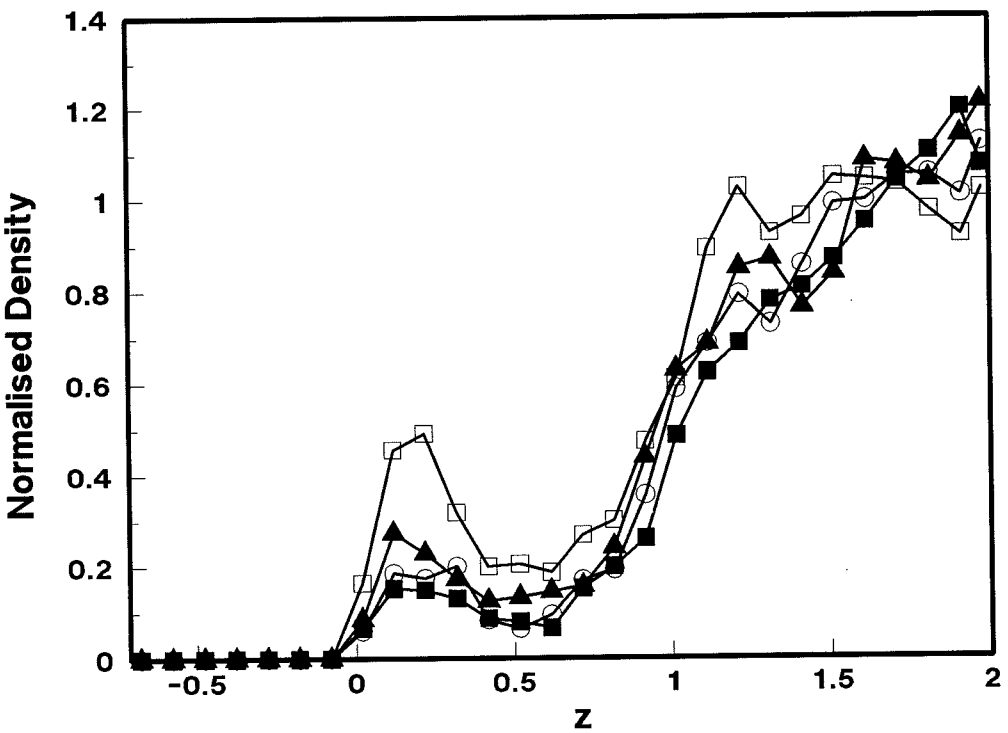

Figure 4.9 The polymer site profiles plotted against the reduced distance from the walls, z. Profiles are shown for the first (□), second (▲), third (○) and fourth sites (■) within the polymer chain. The profiles were recorded for polymer chains between 9-3 walls with ε_{wp}=0.6 and α=2.00.

α	λ_1	λ_2	λ_3	$\overline{P}_2(\cos\theta_1)$	$\overline{P}_2(\cos\theta_2)$	$\overline{P}_2(\cos\theta_3)$
1.00	1.709±0.065	0.309±0.014	0.076±0.003	-0.288±0.033	0.047±0.029	0.238±0.046
1.25	1.593±0.093	0.318±0.008	0.085±0.006	-0.179±0.050	0.022±0.032	0.155±0.038
1.50	1.559±0.062	0.311±0.011	0.092±0.003	-0.138±0.037	0.056±0.020	0.080±0.030
1.75	1.557±0.080	0.315±0.010	0.090±0.002	-0.186±0.024	0.064±0.018	0.119±0.013
2.00	1.539±0.051	0.314±0.008	0.092±0.002	-0.227±0.031	0.065±0.012	0.158±0.033

Table 4.6 The principal axes and the orientation functions for the simulations with $\varepsilon_{ws}=\alpha\varepsilon_{wp}$ and $\varepsilon_{wp}=0.6$.

therefore be caused by a change in the orientation of the chains. As α is increased from 1.00 to 1.50, $\overline{P}_2(\cos\theta_1)$ increases from -0.288±0.033 to -0.138±0.037 indicating that as the polymer chain is displaced from the wall, its first principal axis becomes less strongly orientated parallel to the walls. Increasing α further to 2.00 leads to a decrease in $\overline{P}_2(\cos\theta_1)$ to -0.227±0.031. This decrease in the value of $\overline{P}_2(\cos\theta_1)$ indicates that the first principal axis has again become more strongly oriented parallel to the walls, accounting for the increase in the component of the radius of gyration parallel to the walls. This reorientation of the polymer chain whilst in the centre of the pore is caused by the confining effects of the walls covered in the adsorbed solvent particles.

These results demonstrate that the chain's dimensions between the walls are determined by 2 different effects, depending on the value of α. For small values of α (ie. $\alpha \approx 1$) the polymer chain is able to adsorb at the walls. Increasing the value of ε_{wp} results in the chain flattening against the wall and becoming essentially 2 dimensional. With high values of α (ie. $\alpha \geq 1.50$) the polymer chains are displaced from the walls by the solvent particles and confined to the central region of the pore. The chain dimensions are now only weakly dependent on ε_{wp}.

4.5 Scaling Properties of the Chains

In section 3.1 an equation was introduced relating the squared end-to-end distance of a polymer chain in a good solvent to the number of monomers in the chain (eqn (3.1)),

$$\langle R^2(N) \rangle \cong AN^{2\nu} , \tag{4.17}$$

where R^2 is the square end-to-end distance of the chain, N is the number of monomers in the chain and ν is a scaling exponent whose value is close to 3/5. The value of the exponent ν can be calculated by writing down an expression for the free energy of a polymer chain in terms of a fixed end-to-end vector **R**. The average size of the polymer chain can then be estimated from the value of **R** which minimises the free energy of the chain, yielding in the process the value of ν=3/5.

The end-to-end distance of a polymer chain therefore scales as,

$$\langle R_3 \rangle \cong bN^{\nu} = bN^{\frac{3}{5}} , \tag{4.18}$$

where R_3 is used to denote that the polymer chain is a three dimensional object and b is the square root of A. Eqn (4.18) is true for a polymer chain in a good solvent, but what happens when the polymer chain is confined between walls separated by a distance D? In considering this situation, we follow the analysis of Daoud and de Gennes [2]. If $D \gg R_3$ then one would not expect any change in the shape or dimensions of the polymer chain. However if $D<R_3$ then the chain becomes squeezed and attains an end-to-end distance of R_2, where R_2 is used to denote that the polymer chain is now two dimensional. The end-to-end distance of a two dimensional chain, R_2, must be proportional to $N^{3/4}$ [2] and can be represented by the following relation,

$$R_2 = R_3 f\left(\frac{R_3}{D}\right) = R_3 f(x) . \tag{4.19}$$

In eqn (4.19) f(x) is a dimensionless function that has the following features,

$$f(x \to 0) = 1 , \tag{4.20}$$

$$f(x \gg 1) \cong x^m , \tag{4.21}$$

where m is an exponent whose value has to be determined. Eqn (4.21) implies that for $D \ll R_3$ eqn (4.19) becomes,

$$R_2 \sim R_3^{m+1} D^{-m} \sim N^{\frac{3}{5}(m+1)} b^{m+1} D^{-m} , \tag{4.22}$$

where the sign ~ is used to signify that only the power laws involved are considered. As already stated, the power of N involved must be equal to 3/4 and hence we have that,

$$\frac{3}{5}(m+1) = \frac{3}{4} , \tag{4.23}$$

requiring a value of 1/4 for m.

Therefore eqn (4.22) becomes,

$$R_2 \cong bN^{\frac{3}{4}}\left(\frac{b}{D}\right)^{\frac{1}{4}} . \tag{4.24}$$

For a fixed separation between the walls and for the case of $D \ll R_3$ we therefore have,

$$R_2 \cong N^{\frac{3}{4}} , \tag{4.25}$$

and so the square end-to-end distance of a polymer chain measured parallel to the walls will scale as,

$$\left\langle R_{\|}^2 \right\rangle \cong N^{2\nu} , \tag{4.26}$$

where ν=3/4. The mean square radius of gyration and the square end-to-end distance of a polymer chain are essentially the same [16] and therefore the component of the mean square radius of gyration parallel to the walls scales as,

$$\left\langle S_{\|}^2 \right\rangle \cong N^{2\nu} . \tag{4.27}$$

A similar scaling argument approach can be applied to the adsorption of polymer chains at surfaces [17,18]. In this situation the component of the mean square radius of gyration parallel to the surface also scales in the same way as in eqn (4.27), with the same value for ν of 0.75.

The scaling exponent ν for polymer chains adsorbed at surfaces has been calculated and verified by lattice simulations [19]. Lattice simulations of polymer chains in a good solvent confined in a pore between non-adsorbing walls have also confirmed that the chains scale with an exponent given by ν=0.75 [20].

The scaling analysis that we have presented for a polymer chain confined between walls, or adsorbed at a surface, made no reference to the interaction of the solvent or polymer particles with the wall potential. The analysis simply tells us that under conditions of polymer adsorption in a good solvent, the mean square radius of gyration parallel to the walls scales as eqn (4.27). The simulations that we have performed with 8-mer chains have demonstrated that competitive adsorption effects play an important role in determining the polymer's conformational properties and adsorption behaviour at a surface. An interesting question that we would therefore like to address is what

effect the competitive adsorption processes have on the scaling behaviour of the polymer chains between walls. More specifically, how do the various polymer-wall and solvent-wall interactions affect the scaling exponent ν. To address this question we performed simulations of polymer chains under various conditions of polymer-wall and solvent-wall interactions and then calculated the scaling exponents from the simulations. Before trying to calculate the scaling exponent ν for polymers between walls, we first calculated the scaling exponent for polymer chains in a good solvent. We did this to ascertain whether it was possible to calculate scaling exponents with reasonable accuracy with the relatively short chain lengths accessible to continuum Monte Carlo simulations. Simulations were performed of chains containing between 8 and 32 monomers in a solvent of its own monomers. As detailed in section 4.2 the monomers within the polymer chain and the solvent particles were all modelled by the WCA potential. All the simulations were carried out at $T^*=2.0$ and $\rho^*=0.4$ with periodic boundary conditions imposed in all three directions. The simulations were equilibrated for 10^5 cycles and 5×10^5 production cycles performed. The calculated square end-to-end distances and mean square radii of gyration for the chains are shown in Table 4.7. The Table also includes the scaling exponents calculated from these quantities. Figure 4.10 shows the corresponding log-log plot for the square end-to-end distance and the mean square radius of gyration. For a polymer chain in a good solvent, the mean square radius of gyration and square end-to-end distance both obey the scaling law of eqn (4.17) and the expected value of the scaling exponent is 0.59. Table 4.7 demonstrates that the values of $\langle R^2 \rangle$ and $\langle S^2 \rangle$ calculated in our simulations therefore scale with the appropriate exponent, giving us confidence in our ability to estimate scaling exponents from what are after all small chain lengths. We note that the value of the exponent calculated with the $\langle S^2 \rangle$ values is more accurate than that with the $\langle R^2 \rangle$ values. This is to be expected as all the beads in the chain contribute to the calculation of $\langle S^2 \rangle$ whereas only the two end beads contribute to the calculation of $\langle R^2 \rangle$. In the remainder of this chapter we concentrate on calculating the values of the scaling exponents from the values of the mean square radius of gyration.

To examine the effects of the competitive adsorption processes on the scaling behaviour of the chains, we have performed simulations with 8, 16, 24 and 32-mer chains. For each of the 4 chain lengths simulations were performed with both hard and

N_m	$\langle R^2 \rangle$	$\langle S^2 \rangle$
8	12.267±0.261	1.972±0.023
16	29.248±1.776	4.706±0.192
24	51.238±3.072	7.999±0.243
32	74.553±6.722	11.626±1.162
ν	0.606±0.014	0.595±0.010

Table 4.7 The mean square radius of gyration $\langle S^2 \rangle$ and the square end-to-end distance $\langle R^2 \rangle$, calculated for polymer chains containing N_m monomers in a solvent of its own monomers.

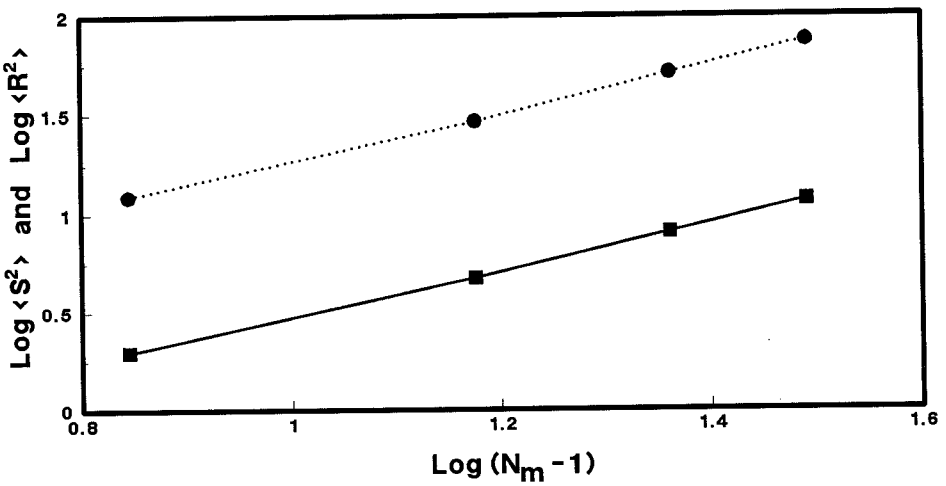

Figure 4.10 Scaling plots for $\langle S^2 \rangle$, the mean square radius of gyration (■) and $\langle R^2 \rangle$, the square end-to-end distance (●).

attractive walls. Attractive wall simulations were performed with $\varepsilon_{ws}=\varepsilon_{wp}$ and $\varepsilon_{wp}=0.6$ and 1.0 for the 4 chain lengths. Further 9-3 wall simulations were performed with $\varepsilon_{ws}=2.0\varepsilon_{wp}$ and $\varepsilon_{wp}=0.6$ and 1.0. The simulations performed with $\varepsilon_{ws}=\varepsilon_{wp}$ and $\varepsilon_{wp}=1.0$ should correspond to the case of strong adsorption of the polymer chains and hence we would expect to recover the scaling exponent $\nu=0.75$. The simulations performed with $\varepsilon_{ws}=\varepsilon_{wp}$ and $\varepsilon_{wp}=0.6$ also correspond to adsorption of the polymer chain but to a lesser extent than in the previous case. With $\varepsilon_{ws}=2.0\varepsilon_{wp}$ and $\varepsilon_{wp}=0.6$ and 1.0 we have shown in section 4.4.3 that the 8-mer chains are displaced from the walls and confined to the centre of the pore.

Table 4.8 presents the mean square radius of gyration calculated parallel to the walls in the various simulations performed. Also presented in the table are the scaling exponents calculated for each of the different types of wall. The results show that the calculated scaling exponents vary significantly among the different wall types.

First we examine the results for the chains adsorbed at the walls. With $\varepsilon_{ws}=\varepsilon_{wp}$ and $\varepsilon_{wp}=1.0$ we obtain $\nu=0.736\pm0.018$, a value which agrees with the expected value of $\nu=0.75$ to within the error in our data. The scaling exponent calculated with the chains between walls with $\varepsilon_{ws}=\varepsilon_{wp}$ and $\varepsilon_{wp}=0.6$ yields a value of $\nu=0.634\pm0.012$. With these wall conditions the 8-mer chains were shown to adsorb at the walls. This calculated value of the exponent is significantly lower than the expected value of $\nu=0.75$. Obviously even though the chains are adsorbing at the walls they are retaining some elements of their 3 dimensional nature and hence are not scaling with the same value of ν as would be expected of 2 dimensional chains.

Now we examine the results for the chains confined either to the middle of the pore or between the walls. With $\varepsilon_{ws}=2.0\varepsilon_{wp}$ and $\varepsilon_{wp}=1.0$ we obtain $\nu=0.730\pm0.006$. Our earlier investigations with the 8-mer chains demonstrated that under these conditions the polymer chains are displaced from the wall and confined to the centre of the pore. Thus the results with $\varepsilon_{ws}=2.0\varepsilon_{wp}$ and $\varepsilon_{wp}=1.0$ are in reasonable agreement with the expected value of $\nu=0.75$. The exponent for the chains between the walls with $\varepsilon_{ws}=2\varepsilon_{wp}$ and $\varepsilon_{wp}=0.6$ is $\nu=0.689\pm0.002$. Once again under these conditions the polymer chain is displaced from the walls and confined to the centre of the pore. The calculated exponent is less than the exponent with $\varepsilon_{ws}=2\varepsilon_{wp}$ and $\varepsilon_{wp}=1.0$. This can be attributed to the adsorption of the solvent particles at the walls. With $\varepsilon_{ws}=2\varepsilon_{wp}$ and $\varepsilon_{wp}=1.0$ essentially all

		$\langle S_{\parallel}^2 \rangle$			
		9-3 Walls			
		$\varepsilon_{ws}=\varepsilon_{wp}$		$\varepsilon_{ws}=2\varepsilon_{wp}$	
N_m	Hard Walls	$\varepsilon_{wp}=0.6$	$\varepsilon_{wp}=1.0$	$\varepsilon_{wp}=0.6$	$\varepsilon_{wp}=1.0$
8	1.47±0.06	1.78±0.07	2.14±0.16	1.57±0.08	1.63±0.05
16	3.85±0.14	4.91±0.45	6.22±0.73	4.50±0.19	4.84±0.11
24	6.79±0.50	8.22±1.40	11.81±1.88	8.16±0.46	9.22±0.38
32	10.59±3.75	11.73±1.71	19.44±6.15	12.19±0.85	14.33±0.81
ν	0.659±0.014	0.634±0.012	0.736±0.018	0.689±0.002	0.730±0.006

Table 4.8 The components of the radius of gyration calculated parallel to the walls in the various simulations. N_m is the number of monomers in the polymer chain.

the solvent particles are adsorbed at the walls and the polymer chain is squeezed between walls which are covered in adsorbed solvent particles. Under the same conditions but with ε_{wp}=0.6 fewer of the solvent particles are adsorbed at the walls and hence the polymer chains are not as strongly confined as in the previous case. This in turn leads to a decrease in the chain dimensions between the walls and the chains scaling with a smaller exponent. Finally the chains confined between hard walls scale with an exponent of ν=0.659±0.014. Again this exponent is significantly lower than that expected for a chain confined between walls of ν=0.75. It should be pointed out that if we were able to simulate chains of length 100-1000 monomers then we would expect the scaling exponent for the chains trapped to the centre of the pore to attain a value of ν=0.75. The scaling behaviour of the polymer chains between the walls is therefore sensitive to the details of the both the wall-polymer and wall-solvent interactions.

4.6 Conclusions

We have investigated the properties of linear polymer chains between walls. The adsorption or depletion of the chains at the walls was found to be determined by competing entropic and energetic factors. The competition between these factors is a function of the solvent-wall and polymer-wall interactions along with their relative magnitudes. Between hard walls the polymer chains are depleted at the walls and site profiles for the chains demonstrate that the first site is more likely to be at the walls than sites within the middle of the chain. This depletion of the sites in the middle of the chains from the walls is due to the fact that it is entropically more favourable to have the head of the polymer chain close to the walls than the body of the chain. Placed between 9-3 walls the polymer chains are either depleted or enhanced at the walls depending on the relative strengths of the wall-polymer and wall-solvent interactions. Under conditions which favour adsorption of the chains at the walls, the chain's site profiles become essentially identical. This indicates that entropic factors are no longer important in determining the chain's conformational properties between the walls. As the strength of the wall-polymer interaction is increased the polymer chain adsorbs at the wall and elongates in the direction parallel to the wall becoming essentially two dimensional as it does so. Under conditions which favour the depletion of the chains at the walls the head of the chain is again more likely to be at the wall than the rest of the

sites in the chain. Entropic effects are therefore once again playing a role in determining the chain's conformation.

We have investigated the scaling behaviour of the chains between the various types of walls. The scaling exponent is found to be sensitive to the details of the wall-polymer and wall-solvent interactions along with their relative magnitudes. Under appropriate conditions the chains are found to scale with the theoretically determined scaling exponent. To the best of our knowledge this is the first time that this particular scaling exponent has been calculated and verified by off-lattice simulations. The value of the scaling exponent can also take on values different to those predicted by theory, depending on the details of the various particle-wall interactions.

The systems studied in this chapter are idealised models of alkane chains in methane. In the following two chapters we will now apply the simulation techniques utilised in the simulations of the polymer and solvent system to a system of current interest, namely the calculation of the equation of state of athermal alkane chains placed between hard walls. In chapter 5 an introduction to the background on the calculation of the equation of state of alkane systems will be given and in chapter 6 we will present our results for the equations of state of 3 athermal alkane systems.

4.7 References

[1] P.G. de Gennes, "Scaling concepts in polymer physics", Cornell University Press, (1979).

[2] M. Daoud and P.G. de Gennes, "Statistics of macromolecular solutions trapped in small pores", J. Phys., **38**, 85-93, (1977).

[3] E. Eisenriegler, K. Kremer and K. Binder, "Adsorption of polymer chains at surfaces: Scaling and Monte Carlo simulations", J. Chem. Phys., **81**, 6381-6394, (1984).

[4] D. H. Napper, "Polymeric stabilization of colloidal dispersions", Academic Press, New York, (1983).

[5] W. Smith and D.C. Rapaport, "Molecular dynamics simulation of linear polymers in a solvent", Mol. Sim., **9**, 25-39, (1992).

[6] J. Luque, J. Santamaria and J.J. Freire, "Molecular dynamics of chain molecules in solution. Static and dynamic properties", J. Chem. Phys., **91**, 584-589, (1989).

[7] B. Smit, A. van der Put, C.J. Peters, J. de Swaan Arons and J.P.J. Michels, "The influence of solvent quality on the static properties of a linear polymer: A molecular dynamics study", Chem. Phys. Lett., **144**, 555-557, (1988).

[8] D. Nicholson and N.G. Parsonage, "Computer simulation and the statistical mechanics of adsorption", Academic press, (1982).

[9] J. Talbot, D.J. Tildesley and W.A. Steele, "A molecular-dynamics simulation of nitrogen adsorbed on graphite", Mol. Phys., **51**, 1331-1356, (1984).

[10] M.P. Allen and D.J. Tildesley, "Computer simulation of liquids", Clarendon press, Oxford, (1987).

[11] A. Yethiraj and C.K. Hall, "Monte Carlo simulation of hard chain-hard sphere mixtures in slitlike pores" J. Chem. Phys., **91**, 4827-4837, (1989).

[12] S.K. Kumar, M. Vacatello and D.Y. Yoon, "Off-lattice Monte Carlo simulations of polymer melts confined between two plates", J. Chem. Phys., **89**, 5206-5215, (1988).

[13] T. Pakula, "Computer simulation of polymers in thin layers. I. Polymer melt between neutral walls - static properties", J. Chem. Phys., **95**, 4685-4690, (1991).

[14] H. Goldstein, "Classical mechanics", Addison-Wesley publishing company, 2nd Edn, (1981).

[15] K. Solc, "Shape of a random-flight chain", J. Chem. Phys., **55**, 335-344, (1971).

[16] P.J. Flory, "Principles of polymer chemistry", Cornell University Press, Ithaca, New York, (1967).

[17] P.G. de Gennes, "Scaling theory of polymer adsorption", J. Phys., **37**, 1445-1453, (1976).

[18] P.G. de Gennes and P. Pincus, "Scaling theory of polymer adsorption : proximal exponent", J. Phys. Lett., **44**, L241-L246, (1983).

[19] E. Eisenriegler, K. Kremer and K. Binder, "Adsorption of polymer chains at surfaces: Scaling and Monte Carlo analyses", J. Chem. Phys., **77**, 6296-6320, (1982).

[20] F.T. Wall, W.A. Seitz, J.C. Chin and P.G. de Gennes, "Statistics of self-avoiding walks confined to strips and capillaries", Proc. Natl. Acad. Sci. USA, **75**, 2069-2070, (1978).

5. The Equation Of State Of Chain Molecules

5.1 Introduction

Empirical equations of state containing adjustable parameters are widely used in industry to obtain the thermodynamic properties of chain fluids, in particular of alkane fluids [1]. Empirical equations of state require a large amount of experimental data with which to fit the parameters in the equations. In addition, these equations are accurate only within the ranges of pressures, temperatures etc., in which the parameters were fitted. The aforementioned difficulties with empirical equations of state make it desirable to have available equations of state for chain fluids which have a sound theoretical basis.

Several equations of state of chain fluids have been reported in the literature. Equations of state have been reported for tangent hard-sphere chains [2,3]. The tangent hard-sphere model of a polymer chain is a bead-rod model with a unit bond length of the type described in section 3.2.2, but with hard-sphere sites rather than WCA sites. Equations of state have also been reported for tangent square-well chains [4]. Because of the highly idealised nature of these models it is difficult to compare the results obtained with these models to experimental data, although the results can be compared to computer simulations. It is therefore of interest to develop theories for realistic models of polymer and alkane fluids in order that accurate equations of state can be computed and compared to experimental data.

A recently introduced theory of the structure of polymer liquids is the polymer-RISM or PRISM theory (polymer reference interaction-site model). This integral equation theory is a generalisation of the RISM theory introduced in chapter 2, to polymer liquids. The theory has been applied to the calculation of the intermolecular structure of polymer melts [5,6,7] and binary blends [8,9]. Site-site radial distribution functions calculated with the PRISM theory have been found to be in good agreement with the results of molecular dynamics [10] and Monte Carlo simulations [11] of tangent hard-sphere chains. The success of the PRISM theory in the calculation of the intermolecular structure of polymer liquids has prompted its application to the calculation of thermodynamic properties of polymer fluids. The PRISM theory has been

used to compute the equation of state for tangent hard-sphere chains using a virial route to the pressure [12]. For polyethylene the virial equation can be written as,

$$\frac{\beta P}{\rho} = 1 - \frac{2\pi}{3}\beta\rho\sum_{\alpha=1}^{N}\sum_{\gamma=1}^{N}\int_{0}^{\infty} dr\, r^3 \frac{du_{\alpha\gamma}(r)}{dr} g_{\alpha\gamma}(r) + R_3 . \qquad (5.1)$$

In eqn (5.1) ρ is the chain density, N is the number of monomers in the polyethylene chain, d is the hard sphere diameter for the monomers within the polyethylene chain, $g_{\alpha\gamma}(r)$ is the radial distribution function and R_3 is a density dependent quantity which depends on three body correlations within the fluid. The term R_3 can be written as,

$$R_3 = -\frac{\beta}{3}\frac{\rho}{N-1}\sum_{\alpha=1}^{N}\sum_{\gamma=1}^{N}\sum_{\lambda=1}^{N}\int dr \int dr'\, \hat{r}.r' \frac{du}{dr} g^{(3)}_{\alpha\gamma\lambda}(r,r') , \qquad (5.2)$$

where $g^{(3)}_{\alpha\gamma\lambda}(\mathbf{r},\mathbf{r}')$ is a three body distribution function for sites α and λ on the same molecule separated by $\mathbf{r}'$ and sites α and γ on different molecules separated by a distance $\mathbf{r}$ and du/dr is the derivative of the potential acting between the sites α and γ. The three body correlations of eqn (5.2) are shown schematically in Figure 5.1. The determination of three body correlation functions is in general a difficult task and hence an approximation to the function $g^{(3)}_{\alpha\gamma\lambda}(\mathbf{r},\mathbf{r}')$ is required. A superposition approximation can be used for $g^{(3)}_{\alpha\gamma\lambda}(\mathbf{r},\mathbf{r}')$ of the form,

$$g^{(3)}_{\alpha\gamma\lambda}(\mathbf{r},\mathbf{r}') \approx w_{\alpha\lambda}(r')\, g_{\alpha\gamma}(r)\, g_{\lambda\gamma}(|\mathbf{r}+\mathbf{r}'|) , \qquad (5.3)$$

where $w_{\alpha\lambda}(r)$ is the intramolecular probability distribution function that two sites α and λ on the same molecule are separated by a distance r. Equations of state were calculated for 4-mer and 16-mer chains using eqns (5.1)-(5.3) and compared to the results of Monte Carlo simulations. The PRISM theory was found to yield pressures in good agreement with the Monte Carlo results for the 4-mer chains, but in significantly poorer agreement for the 16-mer chains. It was subsequently found that the superposition approximation of eqn (5.3) used in the calculation of R_3 was not very accurate [13]. More recently, the equations of state of athermal butane and polyethylene have been calculated using the PRISM theory [14], where the term athermal butane is being used to refer to the hard core representation of butane. These results were used to

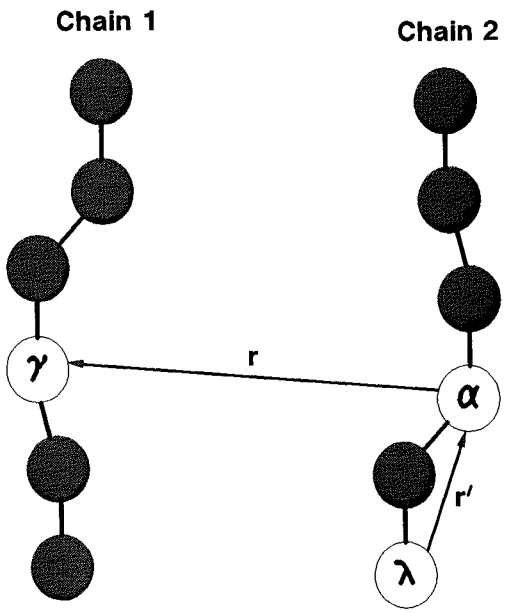

Figure 5.1 A schematic representation of the three body correlations between sites α and λ on chain 2 and site γ on chain 1.

provide the hard-sphere reference system in a thermodynamic perturbation theory approach to the calculation of the equations of state for butane and polyethylene [15]. Unfortunately, the PRISM theory like most integral equation theories, suffers from the disadvantage that the calculated value of the pressure is dependent upon the thermodynamic route used to obtain the pressure. Several routes to the pressure were used with the PRISM theory yielding different estimates of the athermal contributions to the pressure. The results of the perturbation scheme were then compared to the results of molecular dynamics simulations of butane and experimental compressibility measurements for polyethylene melts. The molar volumes calculated from the PRISM theory were in general in reasonable agreement with the simulation results. For polyethylene compressibilities much higher than the experimental results were obtained with one of the routes to the pressure and compressibilities much lower than the experimental results obtained with another route to the pressure. Altering the values of the parameters within the potential model for the alkane chains lead to an improved agreement between the PRISM and experimentally measured compressibilities of polyethylene. At present it is difficult to ascertain whether the discrepancies between the PRISM theory and the experimental compressibilities are due to inherent weaknesses in the PRISM theory as applied to alkane systems, or in the route chosen to calculate the pressure, or inaccuracies in the potential model used for the alkane systems. At present simulation data is not available for athermal alkane systems. This lack of simulation data makes it difficult to ascertain the accuracy of the PRISM theory in the calculation of the intermolecular structure of athermal alkane systems. The radial distribution function for the athermal system is required in the thermodynamic perturbation theory and hence it is important to ascertain the accuracy of the theory in the calculation of this quantity. This in turn makes it difficult to determine whether the PRISM equation is a useful and accurate method of calculating reference system data for use in thermodynamic perturbation theory as applied to chain molecule systems. We were therefore interested in performing simulations of athermal alkanes with which to compare the predictions of the PRISM theory for the intermolecular structure. We were also interested in calculating the equations of state for these athermal alkanes by simulation, once again to test the accuracy of PRISM calculations.

The simulations that we have performed are therefore intended to provide an

unambiguous test of the PRISM theory as applied to athermal alkane systems. We have performed Monte Carlo simulations with a short athermal alkane molecule, butane, and longer athermal alkane molecules, heptane and decane. Simulations were performed in the bulk for these systems to calculate the site-site radial distribution functions. These radial distribution functions were then compared to the results of PRISM calculations. The equations of state were also calculated for these athermal alkanes by simulation and a number of these methods are discussed in section 5.5. The method we have used is the method of Yethiraj *et. al.* [16] in which the chains are placed between hard walls and the pressure of the bulk fluid calculated from the density of sites at the wall. The equations of state were calculated for these alkanes and compared to the results of PRISM calculations.

In section 5.2 an introduction is given to thermodynamic perturbation theory. This is followed in section 5.3 by an account of the PRISM theory. In section 5.4 various methods are discussed for the calculation of the athermal chain contribution to the pressure from PRISM theory. Finally in section 5.5 computer simulation methods for the calculation of equations of state for athermal chains are discussed.

5.2 Thermodynamic Perturbation Theory

The intermolecular pair potential can in many cases be separated into a short range repulsive potential and a smoothly varying long-range attractive component. It is generally accepted that the structure of dense simple liquids is dominated by the short range repulsive potential. The structure of the fluid is therefore dominated by geometric factors associated with the packing of the molecular hard cores [17]. The attractive interactions may be regarded as giving rise to a uniform background potential that provides the cohesive energy for the liquid, but has little effect on the structure. The properties of a given fluid can therefore be related to those of a reference hard-sphere fluid and the attractive part of the potential treated as a perturbation. The hard-sphere fluid is often chosen as the reference system in simple liquids because the thermodynamic and structural properties of this system are well known. To illustrate these ideas, consider a pair potential of the form,

$$u(r) = u_0(r) + u_a(r) \ , \qquad (5.4)$$

where u_0 is the pair potential of the reference system and $u_a(r)$ is the pair potential of the attractive perturbation. The free energy of a system of N particles at a density of ρ, interacting through the pair potential u(r) can be related to the properties of the reference hard-sphere fluid using a perturbation expansion, yielding to first order,

$$\frac{\beta A}{N} = \frac{\beta A_0}{N} + \frac{1}{2}\beta\rho \int g_0(r)\, u_a(r)\, d\mathbf{r} \ . \tag{5.5}$$

In eqn (5.5) $g_0(r)$ is the radial distribution function for the reference fluid interacting through the potential $u_0(r)$, A_0 is the free energy of the reference system and A is the free energy for the system interacting through the potential u(r). Such a first order perturbation theory works well for attractive forces. Therefore to determine the free energy of a given fluid it is necessary to divide the potential into a reference (usually) repulsive potential and an attractive perturbation. Two well known perturbation approaches that have been applied to both atomic and molecular fluids are the Barker-Henderson (BH) theory [18] and the Weeks-Chandler-Andersen (WCA) theory [19]. These two approaches differ in their choice of the reference potential $u_0(r)$ and the perturbation $u_a(r)$. These potential divisions can be illustrated by taking the example of the Lennard-Jones potential of eqn (2.2) for u(r). In the BH theory the reference and perturbation potentials are taken to be the repulsive and attractive branches of the Lennard-Jones potential respectively. Therefore,

$$\begin{aligned} u_0(r) &= u(r) && r \le \sigma, \\ &= 0 && r > \sigma, \end{aligned} \tag{5.6}$$

$$\begin{aligned} u_a(r) &= 0 && r \le \sigma, \\ &= u(r) && r > \sigma. \end{aligned} \tag{5.7}$$

In the WCA theory the separation is,

$$\begin{aligned} u_0(r) &= u(r) + \epsilon && r \le 2^{1/6}\sigma, \\ &= 0 && r > 2^{1/6}\sigma, \end{aligned} \tag{5.8}$$

$$u_a(r) = -\epsilon \qquad r \le 2^{1/6}\sigma,$$
$$= u(r) \qquad r > 2^{1/6}\sigma. \tag{5.9}$$

Although the reference potentials defined by eqns (5.6) and (5.8) are continuous soft-core repulsions, it is usual to perform a second perturbation of the reference system u_0 around a hard-sphere system with an optimised hard sphere diameter. The hard core diameter, d, of the underlying hard sphere potential is chosen in such a way that the free energies of the reference system interacting through u_0 and the hard sphere system have the same values. In BH theory this hard core diameter is given by,

$$d = \int_0^\infty \{ 1 - \exp[-\beta u_0(r)] \} \, dr \, , \tag{5.10}$$

and therefore is dependent only on the temperature once the reference system has been defined. In the WCA theory, d is chosen to satisfy,

$$\int_0^\infty y_{HS}(r;d) \left[\exp(-\beta u_0(r)) - \exp(-\beta u_{HS}(r;d)) \right] r^2 \, dr = 0 \, , \tag{5.11}$$

where the subscript HS denotes the hard sphere system, $u_{HS}(r;d)$ is the hard sphere potential for a hard sphere with diameter d, and $y_{HS}(r;d)$ is the indirect correlation function for the hard sphere system. The indirect correlation function for the hard sphere system can be evaluated analytically [17]. Eqn (5.11) is solved iteratively and the resulting value of the hard core diameter d is dependent on both the temperature and density of the system.

As previously mentioned the reference fluid for simple atomic fluids, is chosen to be the hard-sphere fluid. Accurate radial distribution functions and direct correlation functions are available for this system. To apply the methods of thermodynamic perturbation theory to the calculation of thermodynamic properties of polymer fluids it is necessary to have available the function $g_{HS}(r;d)$ for the corresponding athermal polymer systems.

Once the function $g_{HS}(r;d)$ has been obtained it is possible to calculate the indirect correlation function $y_{HS}(r;d)$ for the hard sphere system from,

$$y_{HS}(r;d) = \exp\left[\beta u_{HS}(r;d)\right] g_{HS}(r;d) \ . \tag{5.12}$$

In addition it is then possible to calculate the radial distribution function for the reference system, $g_0(r)$ required in eqn (5.5) using,

$$g_0(r) = \exp\left[-\beta\left(u_0(r) - u_{HS}(r;d)\right)\right] g_{HS}(r;d) \ . \tag{5.13}$$

The site-site radial distribution function for the hard sphere system $g_{HS}(r;d)$ can be obtained for polymer systems from the PRISM equation which we will now discuss.

5.3 The PRISM Equation

The RISM theory introduced in chapter 2 is a reasonably successful theory of molecular fluids. The RISM equation can be written as,

$$\mathbf{H}(r) = \int d\mathbf{r}' \int d\mathbf{r}'' \mathbf{W}(|\mathbf{r} - \mathbf{r}'|)\, \mathbf{C}(|\mathbf{r}' - \mathbf{r}''|)\left[\mathbf{W}(\mathbf{r}'') + \rho\mathbf{H}(\mathbf{r}'')\right] , \tag{5.14}$$

where ρ is the molecular number density and **H**, **C** and **W** are square matrices of rank N (for molecules containing N interaction sites). The elements of the matrices H, C and W are represented by $h_{\alpha\gamma}(r)$, $c_{\alpha\gamma}(r)$ and $w_{\alpha\gamma}(r)$ respectively. $h_{\alpha\gamma}(r)$ is the total site-site correlation function for sites α and γ on different chains, $c_{\alpha\gamma}(r)$ is the direct site-site correlation function and $w_{\alpha\gamma}(r)$ is the intramolecular distribution function for sites α and γ on the same molecule. The distribution function $w_{\alpha\gamma}(r)$ describes the connectivity and flexibility of the molecule. $h_{\alpha\gamma}(r)$ is related to the intermolecular site-site radial distribution function, $g_{\alpha\gamma}(r)$, by the relation,

$$h_{\alpha\gamma}(r) = g_{\alpha\gamma}(r) - 1 \ . \tag{5.15}$$

The set of coupled, non-linear integral equations contained within eqn (5.14) can be solved by introducing closure relations for $c_{\alpha\gamma}(r)$ and $h_{\alpha\gamma}(r)$. The structure of dense non-polar liquids is known to be dominated by the core repulsive forces [17] and the above equation can be solved in conjunction with closure relations based on the short ranged

core repulsions of the sites within the molecules. These Percus-Yevick closure relations are,

$$h_{\alpha\gamma}(r) = -1, \qquad r \le \sigma_{\alpha\gamma} , \tag{5.16}$$

$$c_{\alpha\gamma}(r) = 0, \qquad r > \sigma_{\alpha\gamma} , \tag{5.17}$$

where $\sigma_{\alpha\gamma}$ is the distance of closest approach of sites α and γ. Eqn (5.16) is an exact statement of the hard core condition, while eqn (5.17) is the approximation at the heart of the RISM theory.

A more compact representation of the RISM equation can be obtained by rewriting the equation in Fourier space to yield,

$$\hat{H}(k) = \hat{W}(k)\,\hat{C}(k)\left[\hat{W}(k) + \rho\hat{H}(k)\right] . \tag{5.18}$$

In eqn (5.18) the caret denotes a three dimensional Fourier transform where the elements of the matrix are defined by,

$$\hat{f}(k) = \frac{4\pi}{k}\int_0^\infty r f(r)\sin(kr)\,dr . \tag{5.19}$$

Once the intramolecular correlation function for a given molecular system has been specified it is possible to solve the RISM equation in conjunction with the closure relations of eqns (5.16) and (5.17). In many molecular systems the structure of a molecule can be represented by a rigid set of bonded atoms with fixed bond angles, bond lengths and dihedral angles (if present within the molecule). In these systems the intramolecular distribution function $\hat{w}_{\alpha\gamma}(k)$ can be represented by,

$$\hat{w}_{\alpha\gamma}(k) = \delta_{\alpha\gamma} + (1-\delta_{\alpha\gamma})\,\frac{\sin(kl_{\alpha\gamma})}{kl_{\alpha\gamma}} , \tag{5.20}$$

where $l_{\alpha\gamma}$ is the distance between sites α and γ. In principle it is possible to directly apply the RISM equation to the problem of chain molecule fluids. However, for flexible molecules the intramolecular structure of the molecule is dependent on the environment in which the molecule is situated. It is therefore necessary to determine the intramolecular and intermolecular correlation functions, $w_{\alpha\gamma}(r)$ and $h_{\alpha\gamma}(r)$, self-

consistently which is a difficult problem. In the original formulation of the PRISM equation this problem was avoided by using the correlation functions $w_{\alpha\gamma}(r)$ for the ideal freely jointed chain model of a polymer. The use of this intramolecular correlation functions was justified by noting that theoretical [20,21,22] and neutron scattering studies [23,24] had established that single-chain configurational statistics in a polymer melt are ideal down to nearly monomeric length scales. In such circumstances the structure of a polymer chain obeys random walk statistics and it is therefore possible to insert the unperturbed intramolecular correlation functions $w_{\alpha\gamma}(r)$, thereby bypassing the need for a self-consistent determination of both the intramolecular and intermolecular correlation functions.

Despite resolving the issue of self-consistency, solving the matrix of integral equations contained within the RISM equation for a polymer with a few hundred monomers would be virtually impossible. These difficulties can be surmounted by taking advantage of the fact that polymer chains are long and hence end effects are unlikely to be important and so can be ignored; ie. the radial distribution function $g_{\alpha\gamma}(r)$ between sites on different chains will be approximately independent of α and γ, provided that α and γ are not near the chain ends. The intramolecular and intermolecular correlation functions are therefore independent of site label and can be represented by, $h(r)\equiv h_{\alpha\gamma}(r)$ and $c(r)\equiv c_{\alpha\gamma}(r)$. The neglect of chain end effects and the assumption of the equivalence of all the sites within the chain results in a reduction of the matrix of integral equations to a single scalar integral equation which can be written in Fourier space as,

$$\hat{h}(k) = \hat{w}(k)\,\hat{c}(k)\,\hat{w}(k) + \rho_m \hat{w}(k)\,\hat{c}(k)\,\hat{h}(k) , \qquad (5.21)$$

where $\rho_m \equiv \rho N$ is the monomer density and $\hat{w}(k)$ is the single chain or intramolecular structure factor given by,

$$\hat{w}(k) = \frac{1}{N}\sum_{\alpha=1}^{N}\sum_{\gamma=1}^{N} \hat{w}_{\alpha\gamma}(k) . \qquad (5.22)$$

Eqn (5.21) is known as the polymer-RISM or PRISM equation.

The PRISM equation can be solved in conjunction with the closure relations of eqns (5.16) and (5.17), namely,

$$h(r) = -1, \quad r \leq \sigma \ , \tag{5.23}$$

$$c(r) = 0, \quad r > \sigma \ . \tag{5.24}$$

Eqns (5.21)-(5.24) represent a numerically tractable integral equation theory for the structure of a polymer fluid.

The PRISM theory requires the intramolecular structure factor, w(r), as an input to the theory. A number of models have been developed for the intramolecular structure factor of polymer chains. Two of the most widely applied models will now be discussed.

5.3.1 Intramolecular Correlation Functions

The intramolecular structure factor can be written in **r** space as,

$$w(r) = \frac{1}{N} \sum_{\alpha=1}^{N} \sum_{\gamma=1}^{N} w_{\alpha\gamma}(r) \ , \tag{5.25}$$

where $w_{\alpha\gamma}$ is related to the probability that sites α and γ on the same chain are a distance r apart. For rigidly bonded molecules the functions $w_{\alpha\gamma}$ are given by,

$$w_{\alpha\gamma}(r) = \delta_{\alpha\gamma}\delta(r) + (1-\delta_{\alpha\gamma})\,\delta(r-l_{\alpha\gamma}) \ , \tag{5.26}$$

where $l_{\alpha\gamma}$ is the distance between the sites α and γ and the functions $w_{\alpha\gamma}$ are normalised such that,

$$\int w_{\alpha\gamma}(\mathbf{r})\, d\mathbf{r} = 1 \ . \tag{5.27}$$

The first intramolecular correlation function that we will consider is that for the freely jointed chain (FJC) model of section 3.4.3. In this model the polymer consists of N spheres or beads of diameter σ, connected by a bond of length l.

This model results in a simple expression for the intramolecular correlation function $\hat{w}_{\alpha\gamma}(k)$ [25],

$$\hat{w}_{\alpha\gamma}(k) = \left[\frac{\sin(kl)}{kl} \right]^{|\alpha-\gamma|} . \tag{5.28}$$

For the FJC model the intramolecular structure factor of eqn (5.25) can be represented in Fourier space by,

$$\hat{w}(k) = 1 + \frac{2}{N} \sum_{|\alpha-\gamma|=1}^{N-1} (N-\tau) \left[\frac{\sin(kl)}{kl} \right]^{|\alpha-\gamma|} , \tag{5.29}$$

where $\tau=|\alpha-\gamma|$. $\hat{w}(k)$ can be evaluated analytically from eqn (5.29) to give [25],

$$\hat{w}(k) = \frac{1 - f^2 - 2f/N + 2f^{N+1}/N}{(1-f)^2} , \tag{5.30}$$

where,

$$f = \frac{\sin(kl)}{kl} . \tag{5.31}$$

Unfortunately the freely jointed chain model of a polymer allows for non-physical overlaps between non-bonded monomers within the polymer chain. It is possible to rectify this situation by removing the non-bonded overlaps from the model, yielding a model of a polymer chain referred to as the non-overlapping freely jointed chain model (NFJC) [26]. The NFJC model of a polymer chain with a bond length of l is defined by,

$$w_{\alpha\gamma}(r) = 0, \qquad r < \sigma , \tag{5.32}$$

$$w_{\alpha\gamma}(r) = \frac{B_{\alpha\gamma}}{(2\pi)^3} \int d\mathbf{k}\, e^{i\mathbf{k}.\mathbf{r}} \left[\frac{\sin(kl)}{kl} \right]^{|\alpha-\gamma|} , \qquad r \geq \sigma , \tag{5.33}$$

for $|\alpha-\gamma| \geq 2$. Eqn (5.32) ensures the removal of all non-bonded overlaps from the model. Eqn (5.33) is the intramolecular correlation function for a chain where the interactions between sites α and γ are treated as those of a freely jointed chain.

The factor $B_{\alpha\gamma}$ in eqn (5.33) is defined such that $w_{\alpha\gamma}(r)$ is normalised to unity, ie.,

$$4\pi \int_0^\infty r^2 w_{\alpha\gamma}(r)\, dr = 1 \,. \tag{5.34}$$

Introducing the function,

$$\hat{J}_{\alpha\gamma}(K) = \frac{2}{\pi K} \int_0^1 dR \sin(KR) \times \int_0^\infty dK' K' \sin(RK') \left[\frac{\sin(K'L)}{K'L}\right]^{|\alpha-\gamma|} , \tag{5.35}$$

where $R=r/\sigma$ and $K=k\sigma$ are dimensionless variables and $L=l/\sigma$ is the reduced bond length for the polymer. The normalisation factors are given by,

$$B_{\alpha\gamma} = \frac{1}{1 - \hat{J}_{\alpha\gamma}(0)} , \tag{5.36}$$

where,

$$\hat{J}_{\alpha\gamma}(0) = \frac{2}{\pi} \int_0^1 R\, dR \int_0^\infty K' dK' \sin(K'R) \left[\frac{\sin(K'L)}{K'L}\right]^{|\alpha-\gamma|} . \tag{5.37}$$

The intramolecular structure factor can now be calculated for the NFJC model from,

$$\hat{w}(K) = \frac{1}{N} \sum_{\alpha,\gamma=1}^{N} \hat{w}_{\alpha\gamma}(K) \tag{5.38}$$

$$= 1 + \frac{2}{N} \sum_{\tau=1}^{N-1} (N-\tau)\, \hat{w}_\tau(K) , \tag{5.39}$$

where $\tau=|\alpha-\gamma|$. Adding and subtracting the freely jointed chain structure factor of eqn (5.29) yields,

$$\hat{w}(K) = \hat{w}_{FJC}(K) + \frac{2}{N} \sum_{\tau=2}^{N-1} (N-\tau) \left[\hat{w}_\tau(K) - \left(\frac{\sin(KL)}{KL}\right)^\tau\right] , \tag{5.40}$$

where $\hat{w}_{FJC}(K)$ is the freely jointed chain intramolecular structure factor.

In eqn (5.40) $\hat{w}_\tau(K)$ is given by,

$$\hat{w}_\tau(K) = B_\tau \left[\left(\frac{\sin(KL)}{KL} \right)^\tau - \hat{J}_\tau(K) \right], \tag{5.41}$$

where,

$$\hat{J}_\tau(K) = \frac{1}{\pi K} \int_0^\infty dy\, y \left(\frac{\sin(yL)}{yL} \right)^\tau \left[\frac{\sin(K-y)}{K-y} - \frac{\sin(K+y)}{K+y} \right], \tag{5.42}$$

and,

$$\hat{J}_\tau(0) = \frac{2}{\pi} \int_0^\infty dy \left(\frac{\sin(yL)}{yL} \right)^\tau \left[\frac{\sin(y)}{y} - \cos(y) \right]. \tag{5.43}$$

B_τ is given by eqn (5.36). The sum in eqn (5.40) must be evaluated numerically.

The PRISM equation can now be solved using the closure relations of eqns (5.23) and (5.24) in conjunction with the intramolecular correlation functions for the FJC or NFJC models to yield the site-site radial distribution function. Once the site-site radial distribution function has been obtained the free energy of the attractive perturbation can be calculated using eqn (5.5). Numerical differentiation of this free energy with respect to volume at constant temperature yields the contribution to the pressure made by the attractive perturbation. At this stage in the calculation all that remains to be determined is the contribution to the pressure made by the reference athermal system. A number of methods for determining the athermal contribution to the pressure from the PRISM theory will now be discussed.

5.4 Equations Of State Of Athermal Chain Systems From PRISM

In the PRISM theory, the structure factor $\hat{S}(k,\rho_m)$ is given by,

$$\hat{S}(k,\rho_m) = \frac{\hat{w}(k)}{1 - \rho_m \hat{w}(k)\, \hat{c}(k)}, \tag{5.44}$$

where ρ_m is the monomer density and k is the wave vector.

The equation of state may be calculated from the zero wave vector component of the structure factor using the compressibility equation [27],

$$\beta P = \int_0^{\rho_m} d\rho_m \, \hat{S}^{-1}(0,\rho_m) \, , \tag{5.45}$$

where $\beta=1/k_BT$, k_B is Boltzmann's constant, T is the temperature and P is the pressure. This method of calculation of the equation of state for a polymer is likely to be inaccurate as it requires an integration of the compressibility from zero density to the density of interest. The PRISM equation is known to be less accurate for polymers at low densities than at high densities, in much the same way as the RISM equation is known to be less accurate for low density molecular fluids [17]. The integration through the low density region is therefore likely to lead to poor accuracy in the calculation of the pressure using this route.

An alternative route to the pressure is based on a functional integration procedure [14] to obtain the free energy of the fluid. The free energy of the fluid is obtained by 'inflating' the polyatomic molecules from point masses of zero diameter to full hard core molecules. The resulting expression for the free energy of a homopolymer is given by,

$$\beta \frac{A-A_{id}}{V} = 2\pi \rho_m^2 d^3 \int_0^1 d\lambda \; \lambda^2 g^{(\lambda)}(\lambda d^+) \, , \tag{5.46}$$

where A is the free energy of the hard core fluid, A_{id} is the free energy of a fluid of noninteracting (ideal) polymer molecules. In eqn (5.46) $g^{(\lambda)}(\lambda d^+)$ is the contact value of g(r) for a polymer fluid containing hard core sites of diameter λd. The pressure is obtained from eqn (5.46) by performing a numerical differentiation of the free energy.

Another method of calculating the equation of state for bulk polymer fluids was introduced by Yethiraj *et. al.* [28] and is known as the wall-polymer-RISM theory or wall-PRISM theory. This method is based on calculating the density profile of the polymer fluid confined between hard walls. The value of the density calculated at contact with one of the walls can then be used to calculate the pressure of the bulk fluid. The density profiles within a pore and at contact with a wall calculated from the

wall-PRISM theory are readily comparable to the results of computer simulation. The predictions of the wall-PRISM equation for the density profiles of tangent hard-sphere 4-mer and 20-mer chains have been compared to the results of computer simulations. The theory was found to overestimate the density of sites at the walls at low chain densities and overestimate the density of sites at the walls for high chain densities.

In our work we have calculated the athermal chain contribution to the pressure using the wall-PRISM equation which will now be discussed in some detail.

5.4.1 The Wall-PRISM Equation

The wall-PRISM theory is a generalisation to polymers of the theories of Henderson *et. al.* [29] for the adsorption of hard spheres at a wall and the theories of Zhou and Stell [30,31] for the adsorption of hard spheres between two walls. The governing equations for chain fluids confined within small pores can be developed by considering a binary mixture of a monomer and a chain molecule. The monomer consists of a hard spherical core of radius R_1 surrounded by a spherical shell of inner radius R_2 and outer radius R_3. In the limit of the monomer mole fraction tending to zero and R_1, R_2 and $R_3 \rightarrow \infty$, a slitlike pore is created such that $R_2-R_1=H$, where H is the pore width. This process of 'growing the adsorbent' has been used in the study of hard sphere fluids confined within slitlike pores [30,31]. A schematic representation of the process of the monomer growing into the pore is shown in Figures 5.2a and 5.2b.

For a binary mixture of monomers, denoted by the subscript 1, and chains denoted by the subscript 2, the polymer-RISM equations may be written as [32],

$$\hat{h}_{11}(k) = \hat{c}_{11}(k) + \rho_1 \hat{c}_{11}(k)\,\hat{h}_{11}(k) + N\rho_2 \hat{c}_{12}(k)\,\hat{h}_{12}(k) , \tag{5.47}$$

$$\hat{h}_{12}(k) = \hat{w}(k)\,\hat{c}_{12}(k) + \rho_1 \hat{c}_{11}(k)\,\hat{h}_{21}(k) + N\rho_2 \hat{c}_{12}(k)\,\hat{h}_{22}(k) , \tag{5.48}$$

$$\hat{h}_{21}(k) = \hat{w}(k)\,\hat{c}_{21}(k) + \rho_1 \hat{w}(k)\,\hat{c}_{21}(k)\,\hat{h}_{11}(k) + N\rho_2 \hat{w}(k)\,\hat{c}_{22}(k)\,\hat{h}_{12}(k) , \tag{5.49}$$

$$\hat{h}_{22}(k) = \hat{w}(k)\,\hat{c}_{22}(k)\,\hat{w}(k) + \rho_1 \hat{w}(k)\,\hat{c}_{21}(k)\,\hat{h}_{21}(k) + N\rho_2 \hat{w}(k)\,\hat{c}_{22}(k)\,\hat{h}_{22}(k) . \tag{5.50}$$

In eqns (5.47)-(5.50), N is the number of monomers within each of the chains, ρ_1 and ρ_2 are the number densities of species 1 and 2 respectively and $h_{ij}(r)$ and $c_{ij}(r)$ are

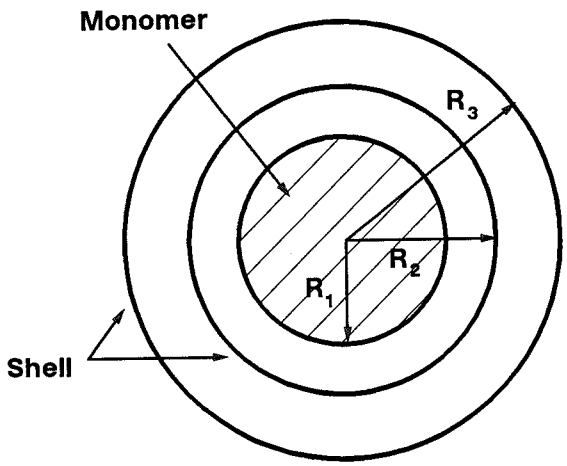

Figure 5.2a. The monomer of radius R_1 surrounded by a shell of inner radius R_2 and outer radius R_3 before the monomer has expanded to become the pore.

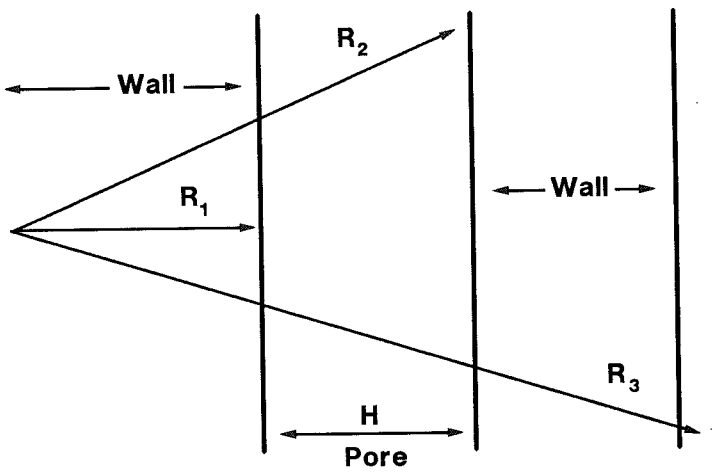

Figure 5.2b The monomer after letting R_1, R_2 and $R_3 \rightarrow \infty$. A pore has now formed of width H and the regions $r \leq R_1$ and $r \geq R_2$ constitute the regions within the walls.

the total and direct correlation functions between species i and j respectively. w(r) is the intramolecular structure factor for the chain fluid and the carets denote three-dimensional Fourier transforms defined by eqn (5.19).

Eqn (5.47) defines the correlation functions between the monomers which will eventually become the walls and therefore need not be considered. As we are only considering a single pore, that is $\rho_1 \to 0$, eqns (5.48)-(5.50) become,

$$\hat{h}_w(k) = \hat{w}(k)\,\hat{c}_w(k) + N\rho_c\hat{c}_w(k)\,\hat{h}_b(k) , \tag{5.51}$$

$$\hat{h}_w(k) = \hat{w}(k)\,\hat{c}_w(k) + N\rho_c\hat{w}(k)\,\hat{c}_b(k)\,\hat{h}_w(k) , \tag{5.52}$$

$$\hat{h}_b(k) = \hat{w}(k)\,\hat{c}_b(k)\,\hat{w}(k) + N\rho_c\hat{w}(k)\,\hat{c}_b(k)\,\hat{h}_b(k) , \tag{5.53}$$

where the subscript 12 has been replaced by the subscript w to denote wall-fluid and the subscript 22 has been replaced by b to denote the bulk fluid. In addition ρ_2 has been replaced by ρ_c to denote the chain number density and the notation $h_{12}=h_{21}=h_w$ and $c_{12}=c_{21}=c_w$ has been adopted. Eqn (5.53) is simply the polymer-RISM equation for bulk chains and may be solved independently of the other equations. Eqns (5.51) and (5.52) are equivalent and either of the two equations may be used to determine the wall-fluid correlations. In the work of Yethiraj *et. al.* [28] eqn (5.51) was used to determine the wall-fluid correlations and is referred to as the wall-PRISM equation.

At this point although we are using the subscript w to denote wall-fluid correlations, the monomer within the system still needs to be grown into the pore. Before doing so, it is convenient to rewrite Eqn (5.51) in **r** space,

$$h_w(r) = \int d\mathbf{r}' \left[w(\mathbf{r}') + N\rho_c h_b(\mathbf{r}') \right] c_w(|\mathbf{r} - \mathbf{r}'|) . \tag{5.54}$$

Converting eqn (5.54) to bipolar coordinates yields,

$$h_w(r) = \frac{2\pi}{r} \int_0^\infty t\,dt \left[w(t) + N\rho_c h_b(t) \right] \int_{|r-t|}^{r+t} y\,c_w(y)\,dy , \tag{5.55}$$

where t and y are dummy variables corresponding to the distances between two monomers and the wall and a monomer respectively. The origin of the coordinates of the system is now shifted so that it is exactly in between the outer surface of the

spherical core and the inner surface of the spherical shell. We define new variables z and s as,

$$z = r - \left(R_1 + \frac{H}{2} \right) , \tag{5.56}$$

$$s = y - \left(R_1 + \frac{H}{2} \right) , \tag{5.57}$$

where H is the pore width. We also now define the functions,

$$c_w^s(s) \equiv c_w(y) , \tag{5.58}$$

$$h_w^s(z) \equiv h_w(r) . \tag{5.59}$$

With the above definitions and growing the monomer into the pore (ie. $R_1 \rightarrow \infty$), eqn (5.55) reduces to,

$$h_w^s(z) = 2\pi \int_0^\infty t\, dt \left[w(t) + N\rho_c h_b(t) \right] \int_{|z-t|}^{z+t} c_w^s(s)\, ds . \tag{5.60}$$

The wall-fluid correlation functions h_w^s and c_w^s are now functions of only one coordinate, z, which is the distance from the centre of the slitlike pore in the direction perpendicular to the walls. The functions $h_w^s(z)$ and $c_w^s(z)$ do not tend to zero as z tends to infinity. Rather, in this limit [28],

$$\begin{aligned} h_w^s(z) &\rightarrow -1 \\ c_w^s(z) &\rightarrow \text{constant} . \end{aligned} \tag{5.61}$$

It is more convenient to deal with functions which tend to zero as z tends to infinity, we replace the functions $h_w^s(z)$ and $c_w^s(z)$ with the functions,

$$g_w(z) \equiv 1 + h_w^s(z) , \tag{5.62}$$

$$C_p(z) \equiv c_w^s(r) + a_1 , \tag{5.63}$$

where,

$$a_1 = - \lim_{z \to \infty} c_w^s(z) \ , \tag{5.64}$$

and has to be determined. With h_w^s and c_w^s replaced by g_w and C_p respectively, eqn (5.60) may be written as,

$$\begin{aligned} g_w(z) = 1 - \left[\hat{w}(0) + N\rho_c \hat{h}_b(0) \right] a_1 \\ + 2\pi \int_0^\infty t\,dt \left[w(t) + N\rho_c h_b(t) \right] \int_{z-t}^{z+t} C_p(y)\,dy \ . \end{aligned} \tag{5.65}$$

In the limit of $z \to \pm\infty$, the last term in eqn (5.65) vanishes as a result of the definition of $C_p(z)$ (eqn (5.63)) and $g_w(z)=0$ and we find that,

$$a_1 = \frac{1}{\left[\hat{w}(0) + N\rho_c \hat{h}_b(0) \right]} \ . \tag{5.66}$$

Substitution of a_1 into eqn (5.65) leads to,

$$g_w(z) = 2\pi \int_0^\infty t\,dt \left[w(t) + N\rho_c h_b(t) \right] \int_{z-t}^{z+t} C_p(y)\,dy \ . \tag{5.67}$$

Eqn (5.67) can be written more compactly in Fourier space, leading to the following expression,

$$\tilde{g}_w(k) = \left[\hat{w}(k) + N\rho \hat{h}_b(k) \right] \tilde{C}_p(k) \ . \tag{5.68}$$

In eqn (5.68) the tildes denote one-dimensional Fourier transforms defined by,

$$\tilde{f}(k) = \int_{-\infty}^{\infty} f(z)\, e^{ikz}\, dz \ . \tag{5.69}$$

Solution of the wall-PRISM equation with one of the expressions for the intramolecular structure factor w(r), requires some additional pieces of information. An expression for the bulk fluid-fluid correlations $h_b(r)$ is required and a closure relation is needed between $c_w(z)$ and $h_w(z)$. The bulk fluid total correlation function $h_b(r)$ is obtained by solving the PRISM equation of eqn (5.21) using the closure relations for

$h_b(r)$ and $c_b(r)$ given by eqns (5.23) and (5.24). The closure relations chosen for $h_w(z)$ and $c_w(z)$ are,

$$g_w(z) = 0, \quad |z| > \frac{H}{2}, \tag{5.70}$$

$$c_w^s(z) = 0, \quad |z| \leq \frac{H}{2}, \tag{5.71}$$

where for a slitlike pore of width H, $|H/2|$ corresponds to the region outside the pore and therefore inside the walls (the origin is in the centre of the pore). Eqn (5.70) is an exact statement of the hard core condition since the walls are impenetrable by the centres of the sites within the chain. Eqn (5.71) is an approximation and is an analogue of the Percus-Yevick closure for hard spheres where the direct correlation function is assumed to be zero outside the hard core.

For the purposes of numerically solving the wall-PRISM equation it is useful to rewrite eqn (5.68) in terms of the function $\tilde{\gamma}_w(k)$,

$$\tilde{\gamma}_w(k) = \tilde{g}_w(k) - \tilde{C}_p(k), \tag{5.72}$$

$$= \left[\hat{w}(k) + N\rho_c \hat{h}_b(k) - 1 \right] \tilde{C}_p(k), \tag{5.73}$$

$$= \left[\frac{\hat{w}(k)}{1 - N\rho_c \hat{w}(k)\hat{c}_b(k)} - 1 \right] \tilde{C}_p(k). \tag{5.74}$$

Eqn (5.74) is solved by a standard Piccard iteration technique [33] using the fast Fourier transform technique as follows.

1) Using the chosen approximation for $\hat{w}(k)$ and the closures on h_B and c_B of eqns (5.23) and (5.24), the PRISM equation is solved in the bulk using the method of Gillan [34].

2) An initial guess is made for the function $\gamma_w(z)$. The function $C_p(z)$ is then calculated using the PY closure,

$$C_p(z) = -\gamma_w(z), \qquad |z| > H/2 , \tag{5.75}$$

$$C_p(z) = a_1 , \qquad |z| < H/2 . \tag{5.76}$$

3) $\tilde{C}_p(k)$ is calculated using the fast Fourier transform algorithm.

4) A new estimate for $\gamma_w(z)$ is obtained by calculating $\tilde{\gamma}_w(k)$ via eqn (5.74).

5) Finally $\gamma_w(z)$ is calculated using the inverse fast Fourier transform.

The iteration process of steps 3-5 are continued until convergence is obtained. In the work that we have carried out with the wall-PRISM equation, we have found that it is not always possible to find stable, convergent solutions to the equation using the Piccard iteration scheme described above. This particular problem was overcome by mixing successive approximations to $\gamma(r)$ before they were used in the next level of iteration. This mixing of successive approximations to a given function within a Piccard iteration scheme has been used in the solution of integral equation theories for simple liquids, such as the Ornstein-Zernike equation [17].

Once the wall-particle correlation function $g_w(z)$ has been obtained from the wall-PRISM equation, it is possible to calculate not only the chain density within the pore, but also the pressure of the corresponding bulk fluid. The relationship between the pressure of a monatomic fluid and the density of the fluid in contact with a hard wall has been known for some time [35]. Consider a monatomic fluid in the presence of a hard wall defined as,

$$u(z) = \infty, \quad z \le 0 , \tag{5.77}$$

$$u(z) = 0, \quad z > 0 , \tag{5.78}$$

and let $\rho(z)$ denote the particle density at a distance z from the wall. The particles at the wall are decoupled and revert to ideal gas behaviour [35], hence,

$$\rho(0) = \frac{P}{k_B T} , \tag{5.79}$$

regardless of the intermolecular potential. It is important to note that whilst the fluid is anisotropic close to the wall, the value $\rho(0)$ yields through eqn (5.79) the bulk pressure. The reference bulk fluid can be identified as the fluid recovered when the wall-fluid potentials are zero. In this limit $g_w(z)=1$ for all z and the density profile $\rho(z)\equiv\rho_b g_w(z)$ is uniform and equal to ρ_b, the bulk density. Therefore the density of the reference homogeneous bulk phase is ρ_b, not the average density of the sites within the pore. In simulations employing the hard wall contact density for the determination of the bulk pressure, the bulk density ρ_b can be identified as the density in the centre of the pore.

Dickman *et. al.* [16] pointed out that in an analogous way, the pressure of a chain fluid can be calculated from the density of chain sites in contact with a hard wall. Once the wall-chain correlation function $g_w(z)$ has been obtained from the wall-PRISM equation, the density profile of the chains in the pore, $\rho(z)$, can be calculated from using the relation,

$$\rho(z) = \rho_b\, g_w(z) \ . \tag{5.80}$$

In eqn (5.80), ρ_b can be identified as the density of chain sites in the bulk fluid. The bulk pressure is then related to the density of chain sites at the wall via the relation,

$$\beta P = \rho(0) \ . \tag{5.81}$$

where $\rho(0)$ denotes the monomer density at the wall.

We now have sufficient information to calculate the bulk fluid correlations for polymer chains using the PRISM equation. The density profiles for chains confined between hard walls can now also be calculated from the wall-PRISM theory and the pressure of the bulk fluid obtained from the density of chain sites at contact with the wall.

In order to test the accuracy of the equations of state obtained from the wall-PRISM equation, it is necessary to be able to calculate the equation of state for athermal chains from simulations. A number of the computational methods available to do so will now be discussed.

5.5 Equations Of State For Athermal Chains From Simulation

Calculation of the equation of state for a fluid of atoms or molecules interacting via soft potentials such as the Lennard-Jones potential is relatively straightforward. Monte Carlo simulations can be performed in the canonical or grand canonical ensemble and the pressure calculated using the virial equation [36] introduced in section 1.2. Monte Carlo simulations can also be performed in the isothermal-isobaric ensemble introduced by Wood [37], where the pressure is an input parameter to the simulation. Alternatively molecular dynamics simulations can be performed in the microcanonical ensemble and again the pressure can be calculated from the virial theorem. For monatomic systems of hard spheres, the equation of state can be calculated from the contact value of the radial distribution function using the relation [17],

$$\left(\frac{\beta P}{\rho}\right)_{HS} = 1 + 4\eta g(\sigma) \ . \tag{5.82}$$

In eqn (5.82) η is the packing fraction for the hard spheres, σ is the hard sphere diameter and $g(\sigma)$ is the value of the radial distribution function at contact. As in the case of soft potentials, isothermal-isobaric ensemble simulations can be performed with the hard sphere potential to obtain the equation of state. At present isothermal-isobaric simulations have not been attempted with athermal chain systems.

As for monatomic systems, the equation of state for hard sphere chains can be calculated from the contact value of the radial distribution function [38]. This is achieved by using the superposition approximation of eqn (5.3) in the virial equation, eqn (5.1) and making use of the following identity for hard spheres,

$$\frac{du_{\alpha\gamma}(r)}{dr}\, g_{\alpha\gamma}(r) = -\frac{1}{\beta}\, \delta(r-\sigma)\, g_{\alpha\gamma}(\sigma) \ . \tag{5.83}$$

The virial equation of eqn (5.1) can now be written as,

$$\frac{\beta P}{\rho} = 1 + \frac{2\pi}{3} N \rho_m \sigma^3 g(\sigma) + R_3 \ . \tag{5.84}$$

The term R_3 now has the form,

$$R_3 = \frac{\rho}{3(N-1)} \sum_{\alpha=1}^{N} \sum_{\gamma=1}^{N} \sum_{\lambda=1}^{N} \int \mathbf{dr}\, \delta(r-\sigma)\, g_{\alpha\gamma}(\sigma) \times \int \mathbf{dr'}\, \hat{\mathbf{r}}.\mathbf{r'}\, w_{\alpha\lambda}(r')\, g_{\lambda\gamma}(|\mathbf{r}+\mathbf{r'}|). \tag{5.85}$$

As pointed out in section 5.1 the superposition approximation of eqn (5.3) is known to be a poor approximation and hence the accuracy of the pressures calculated via eqn (5.84) are likely to be of poor accuracy. In addition, the measurement of the contact value of the radial distribution function $g(\sigma)$ during a computer simulation would be time consuming and make the equations of state for hard sphere chains expensive to calculate.

Dickman and Hall introduced a method for calculating the equation of state of athermal chain molecules based on the trial insertion of a chain molecule into the simulation cell [2]. The pressure of the chain fluid can be related to the probability of a successful chain insertion into the system, yielding the expression,

$$P^*(\eta,N,\beta) = \frac{\eta}{v_N}[1 - \ln p(\eta,N,\beta)] + \frac{1}{v_N}\int_0^{\eta} d\eta'\, \ln p(\eta',N,\beta)\ . \tag{5.86}$$

In eqn (5.86) $p(\eta,N,\beta)$ is the probability of successfully inserting an N-mer chain into a fluid of N-mers at a packing fraction of η, v_N is the volume of an N-mer and $P^*=\beta P$ where P is the pressure. The integration in eqn (5.86) is performed numerically. Using eqn (5.86) Dickman and Hall calculated the equations of state for 5-mer tangent hard-disks and 4-mer tangent hard-sphere chain molecules. The method suffers from the drawback that as the density of the fluid rises, or the length of the chains grows, the probability of insertion of a chain into the simulation cell becomes small and it becomes difficult to obtain reliable estimates of the pressure.

In this work we have calculated the pressure for our athermal alkanes by performing simulations of the alkane systems between hard walls. The pressure of the bulk fluid was calculated from the density of chain sites at contact with the wall using eqn (5.81). This computer simulation method for the calculation of the equation of state of athermal chain systems is conceptually simple, easy to implement and algorithmically efficient. In addition, as we wished to calculate the pressure of the alkane fluid from the wall-

PRISM equation the simulation results would provide a direct test of the accuracy of the wall-PRISM theory in the prediction of the density profiles between the walls and the pressure calculated from the density profile at contact with the wall.

In chapter 6 the results of our simulations with athermal butane, heptane and decane will be presented, both between walls and in the bulk. The results of the simulations will be compared to the PRISM theory predictions for the intermolecular site-site radial distribution function and the density profiles calculated within the pore. In addition the equations of state obtained for these molecules by simulation will be compared to the results of the wall-PRISM theory.

5.6 References

[1] K.C. Chao and R.L. Robinson, "Equations of state: Theories and applications", American chemical society, Washington, D.C., (1987).

[2] R. Dickman and C.K. Hall, "Equation of state for chain molecules - continuous space analog of Flory theory", J. Chem. Phys., **85**, 4108-4115, (1986).

[3] K.G. Honnell and C.K. Hall, "A new equation of state for athermal chains", J. Chem. Phys., **90**, 1841-1855, (1989).

[4] A. Yethiraj and C.K. Hall, "Square-well chains: Bulk equation of state using perturbation theory and Monte Carlo simulations of the bulk pressure and of the density profiles near walls", J. Chem. Phys., **95**, 1999-2005, (1991).

[5] K.S. Schweizer and J.G. Curro, "Integral-equation theory of the structure of polymer melts", Phys. Rev. Lett, **58**, 246-249, (1987).

[6] J.G. Curro and K.S. Schweizer, "Theory of polymer melts - an integral-equation approach", Macromolecules, **20**, 1928-1934, (1987).

[7] K.S. Schweizer and J.G. Curro, "Integral equation theory of polymer melts-density fluctuations, static structure factor, and comparison with incompressible and continuum-limit models", Macromolecules, **21**, 3082-3087, (1988).

[8] J.G. Curro and K.S. Schweizer, "Integral-equation theory for compressible polymer alloys - Thermodynamics, scattering and miscibility of gaussian chains", Macromolecules, **24**, 6737-6747, (1991).

[9] K.S. Schweizer and J.G. Curro, "Analytic reference interaction site model - mean spherical approximation - theory of flexible polymer blends - effects of spatial and fractal dimensions", J. Chem. Phys., **94**, 3986-4000, (1991).

[10] J.G. Curro, K.S. Schweizer, G.S. Grest and K. Kremer, "A comparison between integral-equation theory and molecular dynamics simulations of dense, flexible polymer liquids", J. Chem. Phys., **91**, 1357-1364, (1989).

[11] A. Yethiraj and C.K. Hall, "Monte-Carlo simulations and integral-equation theory for microscopic correlations in polymeric fluids", J. Chem. Phys., **96**, 797-807, (1992).

[12] K.S. Schweizer and J.G. Curro, "Equation of state of polymer melts: General formulation of a microscopic integral equation theory", J. Chem. Phys. 3342-3349, (1988); K.S. Schweizer and J.G. Curro, "Equation of state of polymer melts: Numerical results for athermal freely jointed chain fluids", J. Chem. Phys., **89**, 3350-3362, (1988).

[13] A. Yethiraj, C.K. Hall and K.G. Honnell, "Site-site correlations in short chain fluids", J. Chem. Phys., **93**, 4453-4461, (1990).

[14] A. Yethiraj, J.G. Curro, K.S. Schweizer and J.D. McCoy, "Microscopic equations of state of polyethylene: Hard-chain contribution to the pressure", J. Chem. Phys., **98**, 1635-1646, (1993).

[15] J.D. Curro, A. Yethiraj, K.S. Schweizer, J.D. McCoy and K.G. Honnell, "Microscopic equations-of-state for hydrocarbon fluids: Effect of attractions and comparison with polyethylene experiments", Macromolecules, **26**, 2655-2662, (1993).

[16] R. Dickman and C.K. Hall, "High density Monte Carlo simulations of chain molecules: Bulk equations of state and density profile near walls", J. Chem. Phys., **89**, 3168-3174, (1988).

[17] J.P. Hansen and I.R. McDonald, "Theory of simple liquids", 2nd Edn, Academic press, (1990).

[18] J.A. Barker and D. Henderson, "Perturbation theory and equation of state for fluids. II. A successful theory of liquids", J. Chem. Phys., **47**, 4714-4721, (1967).

[19] H.C. Andersen, D. Chandler and J.D. Weeks, "Relationship between the hard-sphere fluid and fluids with realistic repulsive forces", Phys. Rev. A., **4**, 1597-1607, (1971).

[20] J.G. Curro, "Computer simulation os multiple chain systems - Equation of state of hard sphere chains", J. Chem. Phys., **64**, 2496-2500, (1976).

[21] P.J. Flory, "Statistical thermodynamics of semi-flexible chain molecules", Proc. Roy. Soc. London, Ser. A, **234**, 60-73, (1956).

[22] D. N. Theodorou and V.W. Suter, "Detailed molecular-structure of a vinyl polymer glass", Macromolecules, **18**, 1467-1478, (1985).

[23] D.G.H. Ballard, G.D. Wignall and J. Schelton, "Measurement of molecular dimensions of polystyrene chains in the bulk polymer by low angle neutron scattering", Eur. Polym., **9**, 965-969, (1973).

[24] H. Hayashi, P.J. Flory and G.D. Wignall, "Configuration of polyisobutylene chain according to neutron and x-ray scattering", Macromolecules, **16**, 1328-1335, (1983).

[25] H. Yamakawa, "Modern theory of polymer solutions", Harper and Row, New York, (1971).

[26] K.S. Schweizer and J.G. Curro, "Integral equation theory of polymer melts: Intramolecular structure, local order and the correlation hole", Macromolecules, **21**, 3070-3081, (1988).

[27] K.S. Schweizer and J.G. Curro, "Equation of state of polymer melts - general formulation of a microscopic integral-equation theory", J. Chem. Phys., **89**, 3342-3349, (1988).

[28] A. Yethiraj and C.K. Hall, "Integral equation theory for the adsorption of chain fluids in slitlike pores", J. Chem. Phys., **95**, 3749-3755, (1991).

[29] D. Henderson, F.F. Abraham and J.A. Barker, "The Ornstein-Zernike equation for a fluid in contact with a surface", Mol. Phys., **31**, 1291-1295, (1976).

[30] Y. Zhou and G. Stell, "Fluids inside a pore - an integral-equation approach. I. General formalism and hard spheres inside spherical and slit pores", Mol. Phys., **66**, 767-789, (1989).

[31] Y. Zhou and G. Stell, "Fluids inside a pore - an integral equation approach. II. Cylindrical pores", Mol. Phys., **66**, 791-796, (1989).

[32] K.S. Schweizer and J.G. Curro, "Integral equation theory of the structure and thermodynamics of polymer blends", J. Chem. Phys., **91**, 5059-5081, (1989).

[33] W.H. Press, S.A. Teukolsky, W.T. Vetterling and B.P. Flannery, "Numerical recipes. The art of scientific computing", Cambridge University Press, 2nd Edition, (1992).

[34] M.J. Gillan, "A new method of solving the liquid-structure integral equations", Mol. Phys., **38**, 1781-1794, (1979).

[35] J.K. Percus, "Model for density variation at a fluid surface", J. Stat. Phys., **15**, 423-435, (1976).

[36] M.P. Allen and D.J. Tildesley, "Computer simulation of liquids", Oxford science publications, (1987).

[37] W.W. Wood, "Monte Carlo calculations for hard disks in the isothermal-isobaric ensemble", J. Chem. Phys., **48**, 415-434, (1968).

[38] K.G. Honnell, C.K. Hall and R. Dickman, "On the pressure equation for chain molecules", J. Chem. Phys., **87**, 664-674, (1987).

6. Athermal Alkane Systems

In this chapter we present the results of our simulations with athermal alkane chains between walls and in the bulk. The results of our simulations are compared to the PRISM theory for the intermolecular radial distribution function and the wall-PRISM theory for the density profiles within pores and the calculated equations of state for the athermal alkane systems.

The main aim of the work which we have performed was to test the accuracy of the PRISM theory and the wall-PRISM equation for athermal alkane systems. We recall that it is necessary to have available a single chain structure factor, $\hat{w}(k)$, to solve the PRISM equation. We have discussed in section 5.3.1 two models for the intramolecular structure factor, the FJC and NFJC models. However both of these models are only approximate representations of the single chain structure factor of flexible polymer chains. The presence of the torsional potential and the fixed bond angle constraint within alkane chains are not taken into account in the FJC and NFJC models. If these models were used in the PRISM theory, it would not be possible to determine whether any shortcomings in the radial distribution functions calculated by the PRISM theory were due to inherent weaknesses in the theory itself or in the approximate representations used for the alkane chain intramolecular structure. In addition the density profiles calculated with the wall-PRISM equation require the results provided by the PRISM theory as input to the equation. Any approximations used in the intramolecular structure factor for the alkane chains in the PRISM theory might also therefore feed through into the predicted density profiles. Once again this would make it difficult to determine whether differences between the simulation data and the wall-PRISM equation were due to any inherent weaknesses in the wall-PRISM equation or in the approximate models used for the alkane intramolecular structure. To ensure that the PRISM theory itself was being tested rather than one of the approximate inputs to the theory, we calculated the intramolecular structure factor for the alkane chains in our simulations. This enabled us to use essentially exact single chain structure factors as input to the PRISM theory. The method used to calculate the single chain structure factor, $\hat{w}(k)$, from our simulations is described in section 6.3.

In section 6.1 the potential model that we have used for the alkane systems is

described. This is followed in sections 6.2 and 6.3 by an account of the simulations performed. Sections 6.4, 6.5 and 6.6 contain our results for the density profiles between walls, the equations of state for the athermal chains and the site-site radial distribution functions for the alkanes. Finally we present our conclusions in section 6.7.

6.1 The Potential Model for Alkanes

A widely used potential model in the simulation of alkane systems is that of Ryckaert and Bellemans [1]. In this model the interactions between methyl or methylene groups on different alkane chains is described by a Lennard-Jones potential with parameters σ=3.923Å and ε/k_B=72K. These Lennard-Jones interactions are also present for groups separated by more than three bonds within the same molecule. In addition to the Lennard-Jones potential the model contains a torsional potential acting between sites separated by three bond lengths within the same alkane chain. This torsional potential is given by,

$$\begin{aligned}\left(u_{tors}(\phi)/k_B\right)/K \;=\; & 1116 \;+\; 1462\cos\phi \;-\; 1578\cos^2\phi \\ & -\; 368\cos^3\phi \;+\; 3156\cos^4\phi \;-\; 3788\cos^5\phi,\end{aligned} \tag{6.1}$$

where ϕ is the torsional angle and $u_{tors}(\phi)$ is the torsional potential. The bond lengths and bond angles within the alkane chains are constrained to the values of 1.53Å and 109.47° respectively. The configurational energy, U_{conf}, of a system of N_{mol} alkane molecules containing N_s sites can therefore be expressed as,

$$U_{conf} \;=\; U_{inter}^{LJ} \;+\; U_{intra}^{LJ} \;+\; U_{tors} \;. \tag{6.2}$$

In eqn (6.2) U_{inter}^{LJ} and U_{intra}^{LJ} are the intermolecular and intramolecular Lennard-Jones contributions to the configurational energy and are given by,

$$U_{inter}^{LJ} \;=\; \sum_{i=1}^{N_{mol}-1} \sum_{j=i+1}^{N_{mol}} \sum_{\alpha=1}^{N_s} \sum_{\beta=1}^{N_s} u_{LJ}(r_{ij}^{\alpha\beta}) \;, \tag{6.3}$$

$$U_{intra}^{LJ} \;=\; \sum_{i=1}^{N_{mol}} \sum_{\alpha=1}^{N_s-4} \sum_{\beta=\alpha+4}^{N_s} u_{LJ}(r_{ii}^{\alpha\beta}) \;. \tag{6.4}$$

In eqns (6.3) and (6.4) i and j are molecular indices, and α and β are sites within the

specified molecules, $r_{ij}^{\alpha\beta}$ is the separation between sites α and β on molecules i and j and $r_{ii}^{\alpha\beta}$ is the intramolecular separation between sites α and β on molecule i. Finally the torsional contribution to the configurational energy is given by,

$$U_{tors} = \sum_{i=1}^{N_{mol}} \sum_{\alpha=1}^{N_{tors}} u_{tors}(\phi_{i\alpha}) \ , \tag{6.5}$$

where N_{tors} is the number of torsional angles within a given molecule and $\phi_{i\alpha}$ is the α^{th} torsional angle within molecule i.

In this work we wanted to perform simulations with athermal alkane chains. We therefore wished to replace the interchain Lennard-Jones potential contained within the Ryckaert and Bellemans potential with a hard-sphere interaction. In thermodynamic perturbation theory the hard-sphere diameter of the reference system can be chosen in a number of ways, depending on the method used in the division of the potential into attractive and repulsive parts. In section 5.2 two widely used divisions of the potential were described, the Barker-Henderson (BH) theory and the Weeks-Chandler-Andersen (WCA) theory. As already described in section 5.2, the hard core diameter defined in the BH theory is a function of the temperature of the simulation only, whereas in the WCA theory it is a function of both the temperature and density of the system. For simplicity we have chosen to define our hard core diameter using the Barker-Henderson approach. The hard core diameter is now a function of temperature only and can be obtained from equation (5.10). To obtain the hard core diameter from eqn (5.10), it is necessary to specify the temperature. We have chosen to use a temperature of 300K in the definition of our hard core diameter. Simulations of alkane systems including heptane and decane have previously been performed at this temperature with the Ryckaert and Bellemans potential representation for alkane chains [2]. The hard core diameter calculated from eqn (5.10) has the value d=3.663 Å. The choice of 300K used to define the hard core diameter in our athermal alkane simulations also serves to define the torsional angle distribution within the alkanes through eqn (6.1).

The hard walls used in our simulations were identical to those described in section 4.2 and are of the functional form of eqns (4.2) and (4.3). As for the simulations described in chapter 4, the walls were placed in the x-y plane, separated by a distance of $H\sigma$ along the z axis. The alkane chains in our simulations were moved using the

reptation algorithm.

6.2 Reptation Method For Alkane Chains

As already discussed in chapter 1, in conventional Monte Carlo NVT simulations, phase space trajectories are constructed such that the transition probabilities for the states m and n are given by eqns (1.39)-(1.41) of section 1.4.1. To implement the Metropolis solution to the transition matrix it is necessary to specify the matrix α, where α is the underlying stochastic matrix of the Markov chain. The matrix α is designed to take the system from a state m into a neighbouring state n with equal probability. This is implemented in a computer simulation by choosing a particle, displacing it from its current position $\mathbf{r}_m$ with equal probability to any point $\mathbf{r}_n$ within a cube R. The cube is centred on $\mathbf{r}_m$ and is of side $2\delta r_{max}$ where δr_{max} is the maximum allowed displacement of the particle in any direction. In a computer simulation there are a finite number of trial positions within the cube, N_R, and α is given by eqns (1.42) and (1.43) of section 1.4.1. For chain molecule systems employing the reptation algorithm discussed in chapter 3, the underlying stochastic matrix α is implemented as follows. A bead is removed from one end of the chain molecule, the tail, and placed in a random orientation on the other end of the chain, subject to bond length and angle constraints. This is now the new trial head position. However, for alkane chains this is not the most efficient way to proceed. One of the problems in applying this method to the simulation of alkane systems is the presence of the torsional potential. The torsional potential leads to high rejection ratios in the reptation method because trial moves often result in a new head position for the chain lying away from one of the gauche or trans configurations. This results in a trial move with a high torsional potential and thus also a high probability of rejection of the move. It is therefore much more efficient to use a biassed trial move which samples directly from the torsional distribution itself. Such a preferential sampling scheme for alkane systems was introduced by Almarza *et. al.* [3]. Preferential sampling techniques [4] can be implemented by using an extension of the Metropolis Monte Carlo method.

An extension of the Metropolis Monte Carlo method of the following form is used,

$$\pi_{mn} = \alpha_{mn} \qquad \alpha_{nm}\rho_n \geq \alpha_{mn}\rho_m \qquad m \neq n, \tag{6.6}$$

$$\pi_{mn} = \alpha_{mn}\left(\frac{\alpha_{nm}\rho_n}{\alpha_{mn}\rho_m}\right) \qquad \alpha_{nm}\rho_n < \alpha_{mn}\rho_m \qquad m \neq n, \tag{6.7}$$

$$\pi_{mm} = 1 - \sum_{n \neq m} \pi_{mn} \ . \tag{6.8}$$

In applying this method to the reptation algorithm for alkane systems a non-symmetric underlying stochastic matrix ($\alpha_{mn} \neq \alpha_{nm}$) is used. A trial move results in the removal of the tail bead with the loss of the associated torsional angle ϕ and the creation of a new trial head position with an associated torsional angle of ϕ^*. The stochastic matrix used to generate the trial move is [3],

$$\alpha_{mn} = \exp\left[-\beta u_{tor}(\phi^*) \right] , \tag{6.9}$$

ie. a new angle ϕ^* is chosen from the distribution $\exp(-\beta u_{tor}(\phi^*))$. The trial move is accepted with a probability given by,

$$\min\left[1, \frac{\alpha_{nm}\rho_n}{\alpha_{mn}\rho_m}\right] . \tag{6.10}$$

The ratio ρ_n/ρ_m can be expressed in terms of the Boltzmann factor of the energy difference between the two states,

$$\frac{\rho_n}{\rho_m} = \exp\left[-\beta(\delta U^{LJ}_{inter} + \delta U^{LJ}_{intra})\right] \frac{\exp\left[-\beta u_{tors}(\phi^*) \right]}{\exp\left[-\beta u_{tors}(\phi) \right]} , \tag{6.11}$$

and clearly,

$$\frac{\alpha_{nm}\rho_n}{\alpha_{mn}\rho_m} = \exp\left[-\beta(\delta U^{LJ}_{inter} + \delta U^{LJ}_{intra})\right] . \tag{6.12}$$

Substituting eqn (6.12) into eqn (6.10) gives the probability of acceptance of a trial move as,

$$\min\left[\ 1,\ \exp\left[-\beta(\delta U_{inter}^{LJ} + \delta U_{intra}^{LJ})\right]\ \right]. \qquad (6.13)$$

In the case of athermal alkane chains, the Lennard-Jones interactions in eqn (6.13) are replaced by hard-sphere interactions. This preferential sampling technique can be implemented in our simulations with athermal alkane chains as follows. A chain in the system is chosen at random and the tail bead removed from the chain. The bead now becomes the new head bead for the chain with a torsional angle chosen according to eqn (6.9). The attempted move is then accepted or rejected according to eqn (6.13).

6.3 Simulation Details

Simulations were performed with athermal butane, heptane and decane interacting through the potential described in section 6.1. Starting configurations were generated by placing the first bead in each of the alkane chains on a regular cubic lattice and placing the remainder of each of the chains in an all trans configuration. Starting configurations generated in this manner often contain a large number of overlaps between neighbouring chains. The overlaps were removed by moving each of the chains using the reptation algorithm. If the attempted move of a given chain resulted in an overlap then the move was immediately rejected. If the attempted move resulted in the removal of an overlap from the system then the move was accepted. After removing all of the overlaps from the system it was necessary to perform sufficient cycles to equilibrate the system. All the simulations performed with hard walls took place in a simulation cell of dimension 7σ along the x and y axes and with the hard walls separated by 15σ (where σ is the hard core diameter). Periodic boundary conditions were imposed in the x and y directions. A simulation cell of this size is sufficiently large that it is not possible for the alkane chains to interact with one another through the periodic boundaries. In addition, the walls are separated by a sufficient distance that as will be shown in section 6.4, an isotropic fluid is formed in the central part of the pore and lacks any significant density fluctuations.

The simulations can be conveniently divided up into cycles, which consist of an attempt to move each of the alkane chains in the system. The alkane chains were moved

in the simulations by the reptation algorithm of Almarza *et. al.* described in section 6.2. The parameters controlling the movement of the alkane chains were not adjusted during the course of a simulation and typically between 7 and 70% of the attempted moves were accepted, depending on the density of the simulation. For the simulations performed between the walls, typically $2x10^4$ equilibration and between $3x10^5$ and $2x10^6$ production cycles were performed in each of the simulations. This number of cycles was sufficient to obtain good convergence in the chain conformational properties such as the mean square radius of gyration defined by eqns (4.5)-(4.7) and to obtain symmetric density profiles in our simulation cell. Cell-linked lists [4] were implemented in our code to speed up the calculations.

The monomer density profiles of the alkane chains across the pore were recorded during the simulations by dividing the region between the walls into a number of equally sized bins. The density profiles were typically binned every 100 cycles. In analysing the resulting density profiles, we have made use of the symmetry of the simulation cells to combine the profiles in the left and right half of the cells in the z direction. The density profiles recorded in the simulations were extrapolated to contact with the wall. The monomer density at contact with the wall was then used to calculate the pressures for the athermal alkane chains using eqn (5.81). The pressures calculated from eqn (5.81) are the pressures for the corresponding bulk alkane fluids. The density of this bulk fluid was obtained by calculating the monomer density of the alkane fluid in the central 30% of the pore.

During our simulations we recorded the intramolecular correlations for beads separated by more than two bond lengths within the chains, ie.,

$$w_{nb}(R) = \frac{1}{N} \sum_{|i-j|>2} w_{ij}(R) \ , \qquad (6.14)$$

where the subscript "nb" stands for nonbonded and separated by more than two bond lengths and R is the reduced distance introduced in section 5.3.1 and defined by $R=r/\sigma$.

The single chain structure factor $\hat{w}(K)$ can then be calculated from [5],

$$\hat{w}(K) = 1 + 2\frac{N-1}{N}\frac{\sin(KL)}{KL} + 2\frac{N-2}{N}\frac{\sin(KL_2)}{KL_2} + \frac{4\pi}{K}\int_0^\infty R w_{nb}(R)\sin(KR)\,dR \ , \quad (6.15)$$

where, again as in section 5.3.1, K is the reduced distance $K=k\sigma$. The first three terms in eqn (6.15) are the exact expressions for the terms $\Sigma w_{i,i}/N$, $\Sigma w_{i,i+1}/N$ and $\Sigma w_{i,i+2}/N$ respectively. In the third term L_2 is the reduced distance between beads separated by two bond lengths. The reduced distance L_2 is defined by l_2/σ where l_2 is the distance between beads separated by two bond lengths. This distance is fixed in the Ryckaert and Bellemans representation of alkane chains by the bond angle and bond length constraints. The integral in the fourth term of eqn (6.15) is the Fourier transform of the intramolecular correlation function recorded during the course of a simulation and the integral is evaluated numerically once the simulation has finished.

In addition to the simulations performed between the hard walls, simulations were performed in the bulk with butane, heptane and decane to calculate the site-site intermolecular radial distribution function. Starting configurations were generated in the same way as for the systems placed between hard walls. Again, typically 10^4 equilibration cycles were required to remove overlaps from the systems and 2×10^4 production cycles were performed. The site-site intermolecular radial distribution functions were calculated during these simulations and binned every 100 cycles.

6.4 Density Profiles Between Walls

Simulations were performed with butane, heptane and decane between hard walls. As a test of our simulation method we have calculated the mean square radius of gyration from the single chain structure factor, w(r), calculated within our simulations. This can be achieved by using the relation [5],

$$S^2 = \frac{2\pi}{N}\int_0^\infty r^4 w(r)\,dr \ . \quad (6.16)$$

In eqn (6.16) S^2 is the mean square radius of gyration of the alkane chain with a single

chain structure factor of w(r). As mentioned previously we also calculated S^2 directly during the course of our simulations. A test of our simulation method is therefore to compare the values for the mean square radius of gyration calculated directly in our simulations and the mean square radius of gyration calculated indirectly via eqn (6.16). A comparison of the values calculated for the mean square radius of gyration for our simulations with decane between hard walls is given in Table 6.1. The errors reported in the simulation mean square radius of gyration were calculated by dividing the simulations up into a number of sub-averages of 10^4 cycles length and calculating one standard deviation in the mean of these blocks. As Table 6.1 demonstrates the mean square radii of gyration calculated via eqn (6.16) are in agreement with the values calculated in our simulations, to within the statistical error in our simulation data. In the simulations performed with butane and heptane the two different methods of calculating the mean square radius of gyration were always in agreement with one another to within the statistical errors in the data. The agreement between the mean square radii of gyration calculated by the two differing methods gives us confidence in the accuracy of our simulation data and also in the accuracy of the single chain structure factor w(r) calculated within our simulations.

In our work we have solved the wall-PRISM equation with single chain structure factors, $\hat{w}(K)$, given by the FJC and NFJC models and calculated from our simulation data. Figures 6.1-6.3 compare the single chain structure factors calculated for butane, heptane and decane with the FJC and NFJC models and the single chain structure factors calculated from simulation with these molecules. The comparisons between the various correlation functions are shown on a Kratky plot [6] where $K^2L^2\hat{w}(K)$ is plotted against KL, and L is the reduced bond length. The behaviour of $K^2L^2\hat{w}(K)$ can be divided into three regimes. The first of these is the small KL region which characterises the global dimensions of the chain. The remaining two regions are the intermediate KL region where $K^2L^2\hat{w}(K)\sim1$ and the large KL region where $\hat{w}(K)\sim1$. All the models for $\hat{w}(K)$ are expected to be accurate in the small and large KL regime [6].

Figure 6.1 shows that the FJC and NFJC models for butane are in very close agreement with one another. Both models give qualitatively reasonable representations of butane. Figure 6.2 shows that the FJC and NFJC models are now starting to differ

ρ_b^*	η^*	$\langle S_{sim}^2 \rangle$	S_{ind}^2
0.1041±0.0011	0.0594±0.0006	0.7848±0.0020	0.7845
0.4063±0.0037	0.2318±0.0021	0.7829±0.0008	0.7831
0.5981±0.0045	0.3413±0.0025	0.7822±0.0008	0.7823
0.7010±0.0056	0.4000±0.0031	0.7814±0.0006	0.7813
0.7897±0.0068	0.4506±0.0038	0.7809±0.0008	0.7803
0.8805±0.0079	0.5025±0.0045	0.7805±0.0009	0.7804
0.9814±0.0088	0.5601±0.0050	0.7799±0.0010	0.7800
1.0569±0.0084	0.6031±0.0047	0.7795±0.0013	0.7791
1.1570±0.0137	0.6603±0.0078	0.7791±0.0018	0.7778
1.2564±0.0185	0.7170±0.0105	0.7789±0.0030	0.7769
1.3338±0.0322	0.7612±0.0183	0.7774±0.0047	0.7755
1.3803±0.0339	0.7877±0.0193	0.7801±0.0050	0.7786

Table 6.1 A comparison between the mean square radius of gyration calculated during our simulations with decane $\langle S_{sim}^2 \rangle$ and the corresponding values calculated by the indirect method of eqn (6.16), S_{intl}^2 Also shown in the table are the monomer densities for the bulk fluids in the centres of the pores and the corresponding packing fractions for these bulk densities.

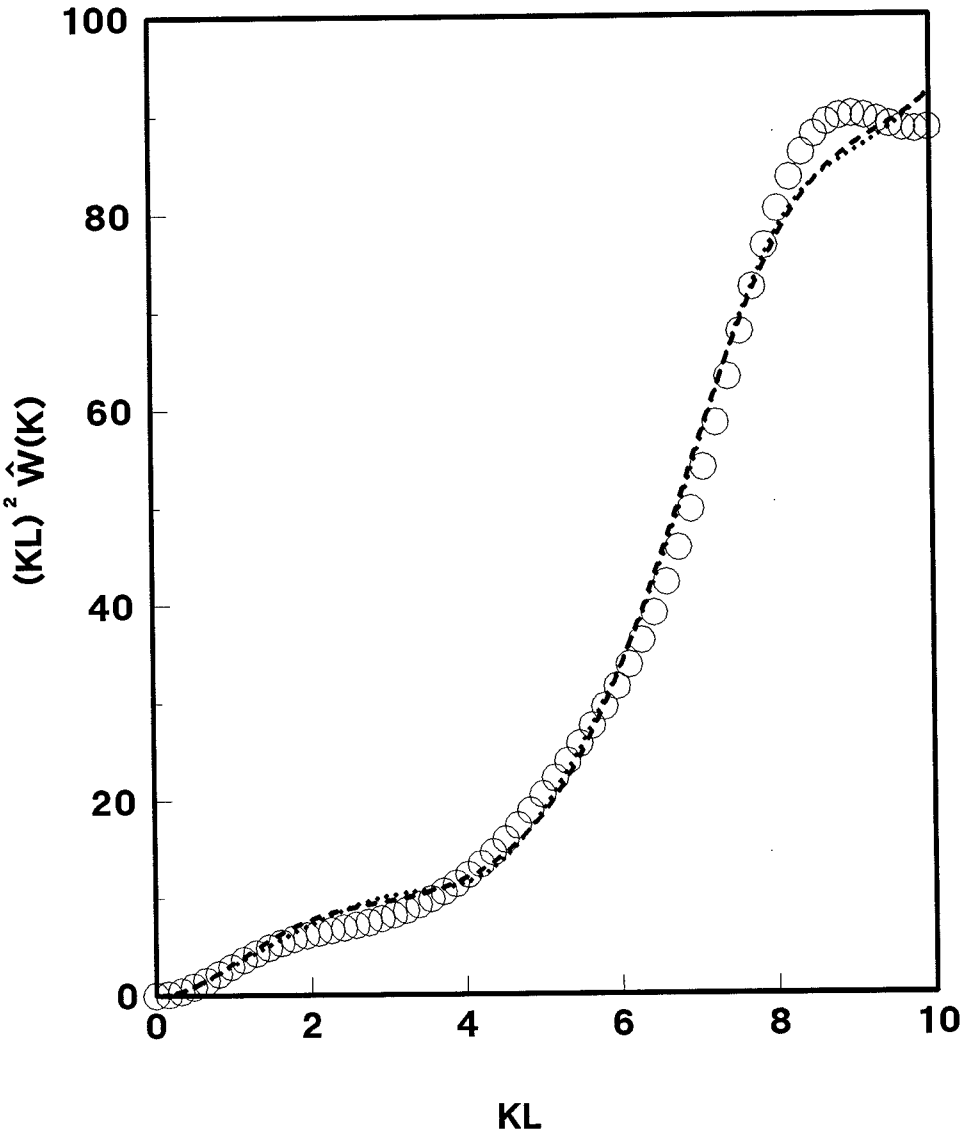

Figure 6.1 Comparison of theoretical predictions using the FJC model (dashed line) and the NFJC model (dotted line) with the simulation results (○) for the intramolecular structure factor, $\hat{w}(K)$, for butane at ρ_b^*=1.3736. The figure is plotted in Kratky form.

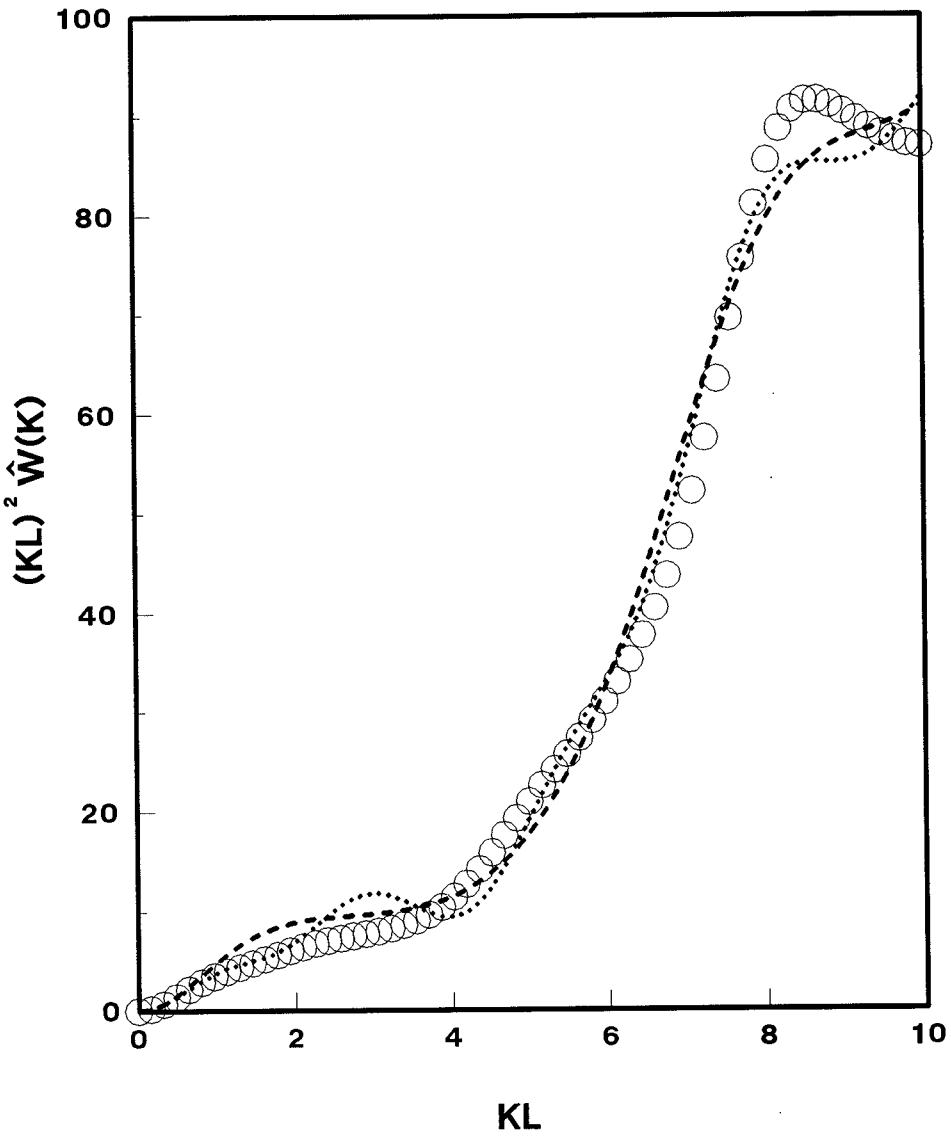

Figure 6.2 Comparison of theoretical predictions using the FJC model (dashed line) and the NFJC model (dotted line) with the simulation results (○) for the intramolecular structure factor, $\hat{w}(K)$, for heptane at ρ_b^*=1.3909. The figure is plotted in Kratky form.

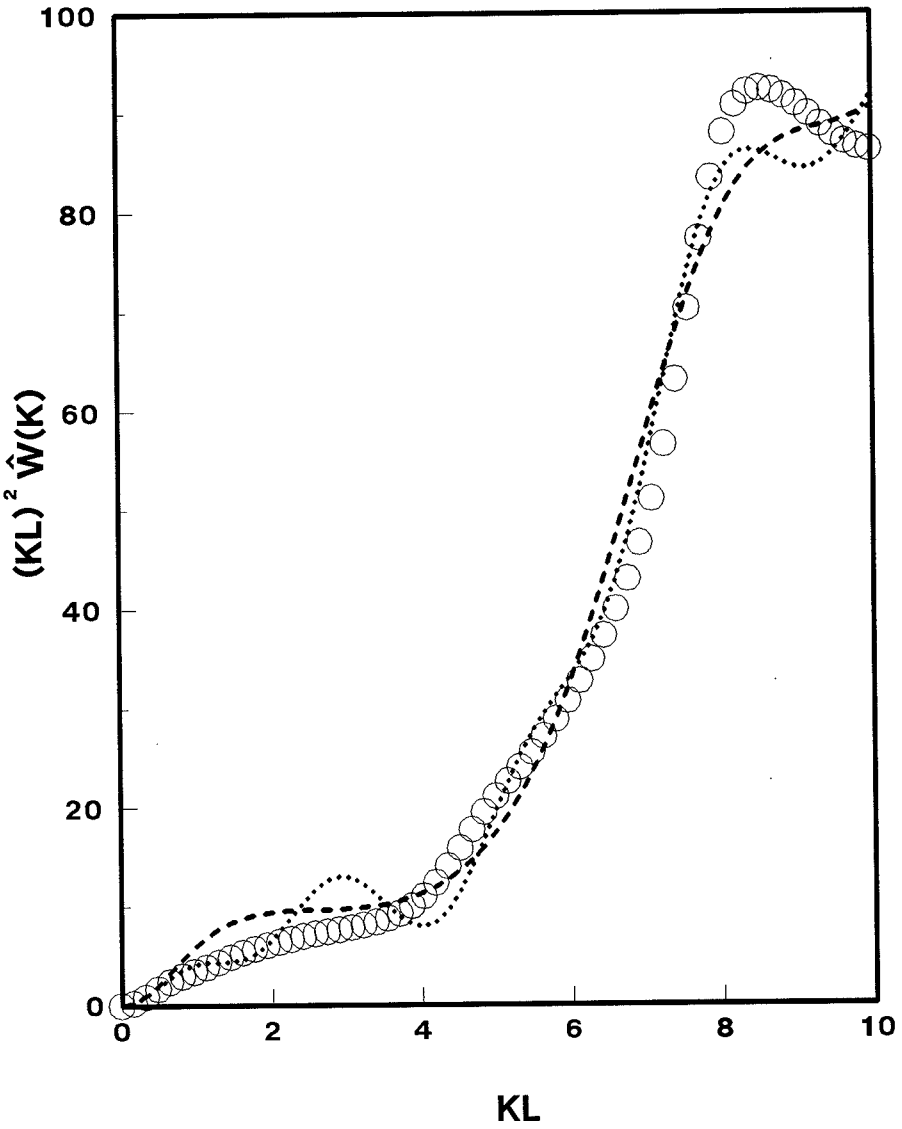

Figure 6.3 Comparison of theoretical predictions using the FJC model (dashed line) and the NFJC model (dotted line) with the simulation results (○) for the intramolecular structure factor, $\hat{w}(K)$, for decane at ρ_b^*=1.3803. The figure is plotted in Kratky form.

from one another. The agreement of these models with the simulation data is again at best only qualitative. To obtain a better understanding of the relationships of the various single chain structure factors to one another, we will now concentrate on the structure factors for decane shown in Figure 6.3.

Figure 6.3 shows that in the small KL regime the three different representations do tend to the same values. In the high KL regime ($KL \geq 10$) the three different representations also come into agreement with one another. For $5<KL<8$ both the FJC models and the NFJC models qualitatively mimic the structure factor recorded in our simulations. In the region $1<KL<4$ the agreement between the FJC and NFJC models and the simulation results is poor, with the FJC model predicting values for $K^2L^2\hat{w}(K)$ that are too large. The overestimation in $K^2L^2\hat{w}(K)$ by the FJC model in this region has been attributed to unphysical overlaps between non-bonded beads in the chain [5]. In the NFJC model these overlaps have been removed. This causes the $K^2L^2\hat{w}(K)$ curve to dip below the corresponding FJC curve in the region $KL \sim 4$. Since the areas under the curves are normalised, this dip in the NFJC curve in the region $KL \sim 4$ results in a higher estimate for $K^2L^2\hat{w}(K)$ than for the FJC model in the region $2<KL<4$. We can therefore conclude from Figure 6.3 that whilst both the FJC and NFJC models qualitatively capture some of the features of the single chain structure for decane, there are significant differences between the models and the simulation data.

The simulation values for $\hat{w}(K)$ presented in Figures 6.1-6.3 were recorded in our simulations in the central region of the pore. This function is required in eqn (5.74) in the solution of the wall-PRISM equation. One of the implicit assumptions made in the wall-PRISM equation is that $\hat{w}(K)$ is not affected by the presence of the walls. The simulations that we performed in chapter 4 demonstrated that the conformations of polymer chains were indeed affected by the presence of the walls. If $\hat{w}(K)$ were affected by the presence of the walls then it would be necessary to reformulate the wall-PRISM equation in such a way as to be able to determine the functions g(r) and w(r) self-consistently with the inclusion of any anisotropies in the chain conformation as a function of the distance from the wall. To determine whether the single chain structure factor, $\hat{w}(K)$, is affected by the presence of the walls, we recorded $\hat{w}(K)$ in the central part of the pore, representing the bulk fluid. $\hat{w}(K)$ was also recorded in the same simulations for chains whose centre of mass were within 0.25σ of the walls. The

comparisons between the various structure factors calculated in simulations of butane, heptane and decane are shown in Figures 6.4-6.6. These figures clearly demonstrate that $\hat{w}(K)$ is not in fact affected by the presence of the walls. This is attributable to the bond length and bond angle constraints within the alkane chains, along with the presence of the torsional potential. Figures 6.4-6.6 therefore demonstrate that it is only necessary to determine $\hat{w}(K)$ for the bulk fluid and in the remainder of the work which we will present, the simulation values for $\hat{w}(K)$ were calculated in the central regions of the pores.

In Figure 6.7 monomer density profiles are shown for butane simulations at bulk monomer densities of ρ_b^*=0.494, 1.048 and 1.336. These bulk densities correspond to packing fractions of 0.205, 0.436 and 0.556 respectively. Also displayed in Figure 6.7 are the density profiles obtained from the wall-PRISM equation with $\hat{w}(K)$ provided by the FJC and NFJC models along with the $\hat{w}(K)$ calculated from our simulation data. The uppermost of the three density profiles shows the whole of the region within the pore whilst the two remaining profiles concentrate on the anisotropic region close to the wall. At ρ_b^*=0.494 the predictions of the wall-PRISM theory with the various single chain structure factors are virtually indistinguishable from one another. The wall-PRISM predictions significantly overestimate the contact value of the density. The height of the peak in the density profile close to the wall is underestimated by the wall-PRISM theory although it is in approximately the correct position. The following trough predicted by theory is barely perceptible and is significantly closer to the wall than the simulation data. At a monomer density of ρ_b^*=1.048 the various models predict profiles that differ slightly close to the wall. All the models now underestimate the contact value of the density. The depth of the first trough is still underestimated by all the models although the position of the trough is in closer agreement with the simulation data than at the lower density. The following peak is also underestimated by the various models and is too close to the wall. Finally the monomer density profiles for butane with ρ_b^*=1.336 are shown in Figure 6.7. Once again the various models used with the wall-PRISM theory are all in close agreement with one another except close to the wall. The models all significantly underestimate the contact value of the density. The predictions for the position and depth of the first trough and the following peak are in reasonable agreement with the simulation data. A second weak trough and following peak have

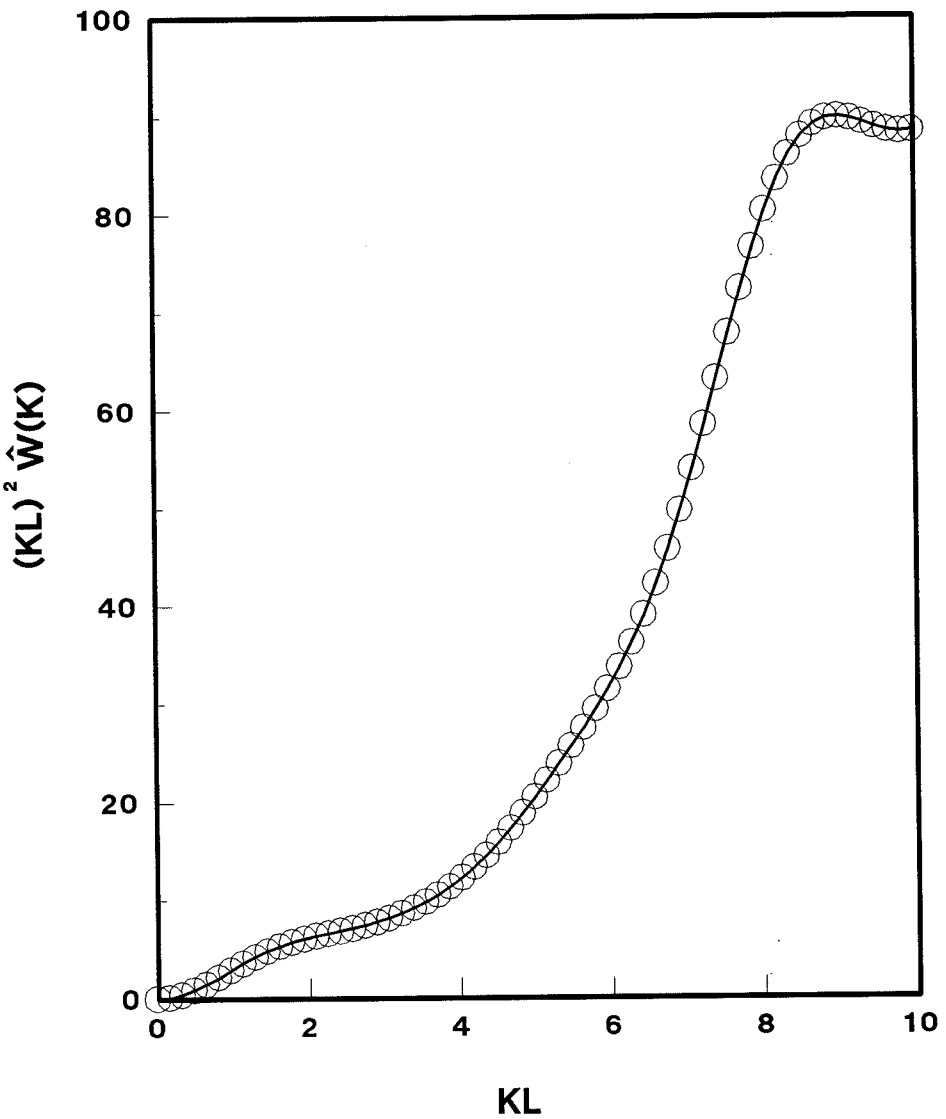

Figure 6.4 Comparison of the simulation results for the intramolecular structure factor, $\hat{w}(K)$, for butane at ρ_b^*=1.3736. The figure is plotted in Kratky form. $\hat{w}(K)$ values are presented for chains in the centre of the pore (line) and for chains whose centre of mass lie within 0.25σ of the walls (○).

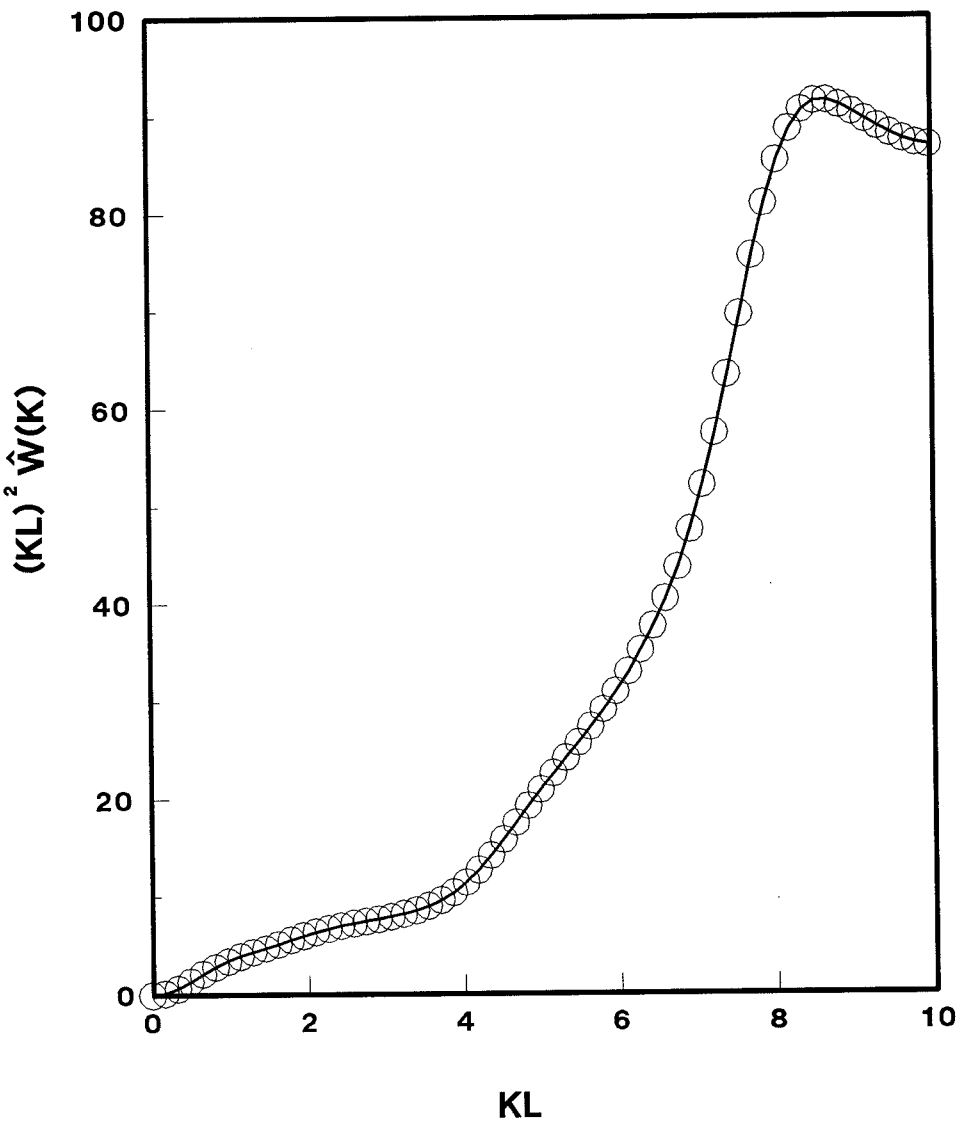

Figure 6.5 Comparison of the simulation results for the intramolecular structure factor, $\hat{w}(K)$, for heptane at $\rho_b^*=1.3909$. The figure is plotted in Kratky form. $\hat{w}(K)$ values are presented for chains in the centre of the pore (line) and for chains whose centre of mass lie within 0.25σ of the walls (○).

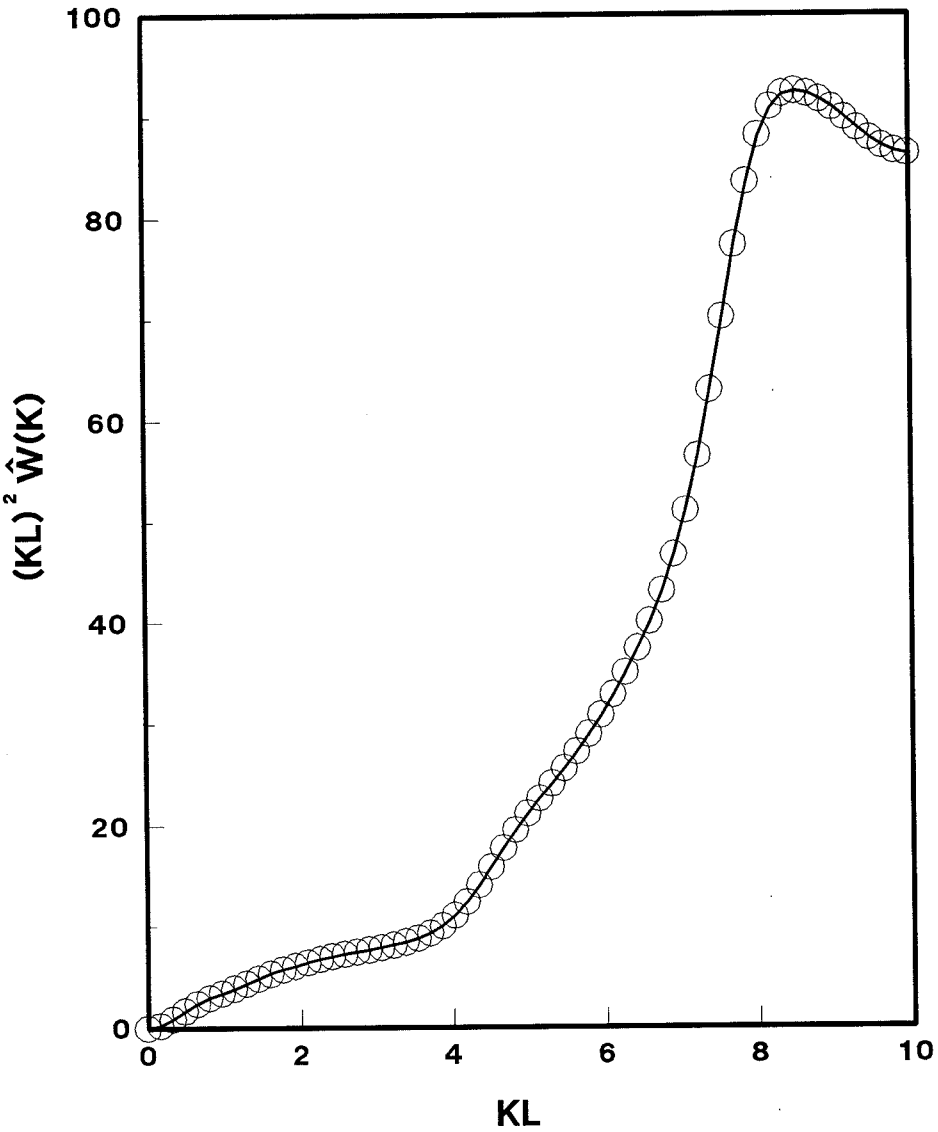

Figure 6.6 Comparison of the simulation results for the intramolecular structure factor, $\hat{w}(K)$, for decane at ρ_b^*=1.3803. The figure is plotted in Kratky form. $\hat{w}(K)$ values are presented for chains in the centre of the pore (line) and for chains whose centre of mass lie within 0.25σ of the walls (○).

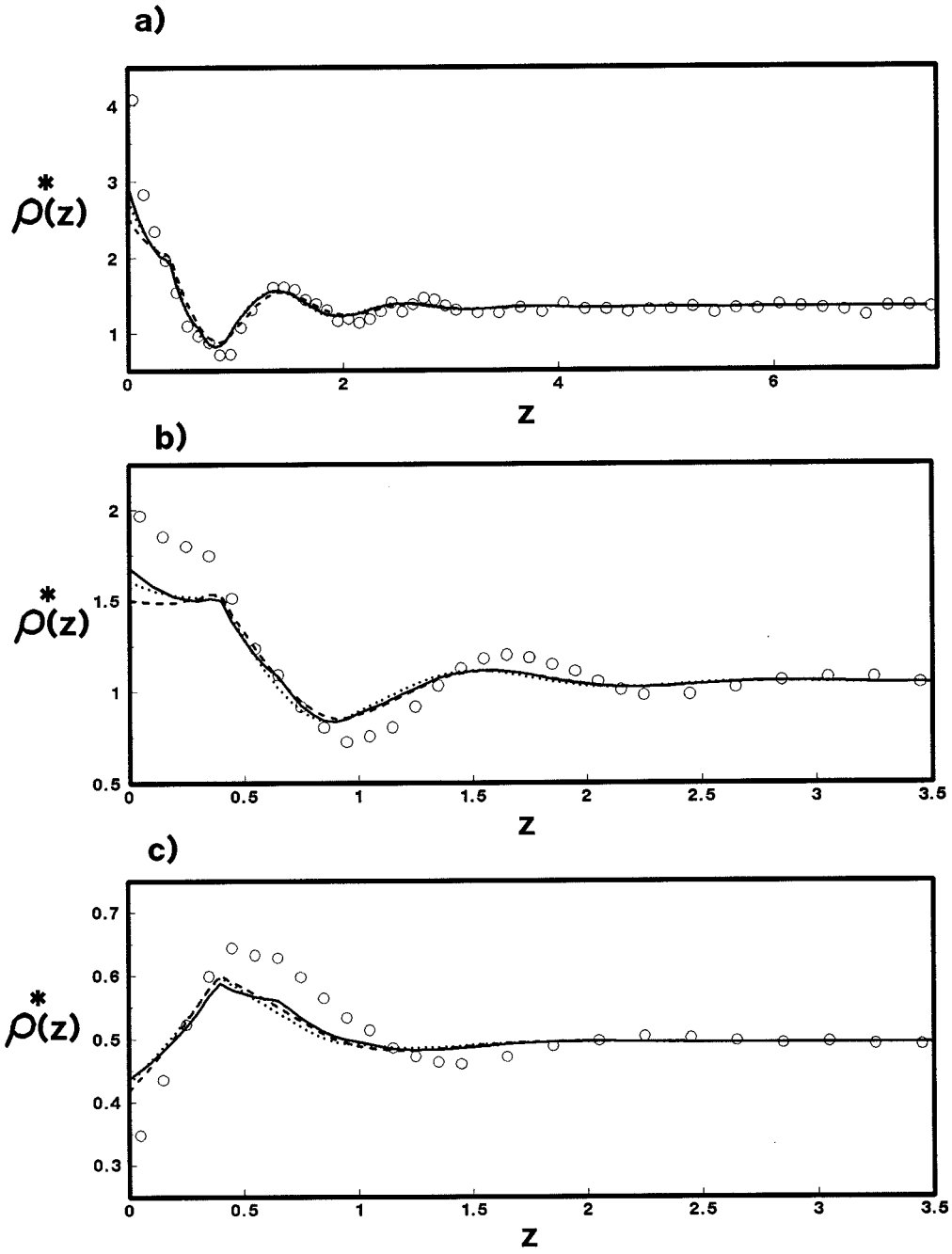

Figure 6.7 Monomer density profiles, $\rho^*(z)$, for athermal butane chains between hard walls. The density profiles are plotted as a function of the reduced distance from the wall, z. Simulation density profiles (○) are compared to the wall-PRISM predictions with $\hat{w}(K)$ from the FJC (dashed line) and NFJC (dotted line) models and the simulation $\hat{w}(K)$ (full line). Profiles are shown for systems with bulk densities of a) $\rho_b^*=1.336$, b) $\rho_b^*=1.048$ and c) $\rho_b^*=0.494$.

appeared in the simulation data, but are once again underestimated by all the models and positioned too close to the wall.

Figure 6.8 presents monomer density profiles for heptane at bulk monomer densities of ρ_b^*=0.784, 1.060 and 1.390 corresponding to packing fractions of 0.447, 0.604 and 0.793 respectively. Again the uppermost of the three profiles shows the whole of the region within the pore whilst the two remaining profiles concentrate on the region close to the wall. The various models for the intramolecular structure factor now yield different density profiles. Once again, at a low monomer density (ρ_b^*=0.784) all the models overestimate the contact value of the density and at a high monomer density (ρ_b^*=1.390) all the models underestimate the contact value of the density. It can be seen that as the density is raised from 0.784 to 1.390 the FJC model gives a progressively poorer representation of the density profile, incorrectly predicting the position and depth of the first trough in the profile and the subsequent following peak in the two higher density profiles. Of the remaining two models the profiles calculated using the simulation values for $\hat{w}(K)$ yield profiles that are in better agreement with the simulation results than the NFJC model. At the highest density shown (ρ_b^*=1.390) the depth of the first trough and the height of the following peak are still underestimated by the various models although they are correctly positioned.

Finally Figure 6.9 presents monomer density profiles for decane at bulk monomer densities of ρ_b^*=0.701, 1.056 and 1.380 corresponding to packing fractions of 0.400, 0.602 and 0.789 respectively. As with Figures 6.7 and 6.8 the uppermost profile shows the whole of the region within the pore whilst the remaining two profiles concentrate of the region close to the wall. It was not possible to solve the wall-PRISM equation for decane with the FJC model using the iteration scheme outlined in chapter 5. The iteration scheme produced non-convergent results regardless of the amount of mixing used between successive iterations in the iterative scheme. It was however possible to solve the PRISM equation with the FJC model at all densities attempted, the results of which will be presented in section 6.6. The monomer density profiles show that the wall-PRISM equation in conjunction with the single chain structure factor $\hat{w}(K)$ calculated from the simulation data is in poor agreement with the simulation data at low density and in better agreement at the higher density. The agreement between the simulation and theory is at best however qualitative. The NFJC model for $\hat{w}(K)$ gives

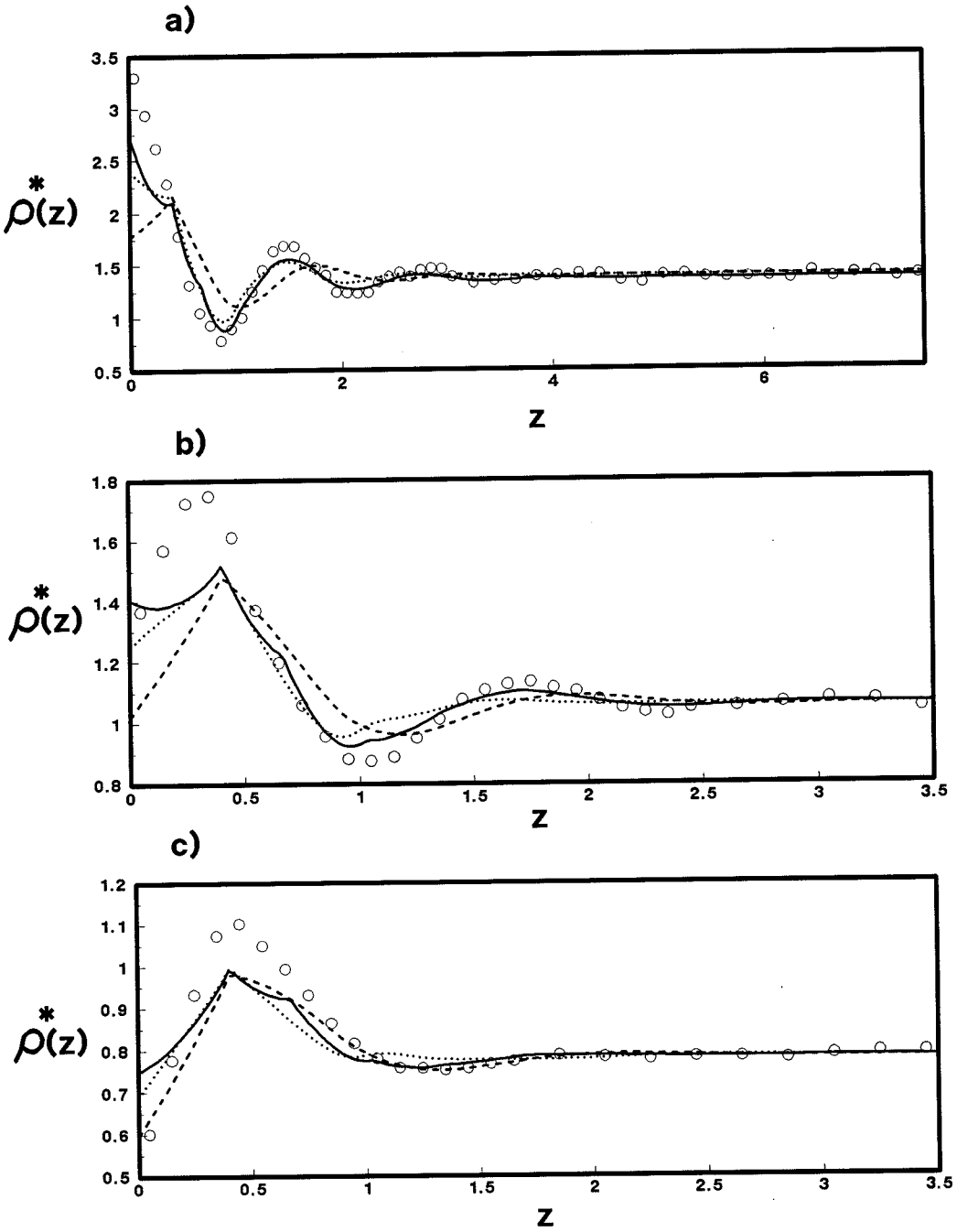

Figure 6.8 Monomer density profiles, $\rho^*(z)$ for athermal heptane chains between hard walls. The density profiles are plotted as a function of the reduced distance from the wall, z. Simulation density profiles (○) are compared to the wall-PRISM predictions with $\hat{w}(K)$ from the FJC (dashed line) and NFJC (dotted line) models and the simulation $\hat{w}(K)$ (full line). Profiles are shown for systems with bulk densities of a) $\rho_b^*=1.390$, b) $\rho_b^*=1.060$ and c) $\rho_b^*=0.784$.

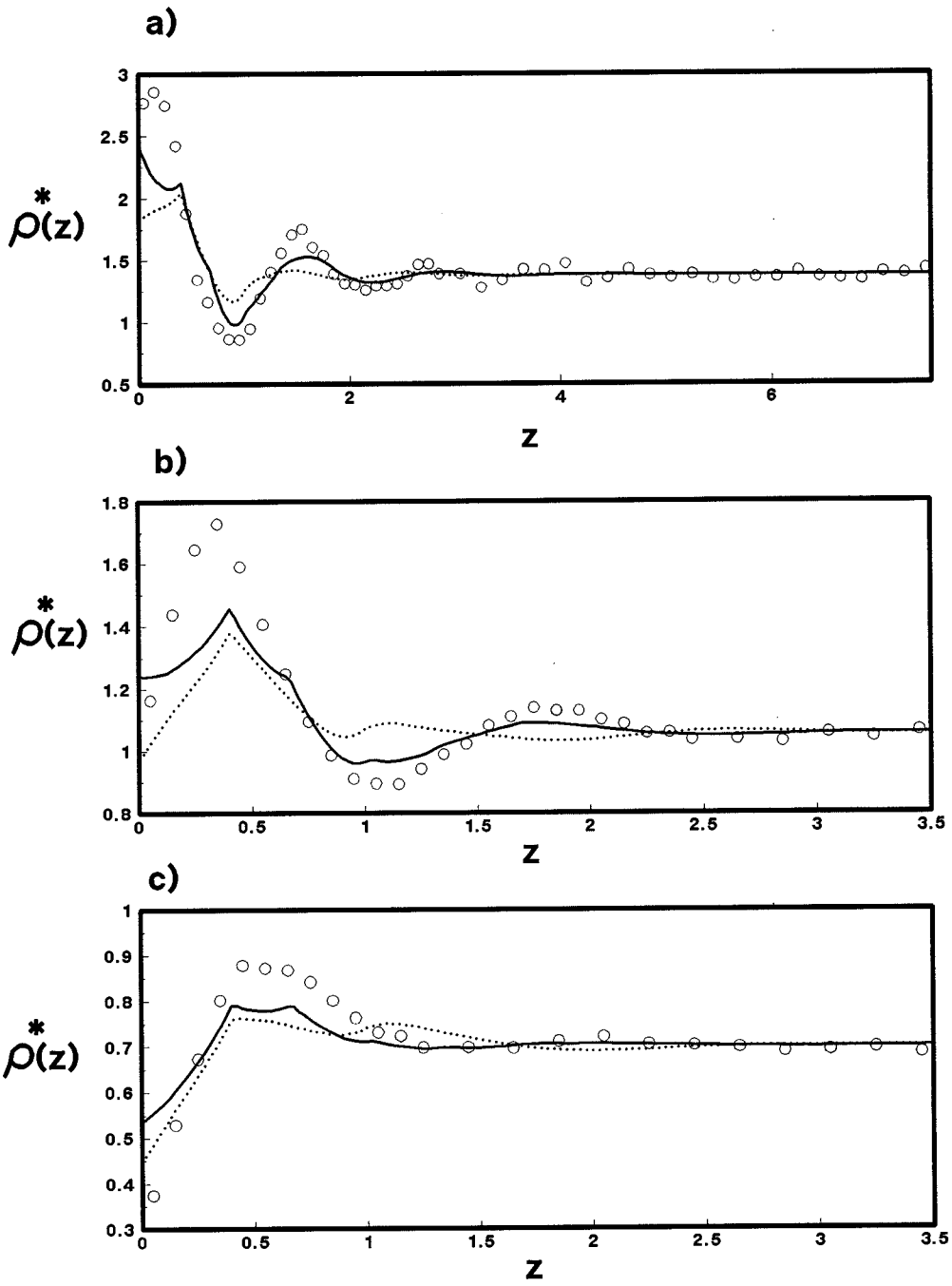

Figure 6.9 Monomer density profiles, $\rho^*(z)$, for athermal decane chains between hard walls. The density profiles are plotted as a function of the reduced distance from the wall, z. Simulation density profiles (○) are compared to the wall-PRISM predictions with $\hat{w}(K)$ from the FJC (dashed line) and NFJC (dotted line) models and the simulation $\hat{w}(K)$ (full line). Profiles are shown for systems with bulk densities of a) ρ_b^*=1.380, b) ρ_b^*=1.056 and c) ρ_b^*=0.701.

a significantly poorer representation of the density profile than the simulation $\hat{w}(K)$. A second peak is present in all the density profiles for decane with the NFJC model which is either absent from the simulation data or in a different position, depending on the value of the density.

6.5 Equations Of State For The Athermal Chains

The monomer density profiles obtained in our simulations were used to calculate the equations of state for the athermal alkanes by the method described in chapter 5. The density profiles close to the wall were extrapolated to contact and the resulting value of the density used to calculate the pressure from eqn (5.81). The pressures calculated using this method are presented in Tables 6.2-6.4. Also contained within the Tables are the pressures calculated using the wall-PRISM equation with the various models, once again by calculating the value of the density at contact with the wall. These results are also plotted in Figures 6.10-6.12.

Figure 6.10 and Table 6.2 show that all the models for butane overestimate the compressibility at low densities and underestimate the compressibility at high densities. The pressures calculated using the simulation $\hat{w}(K)$ in the wall-PRISM theory are higher than those calculated with the NFJC model at all densities. Similarly the pressures calculated with the NFJC $\hat{w}(K)$ are higher than those calculated with the FJC model. The agreement between the wall-PRISM theory with the various models for $\hat{w}(K)$ is poor and becomes progressively worse as the bulk monomer density rises. The equations of state of heptane and decane presented in Figures 6.11 and 6.12 and Tables 6.3 and 6.4 show similar features.

In the low density limit it is expected that $\beta P/\rho \rightarrow 1$, where ρ is the molecular density. If ρ is used to refer to the density of chain sites rather than the molecular density then we find that $\beta P/\rho \rightarrow 1/N$ in the low density limit, where N is the number of sites within the alkane chain. Thus for butane we expect to find $\beta P/\rho \rightarrow 0.25$ as $\rho \rightarrow 0$. Figures 6.10-6.12 show that our simulations with the alkane chains tend to the correct limiting values of the compressibility at low densities. The results of the wall-PRISM equation with the various models for $\hat{w}(K)$ clearly do not tend to the correct low density values for the compressibility. Comparison of the results of the wall-PRISM equation with simulations of diatomic molecules revealed that indeed the wall-PRISM equation does not correctly

ρ_b^*	βP^*			
	Simulation	PRISM (FJC)	PRISM (NFJC)	PRISM (SIM)
0.1108±0.0011	0.0310±0.0019	0.0638	0.0643	0.0645
0.2995±0.0021	0.1223±0.0015	0.2091	0.2130	0.2145
0.4947±0.0023	0.3036±0.0002	0.4165	0.4295	0.4369
0.6827±0.0029	0.6066±0.0039	0.6876	0.7175	0.7369
0.8236±0.0043	0.9920±0.0039	0.9489	0.9992	1.0339
0.9208±0.0057	1.3426±0.0201	1.1646	1.2343	1.2838
1.0485±0.0115	2.0019±0.0241	1.5003	1.6039	1.6805
1.1492±0.0158	2.7138±0.0519	1.8143	1.9534	2.0589
1.2527±0.0289	3.5577±0.1757	2.1903	2.3764	2.5210
1.3360±0.0430	4.3950±0.3099	2.5385	2.7720	2.9575
1.3736±0.0404	5.0176±0.3308	2.7107	2.9689	3.1746

Table 6.2 Equation of state data for athermal butane. The table presents the results of simulations between hard walls and the wall-PRISM theory data. The wall-PRISM results were obtained with intramolecular correlation functions from the freely jointed chain model (FJC), the non-overlapping freely jointed chain model (NFJC) and from simulation (SIM).

ρ_b^*	βP^*			
	Simulation	PRISM (FJC)	PRISM (NFJC)	PRISM (SIM)
0.0996±0.0011	0.0150±0.0014	0.0387	0.0418	0.0426
0.4030±0.0028	0.1173±0.0038	0.2200	0.2368	0.2465
0.5963±0.0028	0.2708±0.0011	0.3867	0.4286	0.4567
0.6951±0.0213	0.3755±0.0030	0.4898	0.5542	0.5973
0.7848±0.0037	0.5218±0.0082	0.5965	0.6878	0.7492
0.8829±0.0041	0.7381±0.0090	0.7291	0.8589	0.9462
0.9715±0.0069	0.9856±0.0160	0.8649	1.0398	1.1569
1.0603±0.0094	1.2864±0.0202	1.0181	1.2504	1.4053
1.1575±0.0116	1.7648±0.0283	1.2077	1.5206	1.7278
1.2548±0.0126	2.3543±0.0243	1.4233	1.8407	2.1109
1.3377±0.0238	3.0880±0.0224	1.6310	2.1605	2.4785
1.3909±0.0275	3.5537±0.0755	1.7785	2.3940	2.7283

Table 6.3 Equation of state data for athermal heptane. The table presents the results of simulations between hard walls and the wall-PRISM theory data. The wall-PRISM results were obtained with intramolecular correlation functions from the freely jointed chain model (FJC), the non-overlapping freely jointed chain model (NFJC) and from simulation (SIM).

ρ_b^*	βP^*			
	Simulation	PRISM (FJC)	PRISM (NFJC)	PRISM (SIM)
0.1041±0.0011	0.0105±0.0007	-	0.0371	0.0380
0.4063±0.0037	0.0848±0.0020	-	0.1945	0.2160
0.5981±0.0045	0.2104±0.0048	-	0.3439	0.4027
0.7010±0.0056	0.3013±0.0040	-	0.4467	0.5349
0.7897±0.0068	0.4252±0.0118	-	0.5504	0.6711
0.8805±0.0079	0.5760±0.0054	-	0.6734	0.8355
0.9814±0.0088	0.7889±0.0265	-	0.8338	1.0526
1.0569±0.0084	1.0554±0.0272	-	0.9729	1.2422
1.1570±0.0137	1.4507±0.0492	-	1.1873	1.5363
1.2564±0.0185	1.9976±0.0997	-	1.4408	1.8864
1.3338±0.0322	2.4963±0.0799	-	1.6720	2.2055
1.3803±0.0339	2.8069±0.0823	-	1.8312	2.4254

Table 6.4 Equation of state data for athermal decane. The table presents the results of simulations between hard walls and the wall-PRISM theory data. The wall-PRISM results were obtained with intramolecular correlation functions from the non-overlapping freely jointed chain model (NFJC) and from simulation (SIM). Results are not presented for the wall-PRISM theory in conjunction with the FJC model as the iterative solution scheme was not convergent for the state points in the table.

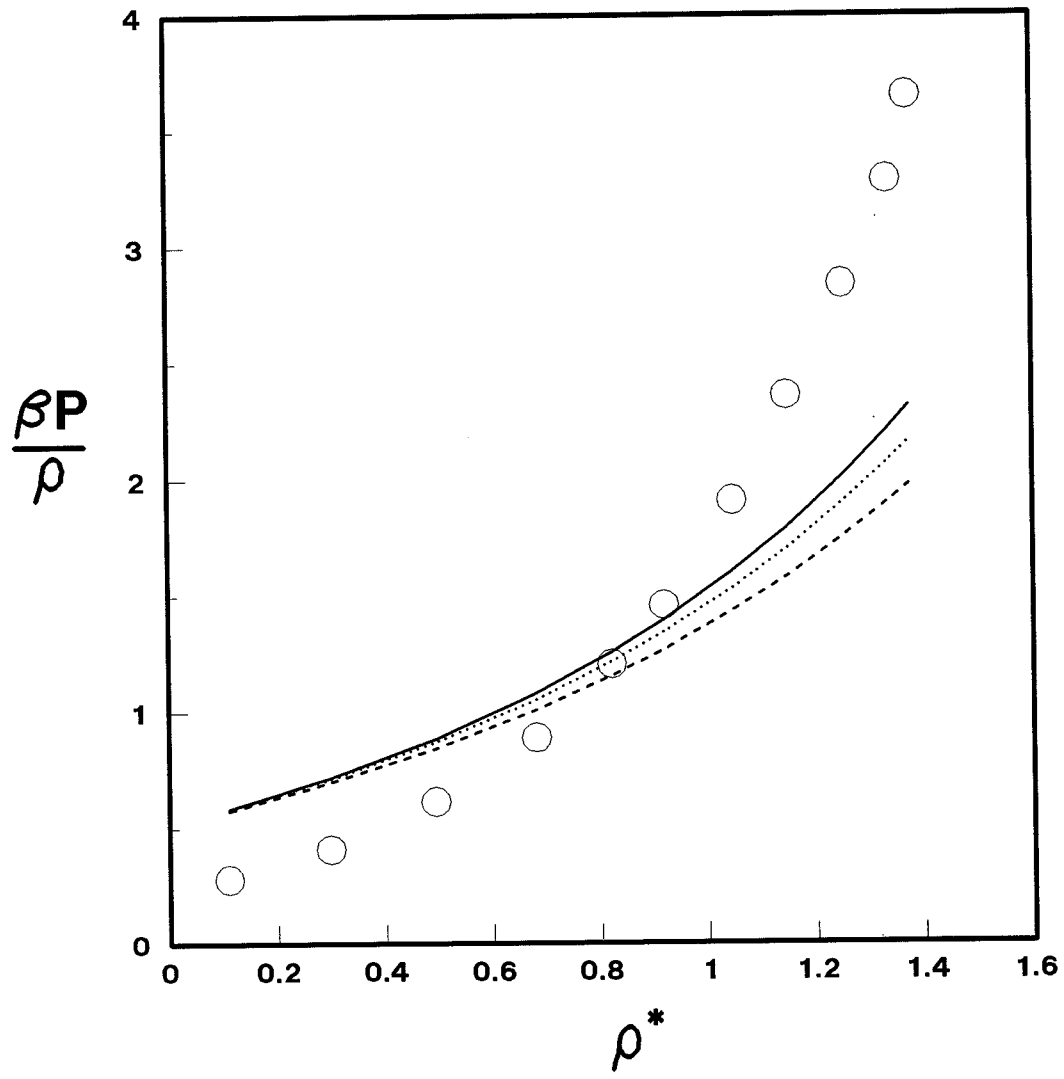

Figure 6.10 The equation of state for athermal butane from simulation (○) and the wall-PRISM equation with $\hat{w}(K)$ from the FJC (dashed line) and NFJC (dotted line) models and the simulation $\hat{w}(K)$ (full line). In the figure the compressibility is plotted against the monomer density ρ^*.

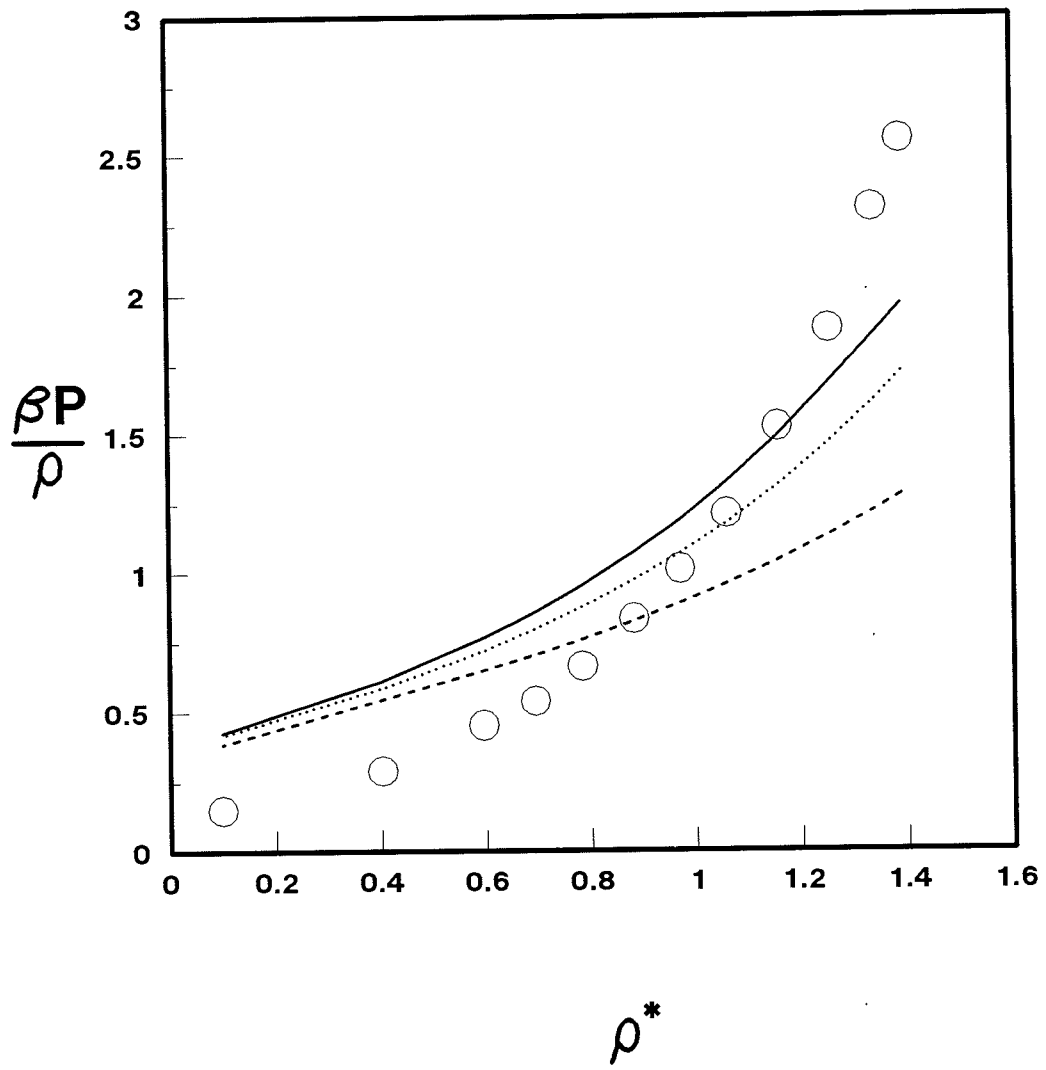

Figure 6.11 The equation of state for athermal heptane from simulation (○) and the wall-PRISM equation with $\hat{w}(K)$ from the FJC (dashed line) and NFJC (dotted line) models and the simulation $\hat{w}(K)$ (full line). In the figure the compressibility is plotted against the monomer density ρ^*.

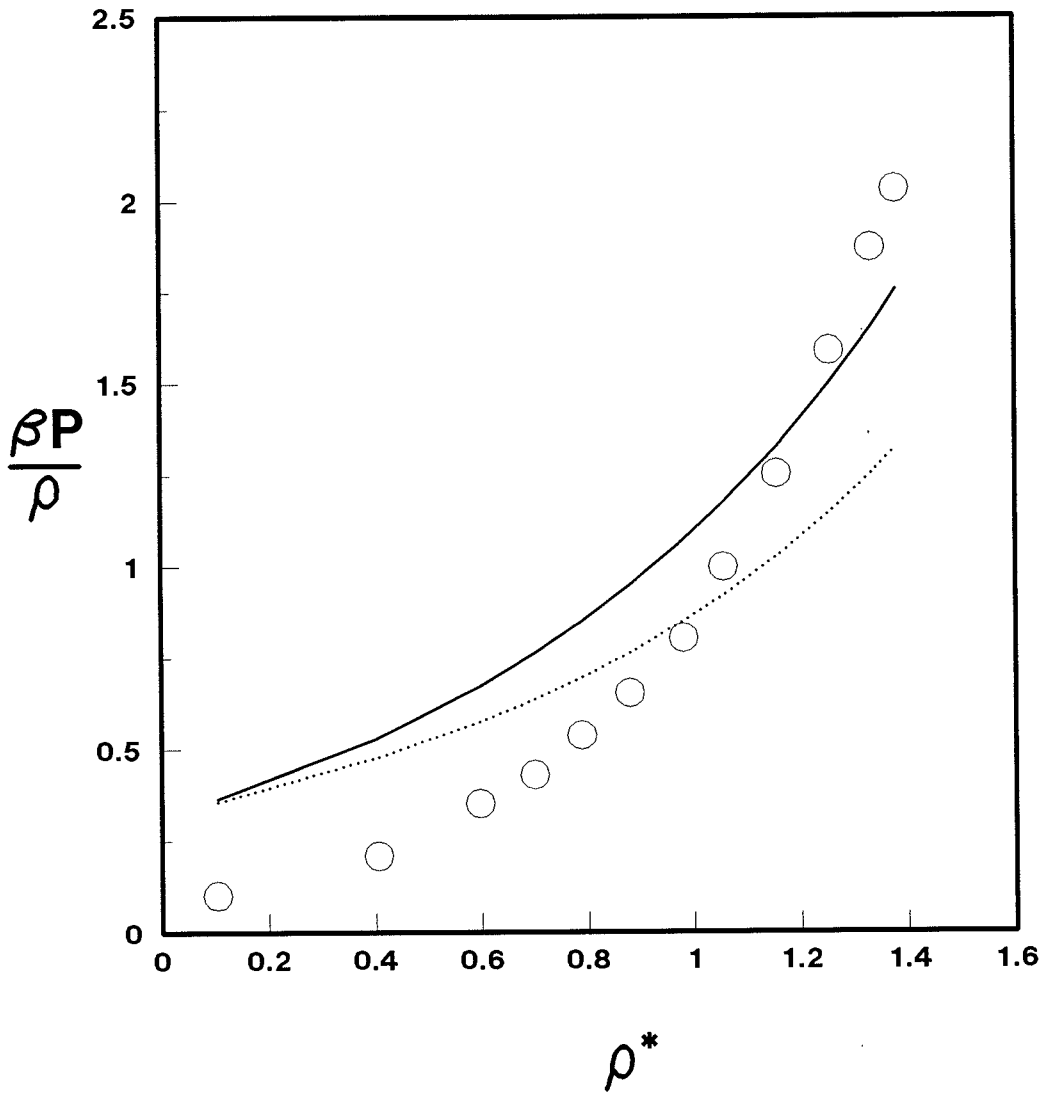

Figure 6.12 The equation of state for athermal decane from simulation (○) and the wall-PRISM equation with $\hat{w}(K)$ from the NFJC (dotted line) model and the simulation $\hat{w}(K)$ (full line). In the figure the compressibility is plotted against the monomer density ρ^*.

reproduce the ideal gas behaviour [7].

These results show that the equations of state calculated by the wall-PRISM theory are in poor agreement with the simulation equations of state. The first stage in solving the wall-PRISM equation is to first solve the PRISM equation for the bulk fluid. It is therefore of interest to investigate the accuracy of the PRISM equation in the calculation of the intermolecular site-site radial distribution function for athermal alkanes. This correlation function is of importance because it would be used in thermodynamic perturbation theory to calculate the free energy of the attractive perturbation to the athermal alkane reference system, through eqn (5.5).

6.6 The Site-Site Radial Distribution Functions

Simulations were performed with athermal butane, heptane and decane in the bulk. Three simulations were performed for each of the molecules at bulk densities corresponding to the densities of the bulk fluids in Figures 6.7-6.9. The intermolecular site-site radial distribution functions $g_{\alpha\delta}(r_{\alpha\delta})$ calculated in these simulations are presented in Figures 6.13-6.15 along with the corresponding distribution functions calculated using the PRISM theory with the various models for $\hat{w}(K)$.

Figure 6.13 presents the radial distribution functions calculated for butane. There is in general a close agreement between the results of the PRISM theory with the various models for $\hat{w}(K)$. At the lowest density presented, $\rho_b^*=0.494$, all the models predict a peak in $g_{\alpha\delta}(r_{\alpha\delta})$ which is significantly smaller than the simulation peak and in the wrong position. As the density is raised the agreement between the PRISM theory and the simulation results improves. At the highest density presented, $\rho_b^*=1.336$, the agreement between the PRISM theory and the simulation results is reasonable although the PRISM theory underestimates the height of the first peak.

In Figure 6.14 the radial distribution functions are presented for heptane. At densities of $\rho_b^*=0.784$ and $\rho_b^*=1.060$ the agreement between the simulation results and the PRISM theory using the FJC model is good. However, at the highest density shown, $\rho_b^*=1.390$, the FJC model is in poor agreement with the simulation results, incorrectly predicting the positions and heights of the first peak and the following trough. At this density the agreement between the simulation results and the PRISM theory with the NFJC model and the simulation $\hat{w}(K)$ is somewhat better than the FJC model although

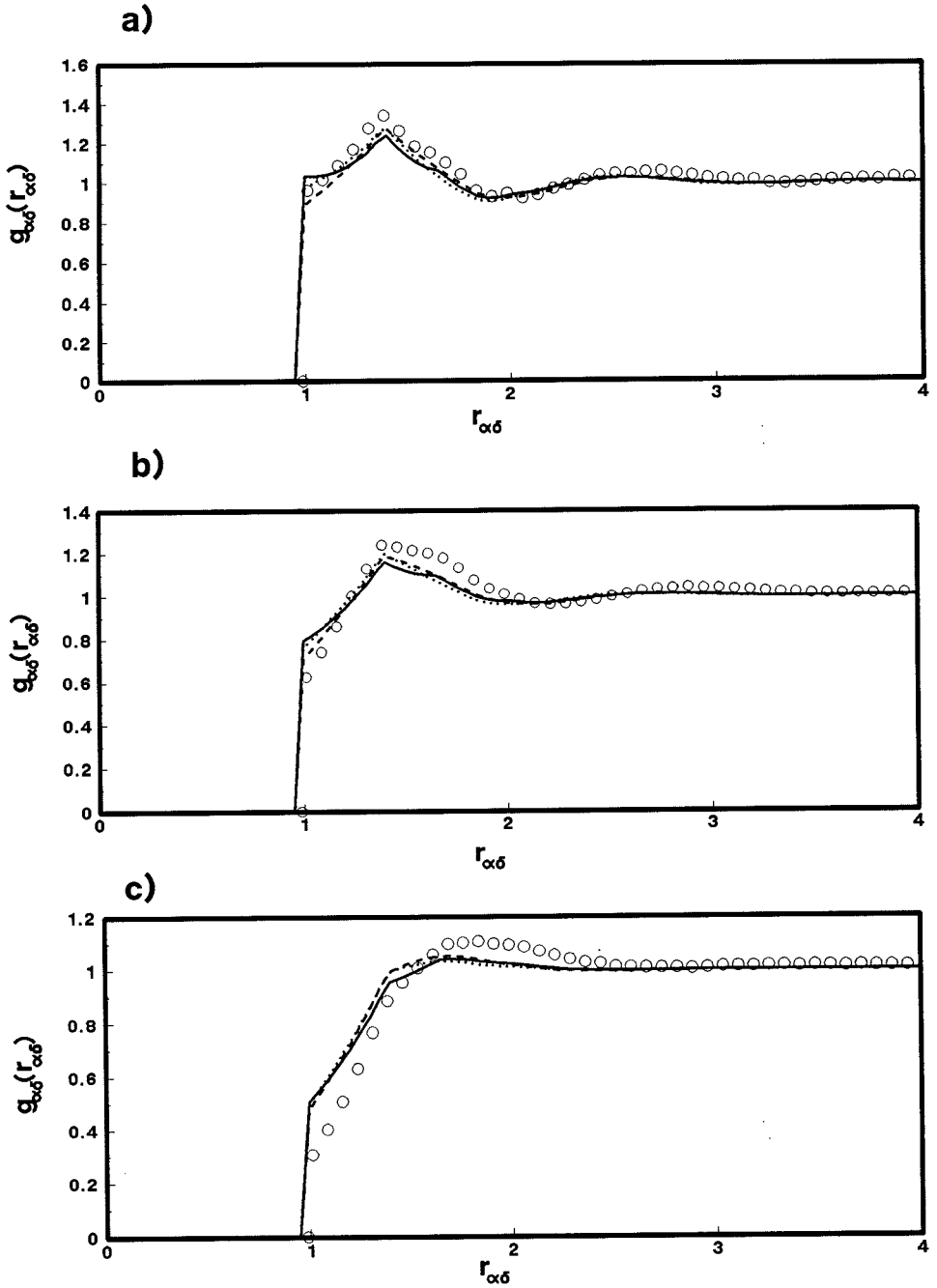

Figure 6.13 Site-site radial distribution functions, $g_{\alpha\delta}(r_{\alpha\delta})$ for butane plotted as a function of the reduced distance $r_{\alpha\delta}$. Simulation values for $g_{\alpha\delta}(r_{\alpha\delta})$ (○) are compared to the PRISM predictions with $\hat{w}(K)$ from the FJC (dashed line) and NFJC (dotted line) models and the simulation $\hat{w}(K)$ (full line). The radial distribution functions are shown for systems with bulk densities of a) $\rho_b^*=1.336$, b) $\rho_b^*=1.048$ and c) $\rho_b^*=0.494$.

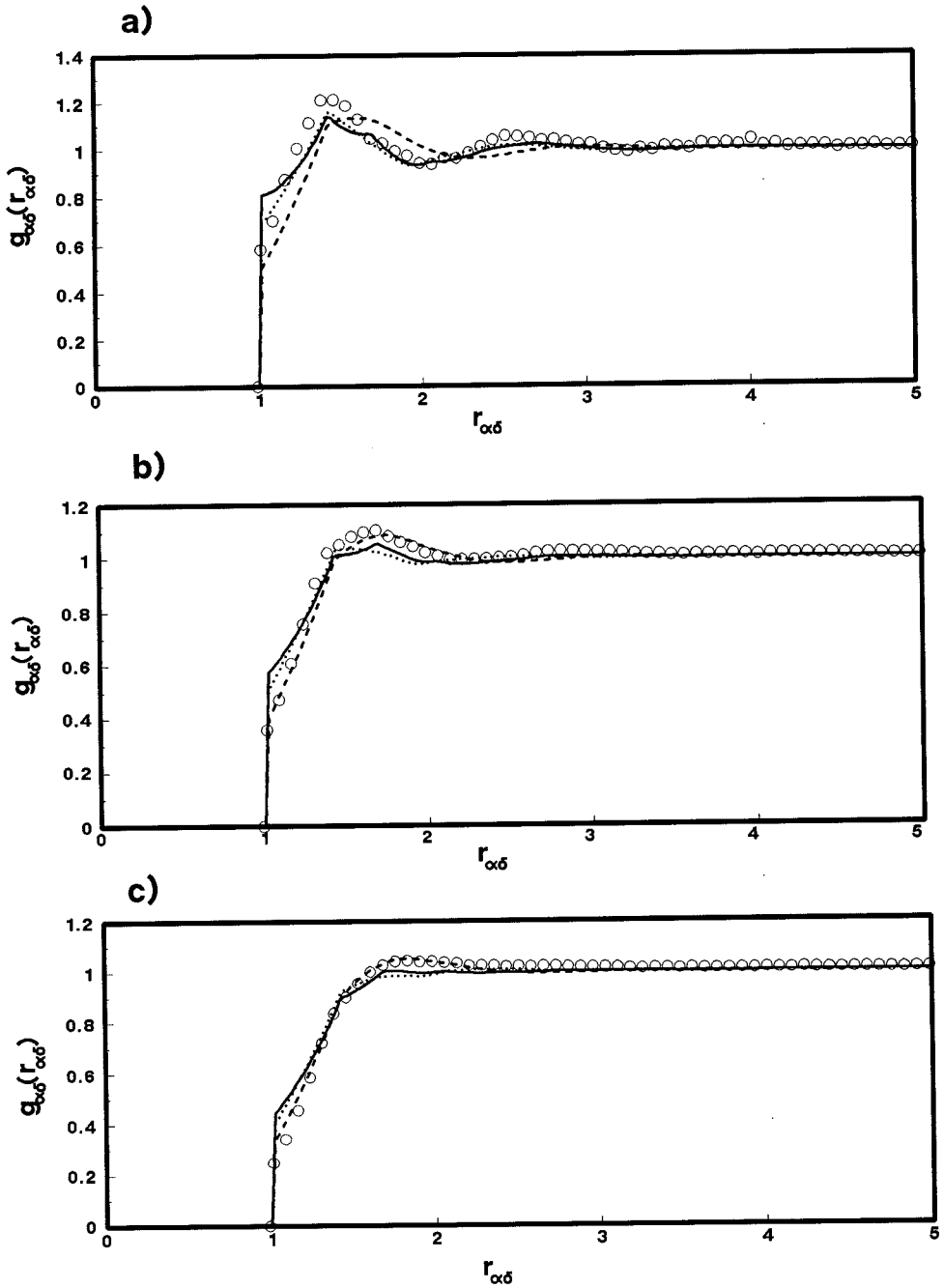

Figure 6.14 Site-site radial distribution functions, $g_{\alpha\delta}(r_{\alpha\delta})$ for heptane plotted as a function of the reduced distance $r_{\alpha\delta}$. Simulation values for $g_{\alpha\delta}(r_{\alpha\delta})$ (O) are compared to the PRISM predictions with $\hat{w}(K)$ from the FJC (dashed line) and NFJC (dotted line) models and the simulation $\hat{w}(K)$ (full line). The radial distribution functions are shown for systems with bulk densities of a) $\rho_b^*=1.390$, b) $\rho_b^*=1.060$ and c) $\rho_b^*=0.784$.

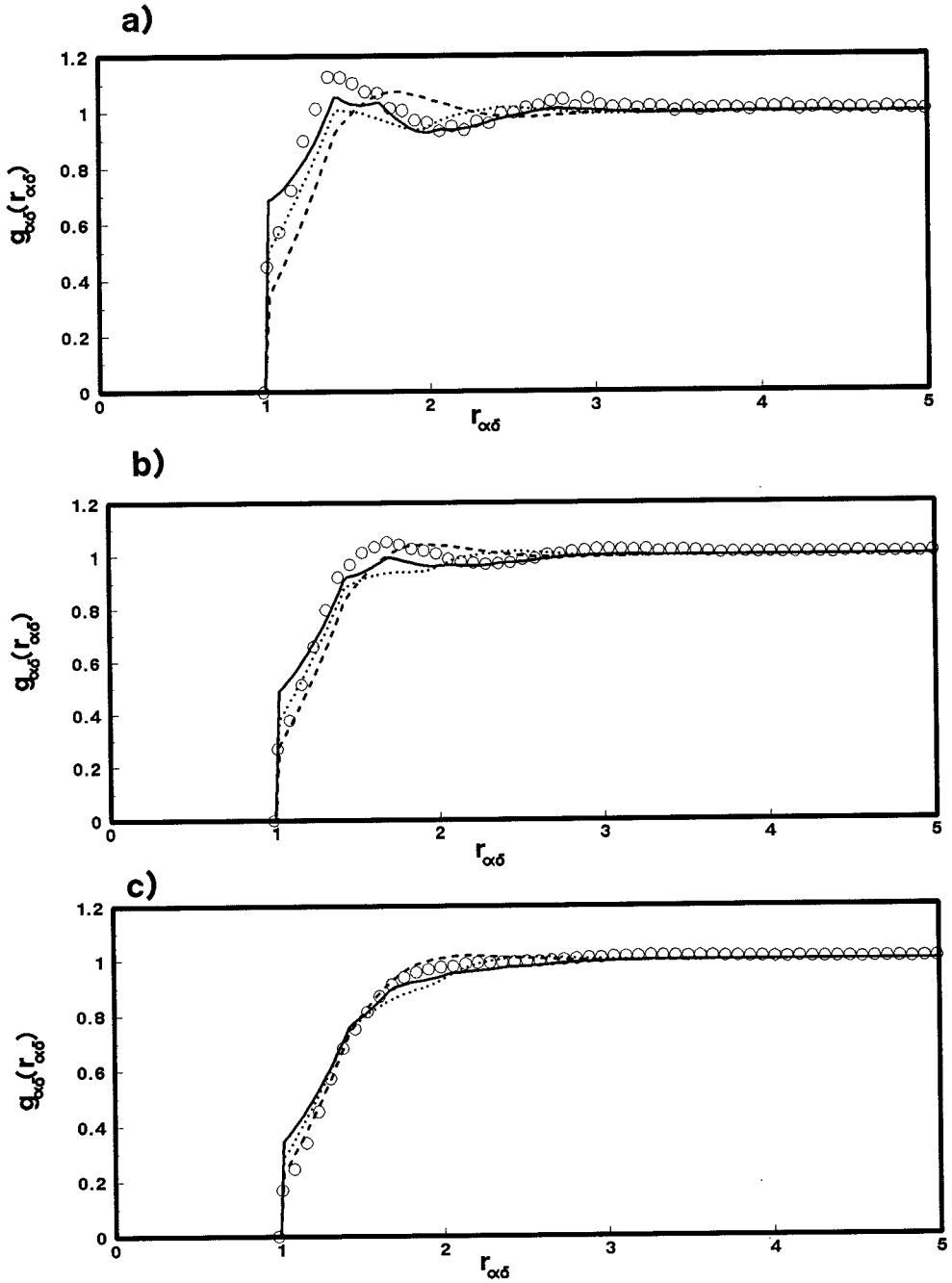

Figure 6.15 Site-site radial distribution functions, $g_{\alpha\delta}(r_{\alpha\delta})$ for decane plotted as a function of the reduced distance $r_{\alpha\delta}$. Simulation values for $g_{\alpha\delta}(r_{\alpha\delta})$ (○) are compared to the PRISM predictions with $\hat{w}(K)$ from the FJC (dashed line) and NFJC (dotted line) models and the simulation $\hat{w}(K)$ (full line). The radial distribution functions are shown for systems with bulk densities of a) $\rho_b^*=1.380$, b) $\rho_b^*=1.056$ and c) $\rho_b^*=0.701$.

again the height of the first peak is underestimated.

Finally the radial distribution functions for decane are presented in Figure 6.5. At the lowest density present, $\rho_b^*=0.701$, all the models used with the PRISM theory yield results that are in reasonable agreement with the simulation results. As the density of the bulk fluid is raised from $\rho_b^*=0.701$ to $\rho_b^*=1.380$ the agreement between the simulation data and the PRISM theory with the FJC and NFJC models becomes progressively poorer. The agreement between the simulation data and the PRISM theory with the simulation $\hat{w}(K)$ is better, although it is at best only qualitative.

6.7 Conclusions

Simulations of athermal alkane systems between hard walls have been performed. The density profiles recorded during the simulations were compared to the density profiles calculated by the wall-PRISM equation in conjunction with various models for the intramolecular structure of the alkane chains. The wall-PRISM equation was found to qualitatively reproduce the density profiles between the walls. The agreement between wall-PRISM theory and the simulation data was better at high densities than low densities. For the shortest alkane studied, butane, the density profiles calculated with the various models for $\hat{w}(K)$ were all of similar accuracy when compared to the simulation data. However for the longer alkane molecules, heptane and decane, the predictions of the wall-PRISM equation with the simulation $\hat{w}(K)$ were significantly more accurate than the profiles calculated with the FJC and NFJC models. From this it would seem that the FJC and NFJC models for $\hat{w}(K)$ yield only qualitative representations of the intramolecular structure of alkane chains. The wall-PRISM equation was found to overestimate the density at the wall at low bulk densities and underestimate the density at the wall at high bulk densities. A similar overestimation of the contact value of the density at low bulk densities and underestimation of the contact value of the density at high bulk densities was observed in simulations of tangent hard-sphere chains between walls [8].

The discrepancies between the wall-PRISM equation and the simulation data could be due to a number of reasons. The results of the wall-PRISM equation might be improved if the intramolecular and intermolecular correlation functions in the PRISM theory and in the wall-PRISM theory were determined in a self-consistent manner. As

described in section 5.3 the PRISM theory was originally formulated in such a way that the intramolecular and intermolecular correlation functions were independent of one another. This approximation has been addressed by the reformulation of the PRISM theory in a self-consistent manner [9]. At present the wall-PRISM equation has not been formulated in such a self-consistent manner. The density profiles obtained in the simulations and from the wall-PRISM theory were used to calculate equations of state for athermal butane, heptane and decane. The agreement between the wall-PRISM results equations of state and the simulation equations of state was at best qualitative. It would therefore seem that the wall-PRISM theory in its present form is not of sufficient accuracy to be used to calculate the athermal contributions to the pressure of an alkane system. It is hoped however that the simulation equations of state will be of use in future investigations of methods of calculating the equations of state for these systems via PRISM theory.

Simulations were performed of athermal butane, heptane and decane in the bulk. The predictions of the PRISM equation for the intermolecular site-site radial distribution function were compared to the simulation data using two models of the alkane intramolecular structure, the FJC and the NFJC models. The FJC model of the alkane chains was found to give a good representation of the intermolecular site-site radial distribution function for heptane and butane at low and intermediate densities. At higher densities the agreement was less good. The PRISM equation with this model gave poor predictions for the structure of decane at low, intermediate and high densities. The NFJC model of the alkanes was found to be of comparable accuracy to that of the FJC model in predicting the structure of butane and heptane. However the predictions of this approximation were significantly worse than the FJC model for the structure of decane. In all the simulations performed the agreement between the simulation data and the PRISM theory with the simulation $\hat{w}(K)$ was reasonable. Discrepancies between the PRISM theory with the simulation $\hat{w}(K)$ and the simulation results could be due to a number of reasons. It is possible that the closure relation used in conjunction with the PRISM theory, a Percus-Yevick type closure, could be a source of some of the discrepancies between the PRISM theory and the simulation data. Yethiraj and Hall [10] solved the PRISM theory for tangent hard-sphere chains with a Yukawa closure for the direct correlation function c(r) rather than the Percus-Yevick closure for c(r) of eqn

(5.24). This closure relation can be written as,

$$c(r) = K \frac{\exp(-z[r/\sigma - 1])}{r} \quad , \quad r > \sigma \ , \tag{6.17}$$

where K and z are density dependent parameters. The value of K is chosen such that the PRISM theory with this closure reproduces the contact value of $g_{\alpha\delta}(r_{\alpha\delta})$ obtained from simulations. The parameter z is then fixed by calculating the compressibility of the chain fluid from the contact value of the radial distribution function via an extension of eqn (5.84) and fitting the results to the compressibilities calculated using Monte Carlo simulations. Using this closure relation the radial distribution functions were obtained for tangent 4-mer and 8-mer chains. The resulting radial distribution functions were in good agreement with the simulation data, although they tended to slightly overestimate the value of $g_{\alpha\delta}(r_{\alpha\delta})$ close to contact. It would be of interest for future work to apply this approach to athermal alkane systems to see if the accuracy of the radial distribution functions calculated from PRISM could be improved.

6.8 References

[1] J. P. Ryckaert and A. Bellemans, "Molecular dynamics of liquid n-butane near its boiling point", Chem. Phys. Lett., **30**, 123-125, (1975); "Molecular dynamics of liquid alkanes", J. Chem. Soc. Faraday Discuss., **66**, 95-106, (1978).

[2] N.G. Almarza, E. Enciso and F.J. Beremejo, "Monte Carlo simulations of liquid n-alkanes. I. Intramolecular structure and thermodynamics", J. Chem. Phys., **96**, 4625-4632, (1992).

[3] N.G. Almarza, E. Enciso, J. Alonso, F.J. Beremejo and M. Avarez, "Monte Carlo simulations of liquid n-butane", Mol. Phys., **70**, 485-504, (1990).

[4] M.P. Allen and D.J. Tildesley, "Computer simulation of liquids", Oxford science publications, (1987).

[5] A. Yethiraj and C.K. Hall, "Monte Carlo simulations and integral equation theory for microscopic correlations in polymeric fluids", J. Chem. Phys., **96**, 797-807, (1992).

[6] J.G. Curro, K.S. Schweizer, G.S. Grest and K. Kremer, "A comparison between integral-equation theory and molecular dynamics simulations of dense, flexible polymer liquids", J. Chem. Phys., **91**, 1357-1364, (1989).

[7] A. Yethiraj, J.G. Curro, K.S. Schweizer and J.D. McCoy, "Microscopic equations of state of polyethylene: Hard-chain contribution to the pressure", J. Chem. Phys., **98**, 1635-1646, (1993).

[8] A. Yethiraj and C.K. Hall, "Integral equation theory for the adsorption of chain fluids in slitlike pores", J. Chem. Phys., **95**, 3749-3755, (1991).

[9] K.S. Schweizer, K.G. Honnell and J.G. Curro, "Reference interaction site model theory of polymeric liquids: Self-consistent formulation and nonideality effects in dense solutions and melts", J. Chem. Phys., **96**, 3211-3225, (1992).

[10] A. Yethiraj and C.K. Hall, "Local structure of fluids containing chain-like molecules: Polymer reference interaction site model with a Yukawa closure", J. Chem. Phys., **93**, 5315-5321, (1990).

7. Conclusions

In chapter 2 we presented simulation results for chlorine, based on two representations of the atoms in the molecule, the RST and the DLJ representation of chlorine. Good agreement was obtained between the two potential functions and previous simulation and experimental data. Qualitatively, neither of the two potential functions used was found to be superior to the other. Whilst anisotropies in the interactions between the atoms in molecules are undoubtedly important in the determination of some properties of a system, they appear to play no role in the determination of phase equilibria. We conclude that for chlorine, the liquid-vapour phase envelope is not sensitive to the details of the potential model and therefore cannot be used to improve the model of the intermolecular forces. The implementation of highly detailed anisotropic potentials adds greatly to the expense of a Gibbs simulation. The increased computational cost in doing so does not appear to be rewarded by a commensurate improvement in the accuracy of the simulation results.

In chapter 2 we also presented the results of our simulations with DLJ molecules with a range of bondlengths. The phase diagrams were directly obtained for these molecules using the Gibbs ensemble Monte Carlo simulation method. The phase diagrams obtained in this way were found to obey the Law of Corresponding States in the gaseous phase but not in the liquid phase. We can conclude from this that the molecular anisotropy forces the phase diagram of the species to depart from the Law of Corresponding States in the liquid phase but not in the gaseous phase.

Finally in chapter 2 we investigated the accuracy of the RISM equation, an integral equation theory of liquid structure. The RISM equation was solved for a number of the DLJ molecules at various points along their respective orthobaric curves. The results from the RISM equation were then compared to the results from the Gibbs simulations and found to be in good agreement in the liquid phase, but in rather poorer agreement in the gaseous phase.

In chapter 4 we presented the results of our investigations into the properties of linear polymer chains between walls. The adsorption or depletion of the chains at the walls was found to be determined by competing entropic and energetic factors. The competition between these factors is a function of the solvent-wall and polymer-wall interactions along with their relative magnitudes. Between hard walls the polymer chains

were depleted at the walls and site profiles for the chains demonstrated that the first site was more likely to be at the walls than sites within the middle of the chain. This depletion of the sites in the middle of the chains from the walls is due to the fact that it is entropically more favourable to have the head of the polymer chain close to the walls than the body of the chain. Placed between 9-3 walls the polymer chains were either depleted or enhanced at the walls depending on the relative strengths of the wall-polymer and wall-solvent interactions. Under conditions favouring adsorption of the chains at the walls, the chain's site profiles became essentially identical. This indicates that entropic factors were no longer important in determining the chain's conformational properties between the walls. As the strength of the wall-polymer interaction was increased the polymer chain adsorbs at the wall and elongates in the direction parallel to the wall becoming essentially two dimensional as it does so. Under conditions which favour the depletion of the chains at the walls the head of the chain is again more likely to be at the wall than the rest of the sites in the chain. Entropic effects are therefore once again playing a role in determining the chain's conformation. The scaling behaviour of the chains between the various types of walls was found to be sensitive to the details of the wall-polymer and wall-solvent interactions along with their relative magnitudes. Under appropriate conditions the chains were found to scale with the theoretically determined scaling exponent. To the best of our knowledge this is the first time that this particular scaling exponent has been calculated and verified by off-lattice simulations. The value of the scaling exponent can also take on values different to those predicted by theory, depending on the details of the various particle-wall interactions.

In chapter 6 we presented the results of our simulations of athermal alkane systems between hard walls. The density profiles recorded during the simulations were compared to the density profiles calculated by the wall-PRISM equation in conjunction with various models for the intramolecular structure of the alkane chains. The wall-PRISM equation was found to qualitatively reproduce the density profiles between the walls. The agreement between wall-PRISM theory and the simulation data was better at high densities than low densities. The wall-PRISM equation was found to overestimate the density at the wall at low bulk densities and underestimate the density at the wall at high bulk densities.

The discrepancies between the wall-PRISM equation and the simulation data could

be due to a number of reasons. The results of the wall-PRISM equation might be improved if the intramolecular and intermolecular correlation functions in the PRISM theory and in the wall-PRISM theory were determined in a self-consistent manner. As described in section 5.3 the PRISM theory was originally formulated in such a way that the intramolecular and intermolecular correlation functions were independent of one another. At present the wall-PRISM equation has not been formulated in such a self-consistent manner. Possible future work could focus on the formulation of the wall-PRISM equation in a self-consistent manner to try to improve the accuracy of the wall-PRISM theory. The density profiles obtained in the simulations and from the wall-PRISM theory were used to calculate equations of state for athermal butane, heptane and decane. The agreement between the wall-PRISM results equations of state and the simulation equations of state was at best qualitative. It would therefore seem that the wall-PRISM theory in its present form is not of sufficient accuracy to be used to calculate the athermal contributions to the pressure of an alkane system. It is hoped however that the simulation equations of state will be of use in future investigations of methods of calculating the equations of state for these systems via PRISM theory.